Numerical Analysis of the Effects of Climate Change on Slope Stability

Owen Davies BSc (Hons) MSc

A thesis submitted for the degree of Doctor of Philosophy (Ph.D) at Newcastle University

School of Civil Engineering and Geosciences

Newcastle University

Newcastle

NE1 7RU

June 2011

Abstract

Embankments and cuttings form an integral part of the infrastructure of the UK. These earthwork structures are susceptible to a number of external influences which can ultimately affect their stability. Climate is one of these influences. There have been many observational correlations drawn between climate and slope deformation and eventual failure. A change in climate is therefore likely to impact on slope stability. It is widely agreed within the scientific community that the climate is changing. Future climates are likely to consist of higher average temperatures, wetter winters and drier summers. It is therefore important that we assess the impacts of future climate on slope stability in order to maintain vital infrastructure.

This thesis describes the development of a novel numerical modelling procedure which allows the assessment of the effects of climate on slope deformation and rate of failure. The procedure employs the use of established hydrological and geotechnical numerical models to firstly calculate the pore pressure response to climate and secondly calculate the mechanical response to pore pressure. The hourly climate data required by the modelling procedure can be obtained from MET office weather stations for back analysis simulations or can be generated for present and future climates using a weather generator. The numerical modelling procedure has been used with present and future climatic data to assess the impacts of climate change on a diagnostic embankment and a cutting in the Newbury area. The procedure has also been used with historical weather data to back analyse an instrumented natural slope in Belfast, in order to determine the failure mechanism.

The development and implementation of the modelling procedure lead to the following key findings. Firstly, laboratory and field permeability measurement techniques are wholly inadequate in measuring macroscopic permeability characteristics of clay slopes. Secondly, slope deformation magnitude is closely linked to annual maximum pore pressures. Wet years and increased wet year frequency will therefore considerably increase deformation and failure rate. Thirdly, the permeability of a slope will determine whether it will be more or less susceptible to increased failure rates when subjected to a future climate scenario. The strength of the study presented here is the amalgamation of the three separate disciplines of climatology, hydrology and geotechnical engineering in order to quantify the significance of each on the stability of slopes.

Acknowledgements

My thanks go to my supervisors Dr Mohamed Rouainia and Dr Stephanie Glendinning for their continual support and encouragement throughout the preparation of this Thesis.

I would also like to acknowledge the help and support of the BIONICS project, headed by Dr Stephanie Glendinning. Being allied to this project enabled me to work alongside academic and industrial researchers without whom this work would not have been possible. In particular I would like to thank Dr Steve Birkinshaw and Dr Paul Hughes, of Newcastle University, for their continuous support and Mott Macdonald Ltd for provision of their extensive research in the area of climatic effects on slope stability.

Thanks also to Mr Rob Hiley of Newcastle University for his help and advice during the model development stage of this work.

I would also like to thank Victor Terente of Atkins Ltd, Newcastle, for his enthusiasm and support with the Belvoir park numerical study.

Thanks also to Ruth Williams for her unwavering support throughout this project.

Contents

Figures

Tables

Chapter 1. Introduction

1.1 Introduction

There is now agreement within the scientific community that the climate is changing and those changes have been quantified for a number of scenarios within the UK by the Tyndall Centre for Climate Change Research (Hulme et al 2002). Engineers must assess how that change will affect infrastructure in order to prepare for such change and minimise disruption. Infrastructure slopes and cuttings constructed within a clay material are susceptible to seasonal changes in pore water pressures, these seasonal pore pressure changes have been monitored by a number of authors (Anderson, 1980,. Smethurst et al, 2006., Ridley et al, 2003 amongst others). Authors have used these observations to numerically model seasonal affects of a present climate on infrastructure (Kovacevic et al, 2001., Nyambayo, 2004., O'Brien et al, 2004) whereby an average summer suction has been applied to a geotechnical model boundary and then an average winter suction applied. This thesis has built upon previous modelling work by applying a future climate scenario to infrastructure slopes. As there is obviously no observational data on pore water pressure change for a future climate the approach adopted within this modelling is to use generated future climatic data from a weather simulator. The effects of this climate on pore water pressure changes will then be modelled within a hydrological model. To fully understand the effects of a changing climate on infrastructure slopes we must therefore first fully understand the effects of a current climate on slopes.

The primary way in which climate affect slopes is through the infiltration and extraction of water. The water within a slope can have several effects on the stability of the slope. If the slope becomes saturated the weight of the slope increases, the pore pressures increase and therefore the effective stresses within the slope will decrease resulting in a loss of shear strength. As the slope becomes unsaturated the weight of the slope decreases and pore pressures decrease. This leads to an increase in effective stress levels within the slope which in turn results in an increase in shear strength within the soil. Suctions will also develop within the pore spaces in a partially saturated soil. These suctions are due to capillary action within the pore spaces. The suctions will also lead to an increase in effective stress and will also lead to increased shear strength within the partially saturated soil. The seasonal cyclic changes in effective stress may

lead to the slope swelling during saturation (winter) and shrinking under drainage (summer). Successive cycles may cause seasonal non-recoverable deformations which in turn may lead to failure of the slope. The magnitude of the potential shrink swell cycles is directly related to the magnitude of pore pressure variations within the slope. To correctly model the magnitude of the seasonal shrink swell cycles, and therefore potential failures, it is vital to correctly model the flow of water into, out of and through the slope.

Flow of water into and out of a slope will take place over the surface of the slope. Infiltration will occur during precipitation events at the slope surface and extraction will take place through evaporation at the surface and also through transpiration from vegetation which can extract water from beneath the soil surface. These two processes by which water can be extracted from the soil are collectively known as evapotranspiration. Maximum potential evapotranspiration rates are determined by climatic factors such as temperature, humidity, wind speed and net radiation as well as vegetation characteristics including leaf area and stomatal resistance. Actual evapotranspiration rates are determined from the potential evapotranspiration rate and the availability of water. To correctly assess the amount of infiltration into and evapotranspiration from the soil surface we must first be able to assess the rate at which water can flow from the surface to depth during infiltration and from depth to the surface during evapotranspiration. The permeability of a soil is a measure of the rate at which fluids can travel through the soil . The permeability of the soil, however, is not constant. The permeability of a soil reduces as the soil becomes partially saturated therefore reducing the rates at which water can infiltrate or be extracted from the soil. If the precipitation rate exceeds the infiltration rate, run-off will occur. The rate at which water can run down the slope also depends on many factors including slope gradient and soil/water frictional properties. If the soil surface is not fully saturated then evapotranspiration cannot take place at the potential rate. Actual evapotranspiration can be estimated from potential evapotranspiration and soil suction. If no precipitation takes place actual evapotranspiration rates will decrease as it becomes more difficult to transport water to the surface through the increasingly drying near surface soils.

There are many numerical programs which can calculate, with varying degrees of accuracy, most of the above processes. Some of these are reviewed within this thesis.

The majority of these programs, however, are only capable of modelling either infiltration, evapotranspiration and flow or deformation and flow. The majority of the hydrological models cannot calculate deformation and the majority of the programs which are capable of modelling the effective stress changes and associated deformations (the geotechnical models), conversely, are not capable of modelling the surface hydrological processes. Within this thesis an overview has been presented of the methods used by both the hydrological models and geotechnical models. A method has then been developed which allows the surface pore pressures calculated by a hydrological model to be applied to a geotechnical model. Pore pressure variation within the slope was then calculated within the geotechnical model. Consequently the method allowed deformation caused by effective stress changes to be simulated.

The method developed uses a hydrological model into which climatic data, soils data and vegetation data is input to calculate the pore pressure variations. Climatic data can be obtained from weather stations. The increment of climatic data used was found to potentially affect infiltration rates and therefore pore pressure variations. Smaller time increments lead to more accurate infiltrations whilst larger increments potentially increased infiltration and therefore pore pressures. The smallest increment of weather data available is therefore desirable to capture the effects of rainfall intensity. Hourly historic climatic data can be made available from a number of MET office weather stations (UK meteorological Office). This data can be used to model the seasonal deformations of a slope for a present climate scenario. Models run with this climatic data can be compared to previous modelling work and published pore pressure observations. Climatic data will also be required for future climate scenarios in order to assess the potential risk of these climates to slope stability. A weather generator, EARWIG, has been developed for the agricultural industry at Newcastle University (Kilsby et al, 2007). This weather generator is capable of generating data for a range of future climate scenarios (based on the UK Climate Impacts Programme 2002 (Hulme, 2002)) for a range of geographical areas within the UK. The future climate scenarios are determined for a range of conditions including CO_2 emission levels and time slices for a number of areas in the UK. Typically daily climate is output. The climate data for a geographical area from these models can then be scaled down to hourly data using a sample set of actual weather data from the area. Inputting this hourly future climatic data into the hydrological model will enable surface pore water pressures to be

predicted. These surface pore water pressures can then be applied to the geotechnical model which will allow the modelling of the associated deformations caused by effective stress changes. The surface pore pressures can be applied at any desirable time increment. Applying daily pore water pressures to the surface of the geotechnical model will allow for peak summer suctions and winter pressures to be accounted for within the model. This process will give a more accurate representation of the infrastructures annual response to a given climate.

1.2 Thesis aims

The aim of the thesis is to assess the influence of future and present climates on slope stability. To achieve this aim the following objectives have been satisfied:

1. Full literature review with particular attention to hydrological and geotechnical numerical modelling of slopes
2. Identification of available numerical models which may be used to model climatic effects on the stability of slopes
3. Development and validation of numerical modelling procedure to model climatic effects on slopes
4. Simulation of slopes subjected to present and future climate scenarios
5. Critical assessment of numerical procedure and results

1.3 Thesis Outline

The following presents an overview of this thesis. The following chapters outline the present modelling capabilities and the development and verification of some of the processes used. Finally the developed model is used for two very different case studies.

1.3.1 Chapter 2

Chapter 2 presents an overview of all the processes involved in the modelling of climatic impacts on slope stability. Firstly an overview is given of flow through a partially saturated media together with an overview of some of the mathematical models used to describe the processes. The effects of partial saturation on the physical soil properties are then reviewed together with some mathematical models used to describe the behaviour of these materials under partially saturated condition. The surface

processes of infiltration, evapotranspiration and run off are then looked at and again some mathematical models used to describe these processes are reviewed. A brief overview is then given of some of the numerical models which are capable of modelling either the hydrological processes and or the geotechnical processes. The reviewed numerical models are either commercially available models or have been developed for research purposes. This chapter then concludes with comments on the current modelling capabilities and identifies the research gap which this thesis is aimed at.

1.3.2 Chapter 3

This chapter sets out the modelling strategy used to bridge the research gap identified within chapter 2. The numerical models used for each process are chosen taking into account their suitability for the task, their adaptiveness to the method proposed and availability to the user. The models used for the hydrological modelling is SHETRAN and the model used for the geotechnical side of the modelling is Flac-tp. The mathematical models by which the chosen models simulate their respective processes are then described. Interestingly Flac-tp uses a two phase method to calculate unsaturated flow taking into account the air phase and the water phase whilst SHETRAN uses a single phase method which makes assumptions about the air phase.

1.3.3 Chapter 4

Chapter 4 outlines the development of the method used to transfer pore pressures from the hydrological model to the geotechnical model. As Flac-tp was a relatively new model, the chapter begins by verifying its unsaturated flow modelling capabilities by comparison to the more established SHETRAN unsaturated flow model. This section includes a comparison of the two different methods these two models use to simulate the same problem of partially saturated flow. The influence each parameter of the two phase flow method has on the simulation output is also reviewed and the chapter then goes on to make assumptions for some of the parameters based upon the output of these simulations. The pore pressure transfer method is then tested and validated for firstly a 1 dimensional scenario and secondly for a two dimensional embankment scenario. The method is then used to calculate slope displacements for a given climatic condition. The chapter concludes that the method of transferring pore pressures from the hydrological model to the geotechnical model is valid and that the method can be successfully used to calculate seasonal slope deformations.

1.3.4 Chapter 5

This chapter contains simulations for a diagnostic railway embankment and an infrastructure cutting in the Newbury area. Numerical models of both of these structures are subjected to present day climatic scenario and a future scenario. The chapter begins with a look at the two different climate scenarios used for the simulations. Weather data was obtained for the Newbury area and this was used to create hourly data for climate scenarios using the EARWIG software for a present day climate and a future 2080 climate scenario based on high CO_2 emissions. The future climate scenario shows no net annual increase in rainfall for the area but does show a significant increase in rainfall intensity. There is also a significant increase in annual temperatures.

An overview of the development of strain softening parameters for the embankment simulations is then given with respect to past modelling practices within the literature. This strain softening model was used when the climate scenarios were applied to a diagnostic railway embankment. The modelling shows that the future climate scenario resulted in less infiltration and more evapotranspiration from the slope. The future slope was subjected to a greater seasonal magnitude of shrink swell cycles but the added shear strength resulting from the high annual suctions within the slope made the slope far more stable than the slope subjected to a present climate.

The same modelling approach was then used for a cutting in the Newbury area. This cutting was heavily instrumented by Smethurst e al (2006) to record pore pressure variation. The results from the monitoring were used to verify the hydrological modelling process and then the deformations were analysed using the pore pressure transfer method. As no geotechnical parameters were given these were assumed from the literature and previous modelling experience. The effects of the grid geometry were also reviewed and a more robust grid and transfer method proposed. The simulation returned a different conclusion to the embankment study and an increased rate of progressive failure was predicted for the future climate simulation. The conclusion was that the rate of failure for a particular climate also relied upon mass permeability.

The chapter concludes with discussions about the methods used and their relevance to the problem. The advances that this modelling capability offers to analysing the effects of climate change are discussed together with the possible shortcomings of the process. Recommendations are then made which will address the shortcomings of this modelling process.

1.3.5 Chapter 6

The developed transfer method has the potential to be a powerful tool for the back analysis of existing slopes both constructed and natural. Within this chapter a case study of a failing natural slope at Belvoir Park in Northern Ireland is analysed. This case study involves a particularly difficult problem of a slope which contains a number of lithologies which has failed undergone some repairs and is still failing. The slope is first modelled within the hydrological program using climatic data from a nearby weather station. The pore pressures from this exercise are then transferred to geotechnical model. This case study defines the limits of the transfer model. There were a certain number of unknowns regarding the water regime and geotechnical parameters within the slope at Belvoir Park and a number of assumptions were required. The depth of roots below the surface was greater than the depth of the cell from which the pore pressure was transferred to the geotechnical model. This resulted in the vegetation roots being restricted to the surface cell within the hydrological model to enable an accurate transfer to take place. The continuing deformation of the slope was also difficult to capture within the model due to the lack of ability to transfer mechanically induced dissipation of pore pressures, predicted within the geotechnical model, back to the hydrological model.

The case study presented areas where the modelling method worked well and areas where improvement was required. The modelling work, however, highlighted the usefulness of such tools in developing a much greater understanding of the processes involved in such complex problems. The chapter shows that this approach of modelling can not only be used a predictive tool for structures where material boundaries and properties are clearly defined but also as a tool to assist the engineer in defining the cause and mechanism of failure for these complex engineering problems.

1.3.6 Conclusions

The thesis concludes with an outline of the findings of the study. The major findings of the modelling development and implementation work are presented. The relative strengths and weaknesses of all findings are discussed and recommendations made to further this research.

Chapter 2. Literature review

2.1 Introduction

It is generally accepted amongst scientists that climate is changing. It is therefore the responsibility of engineers to assess how the change will affect infrastructure. Infrastructure embankments and cuttings (termed infrastructure slopes for the remainder of this thesis) form one third of the total asset value for transportation infrastructure in this country (Perry, 2001). The processes by which climate will affect infrastructure slopes will be predominantly influenced by the infiltration and exfiltration of water. These processes cause effective stress changes which effectively load and unload the material within the infrastructure slope. The suctions present within the soil also affect the shear strength and the permeability of the soil. It is therefore vital to understand the processes by which water can infiltrate and be extracted from a slope surface, the movement of water through the body of the slope and the mechanical affects of suctions within a soil.

This chapter provides a summary of the current understanding of the processes outlined above by first regarding how water moves through a soil body. Mathematical models describing the movement are discussed and conclusions drawn on the benefits and drawbacks of each model. The interaction between suctions and the associated mechanical response of the soil are also discussed and associated mathematical models reviewed. Understanding of the processes between the soil surface and atmosphere which ultimately lead to water infiltration and exfiltration are summarised and mathematical models describing these processes are assessed. Lastly several numerical models which are capable of modelling a number of the discussed processes by use of either the reviewed mathematical models or a close approximation of the reviewed mathematical models are summarised. The chapter ends with an examination of the suitability of one or more of these numerical models for modelling climatic affects on infrastructure slopes.

2.2 Overview of Subsurface water within a slope

Bear (1972) presents a schematic of the subsurface water within a slope. This schematic is shown in Figure 2.1. Bear proposes that the vertical soil profile can be

subdivided into zones dependant upon the amount of water present within the pores of the soil. Within the saturated zone the pore pressures will be positive. Within the partially saturated zone (zone of aeration) the pore pressures will be negative. The surface between the positive and negative pore water pressures is the phreatic surface. At this surface the pore water pressures are zero (relative to atmospheric pressure). Within the partially saturated zone there are further subdivisions. The capillary fringe lies above the water table. Within this subdivision the moisture is held under capillary action. The height of this zone is dependant upon the pore size and distribution within the soil. The next zone is the intermediate zone. This zone is defined by water held under hygroscopic and capillary forces. Water may flow through this zone under the influence of gravity. At the top of the profile is the soil water zone. This zone extends from the surface to below the root zone. The soil water zone is heavily influenced by ground surface conditions. Water moves down through the zone under gravitational forces and upwards due to surface evaporation and water uptake from plants and vegetation. Not all zones may exist in a profile. For example, within areas containing a shallow water table the capillary fringe may rise up to the surface.

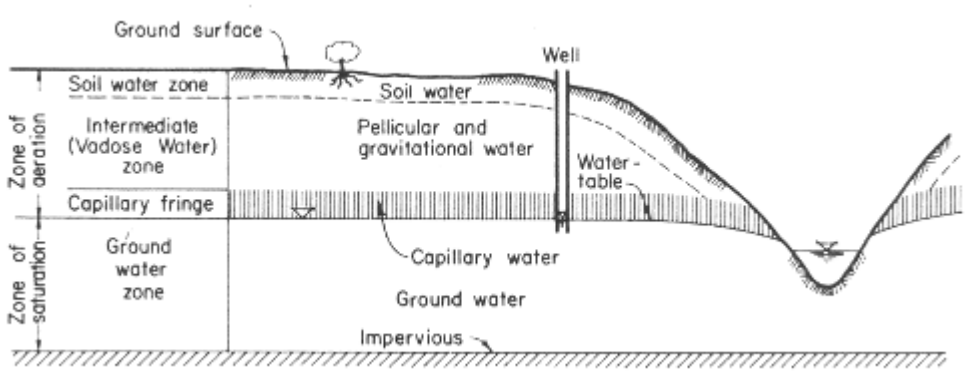

Figure 2.1. Distribution of subsurface water (Bear, 1972).

It is clear from the profiles illustrated above that the within an infrastructure slope, there is likely to exist saturated and partially saturated zones. An understanding is therefore required of how water flows within these two zones and also how the change in level of saturation affects stress changes, strength changes and ultimately stability of slopes.

2.3 Saturated or partially saturated soil mechanics?

In the past the emphasis within soil mechanics has been on studying saturated clays, silts and sands and dry sands where the voids within a soil are completely filled with

either air or water. Flow within a soil was modelled as saturated flow and deformation was modelled with respect to effective stress changes with the void spaces completely filled with either water or air. Within saturated models the shear strength of the soil was directly related to effective stress which was determined by Terzagih's effective stress equation, following;

$$\boldsymbol{\sigma}' = \boldsymbol{\sigma} - u_w I \qquad \textbf{2.1}$$

Where $\boldsymbol{\sigma}'$ is the effective stress tensor, $\boldsymbol{\sigma}$ is the total stress tensor, u_w the pore water pressure and I is the unit tensor. Equation 2.1 was used for saturated soil conditions, and was seen to be generally accurate, up to the point of the air entry value where air enters the soil and it becomes partially saturated. At this point the property of the gaseous phase, air, needs to be taken into account in the effective stress equation. Equation 2.1 therefore becomes unable to calculate the effective stress of the partially saturated soil.

More recently researchers have begun to realise that studies in near surface soil mechanics must be extended to partially saturated soils where the void space is filled partly by water and partly by air. Hydrological and mechanical behaviour of partially saturated soils differs from that of the saturated soil in several ways. The pore water pressures within a partially saturated soil are negative, relative to atmospheric pressure, and are often termed suctions. The magnitude of suction within a soil is related to the moisture content or degree of saturation within that soil. Effective permeability of a partially saturated soil is also related to the degree of saturation (and therefore also suction) with effective permeability decreasing as the soil dries. The suctions generated within partially saturated soil will also affect the shear strength of the soil, often increasing it significantly. This strength increase will be lost on subsequent saturation of the soil. Partially saturated soil may also be subject to volume changes under constant pressure due to changes of degree of saturation. The following sections present an overview of saturated and partially saturated soil mechanics together with the development of the incorporation of some of these phenomena into mathematical models.

2.4 Flow within saturated and partially saturated soils

This section is concerned with the flow of liquid and/or gas through a porous media. For the purpose of this thesis the only liquid considered is water and the only gas considered is air. The porous media will be the soil. If the soil contains only water then it is deemed to be saturated. If water and air are present then it is deemed to be partially saturated. The hydrological properties of partially saturated soil degenerate to those of saturated soil when the soil becomes saturated. This section will therefore define the properties of saturated soils before considering a partially saturated soil.

2.4.1 Saturated soils

During steady state conditions the pore pressures within the saturated zone will be hydrostatic. This means that the pore pressures will increase with depth following the relationship:

$$u = h\rho g \qquad \textbf{2.2}$$

Where u is the pore water pressure, ρ is the density of water, h is the height of water and g is the acceleration due to gravity. Within soil mechanics the pore pressure, u, in kPa is generally quoted, whereas within the discipline of hydrology, head, in metres is generally quoted. Head is the depth of water, during steady state conditions, in relation to the phreatic surface which is discussed later within section 2.4.2. Flow of water within the saturated zone can be calculated using Darcy's law. This law states that the quantity of water flowing through a one dimensional column per unit time is proportional to the hydraulic gradient (the difference in fluid pressure across the column) and the cross-sectional area of the column, i.e:

$$Q = kiA \qquad \textbf{2.3}$$

Where Q is the quantity of water flowing per unit time, k is the saturated coefficient of permeability, i is the hydraulic gradient and A is the cross-sectional area. Lamb and Whitman (1969) list the five soil characteristics that effect the permeability as:

1. Particle size
2. Void ratio
3. Composition

4. Fabric
5. Degree of saturation

Characteristics 1 to 4 are all inter-related and it would be difficult to assess the effect of each individual characteristic on the permeability. Lu and Likos (2004) state that the permeability may vary extensively from one soil type to another. The permeability may also vary several orders of magnitude for the same soil. They also state that the permeability of a soil is sensitive to changes in pore structure and may be anisotropic. Most importantly they state that the effective permeability of a sample was very scale dependant with permeability increasing as the representative soil volume increases.

As the permeability is heavily dependent upon the void ratio it seems reasonable to suggest that with increased depth (increased stress and possibly volumetric strain) void ratio may decrease and therefore permeability will decrease. Potts and Zdravkovic (1999) present an overview of some proposed permeability models. The linear isotropic permeability model assumes an isotropic permeability. It allows the engineer to vary the permeability over depth and the permeability remains constant throughout the analysis. Similar to the previous model is the linear anisotropic permeability model where the permeability is assumed to be direction dependant. The non-linear permeability related to void ratio model calculates the permeability as follows:

$$\ln k = a + be \Rightarrow k = e^{(a+be)} \qquad \textbf{2.4}$$

Where e is the void ratio and a and b are material parameters which need to be defined. The model makes sense in that with decreasing void size, e, there will be decreasing permeability which may be more representative of field conditions over a finite depth, but there are difficulties in obtaining the parameters required. The initial void ratio at the beginning of the analysis would need to be known and determining the parameters a and b would also be difficult when there is little data. Models have also been developed which relate the permeability to mean effective stress. Potts and Zdravkovic (1999) present two nonlinear mean effective stress dependent permeability models the first one uses a logarithmic relationship:

$$ln\left(\frac{k}{k_0}\right) = -ap' \qquad ; \qquad k = k_0 e^{(-ap')} \qquad \textbf{2.5}$$

Where k_0 is the permeability at zero effective stress, p' is the mean effective stress and a is a parameter incorporating the void ratio at k_0 and the coefficient of volume compressibility. The second model uses a power law relationship and takes the form:

$$\frac{k}{k_0} = (p')^{-a} \qquad \textbf{2.6}$$

All the permeability models reviewed here require additional data which is either not available or difficult to obtain. Permeability within slopes is also difficult to measure due to the scale effects noted by Lu and Likos (2004). These affects have been noted during slope investigations with permeabilities of laboratory samples being two orders of magnitude lower than field measured permeabilities (Smethurst et al, 2006). The methods of obtaining field measured permeabilities are also often difficult to execute to a high degree of accuracy and the areas over which the tests are performed are not always representative of the entire slope. The scale of slopes of interest to this thesis is generally in the order of tens of meters. Instrumentation generally records the permeability of a radial section of about 1 to 3 meters around a borehole, depending on the effective permeability. Due to the effects of scale on permeability discussed by Lu and Likos (2004) the mass permeability of the slope is therefore likely to be larger than that measured within a borehole and significantly larger than that measured within a laboratory sample. It seems, therefore, that without significant testing to prove otherwise, increasing the level of complexity of a parameter that is already highly variable within slopes will not attain a significant increase in accuracy.

2.4.2 Partially saturated soil

The partially saturated zone can be thought to consist of three phases, solids, water and air. Fredlund and Rahardjo (1979) proposed adding another phase, that of the soil water interface, yet this seemed to offer no significant advantage and will not be discussed further.

Air and water have different viscosities. This difference leads to a difference in each phases ability to flow through a material. The viscosity is also dependent upon the temperature and the pressure. At atmospheric pressure (101.3 kPa) the viscosity

between 0º and 30º of air is $1.705 \times 10^{-5} - 1.864 \times 10^{-5}$ Ns/m^2 and of water is $1.794 \times 10^{-3} - 0.895 \times 10^{-3}$ - Ns/m^2 (Fredlund and Rahardjo, 1979). This leads to a viscosity ratio of around 50 at 0º and 100 at 30º. The viscosity of a liquid or gas describes the ease at which that substance can flow. With the above viscosity ratios it becomes apparent that the air within a soil can move much more freely than the water.

The air and water within the soil are also both compressible. The compressibility of air at atmospheric pressure is 9.872×10^{-3} m^2/N and the compressibility of water is about 4.4×10^{-10} m^2/N. As compressibility is the inverse of the materials bulk modulus this leads to the bulk modulus of air being 1.01×10^5 Pa and water 2.27×10^9 Pa. The air within the soil is therefore much more compressible than the water.

Between any two immiscible fluids there must exist an interface. The geometry of this interface will be determined by the pressures in each liquid and the interfacial tension between the liquids (Lu and Likos, 2004). In the case of partially saturated soils the system is a liquid / gas system in which the liquid is water and the gas is air. In this system the surface tension of the air can be ignored and we are left with the pressure within the water, the pressure within the air and the surface tension of the water. Within partially saturated soil the interface between the soil and the water is concave on the air side. This indicates that the air pressure is greater than the water pressure. Lu and Likos (2004) present the following equation which relates the pressure difference between the phases, $(u_a - u_w)$, to the surface tension, T_s, and radius, R, of the interface, Equation 2.7.

$$u_a - u_w = \frac{2T_s}{R} \qquad \textbf{2.7}$$

This equation shows that as R tends towards ∞ and the surface becomes flat then;
$u_a = u_w$ and the pressure across the interface is zero. This is the phreatic surface condition.

2.4.3 Soil suction

The negative pore pressure within the partially saturated zone is often termed soil suction. Total soil suctions present within partially saturated soil are made up of a

combination of matric suction and osmotic suction (Fredlund and Rahardjo, 1979). The osmotic (or solute) suction is derived from the fact that vapour pressure over a flat surface of water which contains dissolved salts is less than the vapour pressure over a flat surface of pure water. The difference between these two pressures is the osmotic suction. Osmotic suction can be significant, Fredlund and Rahardjo (1979) present typical suction values for a glacial till at optimum moisture content. The suctions show that osmotic suction accounts for just over 48% of the total suction. There does, however, need to be a significant mineral salt content within the soil. Osmotic suction is constant over the entire saturation range unless the concentration of dissolved solutes changes (Lu and Likos, 2004) changes in osmotic suction are therefore ignored for most geotechnical applications.

The matric suction within a soil is associated with capillary action within the soil. Capillarity is when one liquid has the ability to draw itself into another. In the case of air and water when a tube of narrow diameter is placed into freestanding water at atmospheric pressure, water will rise into the tube as a consequence of interfacial surface tension. This will result in negative pore pressures. A curved meniscus inside the tube will form. The height of the water within the capillary tube, h_c, can be calculated by considering the radius of the capillary tube r, the surface tension of the water T_s , the contact angle the water makes with the capillary tube α, the density of the water ρ_w , and gravitational acceleration g. The relationship is shown below:

$$\frac{2T_s \cos\alpha}{r\rho_w g} = h_c \qquad \textbf{2.8}$$

If the angle α is less than 90º for a liquid then this is known as the wetting fluid. If the angle is greater than 90º then this is known as the non-wetting fluid. The water within the tube is in tension and the pore water pressures are negative. The pressure head at height h_c (u_w) can be calculated using the following equation.

$$u_w = -\rho_w g h_c \qquad \textbf{2.9}$$

It can also be seen from Equation 2.8 and 2.9 that as the angle, α tends towards 90º, i.e. the water air boundary becomes flat, then u_w becomes small.

The pore spaces within the soil skeleton can be thought of as a number of capillary tubes. When the soil is partially saturated water is sucked into the pore spaces by the same mechanism as water is sucked into the capillary tube. This causes a negative pore pressure or suction within the soil. The matric suction, ψ, within the soil can be calculated by considering the air pressure, u_a and the water pressure, u_w , Equation 2.10.

$$\psi = u_a - u_w \qquad \textbf{2.10}$$

It can be seen from Equation 2.10 that the height and therefore negative pressure that can be attained by capillary action is related to the diameter of the capillary tube. The same holds true for the water drawn up into the pore space of the soil. A larger pore space equates to a larger diameter tube and therefore a lower h_c value and consequently a lower negative pressure will be achieved. This relationship highlights the dependency of soil suction on the particle and pore sizes of a soil.

2.4.4 Soil Water Characteristic Curve

Experiments on various soils show that the suction within a soil increases with decreasing moisture content. The variations in suction within a soil can cover a range of many thousands of MPa beginning at 0 kPa where the soil will take up no more water and increasing as the soil becomes dry (Croney, 1977). It is for this reason that it is convenient to plot soil suction on a logarithmic scale. The soil water characteristic curve, SWCC, (also known as the soil moisture retention curve) plots the moisture content of a soil against the matric suction. Figure 2.2 shows a typical example of such a curve and the stages of de-saturation and hence increasing suction. The capillary suction zone indicates that the soil is essentially saturated yet the pore water is in tension, this zone continues up to the air entry value (AEV) or the bubbling pressure. Within the de-saturation zone the water is continually displaced by water until the residual water content is reached. Within the residual saturation zone the water is tightly held to the soil and flow only occurs as vapour flow. This zone is terminated at oven dry conditions approximately 1×10^6 kPa. Water that is still present is chemically bonded to the soil and will not affect the engineering properties (Sillers et al, 2001).

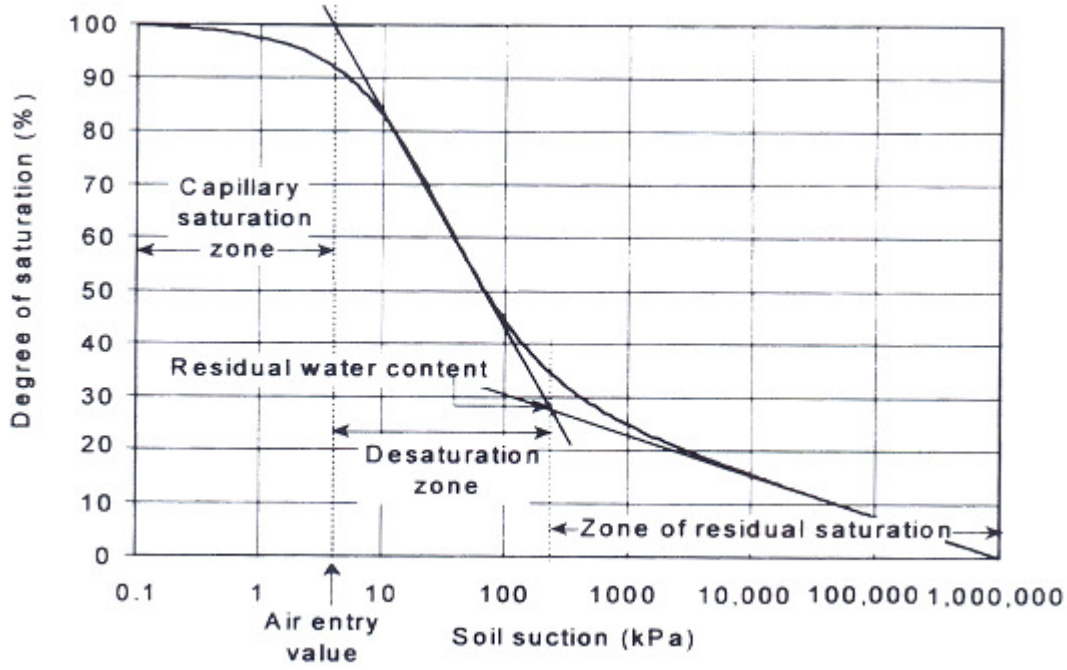

Figure 2.2. Soil-water characteristic curve illustrating regions of de-saturation (Sillers et al, 2001)

Figure 2.3 shows the curves for three soil types, the curves are generally 's' shaped although this becomes less defined for clays.

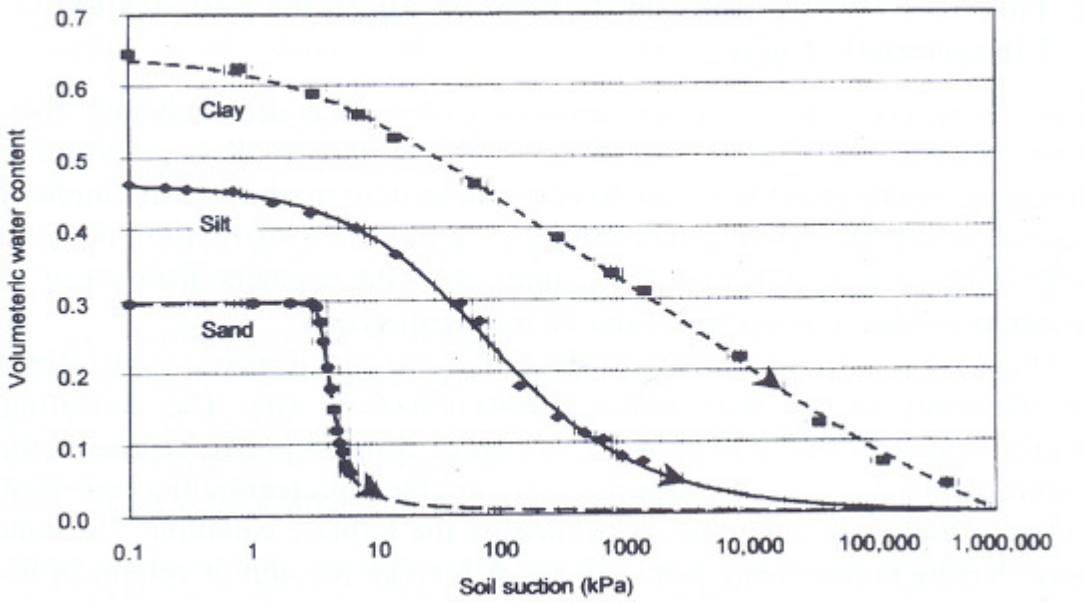

Figure 2.3 Three typical soil-water characteristic curves for a clay, silt and sand (Sillers et al., 2001)

2.4.5 Hysteresis

Hysteresis is a well known and essential phenomena within partially saturated soil mechanics (Li, 2005). It is due to the fact that for a particular soil when the soil water characteristic curve is drawn the wetting soil will follow a different path to the drying soil. Figure 2.4 shows a conceptual illustration of hysteresis within the soil water

characteristic curve. Hysteresis is most pronounced within the area of the curve where absorption or drainage is most rapid, the de-saturation zone. At high suctions the wetting and drying curve tend to converge. At low suctions the wetting curve may not actually reach saturation. This will be due to entrapment of air within some pore spaces.

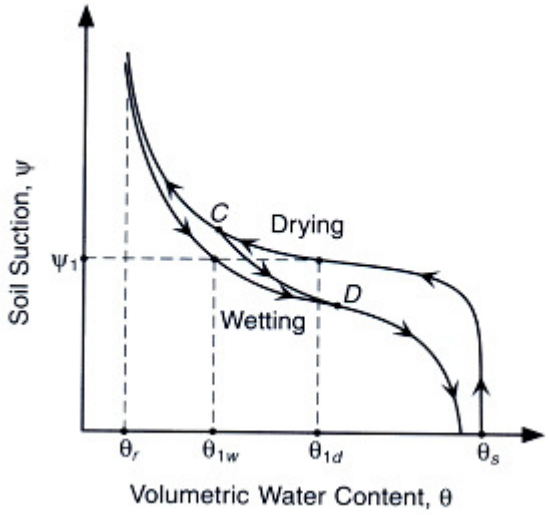

Figure 2.4 Conceptual illustration of hysteresis in soil-water characteristic curve (Lu and Likos 2004)

Several reasons for this hysteresis have been postulated. One theory attributes the cause to a non uniform pore size. As stated previously, the height to which the water may rise into a capillary tube is related to the radius of that tube. For a tube of constant radius, r, water may rise to a maximum height of h_c (see Figure 2.5a). However, the height of the capillary tube may be less than h_c and therefore restrict the capillary rise (see Figure 2.5b). Let us also consider a capillary tube which has a varying radius (Figure 2.5c). On wetting the water may rise up to base of the bulb but cannot rise any further due to the increase in radius of the capillary tube. If the tube was submerged and then drying permitted then the capillary tube radius is of sufficient diameter to form a meniscus at h_c and therefore the water will remain at this height. The capillary tube analogy can also be used for a column of soil (Figure 2.5e). Capillary rise up to height h_c can be achieved within the soil through the pore sizes within the soil that are of equal radius or smaller to r. The water may also rise to greater heights than h_c through continuous pore spaces of smaller radius than r. It can also be seen from Figure 2.5e that water can rise into the soil around large openings but cannot rise into the opening. Due to non-uniform pore size distribution within a soil the above analogy shows that for a particular

soil with a given matric suction the moisture content can vary depending on whether the soil is wetting or drying.

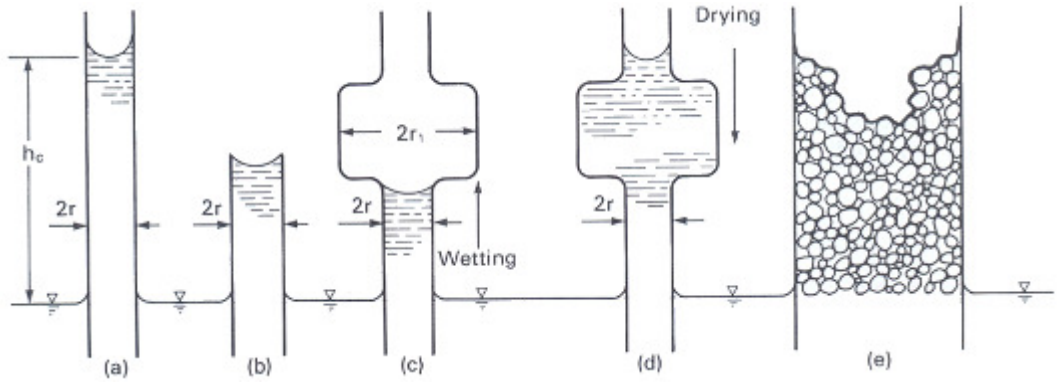

Figure 2.5 Height and radius effects on capillarity (Fredlund and Rahardjo, 1979)

Another theory for the cause of hysteresis is attributed to the fact that the contact angle, α, is generally greater for an advancing interface as opposed to a receding interface. A greater angle at the interface for a point in a soil being wetted would mean a lower suction. Conversely a smaller angle at the interface in the soil being dried would mean a higher suction. A variety of suctions are therefore possible within a soil for one single moisture content value. These angles could therefore also have a significant effect on water retention and corresponding suctions.

2.4.6 SWCC models

As stated previously the SWCC can be drawn from data obtained from laboratory testing. A mathematical function can then be fitted to this curve. Many mathematical models have been proposed within the literature. These models are based on the theory that the effective pore size within a soil is related to the soil suction, this relationship is called pore size distribution. The pore size distribution can be obtained from the SWCC. The pore size distribution together with capillary theory can then be used to model the SWCC. Many authors have used this approach (Li, 2005; Fredlund and Xing, 1994; Kosugi, 1994; van Genuchten, 1980) and these types of model are known as statistical or micromechanical approaches (Sillers et al, 2001). These models offer various advantages over each other within their ability to fit the SWCC, have parameters that are physically based and have a continuing function that covers the entire range of soil suction. The van Genuchten model fits these requirements and has

been implemented into various numerical models concerned with partially saturated flow.

The van Genuchten model (Equations 2.11 and 2.12) fits degree of saturation against soil suction and covers the entire range of soil suction. The parameter *a* is related to the inverse of the air entry value, the *n* value is related to the pore size distribution and the parameter *m* relates to the asymmetry of the model. Within the closed-form of the model the parameter *m* is related to the parameter *n* by Equation 2.11.

$$\theta_e = \left[\frac{1}{1+(ah)^n}\right]^m \qquad \textbf{2.11}$$

$$m = 1 - \frac{1}{n} \qquad \textbf{2.12}$$

Where h is the pressure head, θ_e is the dimensionless water content derived using the water content, θ the saturated water content θ_s and the residual water content θ_r by equation 2.13.

$$\theta_e = \frac{\theta - \theta_r}{\theta_s - \theta_r} \qquad \textbf{2.13}$$

The main disadvantage of the van Genuchten model is that the hysteresis is not addressed. Pham et al (2003) have presented a technical note on the development of a model which can predict the hysteresis of the soil water characteristic curve. Li (2005) has also presented a technical note on the development of a phenomenological approach to model the hysteretic SWCC along arbitrary wetting drying paths. Kool and Parker (1987) presented expressions for modelling of hysteresis within the SWCC. Their model allowed for air entrapment within the model. These models incorporated errors in the form of a pumping effect. The pumping effect means that the hysteretic loops move to unrealistic parts of the water retention function. Lenhard et al (1991) also presented a model capable of modelling hysteresis but eliminated the pumping effect by storing the points at which wetting and drying paths are reversed so that subsequent saturation paths can be predicted (Lenhard et al., 1991). When the model was compared to both experimental data and a non-hysteretic model the model produced favourable

results. Of specific note, the non-hysteretic model predicted the drying particularly well yet could not reproduce the wetting satisfactorily with predictions showing full saturation achieved when actual saturation was considerably less.

2.4.7 Effective permeability of air and water

The permeability of both the water and the air phase within partially saturated soil varies due to the respective saturations. As the degree of saturation within the soil tends to zero the permeability to water reduces significantly, conversely the permeability to air increases. The water and air permeability of partially saturated soil is commonly normalised with respect to the air saturated permeability and water saturated permeability of that soil, respectively. The normalised values are referred to as the relative permeabilities (Lu and Likos, 2004). The relative permeability is a dimensionless scalar that varies from zero to one. The equations for the relative permeabilities are given as follows:

$$k_{rw} = \frac{k_w}{k_{sw}} \leq 1 \qquad \textbf{2.14}$$

$$k_{ra} = \frac{k_a}{k_{sa}} \leq 1 \qquad \textbf{2.15}$$

Where k_{rw} and k_{ra} are the relative permeabilities of water and air respectively, k_w and k_a are the effective conductivities of water and air within the soil and k_{sw} and k_{sa} are the saturated conductivities of water and air at water saturation and air saturation respectively.

The relative permeabilities are unique functions of the saturation. The relative permeability curves can be drawn for both the air and water phases. Typical relative permeability curves are show in Figure 2.6.

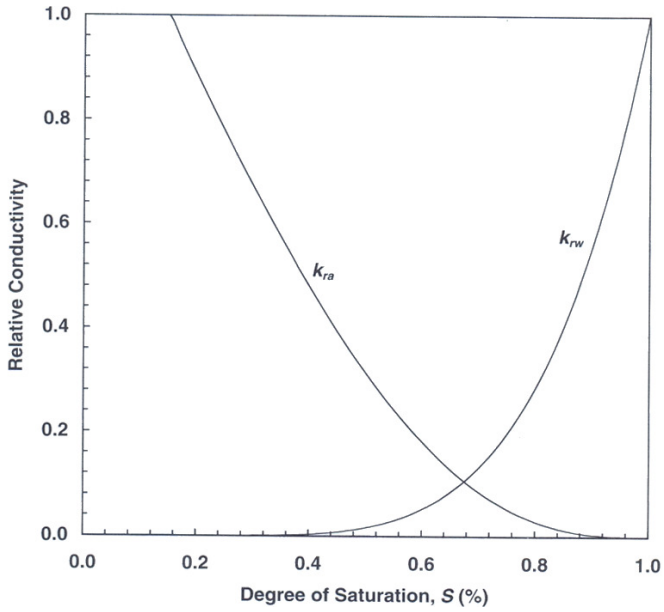

Figure 2.6 Relationships among relative air conductivity, relative water conductivity and degree of saturation (Lu and Likos, 2004)

Investigators have attempted to evaluate the influence of many fluid flow parameters on relative permeability (Bear, 1972). Pressure gradients were found to have a limited effect yet many authors found that the ratio of the viscosities had a significant effect. Bear (1972) reports Yuster (1953) found the viscosity ratio affects the specific discharge of the two fluids viscosity therefore must be included into any partially saturated extension of Darcy's law.

Relative permeabilities are a function of saturation and the relationships are usually empirically determined. Van Genuchten (1980) derived the equation for the relative permeability of water as:

$$k_{rw}(\theta_w) = \theta_e^{1/2}\left(1-\left(1-\theta_e^{1/m}\right)^m\right)^2 \qquad \textbf{2.16}$$

This equation was based on the equations of Maulem (1976). Later work by Parker et al (1987) derived the following equation for the relative permeability of air as:

$$k_{ra}(\theta_w) = (1-\theta_e)^{1/2}\left(1-\theta_e^{1/m}\right)^{2m} \qquad \textbf{2.17}$$

2.4.8 Simulation of partially saturated flow

The differential form of Darcy's law (Equation 2.3) can be written as:

$$v_x = -\frac{K}{\mu}\frac{\partial p}{\partial x} \qquad \textbf{2.18}$$

$$v_y = -\frac{K}{\mu}\frac{\partial p}{\partial y}$$

$$v_z = -\frac{K}{\mu}\frac{\partial p}{\partial z}$$

Where K is the absolute permeability of the medium (independent of the fluid), p is the fluid pressure and μ is the fluid viscosity. Equation 2.18 does not take into account the influence of gravity. For generality Peaceman (1977) takes depth D to be an arbitrary function of coordinates $(x,y,z,)$ although the obvious co-ordinate to use would be z. Including the influence of gravity leads to:

$$v_x = -\frac{K}{\mu}\left(\frac{\partial p}{\partial x} - \rho g \frac{\partial D}{\partial x}\right) \qquad \textbf{2.19}$$

$$v_y = -\frac{K}{\mu}\left(\frac{\partial p}{\partial y} - \rho g \frac{\partial D}{\partial y}\right)$$

$$v_z = -\frac{K}{\mu}\left(\frac{\partial p}{\partial z} - \rho g \frac{\partial D}{\partial z}\right)$$

Therefore for saturated compressible flow (single phase flow) Peaceman (1977) shows Darcy's law can be written in the compact form:

$$\vec{\mathbf{v}} = -\frac{K}{\mu}\left(\nabla p - \rho g \nabla D\right) \qquad \textbf{2.20}$$

Where $\mathbf{v}$ is the velocity vector. Peaceman (1977) then goes on to describe multiphase flow for partially saturated soil where there are two phases (liquids and gas). For two phase flow the saturation, capillary pressure and the relative permeability of each phase needs to be considered. As the voids within the porous media are completely filled by both the phases then:

$$S_n + S_w = 1 \quad \textbf{2.21}$$

Where S_n is the saturation of the non-wetting fluid (air in the case of partially saturated soils) and S_w is the saturation of the wetting fluid (water). Peaceman (1977) presents the difference between the pressure of the non wetting phase and the wetting phase as the capillary pressure:

$$P_c = P_n - P_w \quad \textbf{2.22}$$

Where P_c is the capillary pressure, P_n is the non wetting fluid pressure and P_w is the wetting fluid pressure. For a partially saturated soil P_n and P_w are equivalent to the pore air, u_a, and pore water pressures, u_w, respectively and P_c is equvalent to the matric suction, ψ. If the effects of hysteresis within the SWCC are ignored, the capillary pressure is a unique function of saturation. This leads to:

$$P_c(S_w) = P_n - P_w \quad \textbf{2.23}$$

The single phase form of Darcy's law expressed within equation 2.20 can now be extended to two phase flow by postulating that the phase pressures of each fluid, wetting ($_w$) and non-wetting ($_n$), are the cause of flow for each fluid. This leads to:

$$\vec{\mathbf{v}}_n = -\frac{K_n}{\mu_n}\left(\nabla P_n - \rho_n g \nabla D\right) \quad \textbf{2.24}$$

$$\vec{\mathbf{v}}_w = -\frac{K_w}{\mu_w}\left(\nabla P_w - \rho_w g \nabla D\right) \quad \textbf{2.25}$$

Within equations 2.24 and 2.25 K_n and K_w are the effective permeabilities of the non-wetting and wetting fluids respectively. K_n and K_w can be written in terms of the absolute permeability, K, and relative permeability, k_r resulting in:

$$\vec{\mathbf{v}}_n = -\frac{Kk_{rn}}{\mu_n}\left(\nabla P_n - \rho_n g \nabla D\right) \quad \textbf{2.26}$$

$$\vec{\mathbf{v}}_w = -\frac{Kk_{rw}}{\mu_w}\left(\nabla P_w - \rho_w g \nabla D\right) \quad \textbf{2.27}$$

The two phase flow approach described is an example of immiscible displacement where the two fluids displace each other but there is an interface between them and they do not mix. Miscible displacements are when the two fluids within the media can mix, Bear (1972) describes a theoretical treatment of both immiscible and miscible displacement. Miscible displacement occurs during the inflow of seawater into a fresh water aquifer where the fluids are of differing densities yet may mix. This type of flow is not relevant to partially saturated flow within slopes and is therefore not considered further within this thesis.

Whilst the immiscible flow of liquids has been developed by reservoir engineers partially saturated flow has been developed by hydrologists. Soil hydrologists tend to favour a single phase approach to partially saturated flow. Within the single phase flow approach the air within the system is assumed to be stagnant and at constant atmospheric pressure. This is an approximation yet it leads to techniques of analysis that are accurate enough for most situations (Freeze and Cherry, 1979). There are, however, special cases in which the assumptions of stagnant air at atmospheric pressure do not hold true. These cases are where the air has become trapped and the pressure builds up. The escape of this air will then impede the flow of water through the media. Wilson and Luthin (1963) argue that within a fine grained soil above an impermeable layer rainfall may seal the surface soil, continuing precipitation and flow through the soil by capillarity results in significant air pressures being generated, they then go on to present results of experimentation on infiltration. The results show that the air phase does have a significant effect on the rate of the advance of the wetting front. The experiments were however for a special case in which air was not permitted to flow through the top of the soil column. Realistically, in most situations the air in a soil will be able to escape through the lager voids.

For single phase partially saturated flow where the only liquid taken into account is water Darcy's law for saturated flow in the x direction is:

$$v_x = -K_x \frac{\partial h}{\partial x} \qquad \textbf{2.28}$$

Where K_x is the permeability of water in the x direction and h is the hydraulic head defined as:

$$h = \psi + z \qquad \textbf{2.29}$$

Where ψ is the matric suction and z is the elevation head. Including the effect of partially saturated flow Equation 2.28 can be written as:

$$v_x = -K_x(\psi)\frac{\partial h}{\partial x} \qquad \textbf{2.30}$$

Where $K_x(\psi)$ is the permeability of water in the $\boldsymbol{x}$ direction as a function of soil suction. The $K_x(\psi)$ term may be replaced by the permeability of water in the $\boldsymbol{x}$ direction as a function of saturation $K_x(\theta)$. Tindall and Kunkel (1999) argue that using permeability as a function of saturation is preferable as $K_x(\theta)$ is less hysteretic than $K_x(\psi)$. By assuming that the fluid is incompressible, that porosity remains constant and the medium is homogenous Freeze and Cherry (1979) developed the following equation of flow for transient flow through a partially saturated medium:

$$\frac{\partial}{\partial x}\left[K(\psi)\frac{\partial h}{\partial x}\right] + \frac{\partial}{\partial y}\left[K(\psi)\frac{\partial h}{\partial y}\right] + \frac{\partial}{\partial z}\left[K(\psi)\frac{\partial h}{\partial z}\right] = \frac{\partial \theta}{\partial t} \qquad \textbf{2.31}$$

Where θ is the degree of saturation. Rewriting Equation 2.31 and considering Equation 2.29 and the specific storage capacity, C (defined by Equation 2.33) gives the following relationship which is known as the Richards equation (Richards, 1931):

$$\frac{\partial}{\partial x}\left[K(\psi)\frac{\partial h}{\partial x}\right] + \frac{\partial}{\partial y}\left[K(\psi)\frac{\partial h}{\partial y}\right] + \frac{\partial}{\partial z}\left[K(\psi)\frac{\partial h}{\partial z}\right] = C\frac{\partial \psi}{\partial t} \qquad \textbf{2.32}$$

$$C = \frac{\partial \theta}{\partial \psi} \qquad \textbf{2.33}$$

The Richards equation (Equation 2.32) is directly used by many investigators and in some form within many hydrological software codes to investigate the flow of water through soils. The main disadvantages of this approach, however, are that the soil is assumed to be rigid and incompressible.

2.5 Soil mechanics within partially saturated soils

The volume change and shear strength behaviour within soils can be termed the mechanical behaviour. The mechanical behaviour of partially saturated soils differs from that of saturated soils. This section provides an overview of the observed behaviour of partially saturated soils and some of the mathematical models developed to capture these characteristics.

2.5.1 Observed partially saturated behaviour

One of the characteristics of partially saturated soil behaviour is the increased shear strength. Figure 2.7 shows the increase in shear strength with increase in matric suction for tests conducted by Blight (1967) after (Lu and Likos, 2004). The increase in shear strength can be attributed to the suctions present within the soil.

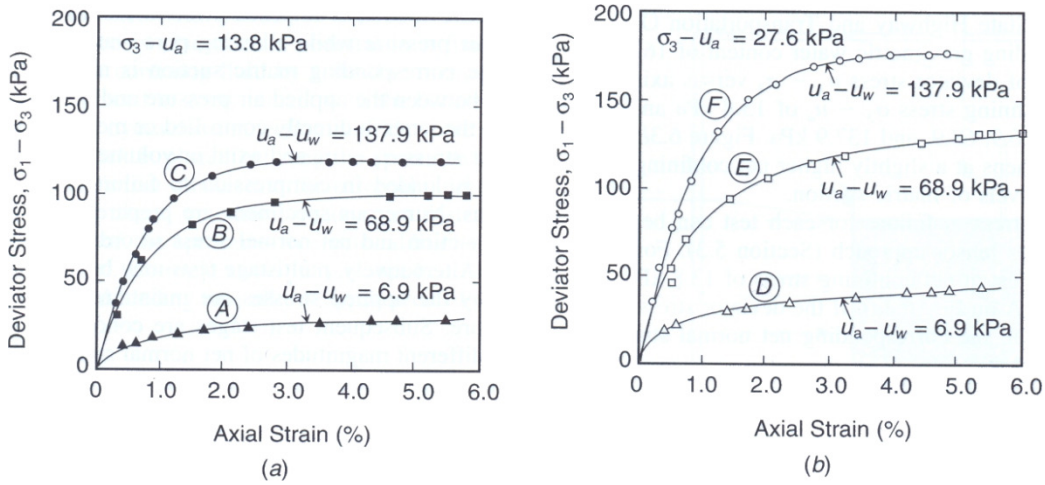

Figure 2.7 Consolidated drained triaxial tests for partially saturated silt (a) net confining stress of 13.8 kPa tests three levels of matric suction A, B and C. (b) net confining stress of 27.6 kPa tests three levels of matric suction D, E and F (same levels of suction as A, B, and C) data from Blight (1967) after (Lu and Likos, 2004).

Other characteristics of partially saturated soil behaviour are changes in volume induced by a change in confining stress and also volume changes induced by a change in moisture content.

Upon drying, before the air entry value is reached, suction can also be thought of as an applied stress to the soil. A suction increase will result in an equivalent increase of isotropic total stress. Furthermore the reduction in total volume is equal to the reduction

in pore water volume. Further suctions beyond the air entry value do not result in an equivalent increase in isotropic stresses and the reduction in total volume does not equal the reduction in pore water volume. The volume changes induced by suctions within a plastic clay are considered to be small and reversible, although at very high suctions suction yielding can occur.

Upon wetting the volume change behaviour of partially saturated soils has been observed by Jennings and Burland (1962). The authors conducted tests on air dry samples of silt soaked at different constant applied stresses and a sample consolidated from slurry. Figure 2.8 shows that all samples showed collapse upon wetting apart from the initially soaked sample at 0 kPa. The collapse upon wetting goes against traditional effective stress theories which predict a volume increase upon wetting. Figure 2.9 shows schematic diagrams of oedometer curves for a partially saturated and saturated soil. At low confining stresses, the soil will undergo some swelling upon wetting. At higher confining stresses a soil will show a collapse, volume decrease, upon wetting and with even higher confining stresses the amount of collapse upon wetting will decrease.

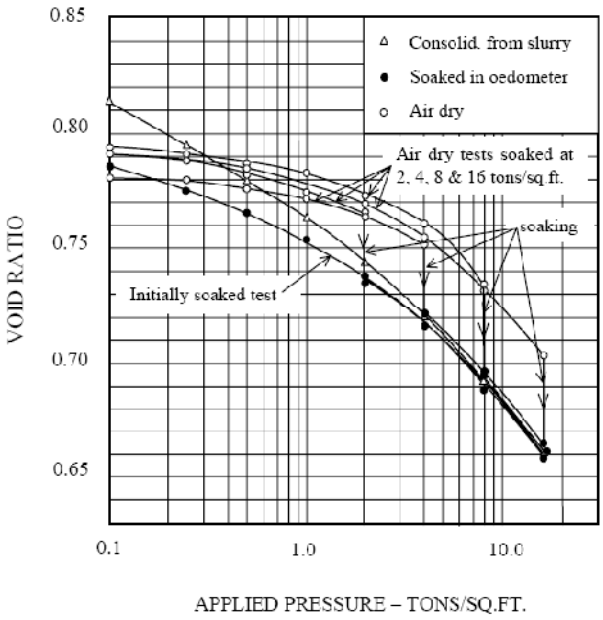

Figure 2.8 Oedometer curves for 5 air dried silt samples soaked at confining pressures of 0, 192, 384, 768, and 1536 kPa and a sample consolidated from slurry (Jennings and Burland, 1962).

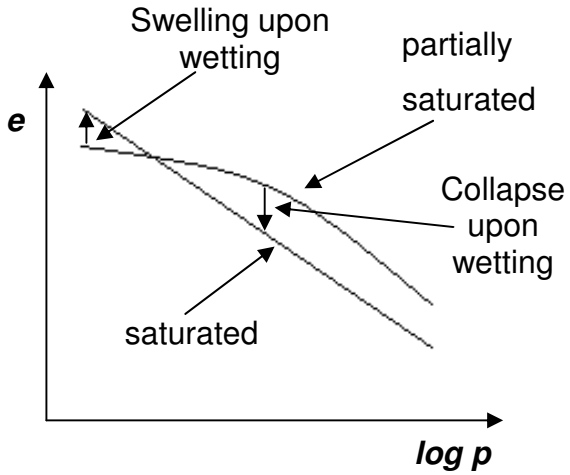

Figure 2.9 Schematic diagram of oedometer curves for a saturated and partially saturated soil

2.5.2 *Effective stress within partially saturated soils*

The mechanical behaviour can be described by the state of stress within a soil (Fredlund and Rahardjo, 1979). The state of stress within a soil can be determined by the stress state variables. These stress state variables should be independent of the soil properties. The stress state variable for saturated soils (see Equation 2.1) has been found to describe the behaviour of saturated soils. This has been termed the principle of effective stress proposed by Terzaghi (1943). Figure 2.10 shows the profiles of water content, total stress and effective stress for a saturated sand. Figure 2.11 shows the water content, total stress and effective stress for the same example but with the water table at the base of the sand. Comparison between Figure 2.10 and 2.11 shows that the water content of the partially saturated sand varies over depth. This variation of water content is related to the pore pressures, u, which is hydrostatic with depth. The shape of the water content curve is determined by the SWCC as discussed earlier. The effective stresses within the partially saturated sand profile are considerably higher than within the saturated sand.

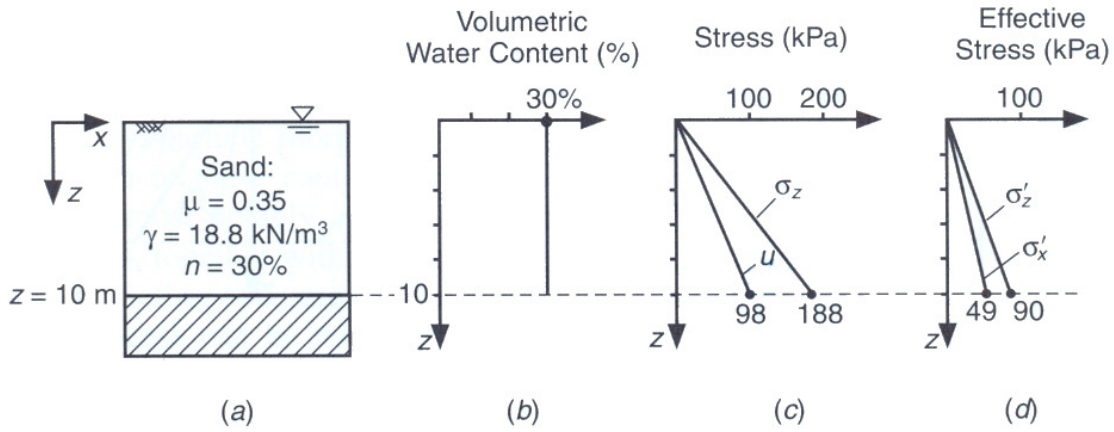

Figure 2.10 Profiles of water content, total stress and effective stress for a saturated sand (Lu and Likos, 2004)

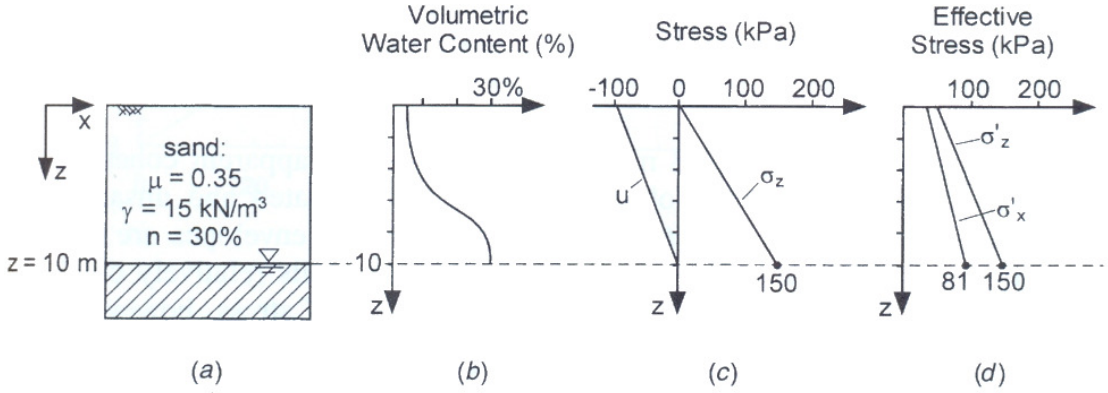

Figure 2.11 Profiles of water content, total stress and effective stress for partially saturated sand (Lu and Likos, 2004)

Within partially saturated soil the three phase nature creates more complexity when calculating the effective stress. Throughout the literature, investigators have proposed many modified effective stress laws for partially saturated soils. Fredlund and Rahardjo (1979) have presented an overview of the history of development of formulae to describe the effective stress of partially saturated soils. Of the proposed modifications to the effective stress equation, one proposed by Bishop (1959) gained widespread reference. Bishop (1959) utilised the terms $(\sigma - u_a)$ and $(u_a - u_w)$ together with an effective stress parameter, χ in Equation 2.34 to calculate the single effective stress state variable σ':

$$\sigma' = (\sigma - u_a) + \chi(u_a - u_w) \qquad \textbf{2.34}$$

The parameter χ, is referred to as the effective stress parameter. χ is related to the degree of saturation or matric suction. Within equation 2.34 both the net normal

stresses, $(\sigma\text{-}u_a)$ and the stresses due to suction $\chi(u_a\text{-}u_w)$ are considered. Bishop's effective stress, whilst being able to capture some characteristics of partially saturated soil behaviour such as the shear strength increase due to suction, could not explain wetting induced collapse. Many authors have challenged the approach used to develop Bishop's effective stress. Their arguments are that using the single stress state variable, σ', will not be able to reproduce the collapse upon wetting observed experimentally. This has been contested by Khalili et al (2004) and Jennings and Burland (1962), amongst others, stipulating that the single stress state variable approach has been developed within a linear elastic framework and that the non-recoverable collapse observed can be described using elasto-plastic theories. Some authors then developed the use of two stress state variables. It can be seen from figure 2.8 that the compressibility of the soil changes due to both the mean net stress and also the degree of saturation. Therefore in order to fully describe the volume changes within partially saturated soil two stress state variables will need to be used; (1) a function of mean net stress (2) a function of suction. The use of two stress state variables has now been accepted by most authors. The use of two stress state variables allows the formulation of constitutive equations which can describe both the increase in shear strength and the volume changes within partially saturated soils. Figures 2.12 and 2.13 show graphical representations of the state surface and failure envelope using two stress state variables.

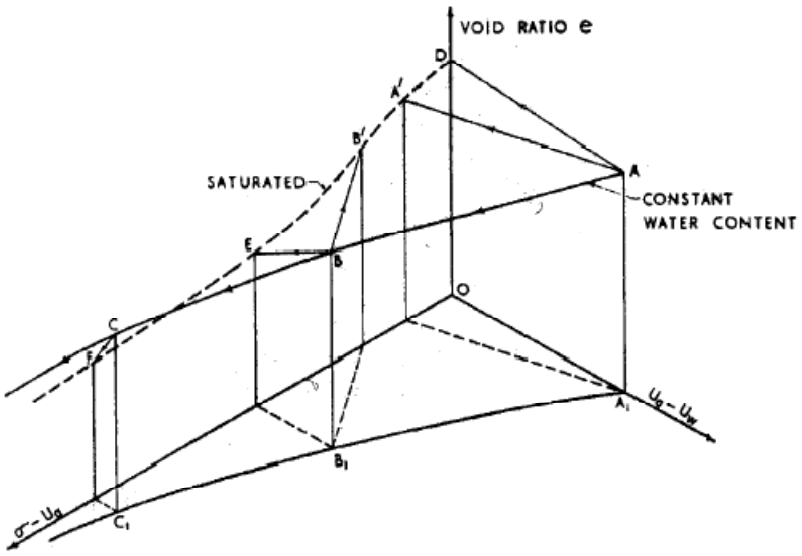

Figure 2.12 Void ratio state surface – Volume changes under all round pressure plotted in a void ratio-stress space Bishop and Blight (1963) after Georgiadis (2003).

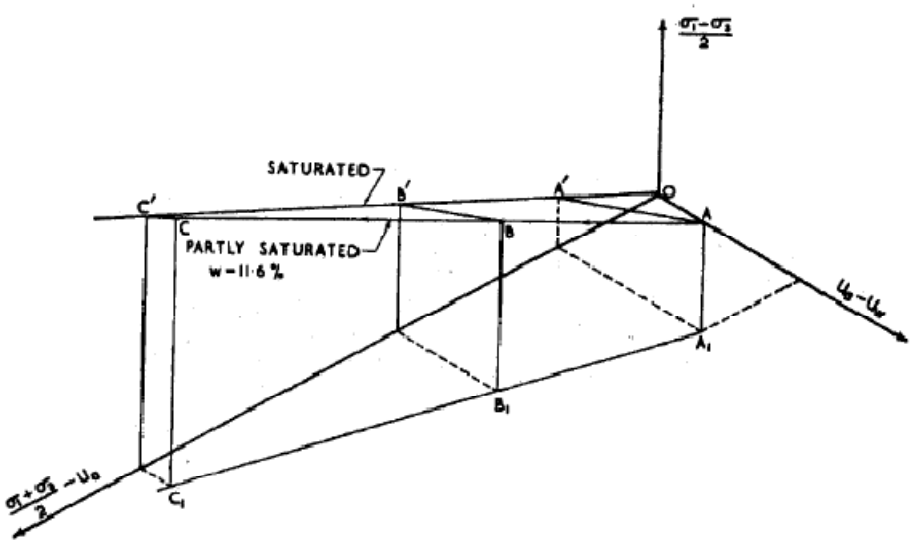

Figure 2.13 Results of tests on saturated and partially saturated Selset clay Bishop and Blight (1963) after Georgiadis (2003).

The advantages over the single stress variable approach when capturing the partially saturated soil characteristics are obvious. Other criticisms of the single stress state variable approach are on the use of a soil parameter. Morgenstren (1979) argued that effective stress is a stress variable and should therefore not include a soil specific property. Lu and Likos (2004) do not agree and argue that '…stress state variables are those which are required to completely describe a system….' and that for partially saturated soil, which is a multi-phase system, material parameters are necessary to describe the relative magnitudes of each phase present.

2.5.3 Stress dependent hydrology

The effect of the stress state on the SWCC has been investigated by a number of authors. (Vanapalli et al, 1999) has investigated the effect of stress history on the SWCC and (Ng and Pang, 2000) have investigated the effects directly. Vanapalli et al (1996) found that the soil water characteristics of a compacted till compacted dry of optimum moisture content were influenced by stress history but the soil water characteristics were not influenced within a sample compacted wet of optimum. Ng and Pang (2000) concluded that within the samples of a decomposed volcanic soil the soil water characteristics were influenced by the stress state of the soil. Significantly the soil showed a trend for higher air entry values for higher stress states. The findings were also applied to a slope stability model where it was found that suctions were lower

using stress dependant SWCC's than suctions for standard SWCC's. This lead to higher effective permeabilities and therefore increased infiltration and instability.

The stress dependency of the SWCC is an important factor in the numerical modelling of slopes Ng and Pang (2000) states that whilst net normal stresses within slopes seldom change over time the net stresses do vary spatially. Care will, therefore, be needed when conducting tests to establish the SWCC for slope material.

2.5.4 Suction and shear strength

Predicting the shear strength of a soil is one of the most fundamental aspects of geotechnical engineering, particularly when assessing the stability of slopes. The maximum shear strength of a soil is the maximum load across a unit area that the soil can resist. Within saturated soil mechanics the shear strength of a soil is generally described by the Mohr-Coulomb failure criterion:

$$\tau_f = c' + (\sigma - u_w)_f \tan\phi' \qquad \textbf{2.35}$$

Where τ_f is the shear stress at failure, *c'* is the effective cohesion, $(\sigma\text{-}u_w)_f$ is the effective stress at failure and ϕ' is the effective angle of internal friction. On a plot of shear stress verses effective normal stress the failure envelope is defined by a straight line with a slope equal to ϕ' and an intercept on the shear stress axis at *c'*. Figure 2.14 after (Lu and Likos, 2004) shows a typical Mohr-Coulomb failure envelope with two Mohr circles A and B. For any combination of effective stress and shear stress that lies beneath the failure envelope the soil is stable and for any combination that lies on the envelope the soil has sheared. The orientation of the failure plane can be determined from the geometry of the Mohr's circle.

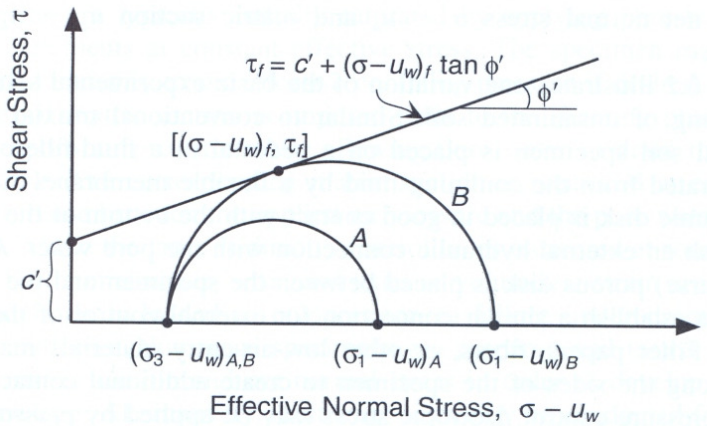

Figure 2.14 Mohr-Coulomb failure envelope for a saturated soil. The state of stress described by circle A is for a stable soil and the state of stress described by circle B represents a failure condition (Lu and Likos, 2004)

As can be seen from Figure 2.7 the shear stress within partially saturated soil increases with increasing suction. Many authors have developed ways of determining the shear strength of partially saturated soils. Bishop (1959) developed an extension to the Mohr-Coulomb failure criterion as:

$$\tau = c' + (\sigma - u_a)\tan\phi' + \chi(u_a - u_w)\tan\phi' \qquad \textbf{2.36}$$

For a completely saturated soil the expression reduces back to the fully saturated Mohr-coulomb failure criterion. The parameter χ varies between 1 for a fully saturated soil and 0 for a dry soil. χ is a function of saturation is non-linear and has been proven hard to determine. Bishop (1954) proposed that χ could be determined indirectly from stresses measured during the failure of specimens and Equation 2.36. Authors have also attempted to determine χ mathematically. Khalili and Khabbaz (1998) proposed an expression for χ as a function of suction ratio:

$$\chi = \left(\frac{u_a - u_w}{u_e}\right)^{-0.55} \text{ for } u_a - u_w > u_e \text{ and } \chi = 1 \text{ for } u_a - u_w \le u_e \qquad \textbf{2.37}$$

Where u_e is the air entry pressure. Vanapalli and Fredlund (2000) also investigated expressions of χ and found two expressions that fitted the data presented by Escario and Juca (1989) reasonably well for suctions ranging between 0 and 1500 kPa:

$$\chi = S^k = \left(\frac{\theta}{\theta_s}\right)^k \quad \textbf{2.38}$$

$$\chi = \frac{\theta - \theta_r}{\theta_s - \theta_r} \quad \textbf{2.39}$$

Where S is the degree of saturation and k is a fitting parameter. Figure 2.15 shows the variation of the parameter χ with respect to degree of saturation for the expressions proposed by Vanapalli and Fredlund (2000).

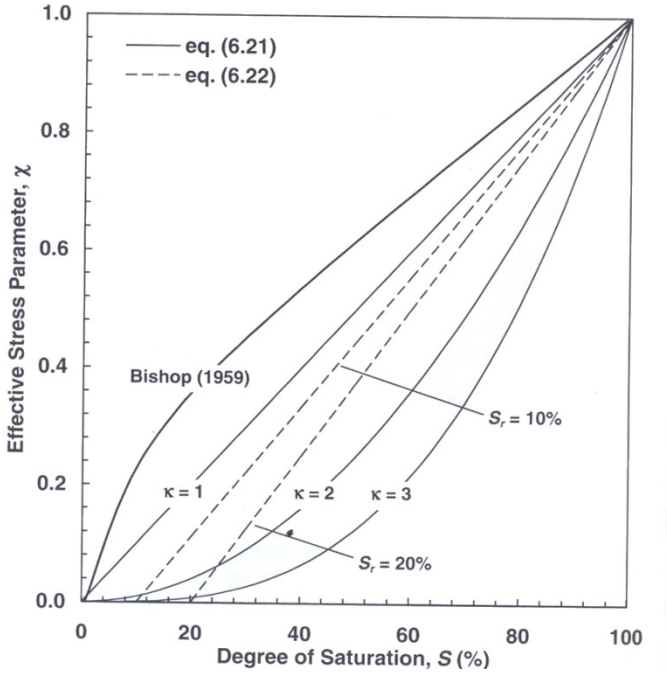

Figure 2.15 Variation of parameter χ with degree of saturation as measured indirectly (Bishop, 1954) and calculated by equations 2.38 and 2.39.

Others have also attempted to develop an extension to the Mohr-Coulomb failure criterion, notably Fredlund et al (1978). They proposed the following expression:

$$\tau = c' + (\sigma - u_a)\tan\phi' + (u_a - u_w)\tan\phi^b \quad \textbf{2.40}$$

Where the parameter ϕ^b is the slope of the failure surface in the shear strength versus suction plane. This parameter is based on the extended Mohr-Coulomb failure envelope shown in Figure 2.16. Figure 2.16 adds another axis to the shear stress verses net normal stress plot. This axis represents the matric suction. Tests carried out on the shear strengths of a saturated and partially saturated clay by Escario (1980) show that

with increasing matric suction the effective angle of internal friction, ϕ', remained constant but the effective cohesion, *c'*, increased. The increase also appeared to be linear. The parameter ϕ^b was introduced by Fredlund et al (1978) to allow for this increase in *c'* (c_1, also known as apparent cohesion).

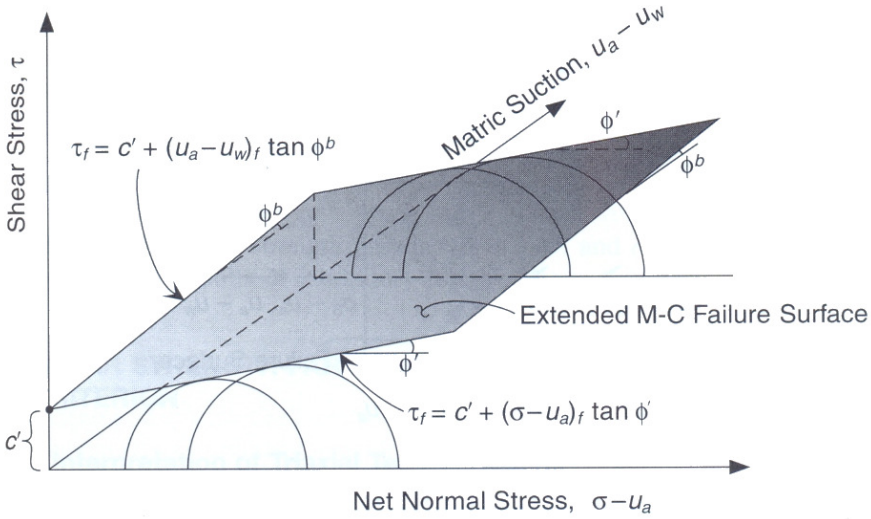

Figure 2.16 Extended Mohr-Coulomb failure envelope for partially saturated soil. After Lu and Likos (2004).

Gan et al (1988) and Escario and Juca (1989) however, presented experimental evidence over a wide range of suctions that showed the relationship between shear stress and matric suction was non-linear. Vanapalli et al (1996) showed that the relationship was linear up to the point of air entry after which the relationship becomes non-linear, Figure 2.17, ϕ^b was then shown to decrease as matric suction increased and could even become negative for some materials.

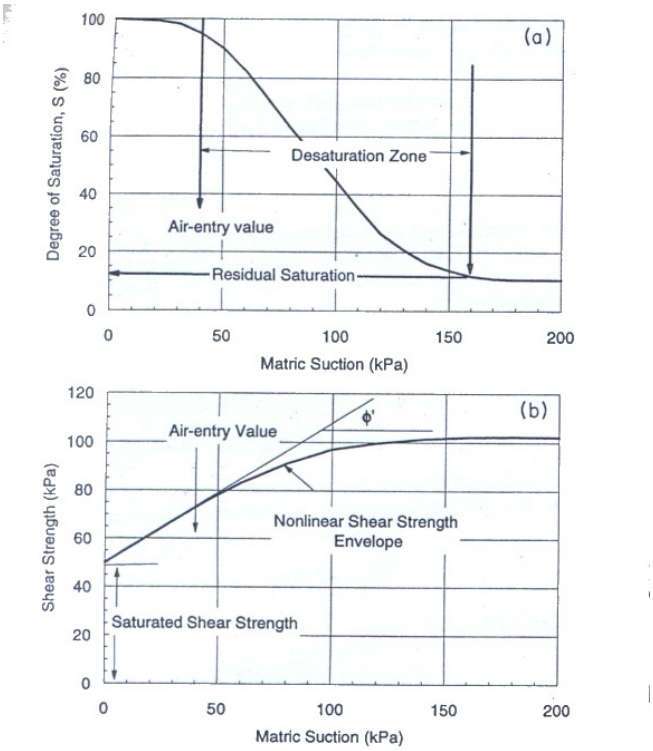

Figure 2.17 (a) a typical SWCC (b) shear strength of soil as it relates to the SWCC (Vanapalli et al, 1996).

At high levels of suction as the soil becomes dry Escario and Juca (1989) showed that the increase in apparent cohesion due to suction tended towards zero. Fredlund et al (1996) and Vanapalli et al (1996) then developed non-linear functions to predict the shear strength of partially saturated soil using the SWCC with some showing good comparison to limited experimental data.

Work has also been carried out by Toll (1990) who carried out tests on partially saturated lateritic gravel from Kenya. He presented a framework in terms of total stresses and suctions which was based on the critical state model for saturated soils. The framework is based on the separate stress state variables $(\sigma\text{-}u_a)$ and $(u_a\text{-}u_w)$ thus avoiding the problems of using a singular stress state variable. This gave an expression for the critical state shear strength as:

$$q = M_a(p - u_a) + M_w(u_a - u_w) \qquad \textbf{2.41}$$

Where q is the deviator stress, p is the mean total stress. The parameter M_a is called the total stress ratio and is linked to the net mean stress. The parameter M_w is called the

suction ratio and is linked to the matric suction. The parameters M_a and M_w are heavily dependant upon saturation and are equal to M_s at full saturation where equation 2.41 reduces to:

$$q = M_s(p - u_w) \qquad \textbf{2.42}$$

The relationship between saturation and the *M* parameters is shown in Figure 2.18.

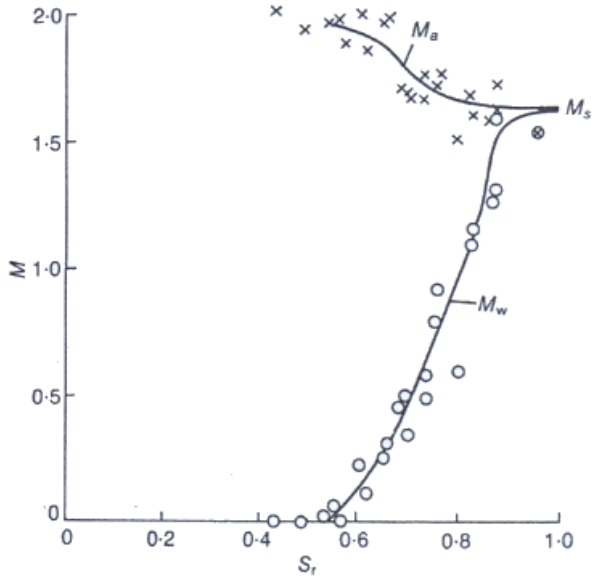

Figure 2.18 Variation of M parameters with degree of saturation (Toll, 1990).

The advantages of the framework proposed by Toll (1990) over the approach proposed by Fredlund et al (1978) are that the parameters M_a and M_w are non-linear and directly related to the degree of saturation. Obtaining these parameters, however, proves difficult.

A lot of development work has been carried out on creating a framework for which the shear strength increase of partially saturated soil can be described. The main differences between approaches are the use of the single effective stress variable and the use of two separate effective stress variables. All models, however, still require extra parameters to be defined.

2.5.5 *Modelling partially saturated constitutive models*

There are numerous saturated constitutive models within the literature which vary from the basic Mohr-coulomb model to more complex critical state models which are capable

of modelling such behaviour as small strain stiffness, soil structure etc. These models are not within the scope of thesis and will therefore not be covered. Of interest to this thesis are the constitutive models which have been developed to simulate the behaviour of partially saturated soils. These models attempt to partially or fully describe the volumetric behaviour of partially saturated soil as well as the increase strength.

One of the first attempts to model the compressibility of partially saturated soil was by Biot (1941). In 1941 Biot presented a three dimensional consolidation theory for soil which contained occluded air bubbles. The model is a linear elastic model where two constitutive relationships were developed, one for the solid phase and one for the liquid phase. Two independent stress variables were used. This approach allowed the stiffness of the soil to vary with saturation and also for the development of pore pressures within partially saturated soil. The model is elastic and does not allow for wetting induced collapse. The use of such a model is therefore not advantageous for assessing slope stability.

Researchers (Alonso et al, 1990, Josa et al, 1992, Wheeler and Sivakumar, 1995 Georgiadis ,2003, amongst others) have been developing elastoplastic models for partially saturated soils. These models are based on the critical state soil mechanics theory. The models allow the simulation of the characteristics of partially saturated soils such as collapse upon wetting and an increase in shear strength due to increased suction.

The BBM (Barcelona Basic Model) developed by Alonso et al. (1990) is perhaps the most well known partially saturated elastoplastic soil model. The model is designed for slightly expansive soils. The model is based upon the modified Cam clay model. The stress state variables used within the model are the net stresses $(\sigma - u)$ and the suction $(u_a - u_w)$. Figure 2.19 shows the three dimensional yield surface for the model. Under saturated conditions the suction equals zero and the model reverts back to the saturated modified Cam clay model. Under partially saturated conditions the yield surface expands with the rate of increase being a function of the suction. Within the BBM model the partially saturated isotropic compression line is assumed to be linear and will therefore constantly diverge from the saturated isotropic compression line, Figure 2.19. This will result in an ever increasing potential collapse for an increasing mean net stress.

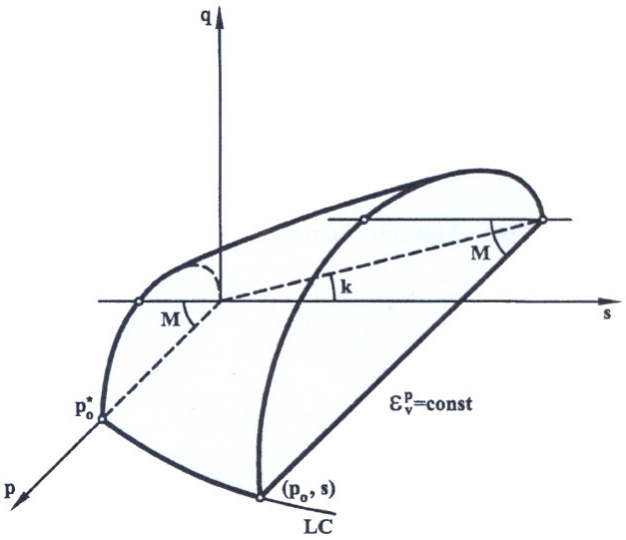

Figure 2.19 Three dimensional yield surface of the Barcelona Basic Model (Alonso et al, 1990)

The Josa et al (1992) model addresses this issue by introducing a modified expression for the expansion of the yield surface with increasing suction. The addition of this modification allows the partially saturated isotropic compression line diverge from the saturated line until a maximum collapse is reached. Wheeler and Sivakumar (1995) further developed the BBM by introducing functions which were more closely based on experimental results. Recently authors have also been working on developing partially saturated soil models within a thermodynamic framework and also incorporating features to capture expansive soil behaviour. Such developments are outside the scope of this thesis and will therefore not be reviewed.

2.6 What is required to model slope stability?

It is clear that there has recently been a lot of development on the modelling of partially saturated soils. The development of these constitutive soil models have implications on the modelling of infrastructure slopes. With the more sophisticated partially saturated soil models further parameters need to be defined. These parameters are sometimes functions of matric suction, water content or degree of saturation but are sometimes empirical and do not have direct physical meaning. They are therefore difficult and expensive to obtain and there must therefore be a compromise between accuracy and practicality. When considering infrastructure slopes, where there may be so many inherent variables within the material of the slope, there is no practical advantage in using more complex constitutive models. It is therefore clear that at some point

increased accuracy offered by additional complexity in the constitutive model will be outweighed by the practicality in obtaining the specific data. This will then lead to uncertainty in the material parameters. It is worth noting, however, that in predicting slope stability it is the shear strength which is the dominant characteristic. Models using two stress state variables would therefore have a limited increase in accuracy but with the additional complexity of defining several additional parameters for which data is scarce. Single stress state variable models are therefore presently deemed to be satisfactory for such slope stability models. The engineer will need to consider the key variables which will need to be calculated from the available data for a particular problem and then choose the most suitable constitutive model.

It is considered, therefore, that to predict slope stability, the shear strength of the partially saturated soil needs to be determined. The single stress state variable models will be sufficient to determine this shear strength. In order to correctly predict the shear strength the degree of saturation or suction will be required. To predict seasonal variation in slope stability models the minimum requirements of the model will be the ability to model pore pressure variation (both saturated and partially saturated) and both saturated and partially saturated shear strength.

2.7 The soil surface condition

To correctly assess the pore pressures variation within a slope there must first be an understanding of how water enters an exits the slope surface. The factors which determine the amount of water which infiltrates into a slope and also water drawn out of a slope are summarised within Figure 2.20.

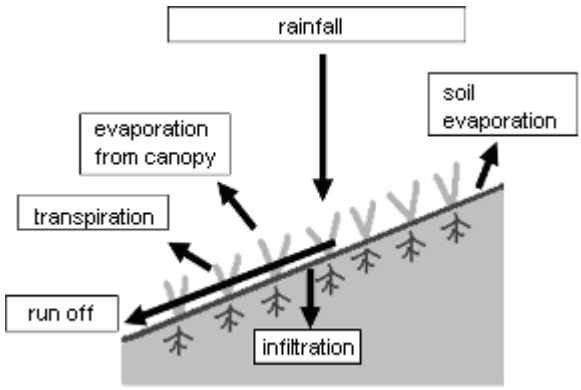

Figure 2.20 The slope surface condition, how water enters and exits the slope surface.

Rainfall falls on the slope and is intercepted by the vegetation canopy, water may evaporate from this canopy. Water is also lost through transpiration from the vegetation, soil evaporation and run off. Within this section an overview is given for each of these mechanisms and there will also be a review of current approaches to modelling them.

2.7.1 Soil evaporation

When considering a body of water with a free surface, molecules of water with enough energy can leave this surface. They will then be in a gaseous state called water vapour, the pressure exerted by this gas is termed the vapour pressure. Molecules of water that are in the water vapour can also collide with air molecules and therefore lose energy and enter the water surface. If the number of water molecules leaving the water surface equals the number of water molecules entering the water surface then the system is in equilibrium and the evaporation rate is zero, with the air above the water surface being saturated with water vapour. If the number of molecules leaving the surface exceeds the number of molecules entering the surface then the evaporation rate increases and evaporation occurs. Conversely if the number of water molecules entering the water surface exceeds the number leaving then condensation occurs. Tindal and Kunkel (1999) state there are four requirements for soil evaporation to occur. These are: (1) a supply of water; (2) a supply of heat; (3) a vapour pressure gradient so that the overlying air is less than saturated; (4) turbulence that carries away the overlying vapour in order to maintain the vapour pressure gradient. The vapour pressure can be calculated by using the dew-point temperature, the temperature at which the air becomes saturated or the wet-bulb temperature, the temperature to which a wetted object cools due to vaporisation of water from its surface:

$$e = e_{SW} - \gamma_T P(T - T_w) \quad \textbf{2.43}$$

Where e is the vapour pressure, e_{SW} is the saturation vapour pressure at T_W, P is the ambient air pressure, T is the temperature and Tw is the wet-bulb temperature. The term γ_T is called the thermodynamic psychometric constant an approximation for which is given by Gay (1972) from Tindal and Kunkel (1999) as:

$$\gamma_T = 6.97 \times 10^{-4}(1 + 0.00115 T_W) \quad \textbf{2.44}$$

To determine the amount of evaporation at the surface the evaporation rate must be known. Factors which influence the rate of evaporation from the soil surface are wind speed, the roughness of the surface (a rough surface increases turbulence and may also increase the surface area from which evaporation can occur), available energy and vapour pressure deficit $(e_s\text{-}e_a)$. Linsey and Kohler (1982) state that the rate of evaporation from a saturated soil surface is approximately equal to rate of evaporation from an adjacent water surface assuming equal temperature (Linsey et al., 1982). Tindall and Kunkel (1999), however, state that the rate of evaporation for a soil surface can sometimes exceed the evaporation for free standing water for special cases where the surface is aerodynamically rough or the surface is rough enough to have a sufficiently increased surface area. The evaporation rate for free standing water can be calculated using the following equation known as the Penman model (1956, 1948):

$$E = \frac{sR_{nw} + \gamma E_a}{s + \gamma} \quad \textbf{2.45}$$

Where E is the evaporation rate, s is the slope of the saturation-vapour-pressure curve at the wet bulb temperature, R_{nw} is the net radiation over water, E_a is a function of wind speed and vapour pressure deficit and γ is the psychometric constant calculated using the specific heat of air, Cp, atmospheric pressure, P, the ratio of molecular weights of water vapour and dry air, ε and the latent heat of vaporisation, L_v, by the following:

$$\gamma = {C_p P}/{\varepsilon L_v} \quad \textbf{2.46}$$

The Penman model assumes that there is constant supply of water to the soil surface, this is effectively the maximum potential evaporation. The soil surface will, however, dry out over time. Tindal and Kunkel (1999) state that there are three stages of soil drying over time. These stages are illustrated within Figure 2.21. At first, when the soil is saturated the evaporation rate is equal to that of free standing water and therefore the potential evaporation. During this stage the soil is able conduct water to the surface. Within the second stage the evaporation rate reduces. The reduction is due to the drying soil profile becoming unable to deliver sufficient volumes of water to the surface. At the third stage the surface water content equals that of the overlying air and cumulative evaporation decrease until it is approximately one third its initial value (Tindall and Kunkel, 1999). The curve described by Figure 2.21 depends on the soil type. As discussed previously the relative permeability of a soil is a function of its moisture content. Therefore as the soil dries it becomes increasingly difficult to transport water to the surface. Tindall and Kunkel (1999) provide an approximation of the flow rate of a column of soil of depth z with the following expressions:

$$\frac{\partial \theta}{\partial t} = \frac{\partial}{\partial z}\left[D(\theta)\frac{\partial \theta}{\partial z} \right] \qquad \textbf{2.47}$$

$$D = \frac{K(\theta)}{\left(d\theta / d\psi_m \right)} \qquad \textbf{2.48}$$

Where θ is the water content, z is the depth $K(\theta)$ is the hydraulic conductivity as a function of water content and ψ_m is the matric potential.

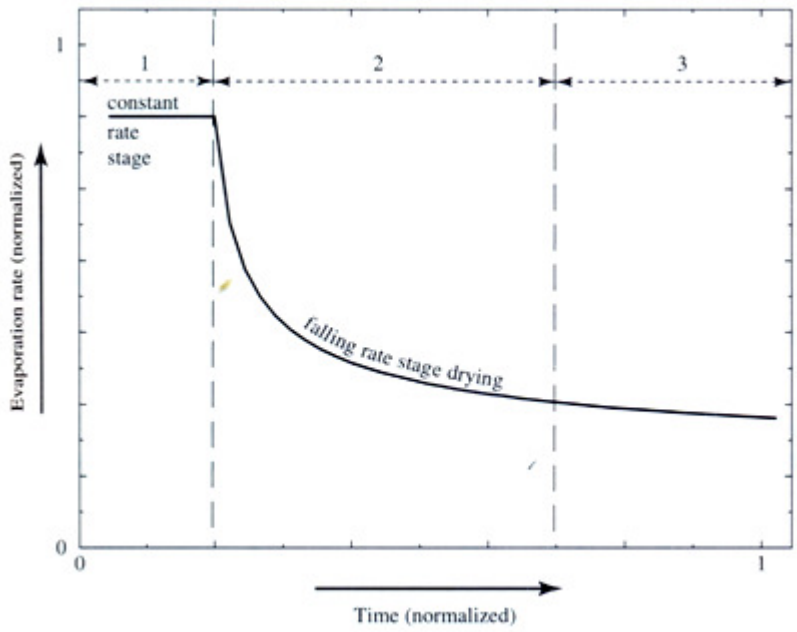

Figure 2.21 Stages of soil drying over time (Tindall and Kunkel, 1999)

Rushton (2003) presents a similar model based on the three stages. Rushton (2003) terms these stages the weather controlled stage, the soil profile controlled stage and the residual slow rate stage. Staple (1974) modified the Penman model by including the effect of a decreasing water content within the soil column. Staple also used the average air temperature, soil surface temperature and the corresponding saturation vapour to calculate the slope of the saturation vapour pressure verses temperature curve. This gave the expression:

$$E_s = \frac{h_s \Delta H + \gamma E_{as}}{h_s \Delta + \gamma} \qquad \textbf{2.49}$$

Equation 2.49 is the modified Penman equation where E_s is the surface evaporation, h_s the relative humidity of the soil, Δ is the slope of the saturation vapour pressure curve, de/dT (e being the actual vapour pressure and T the temperature), H is the net radiation and E_{as} is the drying power of the atmosphere calculated using an average of the air and soil temperatures. Konukcu (2007) suggested taking into account the saturated vapour pressure at soil surface temperature $e_{sat\text{-}s}$ and at the air temperature $e_{sat\text{-}a}$ and the average wind speed at 2m height, u, to calculate the original aerodynamic term, E_{as}, (Penman 1948) which lead to:

$$E_{as} = 0.35(h_s e_{sat-s} - h_a e_{sat-a})(0.5 + u/161) \quad \textbf{2.50}$$

This modification of the Staple method allowed for the differences in soil and air temperature and thus allows for more accurate calculation of evaporation rates. The net radiation is estimated using Equation 2.51 where R_s is the evaporation equivalent incoming short wave radiation, α is a dimensionless constant related to the albedo of the soil (assumed as 0.05 for wet soil and increasing sharply to 0.2 when the surface is dry) and R_{nl} net longwave back radiation calculated by equation 2.28. Within Equation 2.52 σ is the Stephan-Boltzmann constant equal to 1.63×10^8 cm/day and $T_{k(min)}$ and $T_{k(max)}$ are the minimum and maximum air temperatures. ε_{bulk} is the combined earth air emissivity and is defined by Brunt (1932) as Equation 2.53 where e_a is the vapour pressure of air and a and b are regression coefficients.

$$H = R_s(1-\alpha) - R_{nl} \quad \textbf{2.51}$$

$$R_{nl} = \varepsilon_{bulk}\sigma\left[\frac{T^4_{k(max)} - T^4_{k(min)}}{2}\right] \quad \textbf{2.52}$$

$$\varepsilon_{bulk} = a + b\sqrt{e_a} \quad \textbf{2.53}$$

Staple (1974) calculated the relative humidity, h_s, of the soil as a function of matric suction, further modifications were made by Konukcu (2007) by calculating h_s as a function of both the matric and osmotic suction. Konucku (2007) presented data for evaporation rates from a saline and non-saline soil surface. The two rates followed similar trends and the difference was not significant. Calculated evaporation rates were, however, more comparable to measured data for a non-saline soil using the Konukcu (2007) method rather than the Staple (1974) method confirming that using actual soil and air temperatures made a significant difference when calculating soil evaporation.

2.7.2 Interception

When vegetation is present on the surface of the soil precipitation will be intercepted by this vegetation before it reaches the ground. The vegetation canopy will be able to store a certain amount of water and this water may also evaporate from the canopy. The water that is intercepted and then evaporated is known as the interception loss. This loss is heavily dependant on the vegetation type and stage of development together with precipitation intensity and duration. Dingman (1994) presents an overview of the

definitions for the description and measurement of interception, Figure 2.22 (Dingman, 1994). Where *R* is the *gross rainfall* measured above the canopy, *Rt* is the *throughfall* which is the precipitation that reaches the ground surface, *Rs* is the *stemflow* which is the water that runs from the canopy down the vegetation stem to the surface, *Ec* is the canopy *interception loss* which is the water that evaporates from the canopy, *El* is the *litter interception loss* which is the evaporation from leaf litter, *Ei* is the total interception loss accounting for the sum of *Ec* and *El* and *Rn* is the *net rainfall* equal to *R* minus *Ei.*

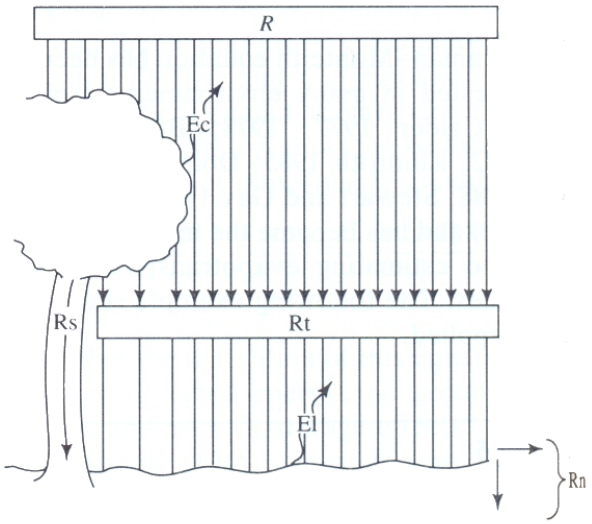

Figure 2.22 Interception diagram after Dingman (1994).

The most widely used model for interception loss is the model published by Rutter et al in 1971 (Dingman, 1994) a conceptual model of which is provided in Figure 2.23.

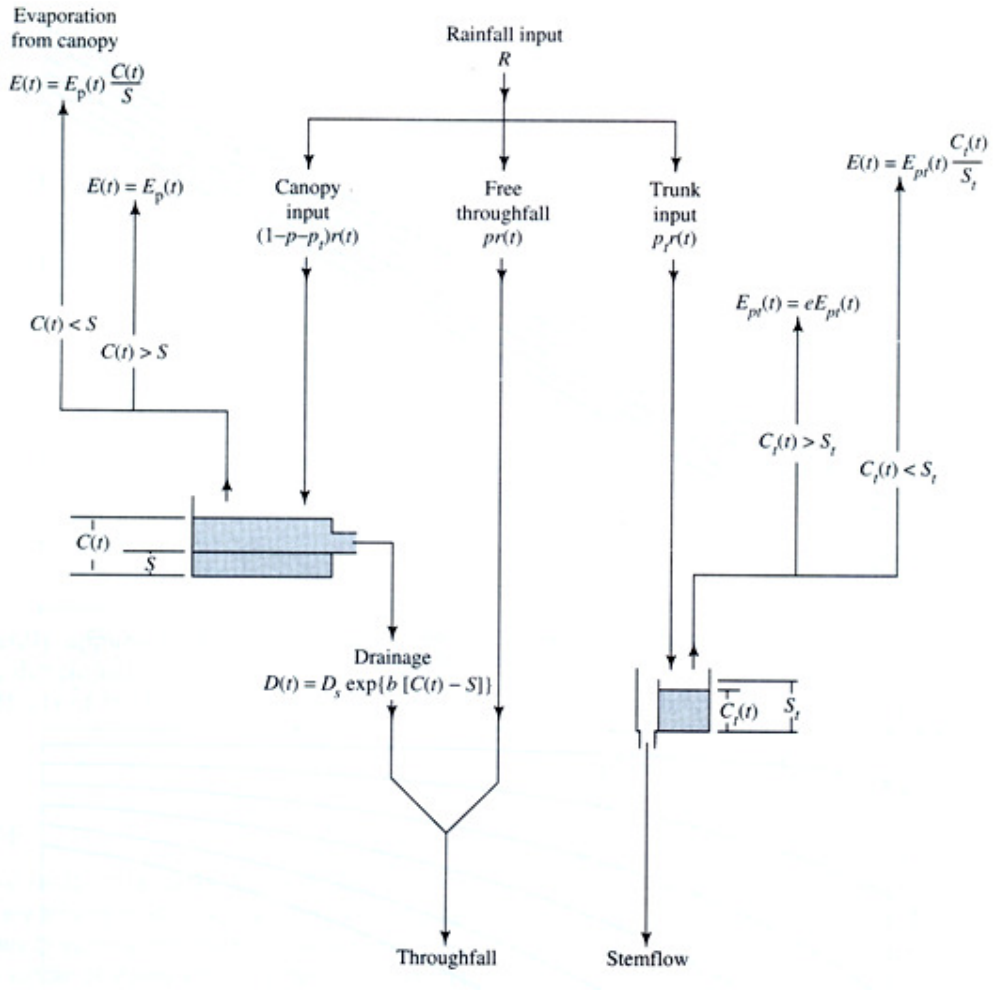

Figure 2.23 Rutter et al (1971) conceptual model of interception after Dingman (1994).

The rainfall is first split into three components; (1) canopy input, (2) free throughfall and (3) trunk input. The canopy is presumed to have a storage capacity S. The trunk storage is also defined as S_t. These storages are filled by the precipitation and emptied by drainage and evaporation. The fraction of rain that reaches the ground is determined by the throughfall coefficient, p and the amount of rain that reaches the trunk is p_t. The amount of water which reaches the canopy ,C_i can be defined as:

$$C_i = (1 - p - p_t)r(t) \qquad \textbf{2.54}$$

Where $r(t)$ is the time-variable rainfall rate. Given C_t is the actual amount of water on the canopy, if C_t is greater than the canopy storage (C_t>S) then evaporation occurs from the canopy at a rate as per the Penman model $E_p(t)$ (Potential Evaporation). However if C_t<S then evaporation occurs at a reduced rate of potential evaporation is defined as:

$$E_t = E_p(t)\left(\frac{C_t}{S}\right) \quad \textbf{2.55}$$

Also when $C_t<S$ drainage from the canopy is assumed to be 0. When $C_t \geq S$ drainage is calculated using the following equation:

$$D(t) = D_s \exp[b(C(t) - S)] \quad \textbf{2.56}$$

Ds and b are empirically determined. Rutter et al (1971/72) found the parameter *b* to vary between 30 and 46 but the variation was found to have a negligible effect on predictions and a mean value of 37 was adopted. The parameter Ds was calculated as:

$$D_s = (3.17 \times 10^{-5})S \quad \textbf{2.57}$$

The parameters for the canopy are derived from regression analysis using field data. This will involve the measurement of storage and drainage within the field and also hourly climatic data for calibration. Although the parameters for the Rutter model and its derivatives Gash (1979) (after Dingman (1994)) are hard to obtain authors have found good correlation between measured and calculated interception loss. Rutter (1971/1972) presented data for interception loss and the model showed good correlation with that data. The parameters derived for the calculation were assumed to remain constant throughout the year. The timescale for modelling the storm events was also small, within the region of 5 minute intervals.

2.7.3 Transpiration

Surface vegetation has a profound impact on the hydrology of the soil. The process by which plants remove water from the soil and release it to the atmosphere is called transpiration. Almost all the water absorbed by the root systems of plants will be released to the atmosphere through transpiration. It is the principle mechanism by which precipitation on land areas is returned to the atmosphere. The amount of water lost to the atmosphere through transpiration is therefore substantially larger than the amount lost due to bare ground evaporation. The amount of transpiration that occurs will vary depending upon the plant type and length of the growing season. The water is lost to the atmosphere through stomata. The stomata are openings in the leaf interior.

The transport of water from the soil through the plant is driven by potential energy gradients. As water vapour exits the stomata this creates a potential energy decrease which results in water being drawn up the vascular system of the plant. Water drawn up the vascular system creates a potential energy drop at the root level resulting in water being drawn from the surrounding soil into the roots. The plant has some control over this process by being able to control the size of the stomatal openings using guard cells. Controlling the stomatal openings controls the exit of water from these openings and therefore the magnitude of the potential energy gradients within the plant. The environmental factors which can affect the opening and closing of the guard cells are; (a) light (b) humidity (c) water content of the leaf (d) leaf temperature and (e) ambient CO_2 concentration (Stewart, 1989, after Dingman 1994). The amount of transpiration from a plant or crop is related to the size and number of stomata, their function and the leaf area (Tindall and Kunkel, 1999). To calculate the potential transpiration of a crop Rushton (2003) states that it is helpful to establish a reference crop. The behaviour of all other crops can then be related back to this crop. The crop generally selected as a reference crop is grass as it will grow throughout the year.

2.7.4 Evapotranspiration

Evapotranspiration is the total loss of water from a soil due to both evaporation and transpiration. The total evaporation is from the bare soil and also from the surfaces of vegetation. There have been a number of models developed by authors to calculate evapotranspiration. Of note are the Penman-Montieth model Montieth (1965) and the Priestly-Taylor (1972) model.

Montieth (1965) proposed an equation as an expansion of the Penman model (see Equation 2.45) taking into account the effects of vegetation. This is known as the Penman-Monteith equation:

$$\lambda E = \frac{s\left(R_N + g\right) + \rho_a C_p \left[\left(e_s - e_a\right) / r_a \right]}{\left(s + \gamma\right)\left[\left(r_a + r_s\right) / r_a \right]} \qquad \textbf{2.58}$$

Where E is the evapotranspiration rate, λ is the latent heat of vaporisation (the amount of energy needed to change a unit mass of water to water vapour at constant temperature

and pressure, at a temp of 20º λ= 2.45 MJ kg^{-1}), R_n is the net radiation, g is the soil heat flux, ρ_a mean air pressure at constant pressure, C_p is the specific heat of air, $(e_s\text{-}e_a)$ is the vapour pressure deficit and γ is the psychometric constant. The parameter r_a is the aerodynamic resistance (also known as the leaf conductance) and the parameter r_s is surface resistance (also known as the canopy conductance). Figure 2.24 shows the processes which these parameters attempt to model.

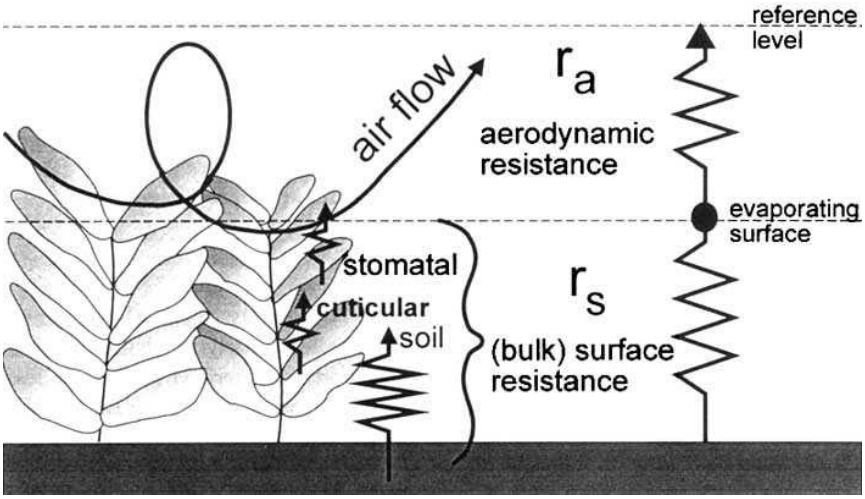

Figure 2.24 Surface resistance and aerodynamic resistance processes (Allen et al, 1998).

The aerodynamic resistance is the resistance of the vegetation to airflow and is calculated using:

$$r_a = \frac{ln\left[\frac{z_m - d}{z_{om}}\right] ln\left[\frac{z_h - d}{z_{oh}}\right]}{k^2 u_z} \qquad \textbf{2.59}$$

Where z_m is the height of the wind measurements, d is the zero plane displacement height, z_{om} is the roughness length governing momentum transfer, z_h is the height of humidity measurement, z_{oh} roughness length governing transfer of heat and vapour, k von Karmen's constant (0.41) and u_z wind speed at height z (Allen et al, 1998). The parameters d, z_{om} and z_{oh} can be estimated using the crop height h in conjunction with the following equations:

$$d = \tfrac{2}{3} h \qquad \textbf{2.60}$$

$$z_{om} = 0.123h \qquad \textbf{2.61}$$

$$z_{oh} = 0.1 z_{om} \quad \textbf{2.62}$$

The surface resistance is the resistance of the flow of water vapour from the ground to the evaporating surface. The surface resistance parameter involves all the processes in this transfer. An estimation of the surface resistance, $\boldsymbol{r_s}$, is given by:

$$r_s = \frac{r_l}{LAI_{active}} \quad \textbf{2.63}$$

Where r_l is the bulk stomatal resistance of a well illuminated leaf and LAI_{active} is the ratio of leaf area to bare ground (leaf area/bare ground area) (Allen et al, 1998). The Penman Monteith model uses the aerodynamic and surface resistance parameters to describe a complicated system involving many different processes. The r_s component can be defined to vary as a function of soil moisture tension as well as vegetation type thus giving a model that can calculate actual evapotranspiration for soils of varying degrees of saturation (Abbot et al, 1986a).

The Priestly-Taylor (1972) model is a semi empirical model. This model calculates the PET (potential evapotranspiration), ET_p which is the evapotranspiration assuming that the soil is saturated and has a constant supply of water. The equation for this model is given by:

$$ET_P = \alpha \frac{s}{s+\gamma}(R_n + G) \quad \textbf{2.64}$$

The parameter α in Equation 2.64 is an empirically derived unit less coefficient estimated to equal 1.26 when water is freely supplied (Stannard, 1993) but can vary from 1.08-1.34. The parameter is sensitive to soil moisture levels and becomes inconsistent for non-evapotranspiration conditions (Tindall and Kunkel, 1999).

There have been many comparisons for differing environmental conditions using these two models together with many others conducted by authors (Fisher et al, 2005, Summer and Jacobs, 2005, Mao et al, 2002) all found correlation between the various models and all the models performed reasonably well once the fitting parameters were

defined. Stanard (1993) however, found that for a study site comprising of sparse vegetation the Penman-Monteith model did not perform well and underestimated the mid day latent heat flux, λE. This was due to the bare ground having access to a shallow water table and therefore high evaporation rates. The Penman-Monteith model assumed a single canopy resistance which was too large and therefore caused an under-estimate of the λ. For this situation where the *rc* value was estimated it was found the Penman (1948) model predicted evapotranspiration more accurately.

2.7.5 Root water uptake

In models where the PET is calculated and the root distribution with depth known (e.g. 40% of roots at depth 0-0.1m 30% of roots 0.1-0.2m 20% of roots 0.2-0.3m and 10% of roots 0.3-0.4m) then the corresponding percentage of PET is applied to the corresponding depth zone. The suction of that depth zone will also determine the amount of water that can be extracted (Monteith, 1965). For models which do not have this capability, a root water uptake model can be implemented. These models have two different approaches, a microscopic approach and a macroscopic approach. The microscopic approach takes into account the water flux to a single root and the macroscopic approach treats the entire root system as a whole. For the purpose of slope stability analysis the microscopic approach will require detailed geometry and will therefore not be suitable. Macroscopic models use a sink term to extract water from the soil. The sink term is a volume of water per unit time per unit volume of soil. The sink term *S(h)* is defined as (Feddes et al, 1978):

$$S(h) = \alpha(h) S_{max} \qquad \textbf{2.65}$$

Where *S(h)* is the actual transpiration rate, α is a dimensionless function of pressure (suction) and S_{max} is the PET rate. Figure 2.25 shows the variation of α with suction. At saturation the roots are assumed unable to function, between h2 and h3 water uptake is at its maximum and between h3 and h4 water uptake is assumed to decrease linearly.

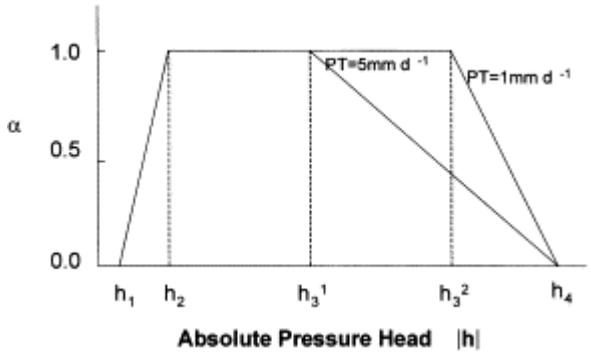

Figure 2.25 Dimensionless sink term as a function of pressure head after Li et al (2001).

The water uptake model is defined as (Hayoe and Dejong, 1988 after Li et al, 2000; Prassad, 1988):

$$S(h) = \frac{2PET}{Z_r}\left(1 - \frac{Z}{Z_r}\right) \qquad \textbf{2.66}$$

Where Z is the soil depth and Z_r is the rooting depth. The described model is the simplest root water uptake model. More advanced models utilise an exponential function root distribution function (Dwyer et al, 1988 after Li et al, 2000) yet the more advanced models require additional parameters to define the vegetation. The described model, with proper inputs, compares adequately with the more complex models (Li et al, 2000).

2.7.6 Run-off

During a rainfall event if the rate of precipitation exceeds the infiltration rate or the water table has risen to the surface therefore preventing further infiltration then the water will either pond on the surface or flow off the surface as runoff. There are many watershed models capable of modelling runoff. The techniques used by these models vary from using simple empirical relations to complex physically based governing equations. Borah and Bera (2003) provide an review of the flow-governing equations for overland flow an overview of their findings is presented here.

Dynamic Wave Equations, these are also known as the St. Venant equations. These consist of a continuity equation and a momentum equation given by:

$$\frac{\partial h}{\partial t} + \frac{\partial Q}{\partial x} = 0 \qquad \textbf{2.67}$$

$$\frac{\partial u}{\partial t} + u\frac{\partial u}{\partial x} + g\frac{\partial h}{\partial x} = g\left(S_0 - S_f\right) \qquad \textbf{2.68}$$

Where h is the flow depth, Q is the flow per unit width, u is the water velocity, g is the acceleration due to gravity S_0 is the bed slope, S_f is the energy gradient, t is the time and x the longitudinal distance.

Diffusive wave equation, these equations are similar to the dynamic wave equations. The continuity equation includes lateral flow (q is the lateral flow per unit width and per unit length) and the momentum equation has been simplified by ignoring the first two terms to give:

$$\frac{\partial h}{\partial t} + \frac{\partial Q}{\partial x} = q \qquad \textbf{2.69}$$

$$\frac{\partial h}{\partial x} = S_0 - S_f \qquad \textbf{2.70}$$

Both the dynamic wave equations and the diffusive wave equations use Manning's formula to calculate flow. This is given by the following equation:

$$Q = \frac{1}{n} A R^{2/3} S_f^{1/2} \qquad \textbf{2.71}$$

Where n is Manning's roughness coefficient, A is cross sectional area and R is the hydraulic radius.

Kinematic wave equations, are defined as within equation 2.67 and 2.68. They simplify the dynamic wave equations further by reducing the momentum equation so that the bed slope equals the energy gradient:

$$S_0 = S_f \qquad \textbf{2.72}$$

The continuity equation is as per the diffusive wave equation. The flow per unit width is calculated by:

$$Q = \alpha h^m \quad \textbf{2.73}$$

Where α is the kinematic wave parameter and m the kinematic wave exponent. These parameters can be related to the Manning roughness coefficient within equation 2.71.

Storage-based or nonlinear reservoir equations are based on a spatially uniform and temporarily variable continuity and an equation for flow (Manning's formula, equation 2.71) giving:

$$\frac{ds}{dt} = I - O \quad \textbf{2.74}$$

Where s is the storage volume of water, I is the inflow rate and O is the outflow rate.

Curve number and empirical equations, as the name suggests use empirically based assumptions in order to maintain water balance. The models reviewed by Borah and Bera (2003) all use the runoff curve number method (SCS 1972 after Borah and Bera 2003) and further empirical relations to solve the following equations:

$$Q_r = \frac{(P - 0.2S_r)^2}{P + 0.8S_r} \quad \textbf{2.75}$$

$$S_r = \frac{24500}{CN} - 254 \quad \textbf{2.76}$$

$$Q_P = 0.0028CiA \quad \textbf{2.77}$$

Where Q_r is the direct runoff, P is the accumulated rainfall, S_r is the potential difference between the rainfall and direct runoff, CN is the curve number for runoff potential for a soil cover complex, Q_p is the peak runoff rate, C is the runoff coefficient, i is the rainfall intensity and A is the watershed area.

The above models each offer varying degrees of simplicity and accuracy and therefore also modelling efficiency. The models incorporating the above equations offer different advantages to the solution of different problems. It depends upon what the user wishes to model, be it a vast area or a small area a continuous simulation or the simulation of a single storm event. The complex models are numerically expensive yet can produce detailed results. The simple models are sometimes incapable of producing the detailed results. Therefore the physically based models using the dynamic wave equations and diffusive wave equations are only suitable for small areas where detailed hydrological studies, involving single rainfall events, are required. The more simplified methods will be more suitable for larger catchment areas.

2.7.7 Soil moisture deficit

The soil moisture deficit, SMD, can also be used to represent the moisture conditions within a soil and is therefore capable of defining soil moisture conditions. The SMD can be defined as the amount of water needed for a soil to reach field capacity θ_{FC}. The field capacity of a soil is the amount of water a free draining soil can hold under gravitational forces (Rushton, 2003). At field capacity the SMD equals 0. Another parameter used to define the SMD is the permanent wilting point which is the moisture content below which roots cannot extract moisture. Figure 2.26 shows how the actual moisture content within a soil relates to the SMD. The actual moisture content available to the root is between the field capacity, θ_{FC}, and the permanent wilting point, θ_{pw}, moisture contents. The moisture profile within diagram 2.26 (i) can be represented by diagram 2.26 (ii) where the volume above the shading is the volume of water required to reach θ_{FC}. To calculate the SMD an equivalent depth is used. This depth is calculated by multiplying the full depth of the soil zone with the moisture content between field capacity and wilting point $(\theta_{FC} - \theta_{pw})$. For the example in the diagram this gives an equivalent depth of 0.6m. The SMD is then calculated as the equivalent depth of water required to reach field capacity.

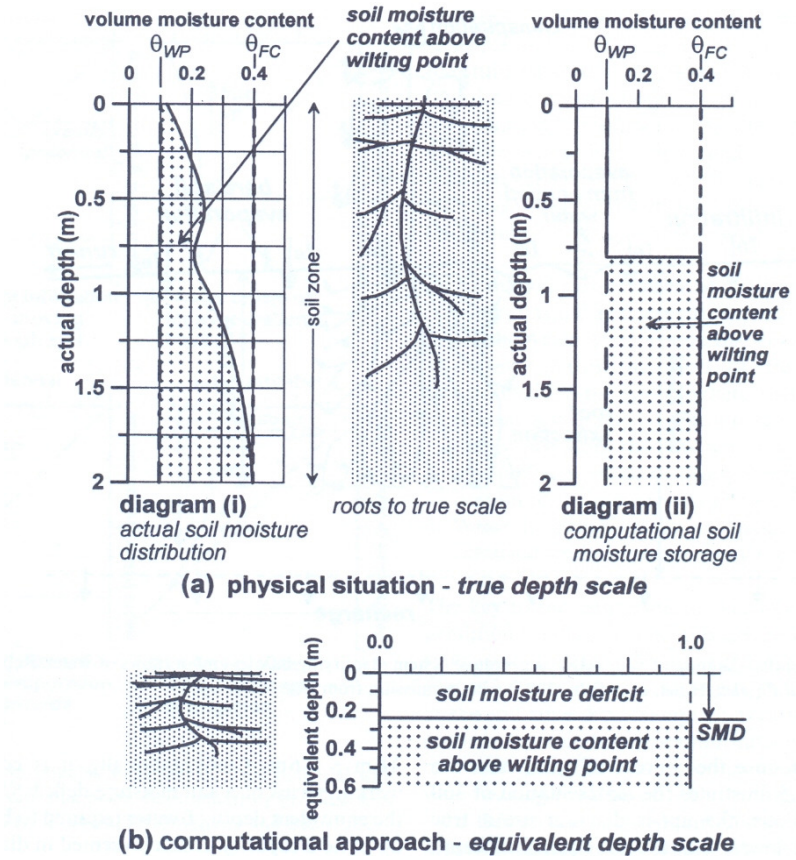

Figure 2.26 Relating actual moisture content with SMD after Rushton (2003).

Models to calculate SMD using water balance equations have also been developed and successfully used to calculate SMD for infrastructure slopes (Smethurst et al, 2006). The SMD can then be related to the pore pressure by use of the SWCC.

2.8 Modelling the effects of seasonal climate change on slope stability

Several models have been developed which are capable of modelling the effects of climate on slopes. Of these models some are capable of modelling saturated flow together with associated stress changes and deformations but not partially saturated flow or the surface condition. These models use a static applied surface seasonal pore water pressure fluctuation to model the climates influence. Some models are capable of modelling partially saturated flow and the surface condition but not the stress changes and associated deformation. There are also models which are capable of modelling partially saturated flow together with associated stress and deformations but there is, however, limited published research of the application of these models to seasonal stress changes and deformation.

It is therefore clear that the current modelling capability is split into two categories. There are those models which are concerned with stress changes caused by pore pressure fluctuations and those concerned with accurately modelling the flow of water through the soil. The models concerned with measuring deformation will be termed mechanical models and those concerned with flow will be termed hydrological models.

This section will first introduce the mechanical models capable of modelling the deformation and eventual progressive failure of slopes due to seasonal climate changes and then introduce several models capable of modelling the flow of water through a vegetated, partially saturated slope. Due to the limited published research on climatic effects on models capable of modelling partially saturated flow and using advanced partially saturated models this aspect will not be covered.

2.8.1 Coupled single phase hydrological/mechanical models

Some of the earliest attempts to model the effects of climate on slopes was carried out by Kovacevic et al (2001) using the ICFEP (Imperial College Finite Element Program). Work at Imperial College, London established that slopes of clay embankments moved as a response to climate. A program began which measured the movement of the slopes of embankments and when this data was plotted against calculated soil moisture deficit data it became clear that there was correlation between the two with the embankment shrinking in the summer and swelling in the winter. Earlier work by Skempton (1985) identified that the clay material which contains platy clay minerals and contains a clay fraction exceeding 20-25% is subject to strain softening. Firstly, at relatively small displacements, the critical state is reached and then, upon further straining, the material reaches a residual strength. The primary softening is due to the particles within the soil becoming re-orientated whereas the secondary residual softening is due to the clay platelets becoming orientated in the direction of slip. The areas where the platelets become orientated are known as shear bands. These shear bands have been observed under the microscope in clays from the slip zones of landslides and also within the laboratory. The shear bands are generally less than 5mm in thickness. Work was carried out within Imperial college by Potts et al (1997) developing a strain softening model within the ICFEP program. This model allowed the reduction of the strength parameters c' and φ' with increasing deviatoric plastic strain in an attempt to model the

degradation of shear strength observed. The rate of softening is illustrated within Figure 2.27.

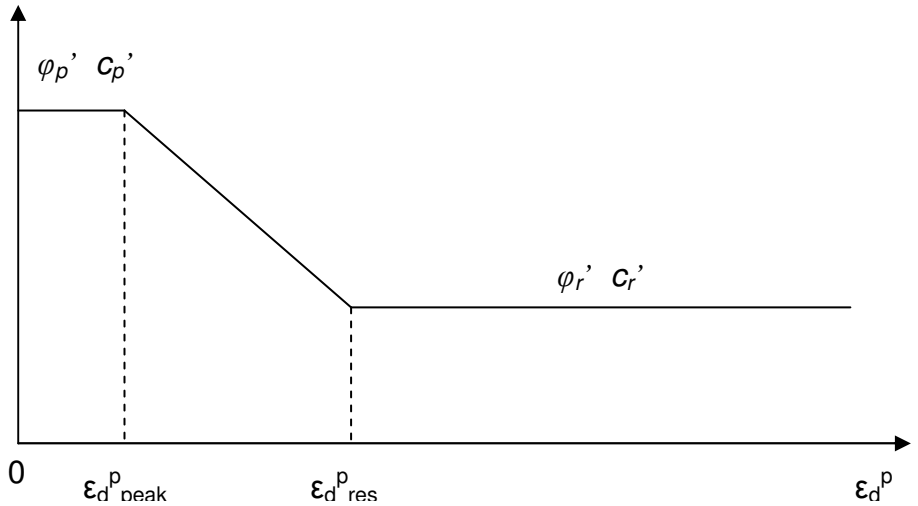

Figure 2.27 Rate of strength reduction with increased deviatoric shear.

Within Figure 2.27, φ_p' and c_p' are peak strengths and φ_r' and c_r' are residual strengths and $\varepsilon_d^p{}_{peak}$ is the deviatoric plastic strain at peak strength and $\varepsilon_d^p{}_{res}$ is the deviatoric plastic strain at residual strength. This process of reducing the strength as a function of deviatoric plastic strain has its inherent difficulties. The solution to the strain softening problem becomes grid dependant and localisation occurs. Figure 2.28 shows the process of localisation. When a square element with side length L is sheared so that the top is displaced a distance of L/2 the shear strain will be 50%. When the smaller element, of side length L/2, is sheared to the same displacement the shear strain will be 100%.

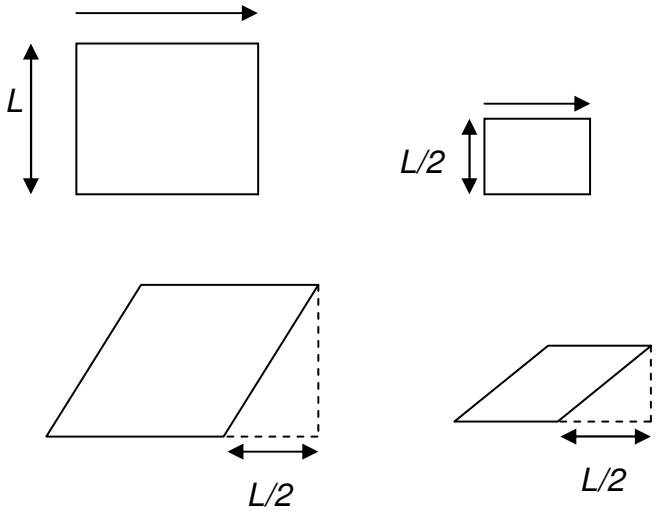

Figure 2.28 Shear strain for different grid element dimensions.

Therefore it is clear that for a decreasing element size failure load will also decrease. Within a numerical model, for a simple test run using a Mohr-coulomb model, as element size is reduced accuracy generally increases until a point where decreasing element size offers no more gain in accuracy and the solution converges to the true solution. Within the strain softening model as the element size reduces the solution diverges due to failure loads also reducing and no solution convergence is reached. The strain softening model is therefore grid dependent and the grid will either need to be fitted to a known solution or a more advanced technique used to make the model mesh independent, this technique is discussed later.

Kovacavic et al (2001) built a diagnostic embankment within the ICFEP code using the Mohr-coulomb constitutive soil model together with strain softening and applied a winter condition pore pressure boundary and ran the model to equilibrium. A summer pore pressure condition was then applied to the model surface boundary and again the model was run until equilibrium. The embankment showed swelling through the winter and shrinking during the summer. Successive winter summer cycles caused strains to develop within the embankment fill material, primarily at the toe. These strains resulted in the softening of the fill material at the toe of the embankment significantly weakening the model. Eventually, after several cycles the softening progressed through the embankment and collapse occurred. By applying the specified hydraulic boundary

to the ICFEP model, flow was forced through the embankment so that the pore pressures reached equilibrium. This effectively raised the water table. The flow within the model was saturated flow yet a simple algorithm was used which allowed saturation to be calculated as a function of suction. The permeability of the material was also related to the effective stress using a logarithmic relationship and another algorithm was also used which allowed the permeability to be reduced as a function of saturation Smith (2003). The decrease in permeability was logarithmic with a linear increase in suction.

As the model was allowed to reach equilibrium after the pore pressure boundary was applied the permeability became effectively inconsequential. The embankment fill material was also assumed to have an effective stress-dependent Young's modulus. This effectively meant that the embankment material became stiffer during the summer months and softer during the winter months. The Poisson's ratio was also alternated for this analysis from 0.3 for loading (summer condition) and 0.2 for unloading (winter condition). Therefore, for the summer condition as the embankment shrinks there will be more movement perpendicular to the load applied than recovered during the winter condition swelling. The stiffness of the material used in the analysis was based upon previous work by Potts et al (1997). The swelling predicted by the model agrees reasonably well with data from oedometer tests on brown London clay obtained by Apted (1977).

This work by Kovacevic et al (2001) highlighted that within the London clay progressive failure as a result of seasonal climate change could significantly weaken an embankment which could eventually lead to a collapse. The hydrological model however needed to be improved upon. A later publication by Nyambayo et al (2004), also using ICFEP, concentrated on the effects of permeability on the magnitude of the seasonal shrink swell cylces within an embankment. A similar hydrological model and approach was used as Kovacevic et al (2001) but the Poisson's ratio was not alternated and the permeability was homogenous. The model was also only permitted to run for six months with the summer condition and six months for the winter condition. Nyambayo et al (2004) also considered the effects of a deciduous tree on the embankment. The condition of six months each for winter and summer, resulting in each summer/winter cycle making one year of analysis, resulted in pore pressure

equilibrium not being reached before the pore pressure boundary was changed. Lower permeabilities resulted in a smaller annual suction range and therefore lower magnitudes of shrinking and swelling. The higher permeabilities had the opposite effect and therefore resulted in accelerated softening and failure. This analysis showed that the permeability within a slope had a significant effect on the stability of that slope.

The Nyambayo et al (2004) analysis needed site specific data for the summer and winter pore pressure condition. This was not always available. The flows that were caused by the application of the summer/winter condition were also of a magnitude that may not be achievable by vegetation during transpiration (Nyambayo, 2004). What was needed was a way of calculating the actual surface pore water pressures. Nyambayo et al (2004) applied a root water uptake model to the ICFEP program. This root water uptake model was based on a model developed by Feddes et al (1978) and Prassad (1988).

This version of the ICFEP model therefore required PET data and associated rainfall data as inputs. The PET and rainfall data used by Nyambayo et al (2004) was calculated by the Meteorological Office using MORECS (Meteorological Office Rainfall and Evaporation Calculation System). MORECS was capable of calculating weekly and monthly rainfall, soil moisture deficit and PET using a variant of the Penman-Monteith method. The PET would be calculated for a number of vegetation types, including grasslands and deciduous trees for a grid comprising of 40km squares throughout the UK. The ICFEP model also allowed for variations in the permeability profile from homogenous to effective stress dependant permeability, although true partially saturated flow was not modelled. A smeared crack model was also applied at the surface. This model assumed that at high suctions cracking would occur which would lead to an increase in permeability. Cracking is assumed to occur at a specified value of σ_3 (σ_{3i}) and cracking is assumed to have reached a maximum at another specified value of σ_3 (σ_{3ii}). The permeability increases from an initial value of k_i to a maximum value of k_f following a logarithmic relationship. The material of the embankment was a London clay which again was assumed to have a mean effective stress dependant permeability. The stiffness of the material was also assumed to be dependent on the mean effective stress. The material was also modelled as a strain softening material as per the Kovacevic simulations. The surface of the embankment

was assumed to be covered with vegetation (deciduous trees) and the influence of the depth of the roots of these trees on embankment stability was analysed. Once the embankment was built and allowed to settle under a surface pore pressure condition of 10 kPa for 5 years (this was the period for which the trees were assumed to establish themselves) the rainfall and PET boundary condition was applied. The boundary was applied for 1 month increments. A January condition was applied for a period of 1 month and then the February condition was applied for 1 month and so on.

The winter boundary condition was applied to the model first. This boundary condition was similar to the initial boundary condition and therefore the model did not respond much. However, Nyambayo et al (2004) found that large movements occurred during the 1st summer, larger than would actually occur in the field. This was assumed to be due to the vegetation being applied instantaneously whereas for a real situation the vegetation would take time to grow. Within the simulation the high pore pressure changes therefore occur over a relatively short period, within a real embankment the pore pressures would have changed incrementally over a much longer period.

Nyambayo et al (2004) conducted analyses to investigate the influence of the maximum rooting depth, material stiffness and cracking induced permeability increase. They altered the maximum rooting depth from 2, 2.5 and 3 metres to investigate the influence of this parameter on the seasonal pore pressures within the embankment. It was found that increasing the rooting depth within the 1st year resulted in the desiccation zone at the toe decreasing in size. This was due to the PET value remaining the same throughout the analysis meaning the same amount of water was drawn up from a 2m rooting zone as per a 3m rooting zone. Over time the actual PET for the 3m rooting zone would exceed the actual PET for the 2m rooting zone. This would be because at 2m the suctions would be high and it will become more difficult for the plant to draw water out of the soil. There will therefore be larger overall suctions within the embankment with a 3m rooting zone. This resulted in there being more settlement for the embankment with the deepest rooting zone (3m). When the simulations were run for a further 4 years the difference in settlements became less pronounced with the maximum settlements within the 1st year still having the greatest influence on subsequent settlements. Nyambayo et al (2004) also spoke of evidence that longer simulations would result in negligible settlement differences. The maximum and

minimum seasonal movements of the embankment for the three rooting depths showed that statistically the maximum movement occurred for the maximum rooting depth. This is reasonable as the most heavily vegetated embankments which it can be assumed therefore have the deepest rooting depths show the greatest seasonal movements. Interestingly the embankment with the rooting depth at 2.5m showed the smallest seasonal shrink swell magnitudes, statistically the 2m rooting depth showed similar maximum minimum seasonal shrink swell magnitudes. The groundwater regime modelled is complex with water inputs being influenced by rainfall amount, permeability and also desiccation and water outputs by rooting depth and soil suction. The rooting depth of 2.5m created the best balance between rainfall and precipitation. The finding highlights the fact that management of vegetation can be an effective way to manage embankment stability.

The effect of changing the stiffness of the material had little overall effect on the failure mechanism of the embankment. The settlement of the stiff and soft embankments was significantly different over the first 12 months and annual movements within the softer embankment were marginally higher. Pore pressures after 1 year were also found to be different but again this seemed to have little significant influence. Kovacevic et al (2001) also investigated the influence of stiffness on the progressive failure of embankments and reached a similar conclusion.

The next analysis involved changing the ratio of permeability of the cracked clay, k_f to intact clay, k_i. The k_f / k_i *r*atio was changed from 10 in the 1st analysis to 100 for the 2nd. The effects of changing the permeabilities resulted in the embankment with $k_f / k_i = 100$ being more stable over time. This is due to the higher permeability allowing more water in during a rainfall event and therefore making water available for evapotranspiration. Water is not extracted from deeper depths and seasonal movements are kept down.

The modelling work by Nyambayo et al (2004) has highlighted some important aspects to consider when modelling vegetated embankments. Of particular note is the influence of permeability on the progressive failure of an embankment. The influence of

desiccation was also considered and further work recommended to develop a constitutive model capable of capturing the behaviours of desiccated clays. The model could be refined, however by firstly using a partially saturated flow model. Nyambayo et al (2004) stated that the use of a saturated flow model was justified as the suctions generated were lower than those required for air entry. This is not the case for most embankments and, since Nyambayo et al's (2004) study a partially saturated flow model has been incorporated into ICFEP details of which will follow. The root uptake model used by Nyambayo et al (2004) produced good results and this method is used within agronomy and seepage analysis. The monthly timescale for the rainfall and PET inputs seems to be too long. For a changing climate where shorter more intense rainfall events coupled together with prolonged dry periods are averaged into a monthly rainfall and evapotranspiration input would mean that important events would be lost from the simulation. The model also does not account for the runoff of rain water. Rainwater may run off the upper slope only to infiltrate at the lower slope. There is also a possibility that the upper slope is less saturated than the lower slope and will therefore have a reduced effective permeability which may lead to a lower infiltration rate and also lower upper slope pore pressures. PET for this model was calculated over a 40km square grid. The PET for a slope will be very site specific as discussed by Smethurst et al (2006). The Penman-Monteith model is particularly sensitive to wind speed. The winds in the UK are predominantly Westerlies so slope aspect will have a significant effect. Whether the slope is shielded from the wind, perhaps by dense forest or structures, will also reduce wind speed and therefore reduce PET. Other factors affecting PET are net radiation and temperature, obviously a South facing slope will receive more radiation and will also have higher temperatures than a North facing slope. This will not only affect the PET but also the rate at which vegetation will grow. There will also be issues with interception that may also be missed within the Nyambayo et al (2004) model. Intercepted rainfall could evaporate from the surface of the canopy and therefore reduce the net rainfall reaching the ground.

During the same time work was being carried out by Nyambayo et al (2004) another researcher Smith (2003) was working with ICFEP. Smith was concerned with the infiltration into a partially saturated slope. The work carried out by Smith (2003) involved implementing a SWCC based upon the van Genuchten model. A suction dependant effective permeability model, which reduced permeability as a function of

suction, was already implemented within the program. The suction dependant effective permeability model was simplistic and not able to reproduce the partially saturated permeabilities of the more sophisticated models such as the van Genuchten model. ICFEP also included a mean effective stress dependant permeability model, where increased effective stress within a soil reduced the permeability. When this was used within the program with the suction dependant effective permeability model, the saturated permeability was first calculated as a function of the mean effective stress and then the suction dependant effective permeability was calculated as a proportion of this. The result of such a combination seemed unclear and whatever accuracy was gained from the stress dependant permeability may have been lost due to the simplistic suction dependant permeability model. A simple partially saturated constitutive model was also implemented within the program. This model was based on the work by Biot (1941). It was unclear as to whether a model including shear strength as a function of suction was used but as failure was not reached this was not important for the modelling.

There was no vegetation model during the analysis and only infiltration was modelled. Smith (2003) presented two case studies, the first case study modelled a slope in Hong Kong at Tung Chung. This slope was a natural slope and was covered with mixed vegetation. The properties for the case study were derived from testing of the site material and literature when the appropriate parameters were not available. Saturated permeability was assumed to be a function of mean effective stress and the power law relationship was used. The model was run in one day increments where the precipitation applied to the boundary for this period was assumed to be the average precipitation for that day. 100% of this precipitation was assumed to infiltrate the surface. If at any point the boundary became saturated and the pore pressure at the surface tended towards positive a threshold, a condition of 0 kPa was applied. This effectively meant that no ponding could occur and any runoff was lost from the calculation. Significant findings by Smith (2003) were that the variation of initial void ratio had no significant effect on pore pressures and that the simulations were sensitive to saturated permeability, the SWCC and the suction dependant permeability values. Influence of the initial pore pressure values was also restricted to the first few days of the simulation. Smith (2003) also significantly noted that to accurately model infiltration into a partially saturated slope the rainfall data needs to be in at least hourly increments and if possible even less. For a simulation where the entire daily average rainfall was applied in just 15 minutes

then most of this rainfall became runoff and deeper suctions within the slope were largely unaffected. If the same rainfall was applied over the period of the entire day then there was little runoff, if at all, and the water could penetrate to deeper within the slope. It was also found that the pore pressure response of the slope during a rainfall event was significantly influenced by the pore pressure distribution before that event. This lead to the conclusion that antecedent rainfall had a significant effect on the stability of a slope. Lastly Smith (2003) undertook the partially saturated simulation within the saturated version of ICFEP. The results of this simulation were much less accurate than any of the partially saturated predictions. This is significant as it shows that even with a simple suction dependant permeability model there is a measurable gain in the accuracy attained.

Further work involving ICFEP has been carried out and of note is the work by Georgiadis (2003) who has implemented two partially saturated constitutive soil models into the ICFEP program. These two constitutive soil models are based upon the Barcelona Basic Model developed by Alonso et al (1990). The two models offer two degrees of complexity of modelling the isotropic compression line. Of note is that the models require 22 parameters that can be obtained from three isotropic compression tests, two triaxial compression tests and one drying wetting test. Obtaining the parameters will therefore be both time consuming and expensive. Upon testing of the model foundations Georgiadis (2003) found significant advantages especially when modelling settlement when the water tables rises. Georgiadis also states that this model can be used in conjunction with partially saturated flow model, presumably the one developed by Smith (2003). Such a combination will provide a powerful tool when modelling coupled partially saturated behaviour. It may also be assumed that the vegetation model developed by Nyambayo et al (2004) could also be coupled with these models. This model will also provide a very useful tool when modelling slope stability although the issues raised by Smith (2003) concerning the rate at which precipitation data is applied will need to be addressed.

Further work considering the impacts of vegetation on the stability of slopes has been carried out at MottMacdonalds (1998, 1999a, 1999b, 2006) and O'Brien et al (2004). The work by MottMacdonald's is similar to the early work of Nyambayo et al (2004) in that a summer/winter pore pressure boundary was applied to the boundary of the slope.

MottMacdonald's used the finite difference program Flac. The commercial finite difference code Flac (Fast Langrangian Analysis of Continua) is capable of modelling geotechnical problems using tradition saturated soil mechanics theories. Work has also been done by considering larger vegetation such as trees. Progressive failure was modelled using a Mohr-coulomb model with strain softening. In an attempt to address the issues raised earlier concerning the mesh dependency of the strain softening model MottMacdonald's developed a technique in which the solution shows some convergence for a decreasing mesh size. As discussed earlier the shear bands which form under shear are generally less than 5mm thick and the elements used for a simulation are generally 0.5-1m in thickness. The shear band can therefore not be represented within the finite difference mesh. It was therefore proposed that displacements can be used instead of strains when specifying a strength reduction. A strain rate was still specified for the material before any softening occurs but after this a displacement is specified for the reduction to post peak strength and a further displacement specified for reduction to residual strength. Figure 2.29 shows the strength reduction for the MottMacdold's model.

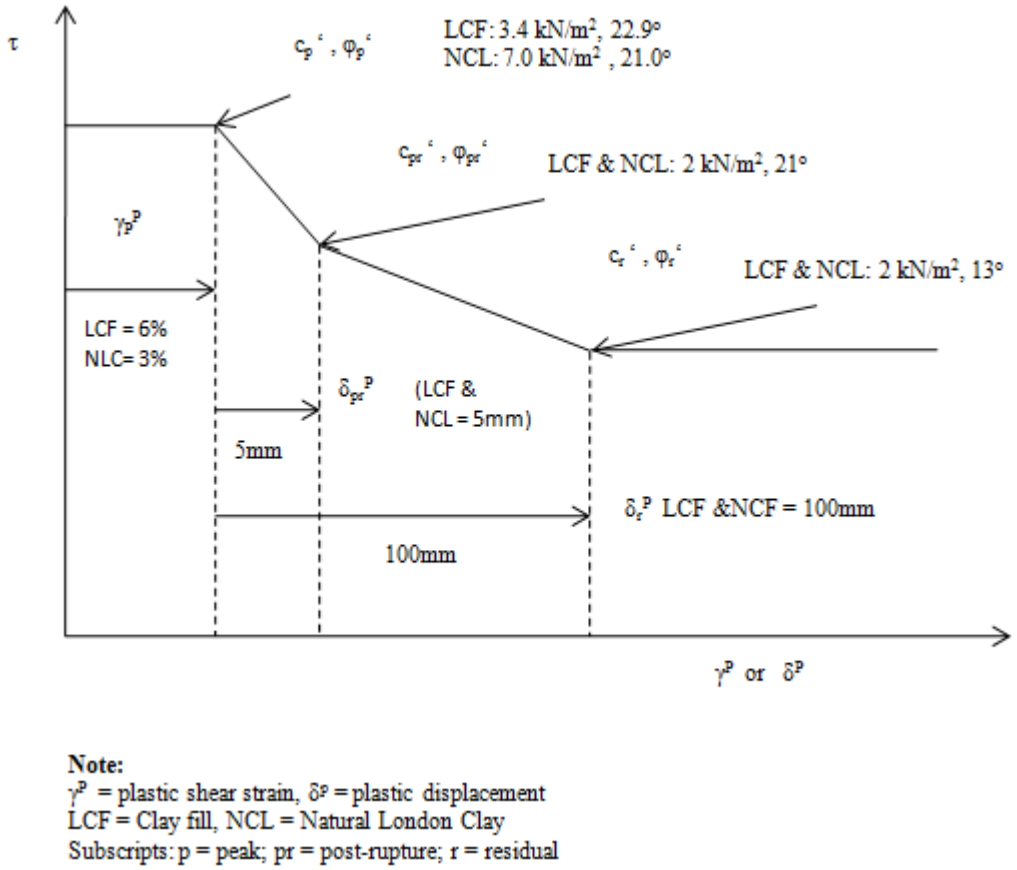

Note:
γ^p = plastic shear strain, δ^p = plastic displacement
LCF = Clay fill, NCL = Natural London Clay
Subscripts: p = peak; pr = post-rupture; r = residual

Figure 2.29 Numerical modelling post-peak degradation of strength (O'Brien et al, 2004).

Once the displacements to post peak and residual strength have been set they will need to be converted back into strains for the Flac input. Therefore for the same displacement a large element will have a smaller strain than a small element.

The finite difference code Flac used by MottMacdonald's also allowed for a decrease in permeability for partially saturated soil. Flac multiplied the flow rates by a factor $\hat{k}$, this was calculated by the following where ***s*** is the saturation:

$$\hat{k}(s) = s^2(3-2s) \qquad \textbf{2.78}$$

The applied surface pore water pressures were also based upon observations as per the initial Nyambayo et al (2004) and Kovacevic (2001) models. The modelling produced good deformation comparisons with observed data and is a good basis for further development.

The process used by MottMacdonald's to address localisation is adequate if sufficient data is available. Within the same program, Flac, Alehossein and Korinets (2000) have implemented a mesh-independent method for strain softening models. Alehossein and Korinets (2000) state that strain softening models require there to be an internal length scale. The problem with the strain softening model implemented within Flac is that it is assumed the element size is the internal length scale. Within their paper Alhossein and Korinets present the implementation of a gradient dependant plasticity model into the Flac program. Because the model includes the internal length scale as a parameter the localisation zone remains the same size independent of the number of elements used to model it. While this method obviously has its advantages the model proposed by Alhossein and Korinets has its drawbacks. The width of the localisation zone needs to be approximately 6 times larger than the element size. This is obviously not practical for modelling shear bands with thicknesses in the order of millimetres in slopes several metres high.

2.8.2 Hydrological models

There are many hydrological numerical models both non-commercial research and commercially available. These models offer a wide range of capabilities and most provide a level of detail which will not be required for a slope stability investigation. The following section provides a brief overview of some hydrological models and their advantages and disadvantages when modelling the development of slope pore water pressures.

The models chosen for review are HYDRUS, VADOSE/W and SHETRAN. These three models were chosen as they each have some distinct advantages over each other when modelling partially saturated, vegetated slope.

HYDRUS. The HYDRUS model is available in 1D, 2D or 3D and was developed to model the flow of water, heat and solutes through a porous media (Simunek at al, 2005). The code will therefore be able to monitor the partially saturated flow through the slope. The HYDRUS model uses the finite element method to solve a modified Richards equation to calculate the flow through the partially saturated media. The SWCC model for simulations can be chosen from a number of models (see Table 2.1) by the user. This offers the user some flexibility as some SWCC models offer better comparison to

the measured SWCC at opposing ends of the saturation scale. The distinct advantage of the HYDRUS code is that it can cope with the hysteretic behaviour of the SWCC. Tami et al (2004) conducted tests studying the effects of hysteresis on the development of pore pressures within a partially saturated slope and concluded that hysteresis did have a significant effect on the matric suctions. The HYDRUS model is the only model reviewed that has this capability. The HYDRUS model is primarily a seepage analysis model and therefore does not calculate evapotranspiration directly. For analysis which involves infiltration into a slope with vegetation present the evapotranspiration will need to be calculated separately and treated as an input parameter. HYDRUS does contain two root water uptake models. These are a root water uptake with compensation and root water uptake without compensation. Root water uptake without compensation is by the methods similar to those outlined within section 2.7.5. Root water uptake with compensation considers a drying soil profile and allows for more water to be taken from roots which are not stressed to compensate for the lack of water from roots which are stressed. This invariably leads to more water being extracted from the soil. Runoff within the HYDRUS code is assumed to be lost within the 2D and 3D models yet within the 1D model the water can be assumed to pond on the surface and infiltrate into the surface.

VADOSE/W has been developed as part of the GEO-STUDIO package developed by GEO-SLOPE international (GEO-SLOPE International LTD (2002). This model is available in 2D only and is also a finite element program which uses a modified version of the Richards equation. The program again offers the user a variety of SWCC models but does not model hysteresis. Actual evapotranspiration is modelled using the Penman-Wilson method (Wilson, 1990). When precipitation exceeds infiltration the user can specify that either the excess water is ignored and therefore lost from the calculation or that the water can be applied lower down the slope as an infiltration at a later time step.

SHETRAN is a 3D coupled surface/subsurface physically based spatially distributed finite difference model for coupled water flow together with sediment and solute transport modelling capabilities (Ewen et al, 2000). For the purpose of this modelling only the water flow component is considered. Data requirements for the model are meteorological data, soils data, vegetation properties and overland flow data together

with boundary and initial condition settings. SHETRAN will then automatically output pore pressures for each cell within the grid. At the surface boundary, interception of precipitation is modelled by a modified Rutter model (Rutter et al, 1971/1972) allowing the calculation of net rainfall reaching the ground together with the amount of stored water on the vegetation canopy and evaporation from the canopy. Evapotranspiration, the movement of water from the soil and within plants, is modelled within SHETRAN using the Penman-Montieth equation for actual evapotranspiration (Monteith, 1965). This is calculated as a loss term to describe the uptake of water through plant roots. Overland flow is also calculated within the programme. The depth of runoff water is determined from the available water from the interception evapotranspiration component and the rate of infiltration into the subsurface. Flow resistance parameters are then used to model the overland flow using approximations of the St. Venant equations of continuity and momentum. The subsurface is assumed to consist of a porous medium with pressure head a function of moisture content as per the van Genuchten relationship. Flow through the medium is calculated by solving the non-linear partial differential Richards equation.

Table 2.1 The surface condition modelling.

	HYDRUS	VADOSE/W	SHETRAN
	Finite element	Finite element	Finite Difference
1D/2D/3D	1D, 2D and 3D	2D	3D
One phase/two phase	1	1	1
Air phase pressure	Assumed atmospheric	Assumed atmospheric	Assumed atmospheric
Partially saturated flow equation	Modified Richards	Richards with modifications for vapour flow by Wilson (1990) and Milly (1982)	Richards
Partially saturated soil hydraulic properties	Brooks and Corey, 1964; van Genuchten, 1980; Vogel and Císlerová, 1988; Kosugi, 1996; Durner, 1994	Arya and Paris (1981); modified Kovacs; Fredlund and Xing (1994); van Genuchten, (1980)	Van Genuchtenen, 1980
Hysteresis accounted for	Yes	No	No
Evapotranspiration model	No	Yes Penman-Wilson (1990)	Yes Penman-Monteith, 1965
Root uptake model	Yes	Yes	Yes
Seasonal vegetation effects	-	Yes	Yes
Runoff	1D model assumes water can stand on surface, 2D and 3D models assume all water that does not infiltrate is lost	Simple model that requires the user to specify where runoff water is to be applied downslope. Otherwise runoff ignored	Yes Modified St. Venant equations

The hydrological models discussed here are all capable of modelling the infiltration and subsequent flow through a slope. HYDRUS, VADOSE/W and SHETRAN assume that the porous media is incompressible. Thus there is no mechanical generation of pore pressures.

2.8.3 Development of combined hydrological mechanical model

It is clear that to correctly model the pore pressure variations within a slope a hydrological model is required and to model deformation due to pore pressure changes a mechanical model is required. The work conducted by Kovacevic et al (2001), Potts et al (1997), Nyambayo (2004), O'Brien et al (2004) and MottMacdonald (1998, 1999a, 1999b and 2006) showed that it is possible to model slope deformation and eventual progressive failure by applying a hydrological boundary condition to a mechanical model. The short-comings of the approaches adopted were due to either the models

inability to model partially saturated flow or inability to model all the surface condition processes to a satisfactory degree of accuracy or sufficient time step.

The next logical modelling step would be to apply surface pore water pressures, which were calculated by a hydrological model, to a mechanical model capable of modelling partially saturated flow. The surface pore water pressures would take into account all the surface processes discussed within Section 2.7. When these are applied to the boundary of a mechanical model, capable of modelling partially saturated flow, this would accurately model the flow of water through the partially saturated and saturated material within the slope. The hydrological model and mechanical model will then return identical pore pressure profiles for a given simulation.

Mechanical models capable of modelling partially saturated flow available commercially include Flac tp (two phase) flow, PLAXIS flow and the Geostudio package amongst others. Of these models the Geostudio package is capable of modelling deformation, partially saturated flow and the surface condition. The Geostudio package, however, is not capable of modelling the progressive failure of a slope due to successive shrink swell cycles. The Flac tp flow model and PLAXIS flow model are both capable of modelling deformation and progressive failure. Of these two models Flac tp flow contains an in-built programming language, FISH, which can easily be used to apply a pore pressure boundary condition at any user defined interval. Flac tp flow uses an explicit solution scheme which enables the user to input their own user defined functions, using FISH language, which can be applied at any interval the user wishes. This enables the user to easily adopt functions such as effective stress dependant Young's modulus and seasonal Poisson ratio changes which were adopted during both the ICFEP and MottMacdonald modelling (Kovacevic et al (2001), Potts et al (1997), Nyambayo (2004) O'Brien et al (2004) and MottMacdonald (1998, 1999a, 1999b and 2006)).

The hydrological model used to calculate the surface pore water pressures will need to be able to effectively model all the critical surface processes. All the models reviewed all have the ability to model the processes discussed within section 2.7. HYDRUS has a more advanced partially saturated flow model as it can model hysteresis in the SWCC. This capability is not available in any of the mechanical models and the accuracy would

therefore be lost if this model was used. One surface process that divides the reviewed models is that of run-off. It has been seen that during the modelling of progressive flow the softening generally begins at the toe of the slope. During a rainfall event all surface water which has not penetrated into the slope will naturally run down slope. The pore pressure variation at this point is therefore critical in assessing stability. The model needs to be able to predict the volume of water which reaches the slope toe in order to correctly predict the pore pressures within this region. The HYDRUS model is incapable of performing this function. Of the remaining two models reviewed the SHETRAN model performs a more robust surface run-off calculation.

2.9 Concluding remarks

From this brief review of the current capabilities of modelling the effects of climate on slopes it is clear that there has been extensive research into the processes involved. Important processes have been identified such as hourly modelling within hydrological models which can calculate evapotranspiration and run off and mechanical models capable of modelling partially saturated flow and shear strength increase. There has also been an identified research gap in that current models do not sufficiently combine a hydrological and mechanical model. This gap can be addressed by modelling a slope within a hydrological model and applying the calculated surface pore pressures to a partially saturated mechanical model. Chapter 3 will address the processes required of the numerical models in more detail and identify the models best suited to the job.

Chapter 3. Modelling strategy

3.1 Introduction

Within Chapter 2, it became apparent that, to correctly assess the effects of climate on the stability of slopes, numerous mechanisms need to be taken into account. The stability and seasonal deformation of the slope is highly dependent on the variation of pore pressures within that slope. As discussed previously the amount of infiltration and extraction of water is dependant upon climate, vegetation and soil type. Current numerical models can be roughly split into two camps based on their ability to model hydrological processes or deformation characteristics. The former camp of models are those which can simulate pore pressure variation due to the effects of climate, vegetation and soil hydraulic properties but cannot model the deformations caused by the variation. The latter camp consists of models which can simulate deformations associated with pore pressure variation but cannot simulate the infiltration and extraction of due to climate and vegetation. The advantages the hydrological flow models have over the mechanical flow models are their ability to accurately model the boundary between the soil body and the atmosphere. As discussed within Chapter 2 there is some overlap between the two frameworks yet there is no commercially available code that can simulate the entire range of mechanisms deemed necessary to assess the effects of climate on stability.

3.2 Aims

Within this chapter a method is proposed which utilises both a hydrological model and a mechanical model. The aim is to apply a hydrological model boundary condition, usually confined to the hydrological models, to a mechanical model. With use of EARWIG, a weather generator, the effects of a changing climate on slope stability can be modelled. The expected outcome is a model that can simulate pore pressure variations within a slope due to effects of climate, vegetation and soil suction and then simulate the associated stress changes, deformations and possible stability issues caused by such variations. To satisfy this aim the following objectives must be achieved:

1. Identify a hydrological model capable of simulating pore pressure variations due to climate effects within a slope. This model must be able to use climate, soil

and vegetation data to simulate infiltration, evapotranspiration, root extraction, run off and unsaturated flow.

2. Identify a mechanical model capable of simulating unsaturated behaviour.
3. Develop and validate a method of transferring the surface pore pressures from the hydrological model to the mechanical model.
4. Identify established numerical methods to simulate the mechanical response of slopes to climate, particularly progressive failure. Develop and test a procedure to simulate these methods within the identified mechanical model.
5. Validate hydrological model with a real instrumented slope identifying parameters which are key to obtaining good a comparison with recorded pore pressures.
6. Perform mechanical simulation for the real slope using geotechnical parameters identified from the literature.
7. Identify effect of future climate scenarios on modelled slopes.
8. Highlight areas where the model performs satisfactorily and areas where improvement is needed and make recommendations for further model development

3.3 Hydrological model selection

As embankments are to be modelled, it can be reasonably assumed that the majority of flow and deformation will occur within a cross section parallel to the downslope direction. Out of plane flow and deformation will therefore be ignored. The hydrological model can, therefore, be a two dimensional model or a three dimensional model which assumes infinite length in the out of plane axis. As suggested by Smith (2003) in order to be able to simulate the response of the slope to individual rainfall events the model, as a minimum, must be able to use hourly rainfall data. As discussed earlier any larger increment of rainfall data will assume less run off and greater infiltration. The model will also need to be able to calculate the amount of rain entering the slope as well as the amount of water flowing over the slope. It would also be advantageous for the model to be able to calculate where such run off may re-enter the slope later in a calculation. This will allow for ponding to occur at critical areas of the slope such as at the toe. The hydrological model must be able to simulate both saturated and unsaturated flow within a slope. The ability to simulate hysteresis within the SWCC would also be advantageous but not critical. The unsaturated component of the flow model will need to be able to estimate the relative permeability for an unsaturated

soil. The saturation near the surface will determine the relative permeability and therefore the rate at which available surface water will be able to enter the slope. The model must also allow the rate of evaporation from the surface to be calculated. To accurately assess this parameter the model will need to be able to use either hourly temperature, humidity, net radiation and wind speed data or potential transpiration data together with soil water retention curve data. The hydrological model will also be required to be able to calculate the effects of vegetation on the pore pressures within a slope. The effects of vegetation which will need to modelled are the interception and the transpiration. These parameters will be able to determine how much water can be stored on the canopy and whether water drains from or evaporates from the canopy. The rates of drainage and evaporation will also need to be determined. The transpiration model will determine the rate at which water can be drawn from the soil by the vegetation roots. To do this, the model will need the root distribution, root resistance to flow and the soil suction at the root zone as well as climatic data. One of the hydrological models reviewed within Chapter 2, SHETRAN, is capable of fulfilling most of the specified criteria; this model was, therefore, employed for the hydrological aspect of the modelling. A synopsis of the SHETRAN model follows.

3.4 SHETRAN

SHETRAN is a 3D hydrological finite difference model. It is capable of modelling both surface and subsurface flow together with sediment and solute transport. Development of the model began with the Systeme Hydrologique Europeen (SHE) (Abott et al 1986a, b). The model was then developed under the safety assessment research programme for the United Kingdom Nirex Limited who were interested in potential deep underground repositories for radioactive wastes. SHETRAN has many functions with which to accurately model flow of water, snow, ice, solutes and also the melting of snow and ice. Details of SHETRAN can be seen in Ewen et al (2000). For the purposes of this study, only the flow of water is considered. The functions within SHETRAN relating to snow, ice and solutes are therefore ignored in this overview. The following section will outline the relevant methods by which SHETRAN fulfils the requirements for the hydrological model outlined in section 3.3.

3.4.1 Mesh

SHETRAN is a catchment model. A catchment area can be represented by a set of rectangular elements. Each element represents a section of land surface. The sub unit includes all the surface water, vegetation present and porous media beneath that land surface. In this work, only the slope surface is to be considered. The slope is discretised into a grid of rectangular elements and each element consists of a variably spaced column of cells. The finite difference computation node is at the centre of each cell. Each surface element is also allocated an elevation. Therefore, to develop a mesh for the simple slope shown in Figure 3.1 the surface topography must first be defined. For this example, the length of the elements will be 1m. As the slope is 2D the width of the elements will not affect the 2D solution. Within the slope crest there will be three surface elements and along the slope length there will be 11 elements.

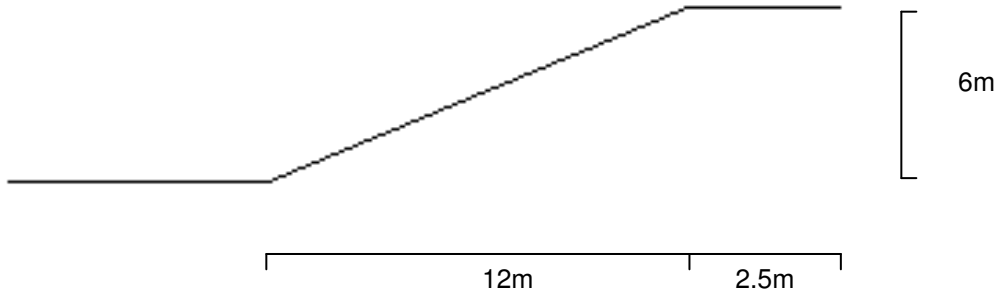

Figure 3.1 Simple slope profile.

If it is assumed that the height of each cell is 0.5m and the foundation depth is 6m then the cross section of the slope as represented within SHETRAN would be as within Figure 3.2

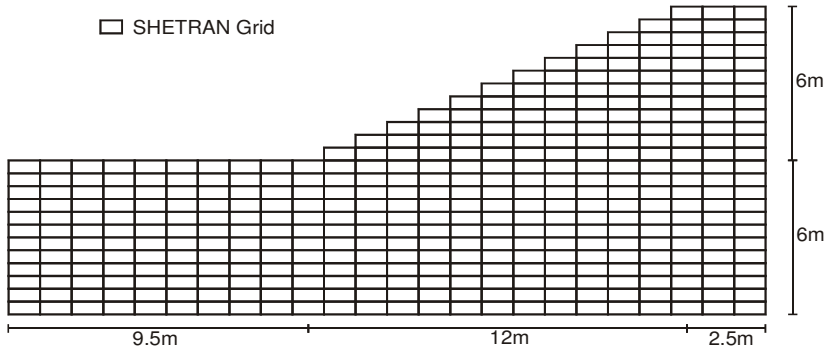

Figure 3.2 Representative SHETRAN grid.

Figure 3.2 represents the subsurface porous media. Each cell is allocated a soil type and the properties of that soil type are then applied to that cell. A number of cells must also be defined above each column, usually two. These cells will contain the canopy and surface water. Each surface cell must be allocated a canopy type. The height of these surface cells must also be sufficient enough to contain the maximum height of vegetation for that canopy and the maximum depth of surface water possible.

3.4.2 Subsurface flow

SHETRAN is a single phase fluid flow model. Atmospheric pressure is assumed to remain constant and the soil body is assumed to remain at constant volume. These assumptions are deemed reasonable to calculate the pore pressure changes within a slope due to climatic changes. SHETRAN uses the extended Richards equation to describe variably saturated flow. This is given in its pressure form for three dimensions in terms of saturated conductivity, K, relative conductivity, k_r, pressure potential, ψ and volumetric flow rate, q, in equation 3.1 (Parkin, 1996).

$$\eta \frac{\partial \psi}{\partial t} = \frac{\partial}{\partial x}\left[K_x k_r \frac{\partial \psi}{\partial x} \right] + \frac{\partial}{\partial y}\left[K_y k_r \frac{\partial \psi}{\partial y} \right] + \frac{\partial}{\partial z}\left[K_z k_r \frac{\partial \psi}{\partial z} \right] + \frac{\partial \left(k_r K_z \right)}{\partial_z} - q \qquad \textbf{3.1}$$

Where η is the storage coefficient defined using specific storage, S_s, porosity, n, volumetric soil water content, θ and the pressure potential as:

$$\eta = \frac{\theta S_s}{n} + \frac{d\theta}{d\psi} \qquad \textbf{3.2}$$

The solution of the Richard's equation proves difficult due to the non-linearity of the hydraulic conductivity and storage terms. The model, therefore, strikes a balance between accuracy, mass conservation and computational requirements. SHETRAN has been developed to provide reasonably accurate robust, mass conservative solutions for conditions ranging from scales of small plots of a few square metres to large catchments up to 100 square kilometres Parkin (1996). Taking into account these applications where there will be an uncertain heterogeneity in the soil mass a highly accurate solution to the Richard's equation will not be of great benefit.

The soil hydraulic properties can be described by four soil hydraulic functions. These are (Parkin (1996):

1. van Genuchten
2. tabulated functions
3. exponential
4. averjonov/tabulated (Averjanov, 1950)

The van Genuchten representation of the soil characteristic function, discussed within chapter 2, will be the form used for all the analysis within this thesis. This representation is the most widely used within hydrological models. This equation is converted to a look up table within SHETRAN by calculating the volumetric water content for pre-defined values of matric potential. The hydraulic conductivity function is also of the van Genuchten form. This is also converted to a look up table calculating relative hydraulic conductivity for pre-defined values of matric potential.

The storage of each cell within the porous media is calculated by two terms. The first term relates to the pressure within the saturated zone and the second is related to the gradient of the soil water characteristic within the unsaturated zone (zero for a saturated cell). The storage coefficient for each cell is calculated using a representative depth, Δz, for each cell as follows (Parkin, 1996).

$$\overline{\eta}_i = \frac{1}{\Delta z'} \int_{z_i - 0.5\Delta z'}^{z_i + 0.5\Delta z'} \eta(\psi_i + z) dz \qquad \textbf{3.3}$$

The flow into a single cell, i, of volume $V_i = \Delta x_i \, \Delta y_i \, \Delta z_i$ within a column can be expressed in terms of the lateral flow rate into face j and vertical flow rates into the top and bottom of the cell (Q_{i+} and Q_{i-} respectively) as (Parkin, 1996):

$$V_i \eta_i \frac{\partial \psi_i}{\partial t} = \sum_{j=1}^{4} Q_{ij} + A_0 (Q_{i+} + Q_{i-}) + V_i q_i \qquad \textbf{3.4}$$

The vertical flow rates are determined using Darcy's equation (Parkin, 1996):

$$Q_{i+} = \beta_{z+,i} [(z + \psi)_{i+1} - (z + \psi)]_i \qquad \textbf{3.5}$$

$$Q_{i-} = \beta_{z-,i}\left[(z+\psi)_{i-1} - (z+\psi)_i\right] \quad \textbf{3.6}$$

Where $\beta_{z+,i}$ and $\beta_{z-,i}$ are coefficients which allow for the spatial averaging of the hydraulic conductivity with the cell above and below respectively.

Lateral flows into cell, ***i***, are calculated using the Darcy equation (Parkin 1996):

$$Q_{i,j} = \gamma^1_{i,j}\left[(z+\psi)_{k,j} - (z+\psi)_i\right] + \gamma^2_{i,j}\left[(z+\psi)_{(k+\delta kj),j} - (z+\psi)_i\right] \quad \textbf{3.7}$$

Where $\gamma^1_{i,j}$ and $\gamma^2_{i,j}$ are coefficients which allow for the spatial averaging of hydraulic conductivities between neighbouring cells.

The equations for vertical and lateral flow are substituted into equation 3.4 which gives a non linear equation in terms of ψ. A time weighting factor is introduced and the finite difference equation for a single cell is produced. The solution algorithm is a Newton-Raphson iteration and contains an inner iteration for each column and an outer iteration for all columns. Vertical flows are more likely to cause the most severe non-linearities in the Richard's equation. It is for this reason that non-linearities are first treated for vertical flow within each column before the non-linearities for lateral flows for all columns.

3.4.3 Time step

The time step for the simulation can be set by the user. SHETRAN is therefore capable of calculating an hourly response of flow of water over and within the slope providing the necessary hourly climatic data is available. Sub hourly time steps are also viable, however, sub hourly weather data is not freely available and would therefore need to be recorded on an as needed basis. Hourly precipitation data is freely available for a number of sites throughout the UK from the Met Office (British Atmospheric Data Centre, 2008). This data will allow SHETRAN to simulate the rate of infiltration and run off for hourly rainfall events together with rates of evapotranspiration. This is obviously more accurate than a daily simulation but not as accurate as sub hourly simulations.

3.4.4 Lower boundary condition

The lower boundary of the SHETRAN model should be of a sufficient depth to not allow significant flows to occur over the period of a given simulation. Flow can, however, be prescribed across the boundary by either defining a flow rate or a head. If a flow rate, q_b , is given then flow across the boundary occurs at this rate. If a head is given then q_b across the boundary is given by:

$$q_b = \frac{2K_{z,b}}{\Delta z_b}\left(h_b - \left(z_b + \Psi_b\right)\right) \qquad \textbf{3.8}$$

The default condition is that no flow occurs across the boundary.

3.4.5 Lateral boundary conditions

Lateral boundary conditions can also be prescribed. Flow rates can be prescribed for any lateral boundary element. One flow rate can be prescribed for one layer or varying flow rates to a number of layers. For a given flow rate, q_l, at the boundary the flow rate through the boundary face, *j,* of a cell, $Q_{i,j}$ is calculated by multiplying q_l by the cross sectional area normal to the direction of flow, $A_{i,j.}$ For a prescribed head boundary condition the flow rate is given by:

$$Q_{i,j} = \frac{K_{i,j}A_{i,j}}{\Delta L_j}\left(h_l - z_i + \psi_i\right) \qquad \textbf{3.9}$$

For a simple 2D slope model a no flow boundary condition is applied to the boundaries parallel to the down slope direction. This will allow water to flow vertically and horizontally along the slope but not laterally across the slope. The slopes modelled are mostly symmetrical and therefore only half the slope is modelled with a no flow boundary specified at the centre of the slope crest. For non-symmetrical slopes, e.g. cuttings, the boundary will also be a no flow boundary but it will be placed at a distance far enough away from the slope crest where the phreatic surface can be assumed to be horizontal. The down slope lateral boundary will be a no flow boundary. As there will be run off from the slope this water needs somewhere to go within the model. For this reason a column of free draining soil can be placed at the adjacent to the down slope lateral boundary and a head specified at the base of this column. This will have the

affect of draining away excess surface water from the model. This column will be placed at a distance far enough away so as to have a minimal affect on the depth of the phreatic surface within the slope. These assumptions will have obvious effects on the model results it is, therefore, up to the user to determine the magnitude of the affects and adjust the boundaries accordingly.

3.4.6 Surface boundary conditions

The ground surface boundary condition used for a certain time step depends upon several factors. These include the amount of available ponded surface water, surface evaporation rate the pressure potential of the surface cell and the maximum possible rate of flow of the surface cell (determined by the effective hydraulic conductivity).

The flux boundary condition when there is no ponded water on the surface is given by:

$$k_r K_z \left(\frac{\partial \psi}{\partial z} + 1 \right) = q_p - e_s \qquad \textbf{3.10}$$

Where $e_{s,}$ is the evaporation rate from the surface. When ponded ground water does exist at the surface the flux boundary condition is given by I as:

$$I = -K_z \left(\frac{\partial \psi}{\partial z} + 1 \right) \qquad \textbf{3.11}$$

At the beginning of the time step if there is surface water available then evaporation occurs at the potential rate. If no ponded water exists than the actual evaporation from the soil surface is calculated as a function of the pressure potential of the top cell.

During a time step the maximum possible rate of flow into the surface cell from external flows and water depths is calculated using the depth of ponded water, $d_{w,}$ the net precipitation, $q_{p,}$ and the net surface evaporation, e_w, as follows:

$$q_1 = \frac{d_w}{\Delta t} + q_p - e_w \qquad \textbf{3.12}$$

The maximum possible rate of flow out of the surface cell is also calculated during the same time step. The flow is calculated between the cell computational node at its centre and the top boundary of the cell as a function of the soil properties and hydraulic head at the computational node and the hydraulic head at the surface by:

$$q_2 = \frac{K_z}{0.5\Delta z_{top}}\left(\psi_{top} - \left(max\left(0, d_w + \left(q_p - e_w\right)\Delta t\right) + 0.5\Delta z_{top}\right)\right) \qquad \textbf{3.13}$$

For the condition of $q_1 < -q_2$ the rate of infiltration at the surface is then calculated by:

$$q_{inf} = -q_1$$
$$\frac{\partial q_{inf}}{\partial \psi_{top}} = 0 \qquad \textbf{3.14}$$

And for the condition of $q_1 \geq -q_2$ the rate of infiltration (negative infiltration or exfiltration for this condition) at the surface is calculated by:

$$q_{inf} = q_2$$
$$\frac{\partial q_{inf}}{\partial \psi_{top}} = \frac{K_z}{0.5\Delta z_{top}} \qquad \textbf{3.15}$$

3.4.7 Interception

If vegetation is present the amount of water that is available at the surface is dependant upon the interception processes. Within SHETRAN the interception component calculates the amount of water reaching the ground through the canopy, the amount of water stored on the canopy and the amount of evaporation from the canopy (Abbott et al 1986a). The interception model within SHETRAN is based upon the Rutter model (Rutter et al 1971/1972) Figure 2.22. As per the Rutter model the canopy is assumed to have a storage capacity, *S*. *S* can be thought of as the amount of water the vegetation can hold when all surfaces are wetted. This storage capacity is filled by precipitation and is emptied by evaporation and drainage. When the depth of water stored on the canopy, *C*, is equal or greater than the storage capacity then evaporation, *E*, occurs from the canopy at the maximum potential evaporation rate, E_p, as defined by the Penman

equation (Equation 2.21). When C is less than S then evaporation occurs from the canopy at a reduced rate defined as:

$$E = E_p \, C/S \qquad \textbf{3.16}$$

Drainage from the canopy is calculated using the rainfall rate, P, the proportion of ground covered by vegetation, p_1, and the ratio of total leaf area to ground covered by vegetation, p_2, the potential evaporation rate, E_p, and drainage parameters b and k using (Abott et al 1986):

$$\frac{\partial C}{\partial t} = Q - ke^{b(C-S)} \qquad \textbf{3.17}$$

Where:

$$Q = p_1 p_2 \left(P - E_p \, C/S\right) \qquad \text{when C < S} \qquad \textbf{3.18}$$

$$Q = p_1 p_2 \left(P - E_p\right) \qquad \text{when C} \geq \text{S} \qquad \textbf{3.19}$$

For the above equations:

$p_1p_2 = p_1p_2$ when $p_2 < 1$

$p_1p_2 = p_1$ when $p_2 \geq 1$

Abbot et al (1986a) state that the model works best for a fully wetted canopy but the introduction of the *C/S* parameter the individual terms can be modified continuously for a dry through to wet canopy. The parameters, S, p_1 and p_2 can also be varied over time within SHETRAN allowing the canopy to change throughout the year and thus allowing for seasonal growing periods. No allowance for stem flow is provided within the SHETRAN interception model. This omission is deemed to have negligible effect on the canopy storage and the drainage and evaporation from the canopy. The effect of individual trees will also not be covered within this thesis therefore the omission for this purpose is further minimised.

3.4.8 Evapotranspiration

The total actual evapotranspiration, E_t, is calculated for each surface element within SHETRAN taking into account the wetness of the canopy, the amount of ground covered by the canopy and the pressure potential of each cell containing plant roots. The equation for the total evapotranspiration uses the ratio of covered ground for an element to calculate the amount of evapotranspiration for each component of the element. The first term calculates evapotranspiration from the canopy the second term evapotranspiration from the soil through the vegetation and the third term calculates evaporation from the bare ground:

$$E_t = p_1 p_2 E_p \, C/S + p_1 p_2 E_{at} (1 - C/S) + (1 - p_1 p_2) E_{as} \qquad \textbf{3.20}$$

$\boldsymbol{E_{at}}$, is the actual evapotranspiration from the vegetation calculated using the Penman Montieth model (Equation 2.34) and E_{as}, is the evaporation for bare soil (Equation 2.21).

3.4.9 Root distribution

The distribution of roots with depth can be specified within SHETRAN by assigning a percentage of the root mass to each depth increment (Figure 3.3). The PET is then scaled for each cell containing roots, i.e. 40% of PET for the top cell, 45% of PET for the second cell and so on.

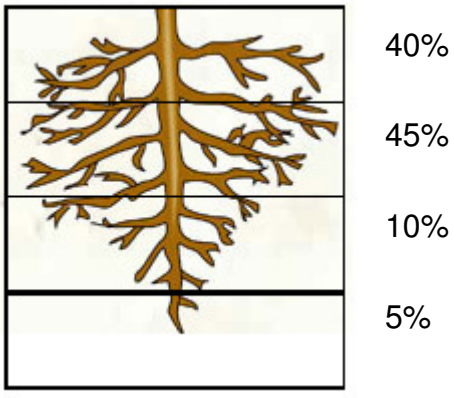

Figure 3.3 Root distribution estimation.

The actual evapotranspiration is, therefore, also calculated for each cell taking into account the soil moisture tension within the Penman Montieth equation parameter $\boldsymbol{r_s}$. This is done by the user specifying the actual transpiration as a fraction of potential.

Within SHETRAN the user must create a look up table by specifying a number of pairs where the fraction of transpiration is given to a corresponding soil moisture tension. There will then be a linear interpolation between each of these pairs. The water extracted due to plant transpiration is subtracted from the sink term $V_i q_i$, in Equation 3.4 for all cells containing roots. This process allows the user to specify the depths at which roots can extract water. Therefore, if the vegetation has mainly shallow roots then water extraction occurs at shallow depths and conversely for deeper roots. The program, however, will not allow for the roots to penetrate to deeper depths to find water as would occur in the field. There is also no facility to allow the vegetation to extract more water from depths where it is available. For example, if the surface is dry and saturated at depth and if 70% of the roots are at the surface and only 30% at depth then the actual evapotranspiration will only be 30% of PET at depth. Vegetation has been shown, however, to compensate by extracting more water where it is available, potentially extracting near 100% of PET from depth. The SHETRAN model has therefore the potential to underestimate the actual evapotranspiration significantly. This feature has been included as an option in some hydrological models and has been shown to significantly affect results. The effects can be minimised by the user varying the root distribution manually but this process will be unreliable. Within the SHETRAN model, root density distribution has minimal affects on PET.

3.4.10 Run off

Ponded water within SHETRAN is able to flow over the ground surface. The rate of flow of surface water is calculated using approximations of the St. Venant equations. The model allows for 2D flow but only 1D flow is considered for the purpose of this thesis. The flow model is written in terms of net precipitation minus infiltration, q, local water depth, h and flow velocity, u, ground slope, S_{ox} and friction slope, S_{fx}:

$$\frac{\partial h}{\partial t} + \frac{\partial (uh)}{\partial x} = q \qquad \textbf{3.21}$$

$$\frac{\partial h}{\partial x} = S_{ox} - S_{fx} \qquad \textbf{3.22}$$

The Strickler/Manning resistance law is applied to the friction slope giving a relationship between water depth and flow velocity:

$$uh = kI^{1/2}h^{5/3} \qquad \textbf{3.23}$$

where k is the Strickler roughness coefficient and I is the surface water gradient (Abott et al 1986a). The roughness parameters need to be determined in order to realistically model the flow of surface water. Obtaining these parameters for a simulation is unlikely and, therefore, they will need to be estimated. The effect of underestimating the roughness parameters could mean all surface water is lost and infiltration is reduced and conversely if they are over estimated then infiltration is increased and excessive ponding occurs. The inclusion of this ability allows the user to model the redistribution of surface water which is essential for slope stability issues. Where ponding may occur at the toe, however, the parameters used must be realistic and numerous simulations will need to be conducted in order to determine the effects on the models outcome.

3.4.11 Summary of SHETRAN input parameters

Table 3.1 summarises the SHETRAN parameters necessary to perform the flow only calculation required for slope analysis.

Table 3.1 SHETRAN parameters.

	parameter	symbol	units
Soil properties	Saturated hydraulic conductivity	K	m/s
	Residual volumetric moisture content	θ_r	-
	Saturated volumetric moisture content (porosity)	θ_s (n)	-
	van Genuchten n	n	-
	van Genuchten α	α	1/m
Vegetation properties	Canopy storage capacity	C_s	m
	Fractional rate of change of drainage water storage	Cb	1/mm
	Leaf drainage rate when storage = C_s	Ck	mm/s
	Actual transpiration as a fraction of potential (Given as a number of pairs of fraction: soil moisture tension)	FET	-
	Canopy resistance factor	RCF	s/m
	Root density function Given as a number of pairs (layer depth : amount of soil moisture absorbed as fraction of total transpiration)	RDF	-
	Leaf area fraction Given as a number of pairs (layer thickness : ratio of leaf area to area of element)	LAF	-
Meteorological data (hourly)	Precipitation	$prec$	mm/h
	Pressure	pa	mbar
	Net radiation	rn	W/m^2
	temperature	ta	^oC
	Wind speed	u	m/s
	Vapour pressure deficit	vpd	mbar

3.4.12 SHETRAN applicability

SHETRAN can be seen to be capable of modelling a range of situations. The equations the model uses to calculate unsaturated flow have been used within many hydrological models with some success. There are, however, also many shortcomings of the equations used. One disadvantage may be the use of the van Genuchten equations. These equations are limited to assuming a unique relationship between moisture content

and soil pressure and also moisture content and relative permeability. It has been shown that the relationships are hysteretic (Section 2.4.5). The assumption may seem unreasonable but not when taken in the context of the scale of the problem to be modelled. The soil slopes to be modelled are several metres high and cover tens or sometimes hundreds of square metres. The material within these slopes can also be highly variable. Investigations into these slopes gives an indication of the material present but the exact spatial variability will remain unknown. The hydraulic properties of the materials will also vary spatially as well as with depth. Using highly advanced soil models will inevitably need more advanced testing to obtain the necessary parameters. The testing of slope material hydraulic properties (SWCC, saturated permeability, porosity etc.) within the discipline of geotechnical engineering is already limited and perhaps insufficient enough for the majority of the most basic models. The use of more complex models for the majority of slopes will therefore not yield more accurate flow modelling. For greater accuracy there will need to be more advanced material testing and also a greater number of tests for a given site. The equations used within SHETRAN are therefore deemed appropriate for the available information and will give a good estimate of the flow within the slope. The same can also be said for the vegetation properties. With a better understanding of particular vegetation types and also rooting depths we will be able to develop more precise methods of modelling the transport of water from the soil through the canopy and into the atmosphere. As a basic requirement we need to identify the types of vegetation present, the percentage quantity of each species, percentage of canopy cover and their rooting depths. This type of testing can be done relatively quickly and cheaply. With this information the methods employed by SHETRAN are capable of making reasonably accurate calculations of root uptake which will have a significant effect on slope stability. The climatic data used is also an important factor. Weather can vary over small distances. Ideally a weather station on the slope will give the best results but where this is not available the closest weather station will need to be used. There will need to be a process to scale the given weather data for slope features such as aspect height, wind shielding etc.

There are, therefore, many factors to consider when attempting to model the hydrological regime of a slope. It will be impossible to measure all factors accurately. The important factors need to be identified. Once identified these factors can be used to produce reasonably accurate models. The techniques used by SHETRAN have been proven both within the SHETRAN model and many other hydrological models within

the literature. It is for this reason SHETRAN has been chosen as the hydrological model for this study.

3.5 Mechanical model selection

The model used for the mechanical calculation needs to be able to model both the deformation of soils due to changes in effective stress and the flow of water through the porous media. There are numerous commercial codes which allow the numerical modelling of earthwork structures, Geo studio, PLAXIS, Flac, and CRISP among others. Most of the codes use a continuum to model the soil mass and either a finite element or finite difference numerical procedure. The soil continuum is represented by a soil constitutive model which describes the stress strain response of the continuum. For a given model using an identical constitutive model both numerical procedures should return comparable results. Either numerical procedure, therefore, offers no advantage in terms of accuracy. Most mechanical models are able to perform flow calculations. Some models allow mechanical and flow only calculations to be run as well as fully coupled. The standard codes almost all assume saturated soil behaviour with the geo studio package being a notable exception. There are, however, add on packages that allow for the modelling of unsaturated flow within the model, PLAXIS flow and Flac tp (two phase) flow being two examples. There are no unsaturated constitutive models within these packages though. Increased shear strength due to suction is modelled as an increase in effective stress only or using a modification of the effective stress equation. The modelling package chosen to satisfy objective 2 (Section 3.2) was Flac-tp. This package allows the modelling of unsaturated flow and also uses Bishop's effective stress to model an increase in shear strength due to suction. The code also contains an in-built programming language called FISH. This allows the user to write functions within the code. These fish commands can be initiated before each computational step allowing the user to update variables during a calculation procedure. The FISH language can therefore be used to transfer the surface pore pressures to the model boundary.

3.6 Flac

The Flac software was developed by Dr Peter Cundall in 1986 for the Itasca Consulting group. The code is available in 2D and 3D although the two phase flow option is only available within the 2D package. The version used for the analysis within this thesis is

therefore a 2D explicit finite difference code. This allows the numerical modelling of earthworks built of soil and rock. The soil continuum is discretised into a number of elements. The stress strain behaviour of these elements is defined by in built constitutive models (although user defined models can also be created). The two-phase flow option within the Flac program is able to model two immiscible fluids within a porous medium. Throughout the remainder of this Thesis, the Flac two phase flow option is referred to as Flac-tp. Assuming the fluids within Flac-tp are air and water allows the modelling of an unsaturated soil. Flac-tp is capable of solving a fluid only calculation, a mechanical only calculation and a fully coupled fluid-mechanical calculation. To do this the model requires soil properties, water properties and boundary and initial conditions to be specified. The FISH code within Flac-tp enables the user to specify property variations within the grid and also unusual boundary conditions which may vary over time.

3.6.1 The explicit finite difference method

Flac uses an explicit time marching scheme in order to find the solution to a given problem. A diagram of this scheme is shown as follows:

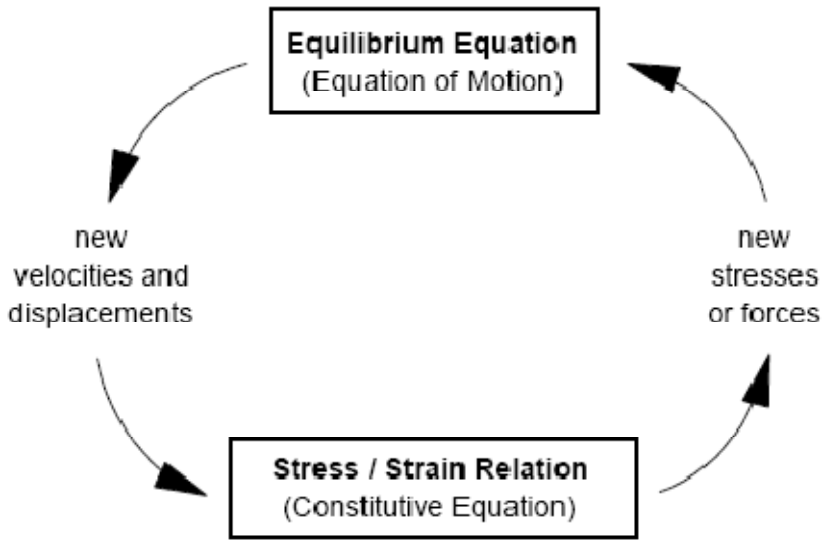

Figure 3.4 Flac basic explicit calculation cycle diagram (Itasca 2002).

Figure 3.4 shows the cycle of one calculation step. Within the top box of the cycle, the equations of motion are invoked to calculate velocities and displacements from the stresses and forces of the problem. The lower box then calculates new stresses from the velocities using the specified constitutive relationship. For each calculation cycle the variables remain fixed and are known. For example the velocities are frozen whilst the

stresses are calculated and the stresses are frozen whilst the velocities are calculated. Within the boxes of Figure 3.4 all grid variables are updated. The calculation cycle is only valid if the time step for each calculation cycle is smaller than the time taken to physically pass information from one element to another. The size of this time step is governed by the stiffness (bulk modulus) of the modelled materials and the grid spacing. The advantages of such a calculation scheme are that the calculation can follow arbitrary nonlinearity in stress strain laws. The disadvantage of such a system is the size of the time step is dictated by the smallest element within the grid and maximum stiffness of any material modelled within that grid. The time step can, therefore, be small for stiff dense grids resulting in impractically long run times.

3.6.2 Field equations

As stated previously Flac invokes the equations of motion and the constitutive equations to describe the deformation of a problem. The equation of motion relates the acceleration of a mass, m, to the applied force, F (the notation, $\dot{}$, signifies the derivative):

$$F = m\frac{d\dot{u}}{dt} \qquad \textbf{3.24}$$

Where the summation of all forces equal zero, acceleration equals zero and a static equilibrium condition applies. The equation of motion for a continuous body is:

$$\rho\frac{\partial\dot{u}_i}{\partial t} = \frac{\partial\sigma_{ij}}{\partial x_j} + \rho g_i \qquad \textbf{3.25}$$

Where ρ is the mass density, t is time, $\dot{u}_i$ are components of the velocity vector, σ_{ij} represents the components of the stress tensor, x_j are the components of coordinate vector, g_i are the components of gravitational acceleration and indices i and j are components in a Cartesian coordinates system. The strain rate is derived from the velocity gradient within the following equation:

$$\dot{e}_{ij} = \frac{1}{2}\left[\frac{\partial \dot{u}_i}{\partial x_j} + \frac{\partial \dot{u}}{\partial x_i}\right] \qquad \textbf{3.26}$$

Where $\dot{e}_{ij}$ are the strain rate components. The mechanical constitutive law takes the form:

$$\sigma_{ij} \Rightarrow M\left(\sigma_{ij}, \dot{e}_{ij}, k\right) \qquad \textbf{3.27}$$

Where ***M*( )** is the functional form of the constitutive law, ***k*** is a history parameter and the symbol $\Rightarrow$ means "replaced by." This equation calculates a new stress tensor from the old stress tensor and the strain rate. For an isotropic linear elastic constitutive model the new stress tensor can be calculated by:

$$\sigma_{ij} \Rightarrow \sigma_{ij} + \left\{\delta_{ij}\left(K - \tfrac{2}{3}G\right)\dot{e}_{kk} + 2G\dot{e}_{ij}\right\}\Delta t \qquad \textbf{3.28}$$

Where δ_{ij} is the Kronecker delta, Δt is the time step, ***G*** is the shear modulus and ***K*** is the bulk modulus. Flac has the option to conduct large strain analysis where the grid can deform and move with the material it is representing. To allow for this, the stress induced by rotation must be added. The stress components are changed by the following equation (note that this adjustment only occurs in the large strain mode):

$$\sigma_{ij} \Rightarrow \sigma_{ij} + \left(\omega_{ik}\sigma_{kj} - \sigma_{ik}\omega_{kj}\right)\Delta t \qquad \textbf{3.29}$$

Where ω_{ij} is given by:

$$\omega_{ij} = \frac{1}{2}\left\{\frac{\partial \dot{u}_i}{\partial x_j} - \frac{\partial \dot{u}_j}{\partial x_i}\right\} \qquad \textbf{3.30}$$

3.6.3 Grid

The solid body of the problem is divided into a finite different mesh. The mesh is composed of quadrilateral elements. Flac then divides each element into two overlaid sets of triangles (see Figure 3.5).

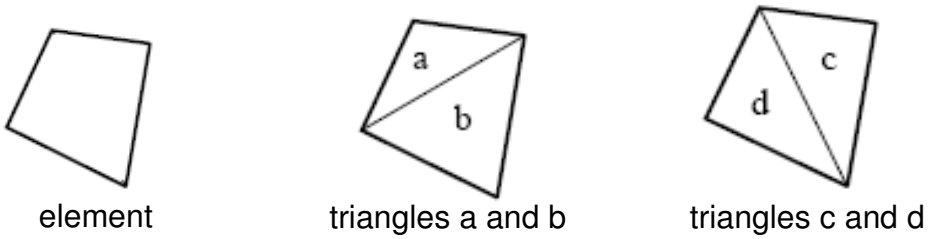

Figure 3.5 Flac grid elements (ITASCA 2002).

Nodes are located at the corners of each triangle and the force vector at each node is taken to be the mean of the two force vectors exerted by each overlain quadrilateral. If one triangle is distorted so that its area is much smaller than its companion then that quadrilateral will not be used. If a triangle in the remaining element becomes badly distorted then the code reports an error. The overlain triangle technique used in Flac has been developed to eliminate hourglass deformations. For polygons with more than three nodes there exist combinations of nodal displacements which cause no nodal forces resulting in unopposed displacements in alternate directions. This results in the element developing an hourglass shape. By substituting a quadrilateral with triangles the displacements cannot occur and the hourglass effect is eliminated.

3.6.4 Time step

As stated earlier the time step within a Flac simulation needs to be smaller than the physical time it takes for information to pass from one node to another. For stability of an element of size Δx the maximum time step can approximated by:

$$\Delta t < \frac{\Delta x}{C} \qquad \textbf{3.31}$$

Where C is the maximum speed at which information can propagate through a material. This is typically the p-wave speed and is defined using the mass density of the material together with the bulk and shear modulus as:

$$C_p = \sqrt{\frac{K + 4G/3}{\rho}} \qquad \textbf{3.32}$$

It can be seen that the time step is therefore related to the stiffness of the modelled material.

3.6.5 Constitutive models

Flac contains several in-built constitutive models. The models within Flac can be divided into elastic models and plastic models. Within the elastic models the stress/strain relationship is linear and all strains are recoverable. The plastic models within Flac involve some degree of non-recoverable deformation. Within Flac these models are characterised by their yield function, hardening/softening functions and flow rule. To assess the stability of a slope the Mohr coulomb constitutive model will be used. This constitutive model is the conventional model used to represent shear failure in soils and rocks (Itasca 2002). Within Flac compressive stresses are negative, therefore the principle stresses are ordered:

$$\sigma_1 \le \sigma_2 \le \sigma_3 \qquad \textbf{3.33}$$

Corresponding strains, $\boldsymbol{\Delta e}$, are composed of elastic strains, $\boldsymbol{\Delta e^e}$ and plastic strains $\boldsymbol{\Delta e^p}$:

$$\Delta e_i = \Delta e_i^e + \Delta e_i^p \qquad _i = 1,3 \qquad \textbf{3.34}$$

The plastic component of the strain increments is zero when there is no plastic flow and the deformation is elastic. The stress strain relationship is linear and follows Hooke's law. The incremental form of Hooke's law in terms of principle stresses and strains is:

$$\Delta\sigma_1 = \alpha_1 \Delta e_1^e + \alpha_2 \left(\Delta e_2^e + \Delta e_3^e\right) \qquad \textbf{3.35}$$

$$\Delta\sigma_2 = \alpha_1 \Delta e_2^e + \alpha_2 \left(\Delta e_1^e + \Delta e_3^e\right) \qquad \textbf{3.36}$$

$$\Delta\sigma_3 = \alpha_1 \Delta e_3^e + \alpha_2 \left(\Delta e_1^e + \Delta e_2^e\right) \qquad \textbf{3.37}$$

Where α_1 is:

$$\alpha_1 = K + \frac{4G}{3} \qquad \textbf{3.38}$$

$$\alpha_2 = K - \frac{2G}{3} \qquad \textbf{3.39}$$

Figure 3.6 depicts the Mohr-Coulomb yield criterion in the plane σ_1 , σ_3 (remember that compressive stresses within Flac are assumed to be negative).

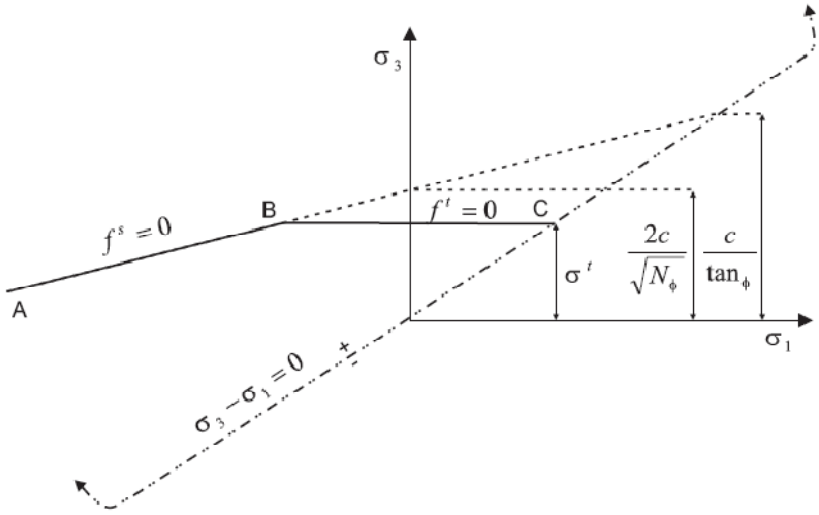

Figure 3.6 Mohr-Coulomb failure criterion.

In Figure 3.6 the failure envelope is defined by the Mohr-coulomb criteria:

$$f^s = 0$$

$$f^s = \sigma_1 - \sigma_3 N\varphi + 2c\sqrt{N\varphi} \qquad \textbf{3.40}$$

$$N\phi = \frac{1+\sin\varphi}{1-\sin\varphi} \qquad \textbf{3.41}$$

and a tensile failure criteria:

$$f^t = 0$$

$$f^t = \sigma^t - \sigma_3 \qquad \textbf{3.42}$$

Where φ is the friction angle and c is the cohesion of the material. It can be seen from figure 3.6 that $\boldsymbol{\sigma^t}$ cannot exceed $c/\tan\varphi$. The plastic component of strain is given by:

$$\Delta e_{ij}^{p} = \lambda\left(\frac{\partial g}{\partial \sigma_{ij}}\right) \qquad \textbf{3.43}$$

This equation represents the flow rule with $\boldsymbol{\lambda}$ being the plastic multiplier. The direction of the plastic strain increment vector is normal to the potential surfaces of the function (g). If $f(\sigma_{ij}) = g(e_{ij}^{p})$ then the material is associative. When $f(\sigma_{ij}) \neq g(e_{ij}^{p})$ the material is non-associative. The Morh-coulomb model used within Flac has a non-associated shear potential function, g^s of the form:

$$g^{s} = \sigma_1 - \sigma_3 N\psi \qquad \textbf{3.44}$$

Where $N\psi$ is the dilation angle calculated by:

$$N\psi = \frac{1+\sin\psi}{1-\sin\psi} \qquad \textbf{3.45}$$

The tensile failure flow rule is associated and has the form:

$$g^{t} = -\sigma_3 \qquad \textbf{3.46}$$

Flac also has an in built strain hardening/softening constitutive model. This model is based on the Morh-coulomb model with the option of increasing or decreasing the cohesion, friction angle, dilation angle and tension cut off after the onset of plastic yield. The rate of softening or hardening is defined by the user by defining linear tables (Figure 3.7).

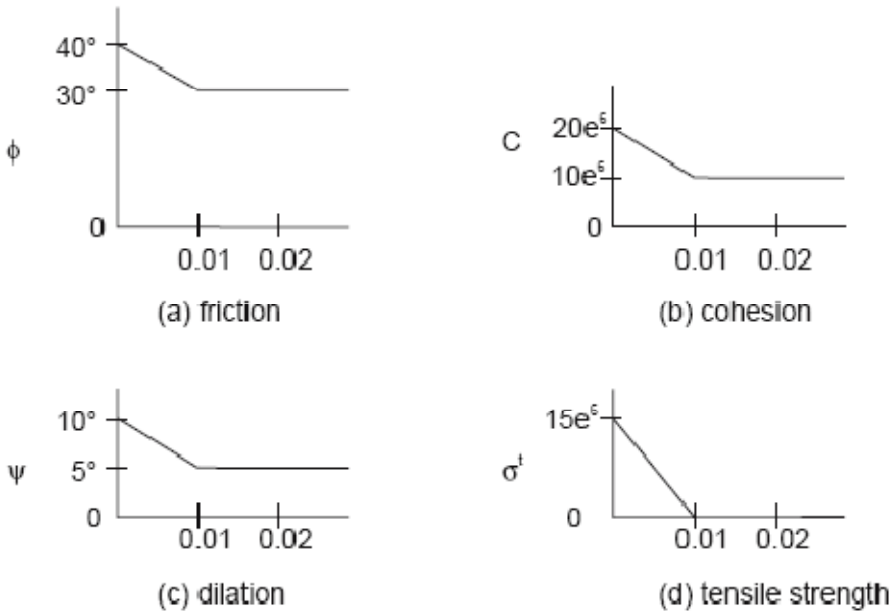

Figure 3.7 Examples of user defined look up tables for softening after onset of plastic yield (Itasca 2002).

The plastic shear strain is calculated using (the extra suffix, ***s*** relates to shear yield):

$$\Delta e^{ps} = \left\{ \frac{1}{2}\left(\Delta e_1^{ps} - \Delta e_m^{ps}\right)^2 + \frac{1}{2}\left(\Delta e_m^{ps}\right)^2 + \frac{1}{2}\left(\Delta e_m^{ps} - \Delta_m^{ps}\right)^2 \right\}^{\frac{1}{2}} \qquad \textbf{3.47}$$

Where:

$$\Delta e_m^{ps} = \frac{1}{3}\left(\Delta e_1^{ps} + \Delta e_3^{ps}\right) \qquad \textbf{3.48}$$

The plastic tensile strain is measured using (the extra suffix, ***t*** relates to tensile yield):

$$\Delta e^{pt} = \Delta e_3^{pt} \qquad \textbf{3.49}$$

After the onset of plastic yield new values of cohesion, friction, dilation, and tensile strength are applied using linear interpolation of the user defined tables, Figure3.6. The application of new values lags one time step behind the corresponding plastic deformation. The error will be small due to the time step being small.

3.6.6 Fluid flow

Flac is able to model single phase fluid flow. The flow of water can be modelled through the porous media as a calculation without or without the mechanical calculation. When the simulation involves both a mechanical and a fluid flow calculation the simulation is termed a coupled calculation. The single phase flow model simulates fully saturated flow and assumes zero pore pressure above the phreatic surface. Any of the Flac in-built constitutive models can be used with the fluid flow calculation. The pressures and saturations within the fluid flow component are assumed to be located at the nodes with pressures in the zones (the area of the element) being calculated by simple averaging of the pressures of the surrounding nodes. The "permeability" used in Flac is actually the mobility coefficient. The mobility coefficient, k, can be calculated using the permeability (also known as hydraulic conductivity), k_H and the density of water, ρ_w, with the following equation:

$$k = \frac{k_H}{g\rho_w} \qquad \textbf{3.50}$$

The fluid transport is calculated using Darcy's law:

$$q_i = -k_{ij}^a \frac{\partial}{\partial x_j}\left(P - \rho_w g_k x_k\right) \qquad \textbf{3.51}$$

Where q_i is the specific discharge vector, k_{ij}^a is the apparent mobility coefficient which is a function of the saturation, s and P is the fluid pressure. The fluid mass balance is calculated using the variation of fluid content, ζ and the volumetric fluid source intensity, q_v by:

$$\frac{\partial \xi}{\partial t} = -\frac{\partial q_i}{\partial x_i} + q_v \qquad \textbf{3.52}$$

The balance of momentum is calculated by:

$$\frac{\partial \sigma_{ij}}{\partial x_j} + \rho g_i = \rho \frac{d\dot{u}_i}{dt} \qquad \textbf{3.53}$$

Within this equation the term ρ represents the bulk density of the material. Dry density, ρ_d, can be calculated using the porosity of the porous media, n and the density of the solid phase of matrix, ρ_s:

$$\rho_d = (1-n)\rho_s \qquad \textbf{3.54}$$

The bulk density of the material can then be calculated using the ρ_d, the density of the wetting fluid, ρ_w, and the porosity, n:

$$\rho = \rho_d + n\rho_w \qquad \textbf{3.55}$$

The constitutive law for the pore fluid at full saturation, *s,* follows Biot's poroelasticity where pore fluid content is a function of pore pressure and mechanical strains. This is given by the equation:

$$\frac{\partial P}{\partial t} = M\left(\frac{\partial \xi}{\partial t} - \alpha\frac{\partial \varepsilon}{\partial t}\right) \qquad \textbf{3.56}$$

Where α is Biot's coefficient (equal to 1 assuming the solid grains within the matrix are incompressible), ζ is the variation of fluid content, ε is the volumetric strain and M is Biot's modulus which is calculated using the bulk modulus of water, K_w by the equation:

$$M = \frac{Kw}{n} \qquad \textbf{3.57}$$

When fully saturated the pore fluid can sustain a tension up to a limit, T_f, which is determined by the user. Where saturation is less than 1 the constitutive response is as follows:

$$\frac{\partial s}{\partial t} = \frac{1}{n}\left(\frac{\partial \xi}{\partial t} - \alpha\frac{\partial \varepsilon}{\partial t}\right) \qquad \textbf{3.58}$$

As stated earlier the pore pressure within the unsaturated zone is zero. Flow of water within the unsaturated zone is, therefore, under the force of gravity only. Permeability in the unsaturated zone is given by:

$$k_{ij}^{a} = k_{ij}\hat{k}(s) \qquad \textbf{3.59}$$

Where $\hat{k}(s)$ is given by the expression:

$$\hat{k}(s) = s^{2}(3-2s) \qquad \textbf{3.60}$$

The small strain constitutive response of the porous media, where H is the functional form of constitutive law is given by:

$$\frac{d}{dt}\left(\sigma_{ij} + \alpha P \delta_{ij}\right) = H\left(\sigma_{ij}, \dot{\varepsilon}_{ij}, k\right) \qquad \textbf{3.61}$$

For elastic relations the constitutive response takes the form:

$$\sigma_{ij} - \sigma_{ij}^{0} + \left(P - P^{0}\right)\delta_{ij} = 2G\varepsilon_{IJ} + \left(K - \frac{2}{3}G\right)\varepsilon_{kk}\delta_{ij} \qquad \textbf{3.62}$$

where the initial state is referred to by the superscript ^{0} and:

$$\varepsilon_{kk} = \varepsilon_{11} + \varepsilon_{22} + \varepsilon_{33} \qquad \textbf{3.63}$$

3.6.7 Fluid flow time step

The minimum stable time step for fluid flow can be estimated using the smallest zone size within the grid, L_z, by the equation:

$$\Delta t = min\left(\frac{L_z^2 n}{kK_w}\right) \qquad \textbf{3.64}$$

As can be seen the time step is inversely proportional to the bulk modulus of water, K_w, which is approximately 2.27×10^9 Pa. This large K_w will lead to small a time step which will lead to a large number of time steps required for a calculation and impractical run times. The time step can be increased by reducing K_w. Reducing K_w will not impact upon finding a steady state condition for a flow only calculation. For coupled calculations, however, K_w must remain large enough so that the water remains incompressible relative to the porous media. It can be shown that it is not computationally necessary for K_w to be larger than $20 \times n(K + 4G/3)$ (Itasca 2002).

The coupled groundwater flow model within Flac is very capable of modelling the response of saturated fluid flow and also the response of the soil to changes in pore pressures. With the use of FISH language the porosity and mobility coefficient of the porous media can also become a function of volumetric strain. However, as discussed within chapter 2 a slope is rarely fully saturated. The flow model within Flac has a very simplistic unsaturated flow model which does not take into account the SWCC of the solid material. Suction also cannot be modelled for the unsaturated zone of the slope and therefore any strength increase due to suction cannot be modelled. To model the increase in strength due to suction the model must be assumed to be full saturated and a high tension limit applied to the water. This has its draw backs also as the total stress of the slope will be overestimated.

3.6.8 Unsaturated flow

Within the Flac code there is the option of a two phase (tp) flow add on. Flac-tp will model the flow of two immiscible fluids through a porous media. No mixing is permitted between the liquids. The voids within the porous media are assumed to be completely filled by the two fluids (equation 3.65) with one fluid wetting the porous media more than the other.

$$S_w + S_g = 1 \qquad \textbf{3.65}$$

Where S_w is the saturation of the wetting fluid and S_g is the saturation of the non-wetting fluid.

Within partially saturated media the pressure in the non-wetting fluid (P_g , air in this case) will be larger than the pressure in the wetting fluid (P_w , water). As per the single phase fluid flow calculation two phase flow can be modelled with or without mechanical phase. Effective stress is calculated using Terzaghi's effective stress increment where the pore pressure increment is replaced by fluid pressure increments calculated as the saturation weighted mean average of the two fluids present. Volumetric deformations in the porous media can cause fluid pressure changes (and therefore flow) and fluid pressure changes can cause volumetric deformations. For constitutive models involving plasticity yield is detected using Bishop's effective stress (see Equation 2.36).

The difference between the pressures of the two fluids is the capillary pressure P_c:

$$P_C = P_g - P_w \qquad \textbf{3.66}$$

The suffixes ($_g$) and ($_w$) will be used throughout this thesis and represent the non-wetting fluid and wetting fluid respectively. The capillary pressure has a unique relationship to the effective saturation via the van Genuchten relationship illustrated by the following equation:

$$S_e = \left[\left(\frac{P_c}{P_0} \right)^{\frac{1}{1-a}} + 1 \right]^{-a} \qquad \textbf{3.67}$$

Where parameter a is a van Genutchen constant and S_e is the effective saturation which relates to both the actual saturation, S_w and the residual saturation, S_w^r;

$$S_e = \frac{S_w - S_w^r}{1 + S_w^r} \qquad \textbf{3.68}$$

P_0 is also a van Genuchten constant and is larger for finer materials. It is defined by:

$$P_0 = \frac{\sigma}{\sqrt{\frac{k}{n}}} = \frac{\rho_w g}{\alpha} \qquad \textbf{3.69}$$

where σ is the surface tension, a property of the porous matrix, k is the intrinsic permeability of the matrix and n is the porosity. The alpha coefficient is sometimes used in place of P_0 the relationship between P_0 and the alpha coefficient is also shown in Equation 3.69 where ρ_w is the density of the wetting fluid and g is the force due to gravity.

Fluid transport within Flac-tp is calculated using Darcy's law. For two phase flow it is postulated that the phase pressures described earlier are involved in causing each fluid to flow. The velocities for each fluid are described in equations 3.70 and 3.71 where k_{ij} is the saturated mobility coefficient, k_r is relative permeability and μ_w/μ_g is the viscosity ratio between the two fluids.

$$q_i^w = -k_{ij}^w k_r^w \frac{\partial}{\partial x_j}\left(P_w - \rho_w g_k x_k\right) \qquad \textbf{3.70}$$

$$q_i^g = -k_{ij}^g \frac{\mu_w}{\mu_g} k_r^g \frac{\partial}{\partial x_j}\left(P_g - \rho_g g_k x_k\right) \qquad \textbf{3.71}$$

The van Genuchten laws describe k_r as a function of saturation. The relationships are shown as follows:

$$k_r^w = S_e^b \left[1 - \left(1 - S_e^{1/a}\right)^a\right]^2 \qquad \textbf{3.72}$$

$$k_r^g = \left(1 - S_e\right)^c \left[1 - S_e^{1/a}\right]^{2a} \qquad \textbf{3.73}$$

where parameters a, b and c are constants. When modelling air and water within the porous media the above equations directly correlate with the equations for the relative permeability of water proposed by van Genuchten (1980) and air Parker et al (1987), Equation 2.24 and Equation 2.25. The a constant is therefore equivalent to the van Genuchten m constant and the constants b and c for water and air are both equal to 0.5.

Fluid balance laws are for each liquid are identical to the single phase fluid balance laws and are as follows:

$$\frac{\partial \xi_w}{\partial t} = -\frac{\partial q_i^w}{\partial x_i} + q_v^w \qquad \textbf{3.74}$$

$$\frac{\partial \xi_g}{\partial t} = -\frac{\partial q_i^g}{\partial x_i} + q_v^g \qquad \textbf{3.75}$$

The balance of momentum is also calculated as per the single phase calculation:

$$\frac{\partial \sigma_{ij}}{\partial x_j} + \rho g_i = \rho \frac{d\dot{u}_i}{dt} \qquad \textbf{3.76}$$

Within two phase flow the bulk density, ρ, is calculated as:

$$\rho = \rho_d + n\left(S_w \rho_w + S_g \rho_g\right) \qquad \textbf{3.77}$$

For the purpose of modelling unsaturated flow the density of the air phase is assumed to be zero and so Equation 3.77 reverts back to the expression used for single phase flow. Therefore the balance of momentum in two phase flow is calculated the same way as for single phase flow for unsaturated flow.

The constitutive laws for both fluids within Flac-tp are:

$$S_w \frac{\partial P_w}{\partial t} = \frac{K_w}{n}\left[\frac{\partial \xi_w}{\partial t} - n\frac{\partial S_w}{\partial t} - S_w \frac{\partial \varepsilon}{\partial t}\right] \qquad \textbf{3.78}$$

$$S_g \frac{\partial P_g}{\partial t} = \frac{K_g}{n}\left[\frac{\partial \xi_g}{\partial t} - n\frac{\partial S_g}{\partial t} - S_g \frac{\partial \varepsilon}{\partial t}\right] \qquad \textbf{3.79}$$

Combining Equations 3.74 and 3.75 with 3.78 and 3.79 gives the expressions:

$$n\left[\frac{S_w}{K_w}\frac{\partial P_w}{\partial t}+\frac{\partial S_w}{\partial t}\right]=-\left[\frac{\partial q_i^w}{\partial x_i}+S_w\frac{\partial \varepsilon}{\partial t}\right] \quad \textbf{3.80}$$

$$n\left[\frac{S_g}{K_g}\frac{\partial P_g}{\partial t}+\frac{\partial S_g}{\partial t}\right]=-\left[\frac{\partial q_i^g}{\partial x_i}+S_g\frac{\partial \varepsilon}{\partial t}\right] \quad \textbf{3.81}$$

The term $\frac{\partial \varepsilon}{\partial t}$ refers to the volumetric strain of the porous media. For a flow only calculation this term is omitted. Equations 3.80, 3.81, 3.66 and 3.65 can then be solved for the unknowns P_w, P_g, S_w and S_g.

Within the two phase flow model the constitutive response of the porous media to the change in effective stress has the form:

$$\Delta\sigma'_{ij}=H\left(\sigma_{ij},\Delta\varepsilon_{ij},k\right) \quad \textbf{3.82}$$

Where $\Delta\sigma'_{ij}$ takes the form:

$$\Delta\sigma'_{ij}=\Delta\sigma_{ij}+\left(S_w\Delta P_w+S_g\Delta P_g\right) \quad \textbf{3.83}$$

Bishop's effective stress, σ'_b is used to detect failure in constitutive models involving plasticity. This takes the form:

$$\sigma'_b=\sigma-\left(S_wP_w+S_gP_g\right) \quad \textbf{3.84}$$

Combining equation 3.84 with Equation3.65 gives:

$$\sigma'_b=\left(\sigma-P_g\right)+S_w\left(P_g-P_w\right) \quad \textbf{3.85}$$

This becomes equivalent to Equation 2.34 when S_w equals χ.

Within Flac-tp the smallest stable time step is based on the diffusivity of the fluids. An estimation of this time step is given in equation:

$$\Delta t = L_Z^2 n \times min\left(\frac{1}{k_w K_w}, \frac{1}{k_g K_g}\right) \quad \textbf{3.86}$$

Where L_z is the smallest zone size of the simulation and k_g is the saturated mobility coefficient of the non-wetting fluid calculated from the wetting fluid mobility coefficient and the viscosity ratio by:

$$k_g = k_g \frac{\mu_w}{\mu_g} \quad \textbf{3.87}$$

The size of time step is therefore inversely proportional to the bulk modulus of either the wetting or non-wetting fluid. If a realistic bulk modulus of water is used (2.27×10^9 Pa) then the time step again becomes very small and the computational time increases to such an extent that the simulation is impractical. The bulk modulus can again be decreased to such an extent that the water within the simulation is relatively incompressible to the soil, as within a single phase calculation. This will increase the time step. But it can be noted from Equations 3.80 and 3.81 that discharge rate of each fluid is related to its bulk modulus as well as changes in fluid pressure and saturation. Therefore, a more compressible fluid will experience a slower rate of discharge than a less compressible fluid. The user must therefore be careful with the choice of bulk modulus used for the fluids for a simulation and strike a balance between a usable time step magnitude and solution accuracy.

3.6.9 Summary of Flac-tp input parameters (Mohr-Coulomb model)

Table 3.2 summarises the parameters required for a fully coupled mechanical / fluid flow, two phase numerical simulation (Mohr-Coulomb constitutive model).

Table 3.2 Flac-tp input parameters.

	Parameter	Units
Mechanical model	Bulk density	kg/m^3
	Bulk modulus	Pa
	Shear modulus	Pa
	Cohesion	Pa
	Friction	^{o}
	Dilation	^{o}
	Tensile strength	Pa
Single phase flow	Bulk modulus	Pa
	Density (water)	kg/m^3
	Dry density (soil)	kg/m^3
	Mobility coefficient	$m^2/(Pa\text{-}s)$
	porosity	%
Two-phase flow (in addition to single phase)	van Genuchten a	-
	van Genuchten b	-
	van Genuchten c	-
	P_0	Pa
	Bulk modulus (non-wetting fluid)	Pa
	Viscosity ratio	-

3.6.10 Flac-tp suitability

The Flac numerical model has been used extensively by researchers in academia and industry. It has been proved to be a highly efficient, flexible and accurate tool for many purposes. The single phase version of the code has been used successfully within industry for similar studies on the effects of vegetation and climate on slope stability. The constitutive models used by Flac have also been used with success within many

other geotechnical codes such as PLAXIS, ICFEP and CRISP. The advantage Flac has is with its use of the in built programming language FISH. This language allows the user access to all of the processes of the code allowing the user to tailor the code to their individual needs. The two phase flow option offers a distinct advantage over the single phase model. With the ability to model unsaturated flow within the soil, pore pressures can be more accurately predicted for a greater range of materials. It is these pore pressures which determine the stability of the slope. Flac-tp uses the same van Genuchten equations as SHETRAN but models the flow of two liquids (air and water) through the soil. For the purpose of slope stability analysis the flow of the air can largely be ignored. The solutions of Flac-tp and SHETRAN should therefore be comparable. This will be explored in Chapter 4. The constitutive models implemented within Flac have been employed for many years to assess the stability of slopes. There are many more advanced constitutive models within the literature which may be more suitable to the application of assessing the effects of climate on slope stability. One such recent advance is the development of unsaturated constitutive models as discussed within Chapter 2. These models will allow for a more accurate prediction of volume change and strength due to a change in moisture conditions. Yet, as for the hydrological modelling, there will need to be more advanced testing and a greater number of tests carried out in order to account for the variability within the slope. This will not always be available. It has, therefore, been deemed reasonable to use a Mohr-Coulomb model to assess the influence of climate on slope stability. The code does, however, have the option of using a user developed code. A more advanced constitutive model could, therefore, be implemented at a future date.

3.7 Concluding remarks

This chapter has outlined the techniques used by finite difference codes. The equations used by both SHETRAN and Flac have been around in the literature for a long time and have been shown to be successful in modelling their respective problems. The equations employed by both codes may not be the most advanced in terms of modelling capability but are deemed to be sufficient when considering the scale of the area to be modelled. It is hoped that the combination of the two models will be used to carry out assessments of the impact of climate on, particularly, infrastructure slopes throughout the U.K. When considering the 1000's of km of infrastructure cuttings and embankments within the U.K. each consisting of variable material and differing levels of spatial variability material information is going to be scarce. The numerical models

used by SHETRAN and Flac-tp are therefore considered appropriate for such a general study. Flac has the capability to use FISH language to apply a hydrological boundary condition to the model thus eliminating the need for SHETRAN. SHETRAN, however, has undergone years of development to reach the version available to date and to code in such an advanced model into Flac-tp would be a considerable undertaking. It is for these reasons it was decided that for a preliminary study into the effects of climate on slope stability a combination of the two models would be more advantageous at this stage.

Chapter 4. Model Development

4.1 Introduction

Within the previous section the capabilities of the two numerical models SHETRAN and Flac-tp were outlined. As SHETRAN is capable of modelling the surface boundary condition and Flac-tp is capable of modelling coupled unsaturated mechanical models it was decided that SHETRAN would be used to calculate the surface pore water pressures for the slope and then transfer these surface pore water pressures to the top boundary of the Flac-tp model to then run a fully coupled simulation. This method has the advantages of accurately measuring the pore pressures along the slope length using an established hydrological model and using these surface pore water pressures to simulate the response of the embankment or cutting with an established geotechnical model. This is the next logical development of the work carried out by Kovacevic et al (2001) and Nyambayo (2004), where the surface boundary conditions were assumed from observations. This method has many advantages over the method used by these authors in that surface pore water pressures can be calculated along the length of the slope, thus allowing for varying degrees of suction from the slope crest to the slope toe. This will allow for a more realistic simulation of field conditions. The pore water pressures can be calculated for any time interval, this will allow the applied surface pore water pressures to follow a more realistic trend from high summer suctions to low winter suctions rather than a static applied summer suction instantaneously switched to a lower winter suction. Calculating the daily surface pore pressures from real weather data will also allow for extended wet winters and dry summers, and also the accelerated deformation that may be caused by peak summer suctions and also for peak wet winter periods.

As the Flac-tp has not been widely cited within the literature, this chapter begins with a validation of the Flac-tp model against the more established SHETRAN model for a simple one dimensional caisson test. The effects of the various parameters used within Flac-tp, for the two phase analysis which are not used within SHETARN, are also explored. The method of transferring surface pore water pressures from SHETRAN to

Flac-tp is then outlined and validated. A summary of the findings of this chapter can be found within Davies et al (2008a).

4.2 Caisson comparison

4.2.1 Introduction

This caisson example was similar to those published by Forsyth et al (1995) and Itasca (2002). For the exercise, a simple caisson was constructed within both the SHETRAN and Flac-tp codes. As the example was designed to validate the Flac-tp model against SHETRAN, the mechanical component of the Flac-tp model was turned off and a flow only calculation performed.

The caisson dimensions were 6m height and 0.3m width. It was assumed to be filled with a material with properties identical to those used for a Bandalier Tuff material published by Itasca (2002) which were derived from those published by Forsyth et al (1995). These are detailed within Table 4.1

Table 4.1. Flac-tp caisson test soil properties (Flac tp flow notation used or unsaturated soil properties).

Saturated mobility coefficient	2.92×10^{-10} m²/(Pa-s)
Porosity	0.33
Residual saturation	0
P_0	0.699×10^{4} Pa
a	0.336
b	0.5
c	0.5

The grids used for both the SHETRAN and Flac-tp example were identical. A single column of 20 zones was chosen with each zone being 0.3m wide and 0.3m high. These dimensions were also used for the simulations run by Itasca (2002). Hydrostatic initial conditions were assumed within the caisson with a surface suction of 60 kPa and 0 kPa at the base. The pore water pressure at the base of the simulation was fixed to simulate drainage at saturation. At the top of the caisson an infiltration rate of 0.2 m/day was specified until the caisson became fully saturated at which point the top boundary condition was removed and the caisson allowed to drain under gravity from the base. The SHETRAN simulation was taken as the benchmark for the test. Two Flac-tp models were run. The first Flac-tp model had the non wetting pore pressure (pore air pressure) fixed at zero throughout the simulation. Fixing the non wetting pore pressure

to zero, not allowing volumetric strains within the soil skeleton (mechanical component turned off) and assuming the density of air to be zero, meant the flow equations within the Flac-tp simulation theoretically equate to the Richards equation solved within SHETRAN. The second Flac-tp simulation explored the effects of fixing the non wetting pore pressure at zero for only the bottom boundary of the simulation. This will allow the generation of pore air pressures within the caisson which would affect the flow of water. The second simulation, therefore, explores the effects of air becoming trapped due to the advancing wetting front and hindering the flow of water during escape as observed by Wilson and Luthin (1963). Lastly, an analysis of the effects of varying the viscosity ratio between the air and water was analysed. Increasing the viscosity ratio effectively results in an increase in flow rate of the air relative to the water. It may prove that accuracy can be increased by allowing air pressures to be generated within a simulation. The viscosity ratio would, therefore, prove an important parameter in determining the rate of dissipation of such pressures. Understanding the magnitude of the effects of such parameters allowed the model to be tailored to suit requirements and increase accuracy.

4.2.2 Caisson test with air pressure fixed at zero (Richard's equivalent)

The air pressure for these simulations was fixed at zero throughout the grid and simulation. The simulations were, therefore, analogous to a system where the air pressure within a soil skeleton remains equal to atmospheric air pressure and the air is free to move through the soil skeleton freely and unhindered relative to the water. This assumption is valid for situations where a wetting front will not trap the air within the soil. Once wetting began, profile plots were drawn of pore pressure and moisture content. Figures 4.1 and 4.3 below show snapshots of the pore pressure profiles during the wetting, (Figure 4.1) and the subsequent drying (Figure 4.3). The wetting plot shows that there is exceptional comparison between the SHETRAN and Flac-tp model after 2.5 days of wetting. The upper section of the profile shows that both models predict near-zero pore pressures for the wetted part of the caisson. The wetting front for both models was shown to be between elevations of 4.5m and 3.3m with the wetting beginning at exactly 3.3m elevation for both models. The SHETRAN model did show marginally higher pore pressures between the start of the wetting front and the saturated zone but the discrepancy was minimal. After 4.25 days of wetting the divergence between the two models had slightly increased although the error was still minimal.

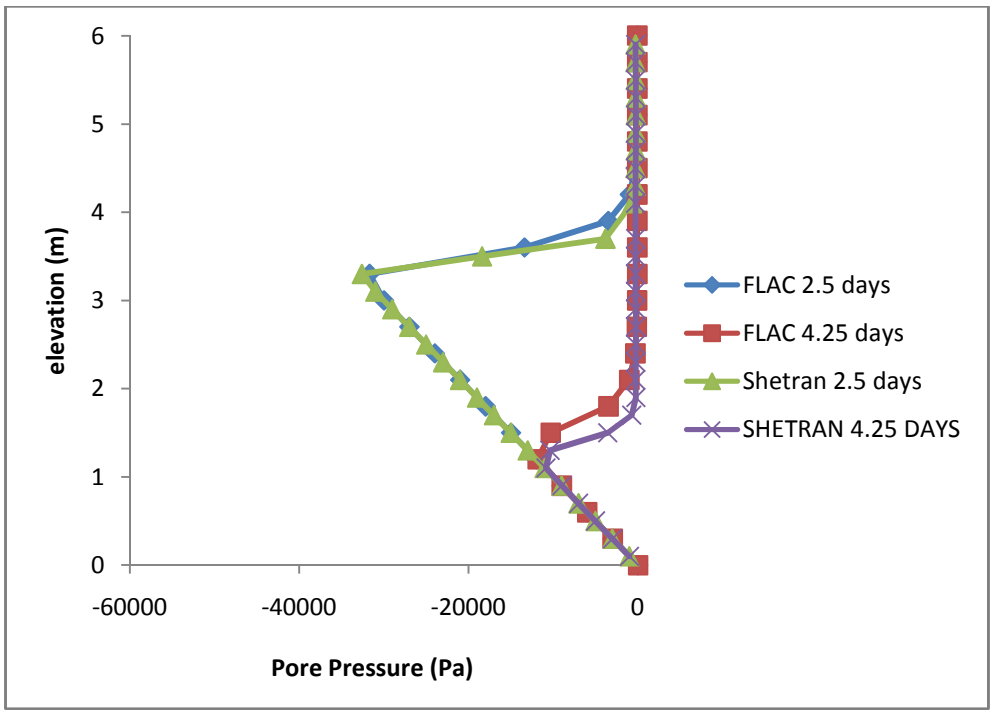

Figure 4.1 Pore pressure profiles within a caisson during wetting with pore air pressure fixed at 0 for Flac-tp and SHETRAN simulations

The moisture contents of the two models duing the wetting phase are shown in Figure 4.2 The moisture contents can be seen to be comparable between the two models. This was expected as, with the pore air pressure fixed at zero, the total pore pressure within the Flac simulation had a unique relationship with the saturation via Equations 3.66 and 3.67.

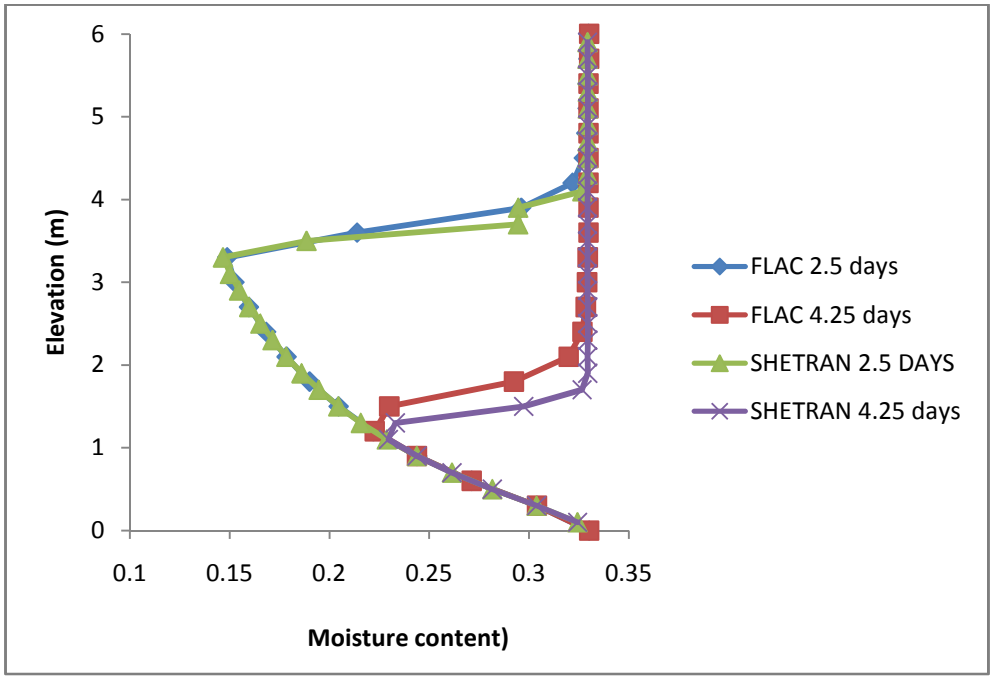

Figure 4.2 Moisture content profiles within a caisson during wetting with pore air pressure fixed at 0 for Flac-tp and SHETRAN simulations

Once full saturation of the caisson was attained, drainage was permitted from the base and snapshot pore pressure profiles were drawn for 1, 4, 20 and 100 day intervals during the simulated drying process. Figure 4.2 shows that the two models had very good pore pressure comparison for the full drying period. There was, however, some divergence as the simulation progressed. This divergence was minimal as can be seen from the pore pressure profile at 100 days.

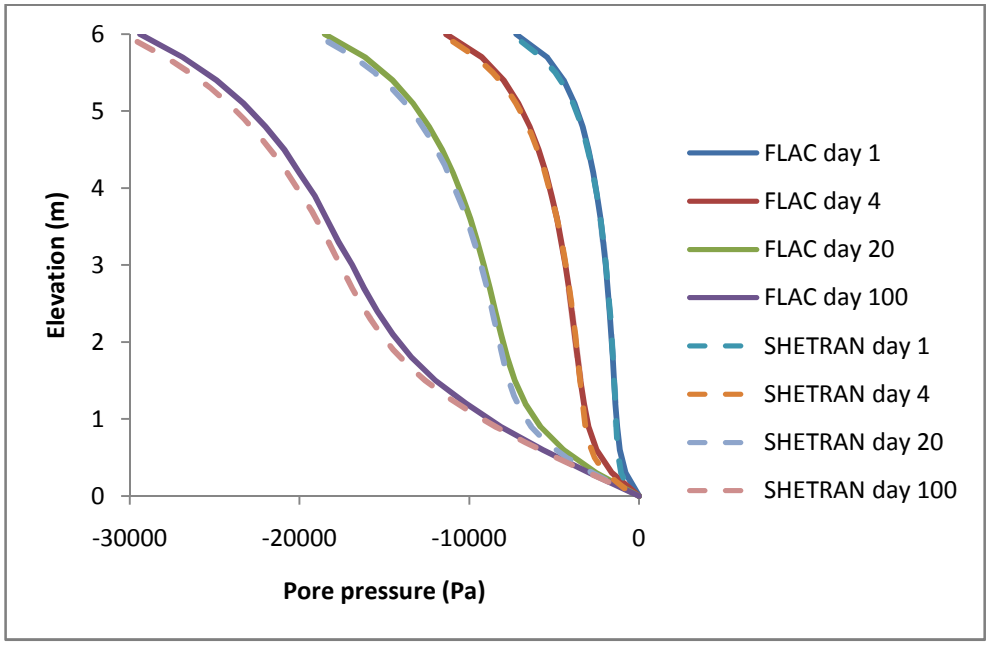

Figure 4.3 Pore pressure profiles within a caisson during drying with pore air pressure fixed at zero for Flac-tp and SHETRAN simulations

The moisture content profiles shown in Figure 4.4 once again show the same picture as during the wetting phase.

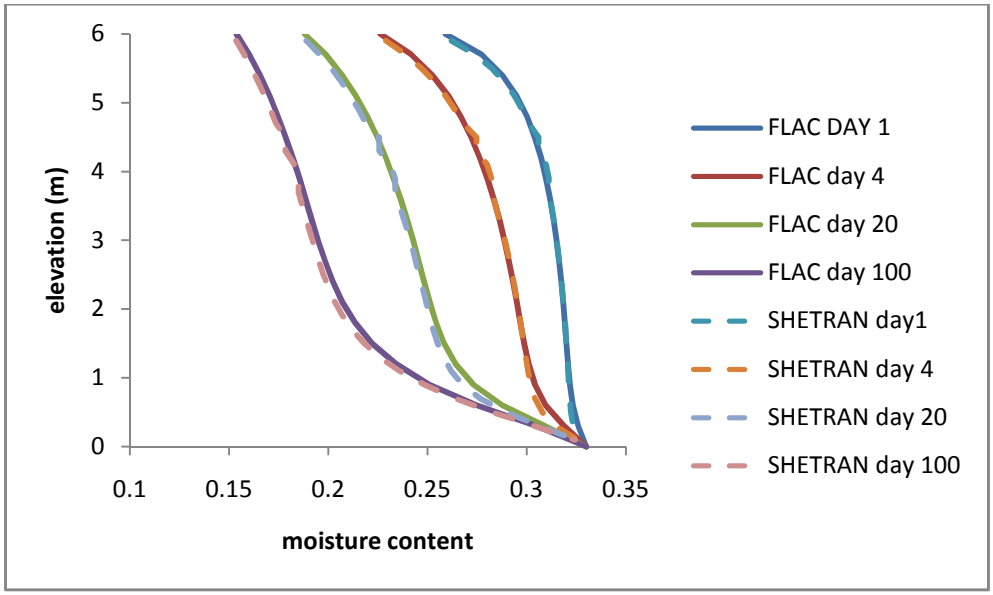

Figure 4.4 Moisture content profiles within a caisson during drying with pore air pressure fixed at zero for Flac and SHETRAN simulations

These simulations showed that the Flac-tp procedure used to model unsaturated flow for an unsaturated caisson, under certain conditions, was comparable to that of the established SHETRAN hydrological model.

4.2.3 Caisson test with generated air pressure

Within the previous simulations the air pressure was assumed to remain fixed at zero. It follows that the air was displaced by the infiltrating water instantaneously offering no resistance to the flow of water. Therefore, infiltration into an unsaturated cell created no positive pore air pressures within that cell and therefore no increase in total pore pressure. The following simulations, where air pressure is not fixed at zero, positive air pressures were generated within a cell therefore increasing the total pore pressure. It should be noted that a flow only simulation was considered where the volume of the pore space is constant.

The same procedures of wetting and drying were followed as per the previous simulation. Water flowed down through the caisson under gravitational forces. Within a partially saturated cell Equation 3.65 dictates that the pore space is filled entirely with air and water. Infiltration of water into a cell requires that the volume of the air phase decreases. The rate of flow of air out of the cell is defined by Equation 3.71. As flow of air cannot take place without an increase in air pressure (the air phase has zero density) the infiltration of water into the cell results in a slight compression of the air phase and therefore a positive pore air pressure. As infiltration continues the air is expelled and the cell tends to full saturation with water. The relative permeability of the air phase therefore tends to zero, as defined by Equation 3.73, and it becomes increasingly difficult for the remaining air within the cell to be expelled. As the air is trapped under pressure it can exert a pressure on the pore water within the cell. At equilibrium this will also result in a small positive pore water pressure. It is therefore possible for an unsaturated cell to return a positive pore water pressure.

For this section of the analysis air pressures were permitted to be generated by the advancing wetting front. The bottom boundary condition has been defined as saturated as per the previous simulation. As the bottom boundary was saturated with water it was, therefore, impermeable to air. The sides of the caisson were again assumed to be impermeable to air and water. The discharge was applied to the entire upper boundary

of the model this boundary was, therefore, impermeable to the air phase. The wetting front advanced through the profile during infiltration as per the previous simulation. This wetting front, as it represents the saturated / partially saturated boundary, was also impermeable to the air. The air has been given a bulk modulus 3 magnitudes lower than that of the water and is therefore relatively compressible. Figure 4.5 shows the variation in pore pressure for the same time periods as the previous simulation. Once more, the pore pressures calculated by Flac-tp have been compared to the SHERAN model benchmark values. It can be seen from this figure that a small positive pore pressure has been generated within the saturated region of the caisson. This was due to the small amount of trapped air within this section of the caisson as discussed earlier.

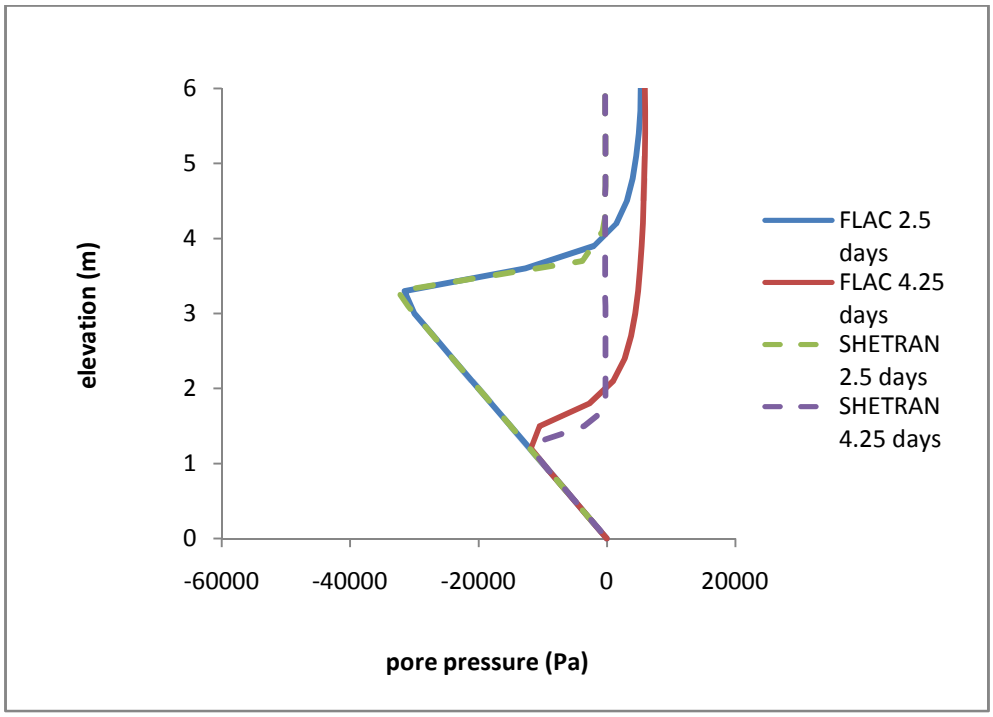

Figure 4.5 Pore pressure profiles within a caisson during wetting for Flac-tp and SHETRAN simulations. Pore air pressures were permitted to be generated with the Flac-tp simulation

As can be seen from a similar plot of the pore air pressure (Figure 4.6) there has been an increase in the pore air pressure of the same magnitude as the pore water pressure. It can be seen from Figure 4.6 that the pore air pressure increase occurs at a comparable time to the pore water pressure increase. It can also be seen from Figure 4.6 that in the vicinity of the wetting front there exist several cells which contain a positive pore air pressure and a negative pore water pressure. This is due to the advancing wetting front forcing air out of the cells and down the column. In the upper section of the caisson the pore air pressure and pore water pressure appear to have reached a maximum. This is where the air has become trapped under pressure and exerts a pressure on the pore water within the column.

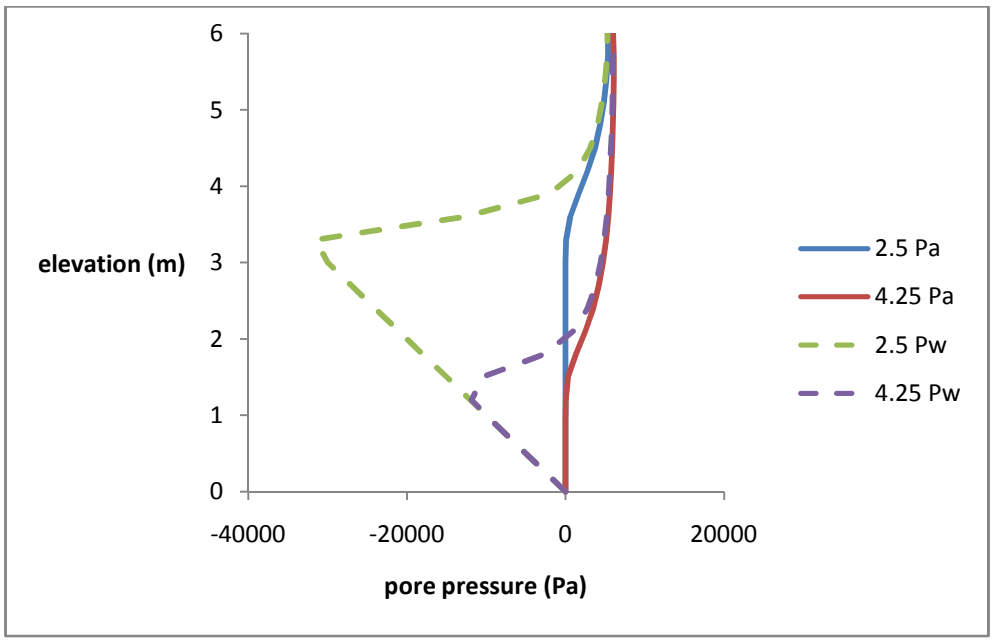

Figure 4.6 Pore air (Pa) and pore water (Pw) pressures during infiltration under gravity

Wihin this section, the pore water pressure is slightly higher than the pore water pressure. Upon subtracting the pore water pressure from the pore air pressure to calculate the capillary pressure, Equation 3.66, the following chart showing the total combined pressure within the model can be produced, Figure 4.7.

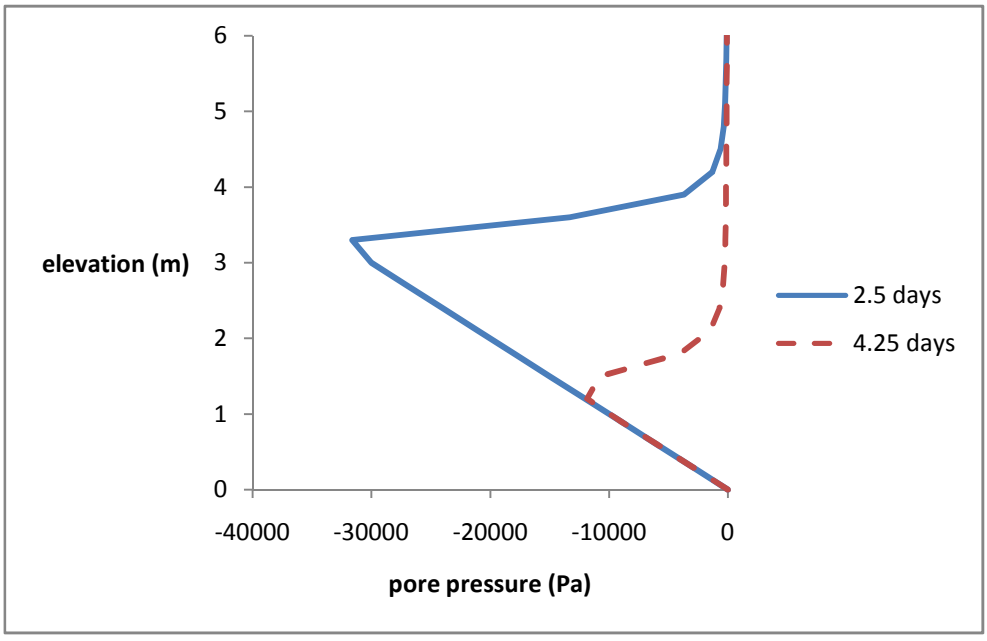

Figure 4.7 Total pore pressure during infiltration

This chart shows comparable total pressures to the simulation carried out with the pore air pressure fixed at zero. The moisture contents within Flac-tp are related to the total suction, via saturation and porisity, by Equation 3.67. The moisture content profiles

created during this simulation are shown in Figure 4.8 and can be seen to remain comparable to the SHETRAN profiles.

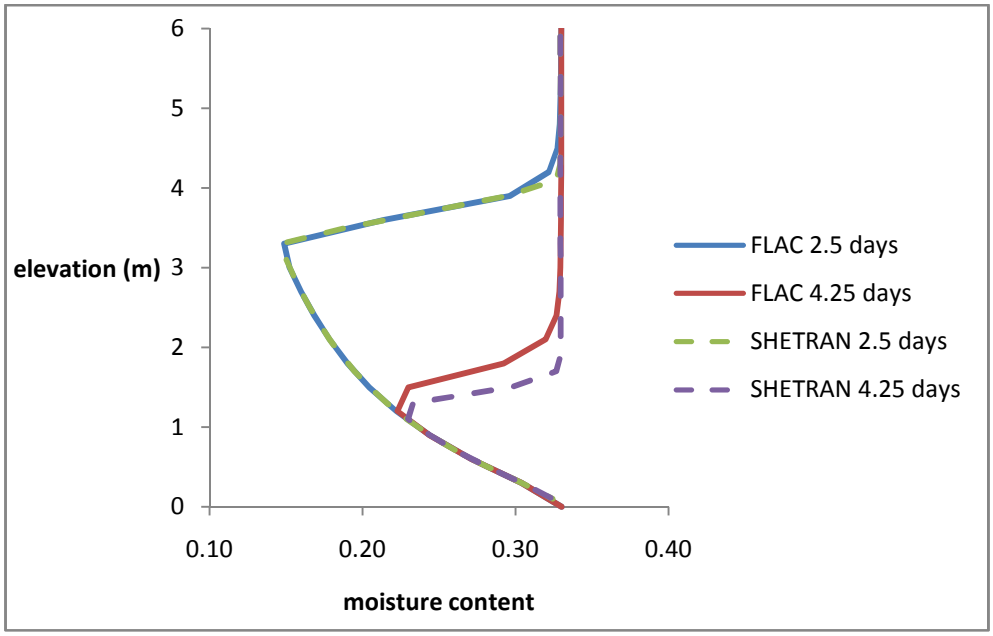

Figure 4.8 Moisture content profiles of Flac-tp, with air pressure generation permitted, and SHETRAN.

The higher pore water pressures generated during the infiltration phase of the simulation persisted into the beginning of the drainage phase. Figure 4.9, therefore, shows that the Flac-tp calculations show much higher pore water pressures than the SHETRAN calculations. The pore water pressures after 20 days are also slightly more negative than the fixed air pressure simulation giving a better comparison to the SHETRAN simulation.

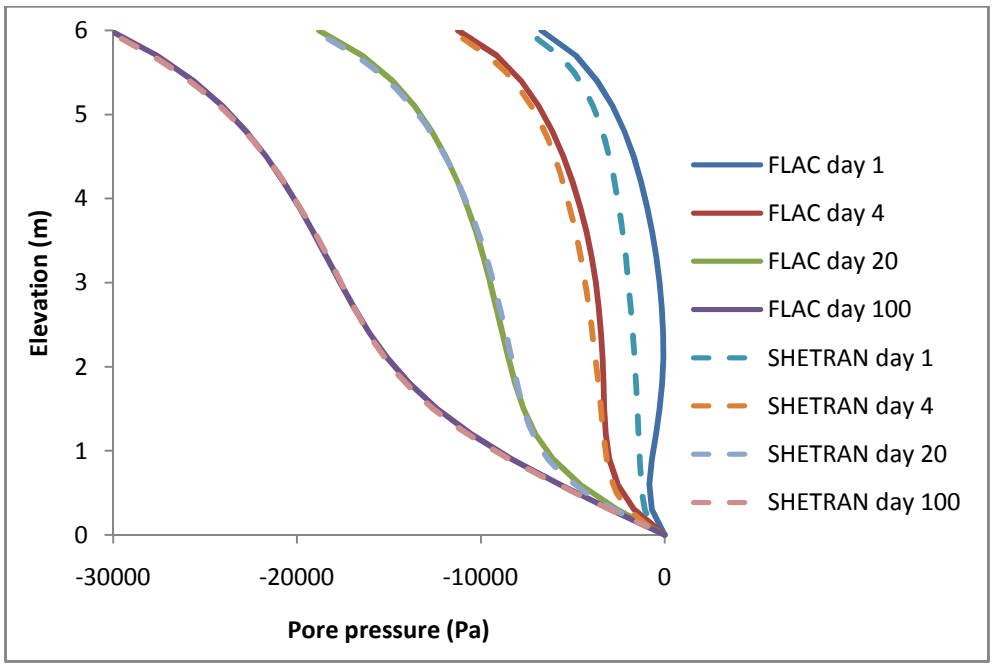

Figure 4.9 Pore water pressure during drainage for Flac-tp simulation with pore air pressure generation permitted and SHETRAN

The increased pore pressure within the initial drying pore pressure profiles has once again been matched by an increase in the pore air pressure (Figure 4.10). The excess pore air pressure dissipates within the initial stages of the drying as it is able to flow out of the column from the top and the bottom. It then becomes uniformly negative along the column depth.

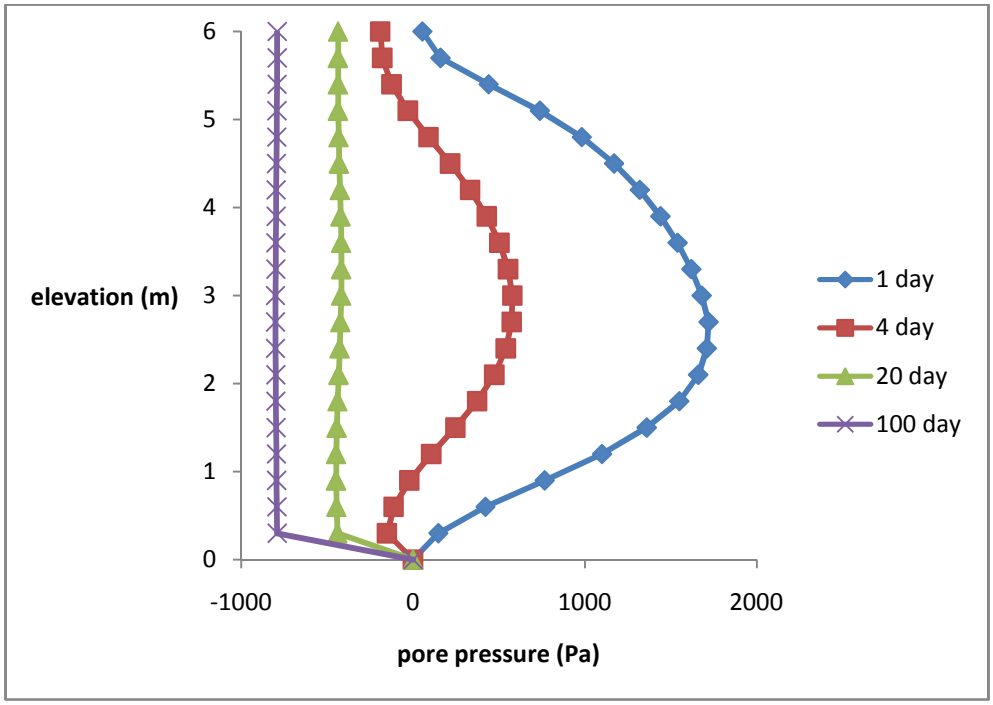

Figure 4.10 Pore air pressure dissipation during the drainage phase of the Flac-tp simulation.

This negative pore air pressure has an effect on the capillary pressure shown in Figure 4.11. This shows, once again, that the cappilary pressure is very comparable to the first simulation where pore air pressure was fixed at zero.

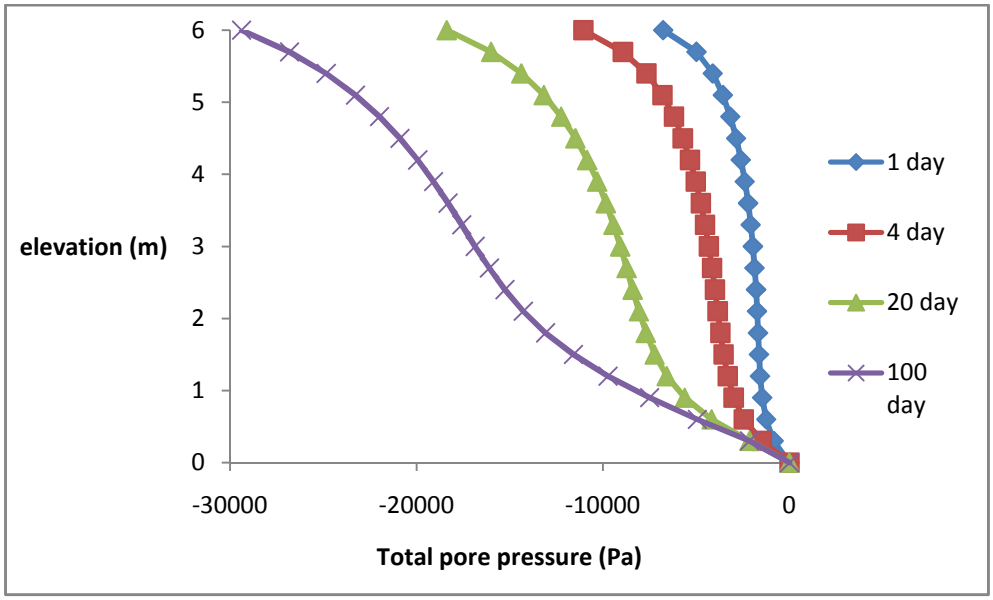

Figure 4.11 Total pore pressure during Flac-tp simulation with pore air pressure generation permitted

The moisture content profiles during the drying phase, therfore, continue to remain comparable to the SHETRAN moisture content profiles, Figure 4.12.

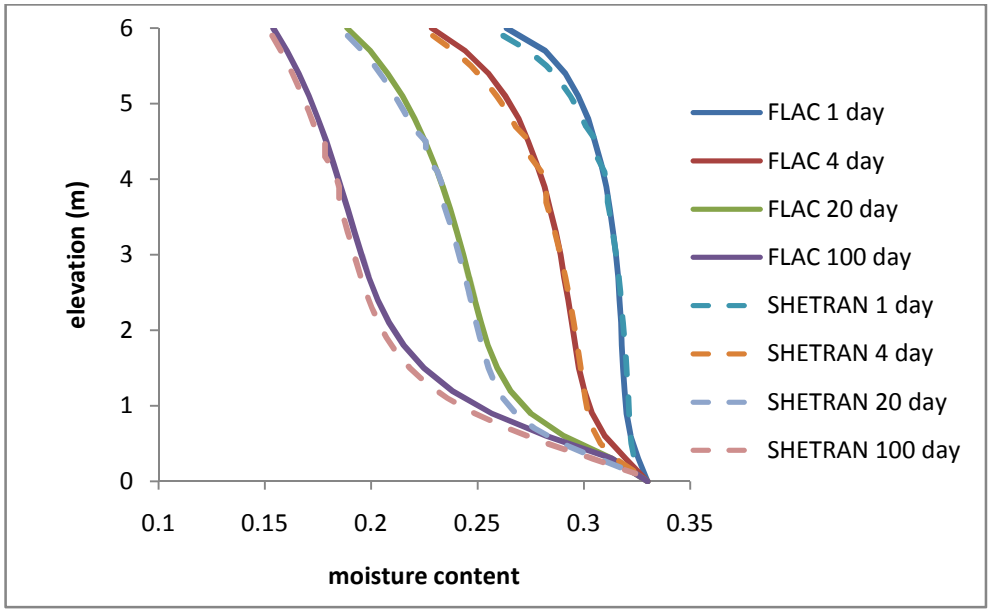

Figure 4.12 Moisture content profiles for Flac-tp simulation with pore air pressure generation permitted and SHETRAN.

Allowing the generation of air pressures within has been shown to not significantly affect the capillary pressures but it has a significant effect on the individual air and

water pressures within the simulation. As the total pore pressures have not been significantly affected there has been no significant effect on the moisture content profiles. It is to be noted, however, that when allowing air pressures to be generated there is no longer a unique relationship between the pore water pressure and moisture content, the pore air pressure needs to be taken into consideration.

4.2.4 Caisson test with varying viscosity ratio

The viscosity ratio (μ_w/μ_g), is used within Flac-tp (Equation 3.71) rather than the individual viscosities of the fluids within the media. The viscosity ratio dictates that an increase in this value leads to an increased flow rate for the air phase relative to the water phase. Fredlund and Rahardjo (1979) have determined by experiment that the viscosity of air is roughly 100 times less than the viscosity of water. Such a value would dictate that the air within the model will flow much more readily than water. Tests were run for a viscosity ratio of 100 with pore air pressures permitted. Figure 4.13 shows the pore pressures within the caisson during the wetting phase of the simulation. It can be seen that the pore pressures within the saturated zone of the caisson are significantly lower due to the air pressure being able to dissipate more rapidly. There still, however, remains a positive air pressure within the saturated zone. This is significantly less than the simulations run with a viscosity ratio of one. The rate at which the wetting front advances remains largely unchanged although a slight increase in pore pressure at the base of the wetting front was noted as the viscosity ratio was increased.

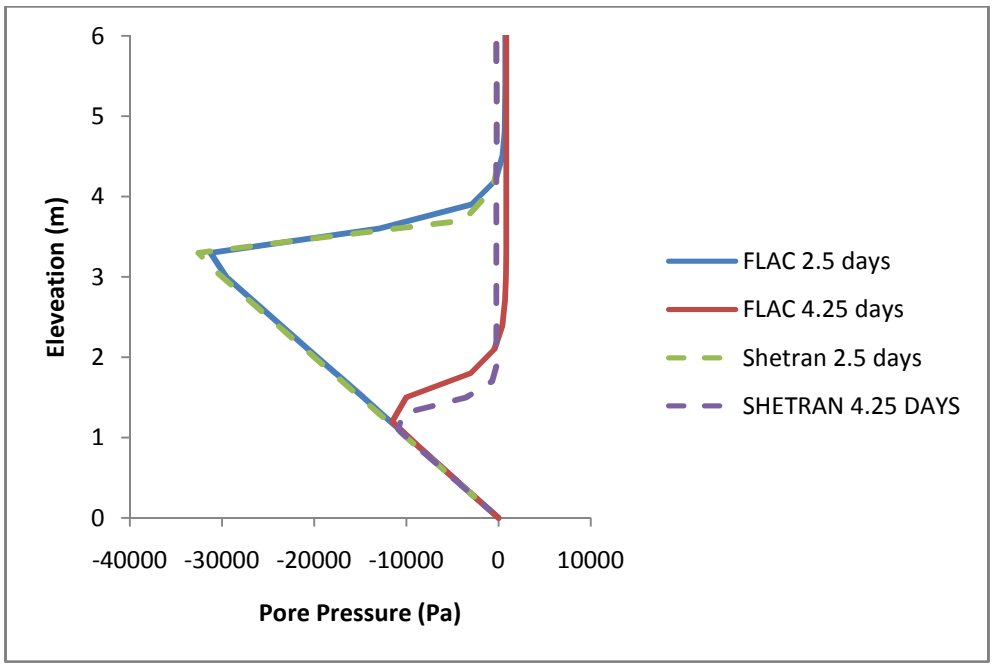

Figure 4.13 Pore pressures within Flac-tp (pore air pressure generation permitted and a viscosity ratio of 100) and SHETRAN.

The capillary pore air pressures for this simulation were shown to increase throughout the profile. The air was much more mobile due to the increased fluid viscosity ratio. The infiltration of water expelled the air from the top most cell and this had a knock on effect on the pore air pressures throughout the whole of the column Figure 4.14.

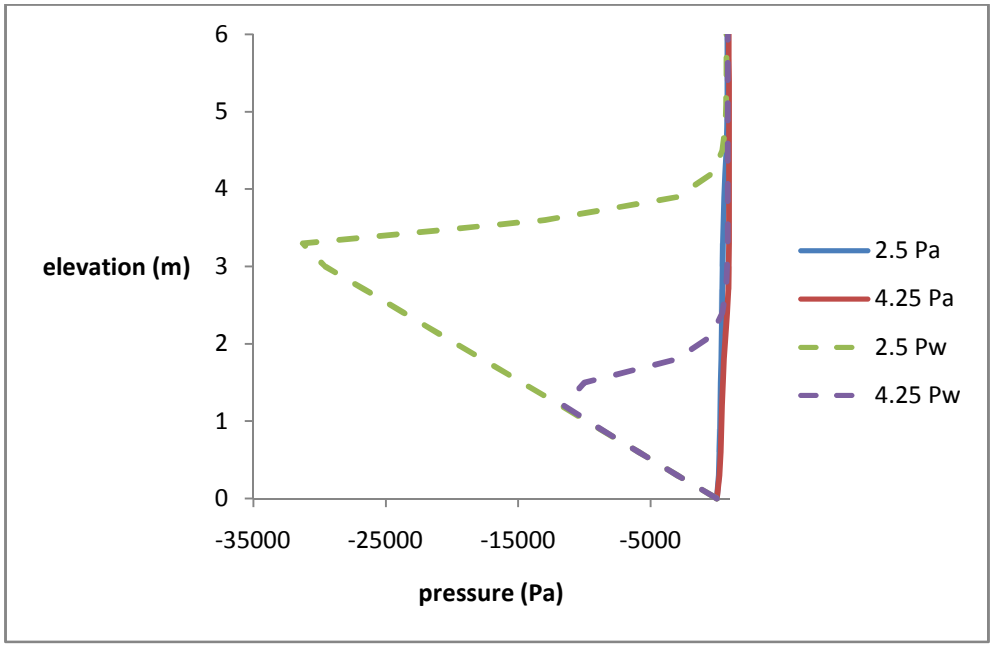

Figure 4.14 Pore air and pore water pressure during infiltration for Flac-tp model with air pressure generation permitted and a water/air viscosity ratio of 100.

The positive pore water pressures again mirrored the pore air pressures and the plot of capillary pressure is comparable to those of the previous simulations Figure 4.15.

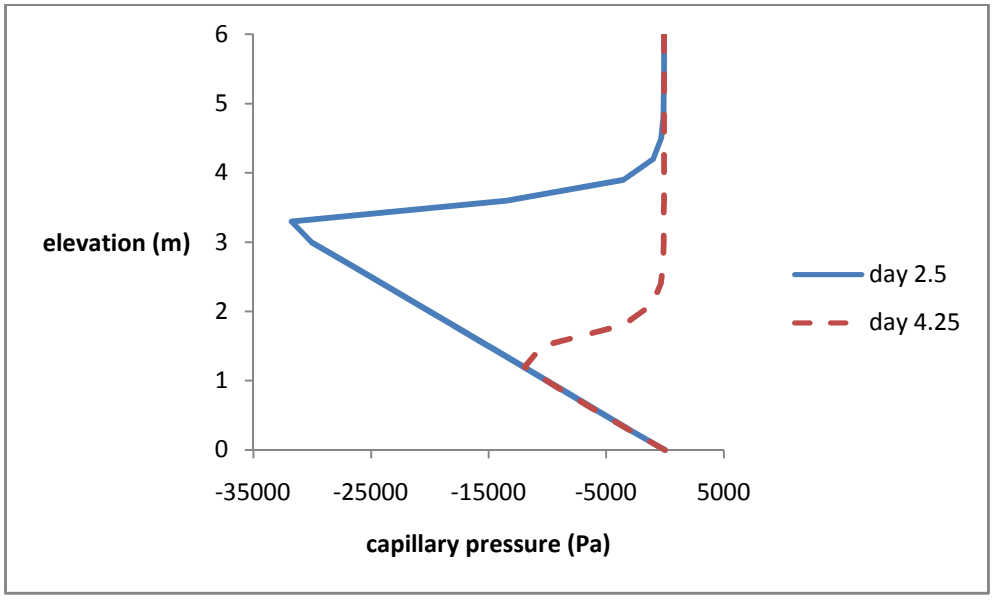

Figure 4.15 Capillary pressure during infiltration for Flac-tp model with air pressure generation permitted and a water/air viscosity ratio of 100.

The drying pore pressure curves for this simulation show a much larger divergence from the previous results. Figure 4.16 shows a much lower pore pressure profile.

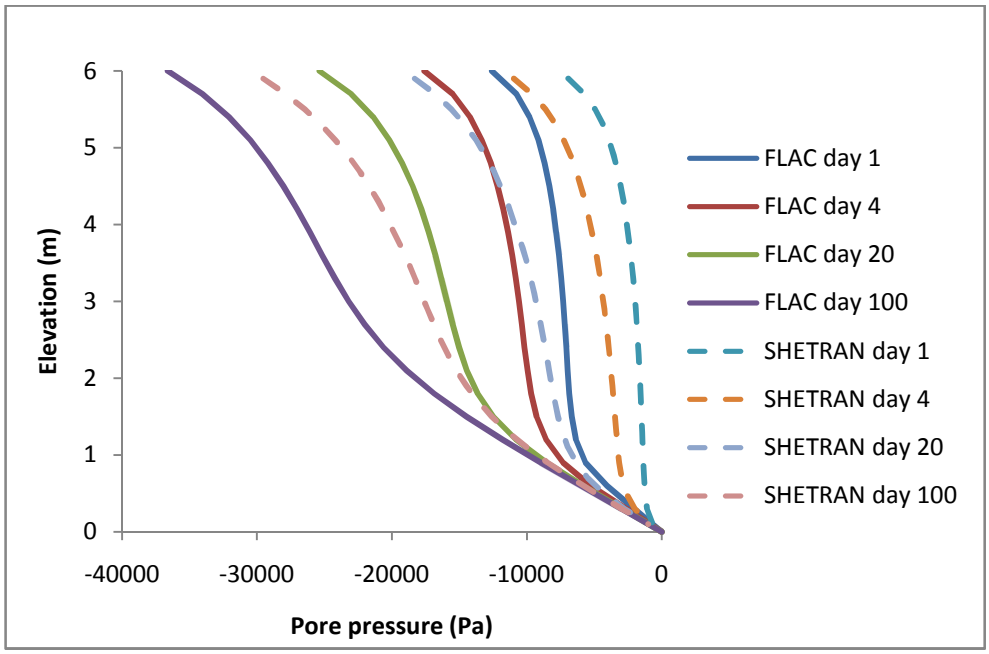

Figure 4.16 Pore water pressure variation under drainage for Flac-tp model with air pressure generation permitted and a water/air viscosity ratio of 100.

The pore air pressure plot, Figure 4.17, goes some way to explaining the drop in pore water pressure. Negative pore air pressure has reached over 7 kPa. The drop in pore air pressure is due to the increased rate at which the air can escape the column during the wetting phase.

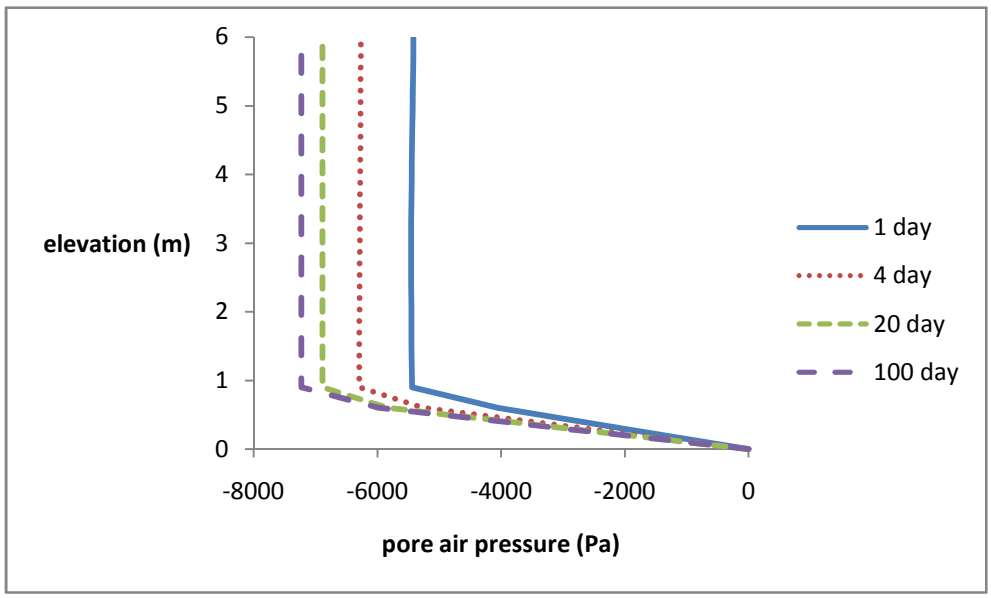

Figure 4.17 Pore air pressure variation under drainage for Flac-tp model with air pressure generation permitted and a water/air viscosity ratio of 100.

The reduction of the pore water pressures at the top of the column from previous simulations is entirely down to the high negative pore air pressures as can be seen from Figure 4.18. These pressures have built up as the the water has vacated the upper cells reducing the air pressure. As air saturation was very low the permeability to air was also very low which therefore restricted the free inflow of air into the cell. The bottom of the column, however, shows a much different picture to previous simultions. The lowest three cells of the simulation show a capillary pressure of zero. In this area the pore air pressures and pore water pressures are identical and the cells are almost saturated with only a negligable amount of air still present.

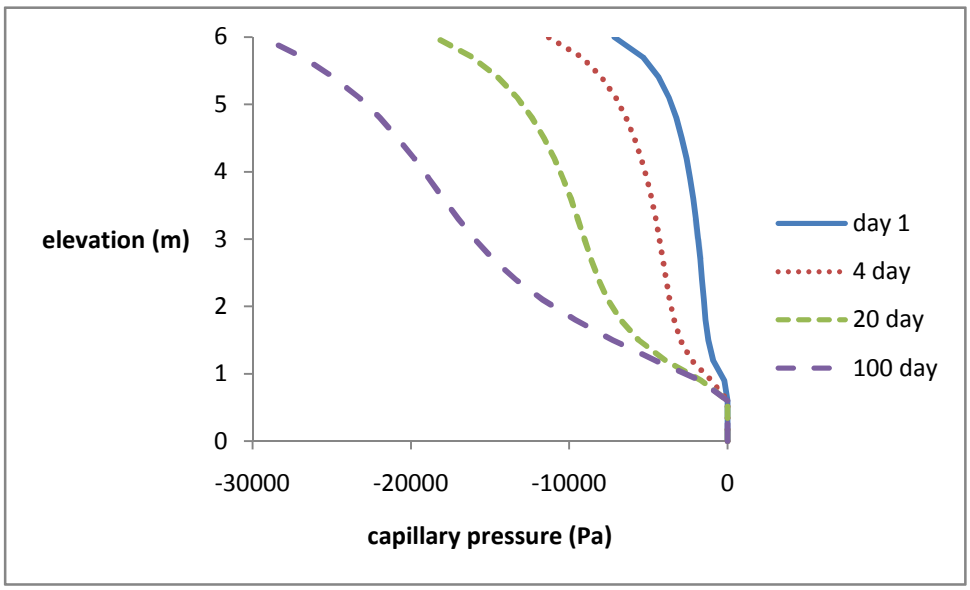

Figure 4.18 Capillary pressure during drainage for Flac-tp model with air pressure generation permitted and a water/air viscosity ratio of 100.

With the air allowed to move more freely during the wetting phase the water was able to expel almost all the air from the bottom of the colum, the expulsion of air at the base resulted in a high water saturation which has persisted throughout the drying phase, Figure 4.18. The moisture content profiles for the drying phase of the simulation therefore also show a greater divergence from the SHETRAN results. It can be seen from Figure 4.19 that the bottom metre of the caison remains saturated during the entire length of the drainage phase whereas the moisture content profiles at the top of the caisson show good agreement with the SHETRAN simulation. Negative air pressures and water pressures are persisent throughout the caisson profile. The air pressures within this simulation, during both wetting and drying phases, are much lower than the previous simulations. This was due to the increased flow rate of air permitted by raising the viscosity ratio during the wetting phase which lead to a low air saturation and therefore reduced permeability to air during the drying phase.

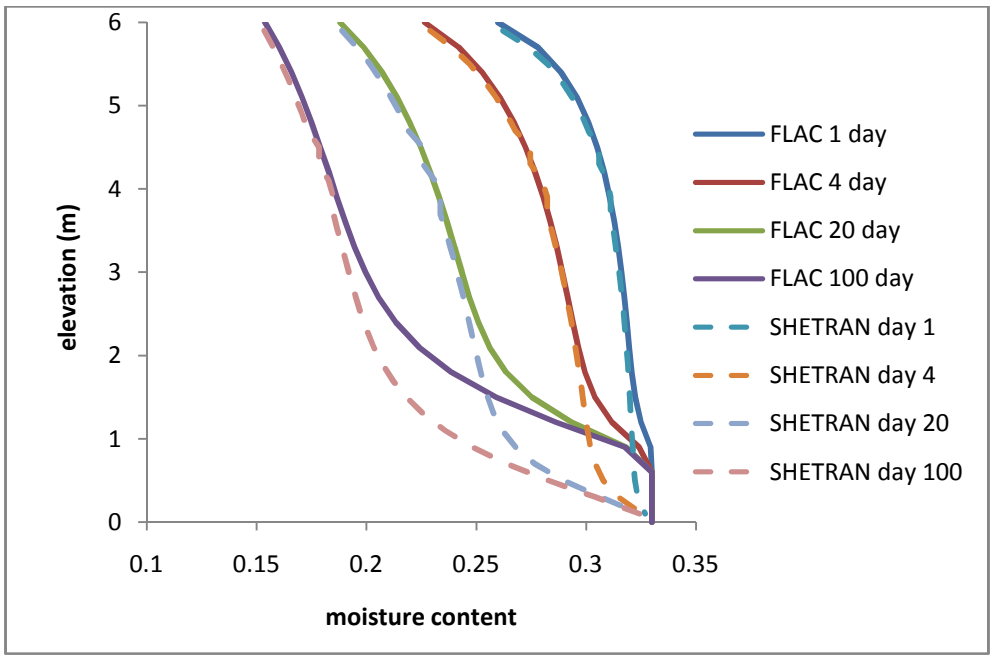

Figure 4.19 Moisture content profiles during drainage for Flac-tp model with air pressure generation permitted and a water/air viscosity ratio of 100 compared to SHETRAN.

4.2.5 Effects of fluid bulk modulus

Within Flac-tp the bulk modulus of air and water is required within a calculation (Equations 3.80 and 3.81). The bulk modulus of water is around $2.2X10^9$ Pa and the bulk modulus of air is around $1.0X10^5$ Pa, however as discussed in Chapter 3 the time step Flac-tp uses is highly dependent on the bulk modulus used. The bulk modulus must therefore be reduced in order for the simulation to be practical. The magnitude of reduction must be small enough to have a negligible effect on the accuracy of the calculation. The bulk modulus of air must also be defined so that the air phase remains relatively compressible when compared to the water.

The previous simulations used a water bulk modulus of $1x10^6$ Pa and an air bulk modulus of $1x10^3$ Pa. For the following simulations bulk moduli of $1x10^8$, $1x10^6$ and $1x10^4$ Pa are used with air bulk moduli of $1x10^5$, $1x10^3$ and $1x10^1$ Pa respectively to assess the sensitivity of simulation to this parameter. The first simulation has been carried out with air pressure fixed at zero. Figure 4.20 shows the wetting profiles compared to the profiles generated by SHETRAN. This figure shows that a reduced water bulk modulus ($1x10^4$ Pa) simulation does not compare well with the SHETRAN simulations. There has been virtually no infiltration into the caisson. For the higher bulk moduli of $1x10^6$ and $1x10^8$ Pa the results compare well with the SHETRAN simulation at 2.5 days. At 4.25 days however the $1x10^8$ Pa simulation shows greater agreement with the SHETRAN simulations.

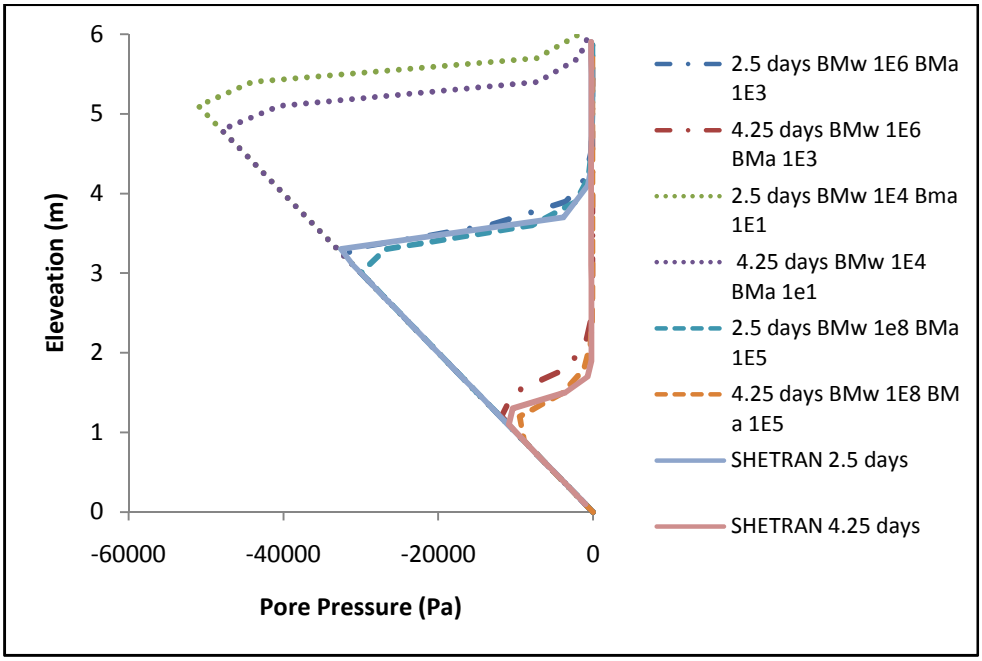

Figure 4.20 Variation of pore pressure during wetting for varying bulk modulus of water and air

The drying profiles show a similar picture, Figure 4.21. It can be seen from these results that as the bulk modulus is increased the compatibility with the SHETRAN results increases also. The profiles of the Flac solution show convergence to the SHETRAN results. A bulk modulus of $1x10^4$ Pa for the water has been proven to be inaccurate whereas a bulk modulus of $1x10^6$ Pa has been shown to give a good comparison to the SHETRAN results. A bulk modulus of $1x10^8$ Pa has increased the compatibility further. Increasing the bulk modulus of water within a simulation does however increase the processing time to reach a solution significantly (Equation 3.86). From these tests it can be concluded that a minimum bulk modulus of $1x10^6$ Pa is needed to give a reasonably accurate SHETRAN comparison for a flow only calculation. It is worth noting, however, that for coupled fluid/mechanical calculations the bulk modulus of water will need to be relatively incompressible compared to the porous media as discussed within Section 3.67.

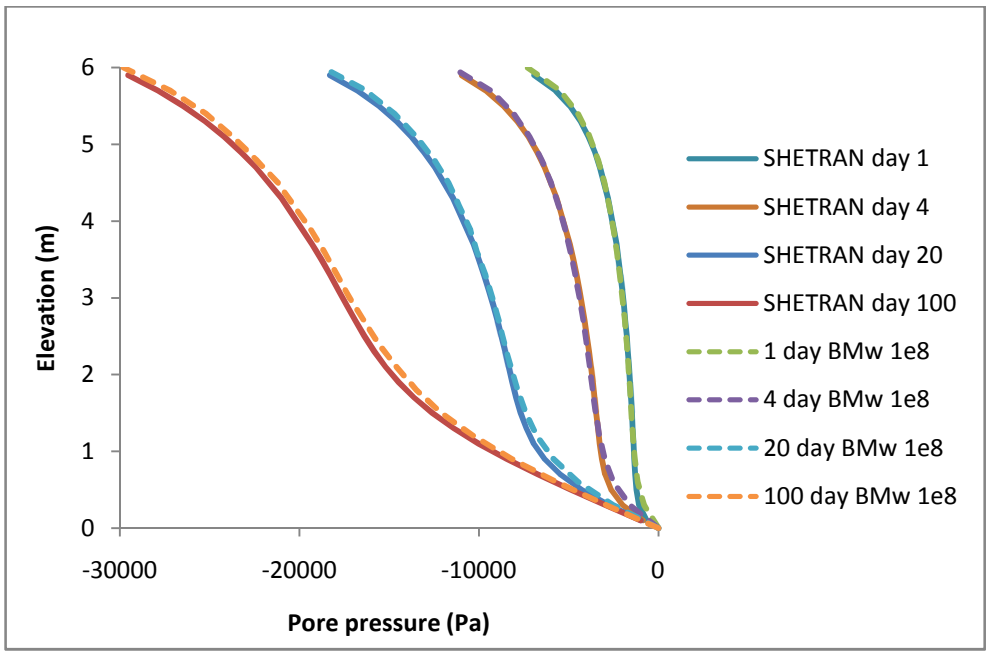

Figure 4.21 Variation of pore pressure during drying for bulk modulus of water 1e8 Pa and air 1e5 Pa.

The next simulations are run allowing the generation of air pressures with reduced bulk modulus of the air phase. The viscosity ratio was kept at one and the bulk modulus of water was $1x10^6$ Pa. The bulk modulus of air was reduced to 10 Pa. This simulation can therefore be compared to the results shown in Figure 4.6. Figure 4.22 shows the wetting profiles against those of the SHETRAN simulation. The results show that negligible excess pore water pressures have been predicted within the saturated zone of the caisson unlike the profiles within Figure 4.6. These profiles show good comparison with Figure 4.1 where air pressure was fixed at zero.

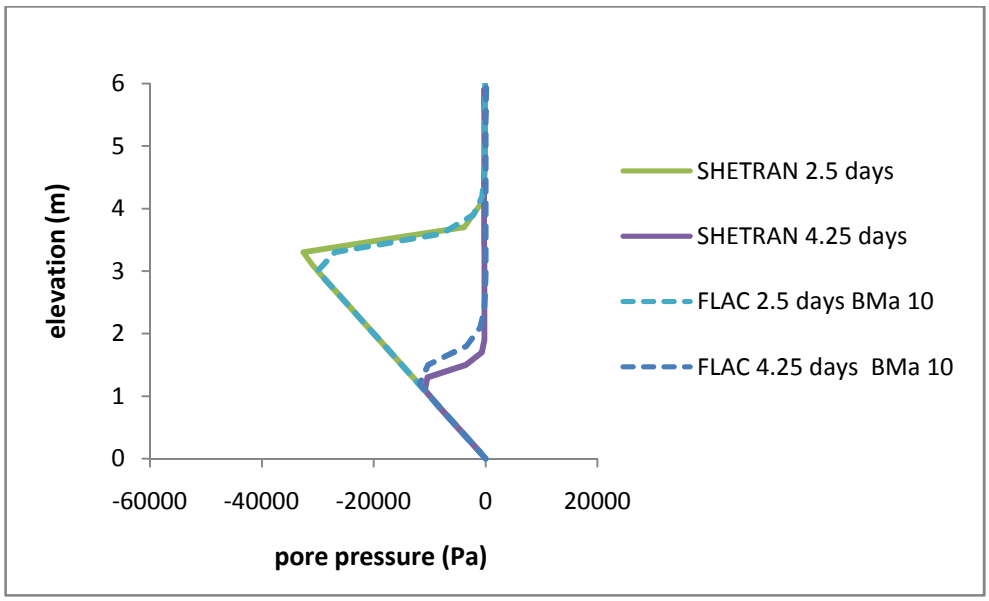

Figure 4.22 Wetting profiles for SHETRAN simulation and Flac-tp simulation with air pressure generation permitted and reduced air bulk modulus.

The drying profile also has a much improved comparison with the SHETRAN data. Figure 4.23 shows that due to no excess pore air or water pressures during the infiltration phase the comparison at day one with the SHETRAN data is very good.

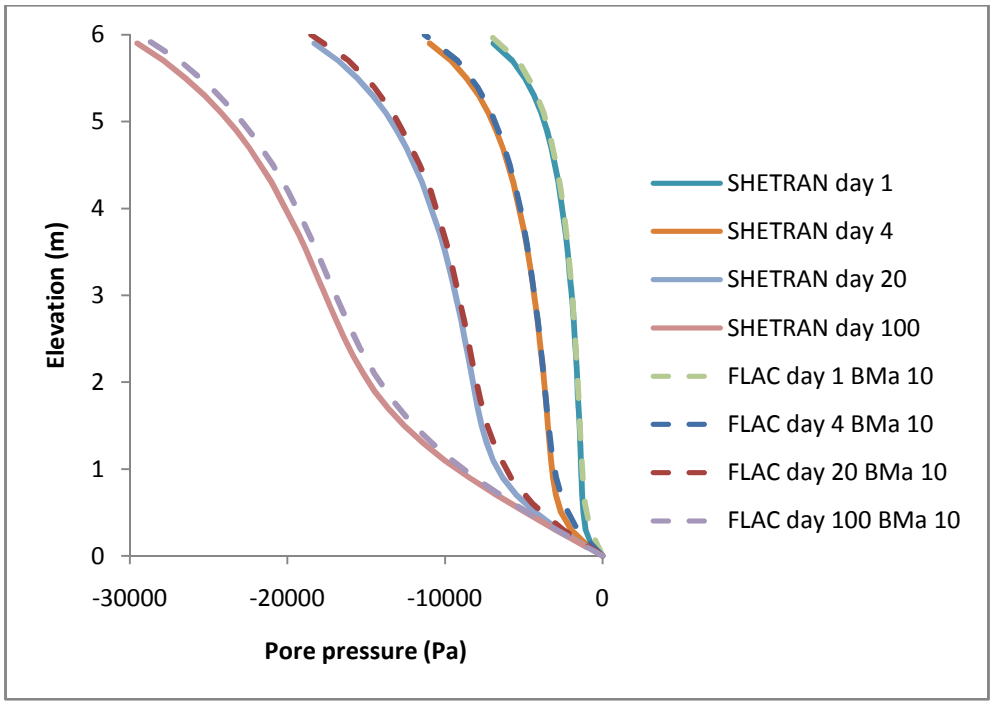

Figure 4.23 Drying profiles for SHETRAN simulation and Flac-tp simulation with air pressure generation permitted and reduced air bulk modulus.

This improved comparison is due to the lower air pressures within the saturated zone of the caisson. The lower air pressures are due to the air being far more compressible within this simulation. The trapped air is, therefore, unable to exert a significant

pressure on the water. The air pressure is small and therfore the profiles are similar to those of the simulation with air pressure fixed at zero. The moisture contents are identical to the simulation with the higher pore air pressure.

4.2.6 Concluding remarks of caisson comparison

It has been proved here that Flac-tp is capable of modelling the infiltration of water into a caisson to a comparable accuracy to that of an established hydrological model. There are parameters required by the Flac-tp model that are not usually required for a hydrological model. This is because the Flac-tp low model has been designed to be capable of modelling the flow of any two immiscible fluids through the porous media. One advantage of the Flac-tp model is its ability to model the non-wetting fluid, or in the case of partially saturated flow, the air. SHETRAN and other established hydrological models often ignore the flow of the air in a calulation. The air within the simulation is assumed to be able to move freely and instantaneously into and out of the system. This can be modelled wihin Flac-tp flow by fixing the air pressure at zero and has been demonstrated above. Simulations within Flac-tp which allow the generation of pore air pressures have also been run for comparison purposes. Allowing air pressure to be generated within the caisson can lead to increased pore water pressure also. Where the viscosity ratio between the water and the air is fixed to one the capillary pressure remains comparable to the simulations where the air pressure was fixed at zero. Where the viscosity ratio is larger than zero the air is enabled to move more freely. This may seem like the more realistic simulation but the flow of air out of the caisson dictates that the relaive permeability of the soil to air decreases. This leads to air becoming trapped in the soil and unable to leave. It also becomes difficult for air to enter the soil due to the low permebility. This leads to unrealistic saturations associated with high pore water tensions. This phenomena may be overcome by assigning more realistic van Genuchten properties for the air phase (van Genuchten properties b and c) but information regarding these properties is sparce and including extra unknown parameters may introduce additional errors into the calculation. Reduing the bulk modulus of the air leads to the air phase becoming more compressable and therefore a reduction in the pore pressure it can generate. The reduction of the bulk modulus is however not representative of the air modelled and it would be more realistic to assume the air is allowed free movement to escape and therefore the assumption that air pressure is fixed at zero is more valid. The bulk modulus of water used within the simltions has been shown to have a significant effect on the solution. As the value of

the bulk modulus of water increases towards its realistic value the solution becomes increasingly more comparable to the SHETRAN solution. The increase in comparability is however not a linear one. It has been shown that a bulk modulus of $1x10^6$ Pa gives reasonable comparison to the SHETRAN results. Increasing the bulk modulus further gives a slightly more accurate comparison but this accuracy comes with the price of significantly increased processing time. Perhaps a more pressing constraint on the value used for the bulk modulus of water will be when coupled calculations need to be run. During a coupled calculation the bulk modulus of water will need to be significant enough so that the water within a simulation is incompressible in comparison to the media in which it flows. As a rough guidline Itasca recommend a minimum value of at least 20 times the maximum material bulk modulus for the water.

The following simulations will therefore be run with a minimum water bulk modulus of $1x10^6$ Pa with bulk modulus of air 3 magnitudes lower than that of water. Air pressures will also be fixed to zero throughout the grid to simulate free unrestricted water movement throughout the system.

4.3 Surface pore water pressure transfer method

4.3.1 Introduction

From the previous section it has been shown that under certain conditions the Flac-tp model was capable of modelling the flow of water through an unsaturated media to a level of accuracy comparable to that of an established hydrological model. This comparison work was undertaken by applying an identical infiltration rate to the hydrological model and the Flac-tp model. The infiltration boundary condition for the Flac-tp model was defined as a discharge into the model whereas within the SHETRAN model a constant rainfall was applied to the model which equated to a discharge equal to that applied to the Flac-tp model. The SHETRAN boundary condition, as discussed in Chapter 3, can calculate evapotranspiration, ponding and run off. Within the previous calculation the weather file within the SHETRAN simulation was designed so that no vegetation existed on the caisson surface and there was no evaporation. The rate of the rainfall was also low enough so that no ponding occurred. For this section, a weather file was used within SHETRAN which permitted evaporation and surface ponding.

The SHETRAN model was run for a duration of one year and a file created storing the daily pore pressures for the top cell. As Flac-tp cannot model these processes the pore pressures from the top cell of the SHETRAN simulation were transferred to the Flac-tp caisson. The SHETRAN pore pressure for day one was applied to the surface and Flac-tp run for one day. The SHETRAN pore pressure for day 2 was then applied to the Flac-tp boundary and the model again run for one day. The above process was repeated until the end of the year simulated by SHETRAN. The pore pressure history at various depths within the caisson for both the Flac-tp and SHETRAN models were compared to establish the agreement between the two models. The objective was to establish whether the Flac-tp, with the daily pore pressure transfer, was of comparable accuracy to the SHETRAN simulation.

Applying a pore pressure to the Flac-tp fixes the boundary at that pore pressure. The saturation at the boundary is also calculated from the pore pressure using the van Genuchten parameters and then applied to the surface also. Once the pore pressure at the surface has been fixed and the model run then water either flows into or out of the grid depending on the magnitudes of the surface pore pressure and the pore pressure at the next grid point beneath the surface. Applying a pore pressure, therefore, equates to either water infiltrating into the surface or water being extracted from the surface. The choice of applying a pore pressure instead of an infiltration has been made as Flac-tp would automatically calculate and return a pore pressure for the surface when provided with an infiltration rate. As SHETRAN already outputs a pore pressure it was simpler take this value and directly apply it to the surface.

Once the pore pressures from SHETRAN were transferred and the accuracy of the transfer proven, Flac-tp would be capable of running coupled simulations to calculate the mechanical response of the model due to variations in pore pressure. This section begins by outlining the transfer method and all the assumptions made, it then details the results and comments on the accuracy of the process.

4.3.2 The transfer method

As stated within the previous section the SHETRAN model was run first for the full length of time of a given simulation. The SHETRAN model was set to create an output for each day of the simulation.

The output file was then transferred to a program called CYGWIN which used unix language to manipulate ASCII files. The code shown below read through the SHETRAN out file and created a new ASCII file containing a list of the daily surface pore water pressures.

```
for file
do
grep HEAD $file|sed -e's/SUBS. HEAD (m) *//' -e's/ .*//'
>flac/`basename $file`
done
```

The file containing the list of surface pore water pressures was then placed within the Flac-tp file containing the code for the simulation. The first surface pore pressure was applied to the Flac-tp model using the inbuilt fish language. The Flac-tp model was then run for one day. The next surface pore pressure was then applied to the surface and so on until the end of the simulation.

The initial conditions of both simulations were once again identical. The Flac-tp grid was, however, changed slightly. The pore pressure output for the SHETRAN surface cell represents the pore pressure at the centre of the cell. Therefore for a cell of height of 0.3m the pore pressure output will be for a depth of 0.15m. It was assumed that the top 0.15m of the Flac-tp model was not to be modelled and therefore the total height of the Flac-tp caisson was 5.85m. The assumption means that the two models will return the same pore pressure variation for each depth. For coupled models where a mechanical response is required a small surcharge was to be applied to simulate the weight of the upper half of the surface cell.

4.3.3 Caisson test with weather data

For this test a caisson simulation was run within SHETRAN using weather data supplied by the Met office (British Atmospheric Data Centre, 2008) which was obtained from a weather station near Larkhill. This weather data was hourly and typical of the weather data to be used for subsequent simulations. The precipitation data and temperature data are shown within Figures 4.24 and 4.25.

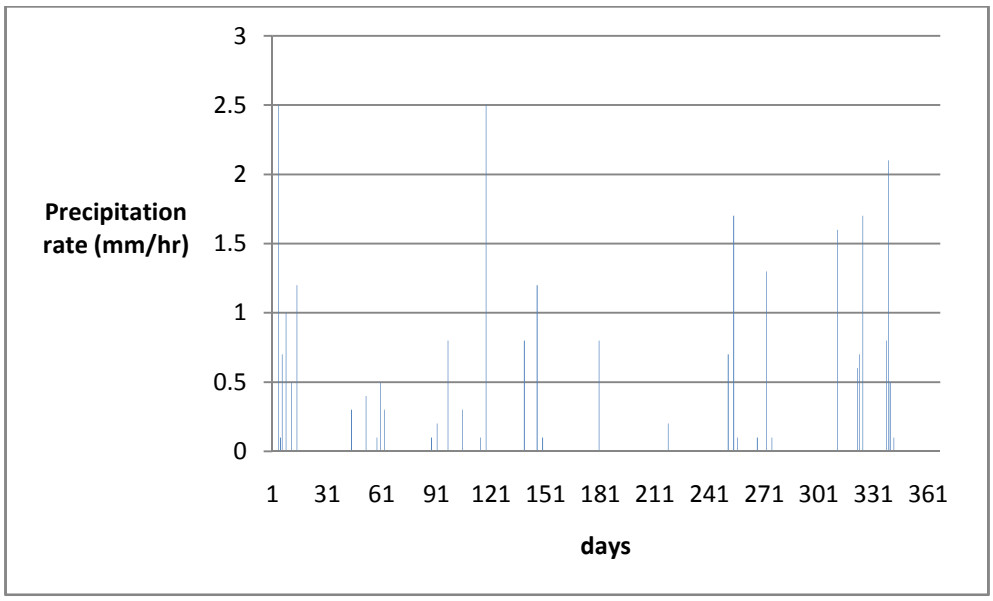

Figure 4.24 Precipitation data from Larkhill (2000).

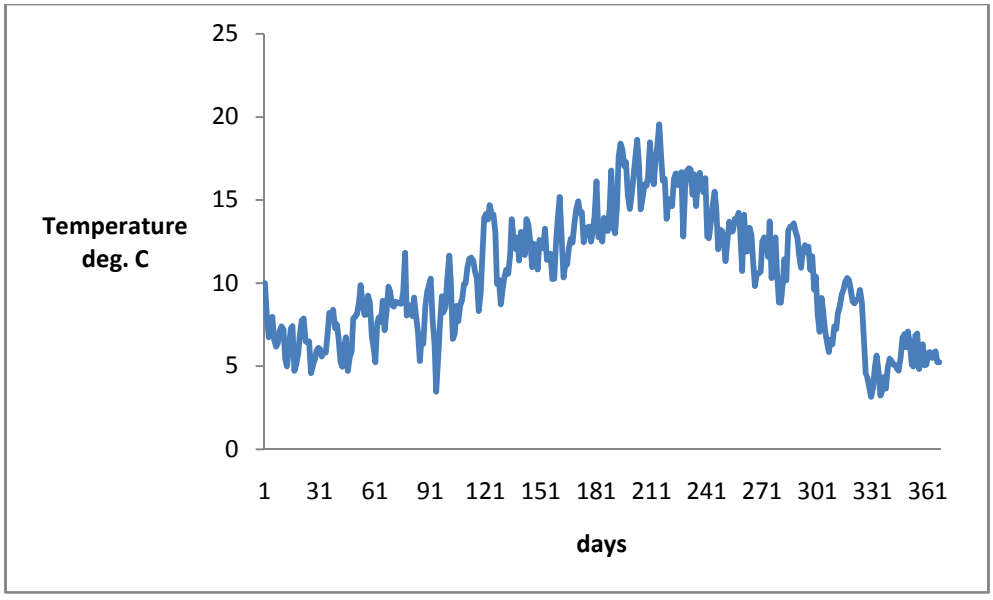

Figure 4.25 Temperature data from Larkhill (2000).

These figures show that there will be a high precipitation rate at the beginning of the simulation combined with low temperatures. This will lead to a high infiltration and low evaporation rate. During the summer months the precipitation eases and temperature increases. For this section of the simulation evaporation form the surface would be expected to exceed infiltration. Towards the end of the simulation, precipitation once again increases combined with a drop in temperature indicating infiltration will once again be dominant.

The simulation was run with the same initial conditions as the previous simulations. The surface was assumed to be bare ground and therefore no vegetation data was used.

Evaporation was, however, modelled within the simulation. The surface pore pressures were entered into a text file using CYGWIN and this file transferred to the Flac-tp model folder. The Flac-tp grid can be seen in Figure 4.26.

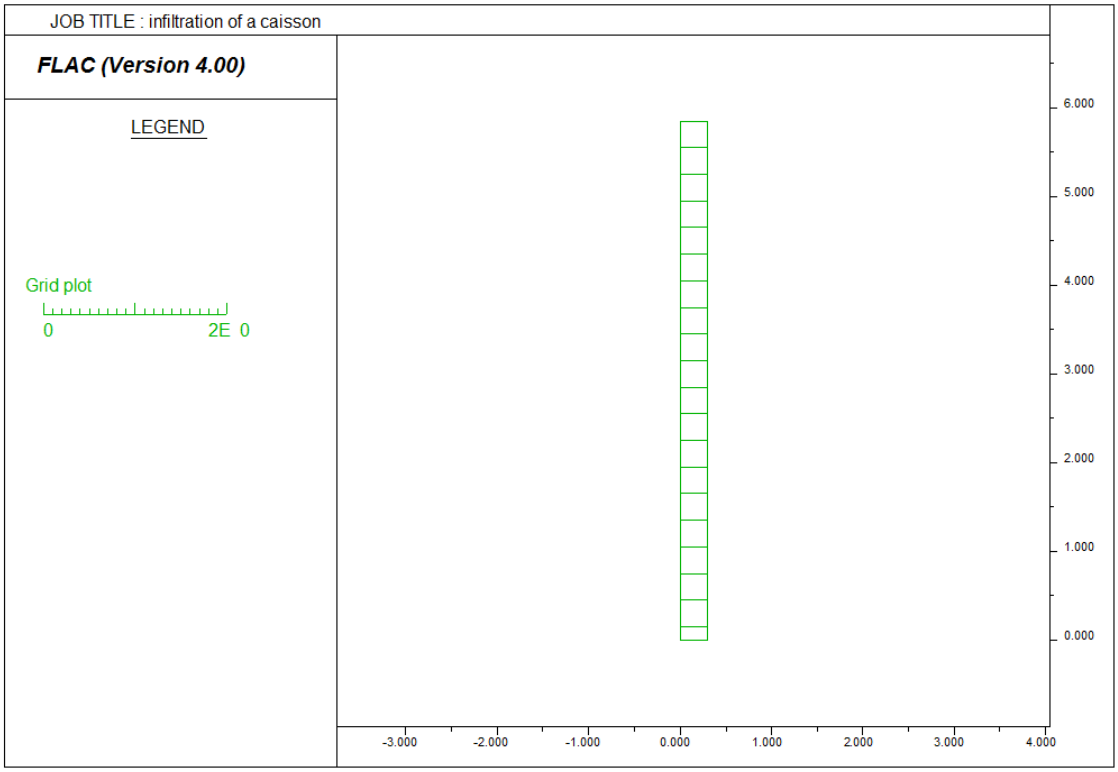

Figure 4.26 Flac-tp grid used for caisson comparison.

When applying a new pore pressure to the grid the saturation for that pore pressure also needs to be set. Fish code was therefore written to recalculate saturations within the grid each time a new pore pressure was applied to the surface. Figure 4.27 shows the variations in pore pressure for the caisson for the simulation. The pore pressures for this plot have been taken from the grid point at the base of the third and fifteenth cell from the surface within Flac-tp model and the centre of the fourth and sixteenth cell from the base within the SHETRAN model. These pore pressure readings are, therefore, from identical heights (1.05m depth and 4.25m depth respectively) within each caisson model. It can be seen from this comparison that there was excellent comparison between the two models. There was a large increase in pore pressure near the top of the model but minimal change near the base of the model. The SHETRAN model showed that the large infiltration rate at the beginning of the simulation, lead to a large increase in pore pressure at the top of the caisson. During the summer months evaporation from the surface took place and the pore pressure decreased but not to the levels seen at the beginning of the simulation. At the end of the simulation precipitation

increase lead to an infiltration increase and therefore an increase in pore pressure. The large pore pressure variation at the top of the model was captured well within the Flac-tp model both in terms of response and magnitude. The variation in pore pressures calculated by Flac-tp from the applied SHETRAN surface pore pressure compares very well with the SHETRAN pore pressure variation. The smaller pore pressure variation shows some divergence between the models but this is minimal. There was now confidence that the surface pore pressures from SHETRAN could be transferred to Flac-tp with a minimal loss of accuracy in the calculation of pore pressure variation at depth.

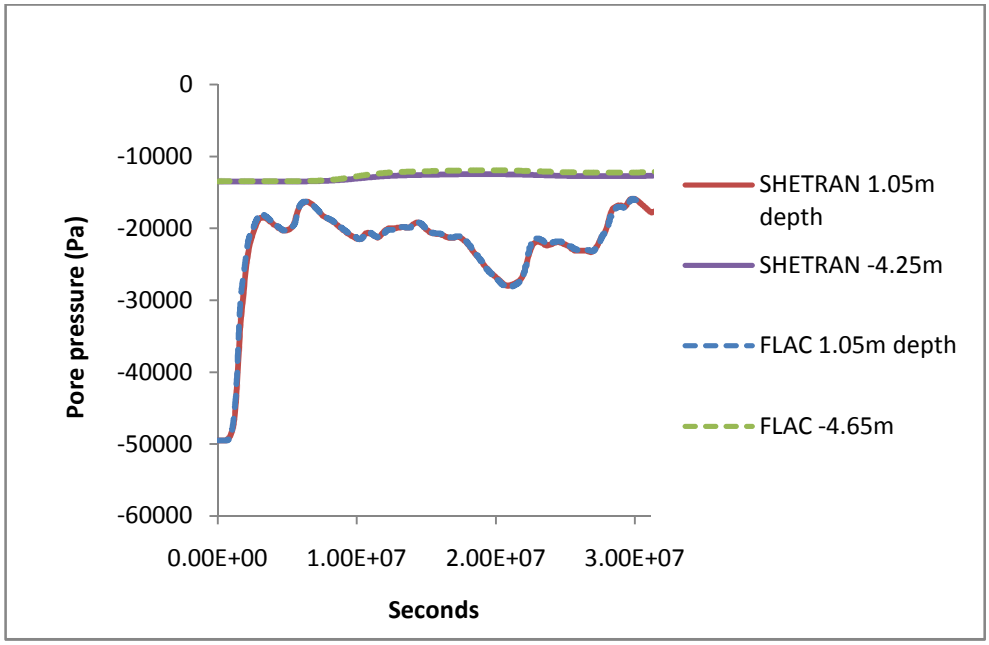

Figure 4.27 Pore pressure variation at 1.05 and 4.25 m depth for SHETRAN caisson with Larkhill weather data and Flac-tp caisson with surface pore pressures transferred from SHETRAN model.

4.3.4 Embankment test

The last simulation showed that surface pore pressures can be transferred from SHETRAN to Flac-tp for the case of a one dimensional caisson. This section assesses the accuracy of such a method for a two dimensional embankment model. The embankment modelled was the conceptual embankment designed for use within the BIONICS project (Hughes et al, 2009). The embankment was 6m high with a slope length of 12m. The crest length was 6m. The hydrological properties of the material for this simulation are detailed within Table 4.2.

Table 4.2 Embankment test Flac-tp soil properties.

Saturated mobility coefficient	2.04×10^{-10} m²/(Pa-s) (Equivalent to 2e-6 m/s)
Porosity	0.5
Residual saturation	0.15
P_0	9.810×10^4 Pa
a	0.16667
b	0.5
c	0.5

The initial conditions for the simulation were set as hydrostatic throughout the grid with -80 kPa surface pore water pressure at the top of the crest. The climate data used for the simulation was the Larkhill weather data, the same as that used for the previous caisson simulation.

Within the SHETRAN grid each cell is 0.5m high and 1 m long. The grid is shown in Figure 4.28. The cells for which the surface pore pressure is to be transferred are highlighted.

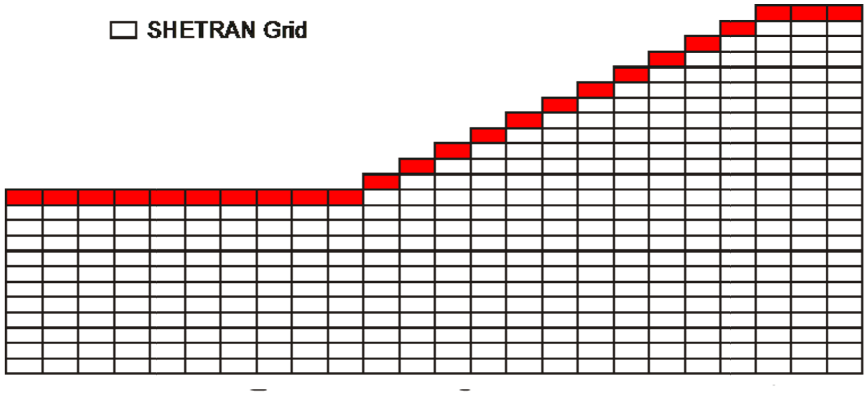

Figure 4.28 The SHETRAN grid.

The Flac-tp grid had the same external boundary dimensions as the SHETRAN grid but with the top half of the SHETRAN surface cell (0.25m) removed as per the caisson simulations. The pore pressure was transferred from the centre of the highlighted SHETRAN cell to the grid point of the Flac-tp grid shown in Figure 4.29.

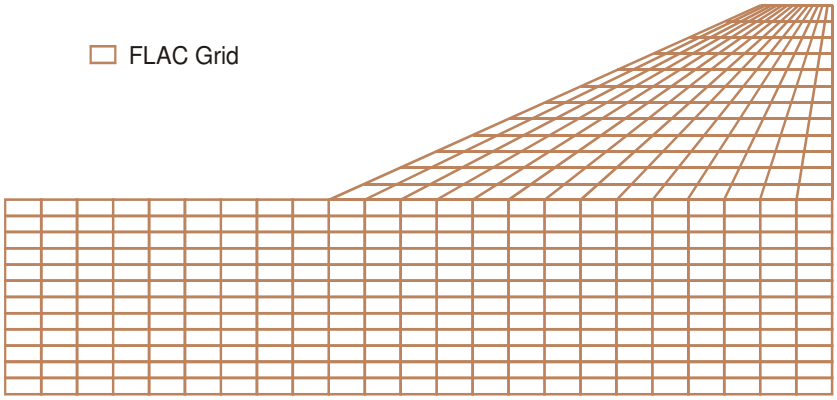

Figure 4.29 The Flac-tp grid.

4.3.5 Embankment with bare soil slopes

The first embankment simulation was run for an embankment with slopes of bare soil. There is therefore no evapotranspiration from vegetation and, therefore, no water extraction from roots. Time series plots of the variations in pore pressure were plotted for the two models at three points within the embankment model. These plots are shown in Figures 4.30, 4.31 and 4.32.

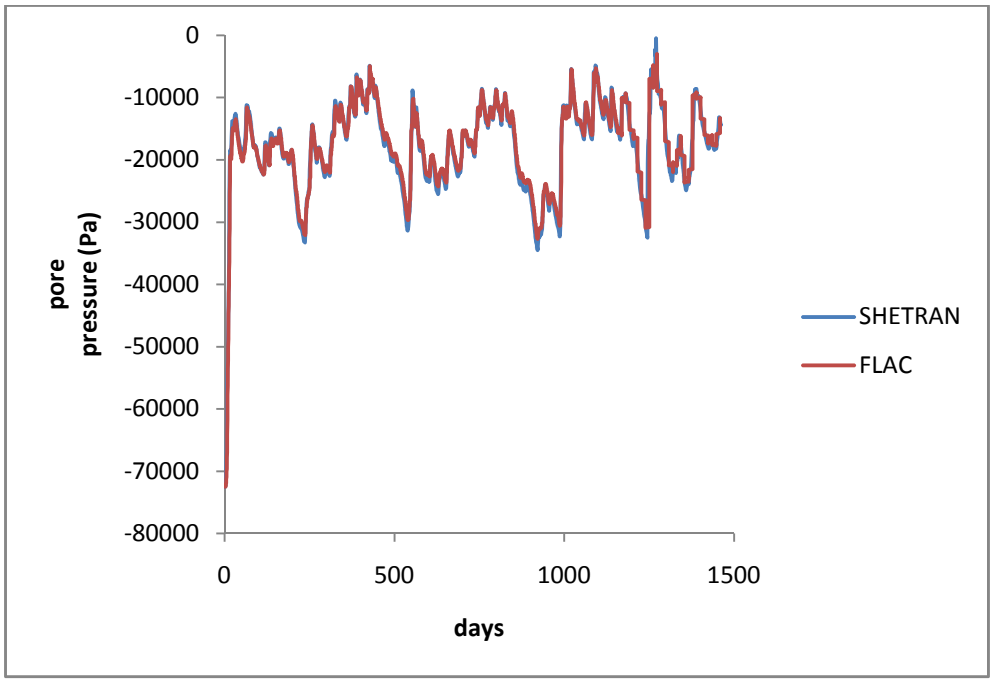

Figure 4.30 Pore pressure time series comparison for SHETRAN and Flac-tp model 5.25m above foundation and 0.5m from centreline.

The pore pressure variation calculated by Flac-tp at the top of the embankment just below the crest compares very well with the SHETRAN pore pressure variation. It can be seen that there has been no loss of accuracy at this position. However, the

calculation for this position has only covered 0.5 m depth within the Flac-tp calculation so there has not been much been much room in which errors can occur.

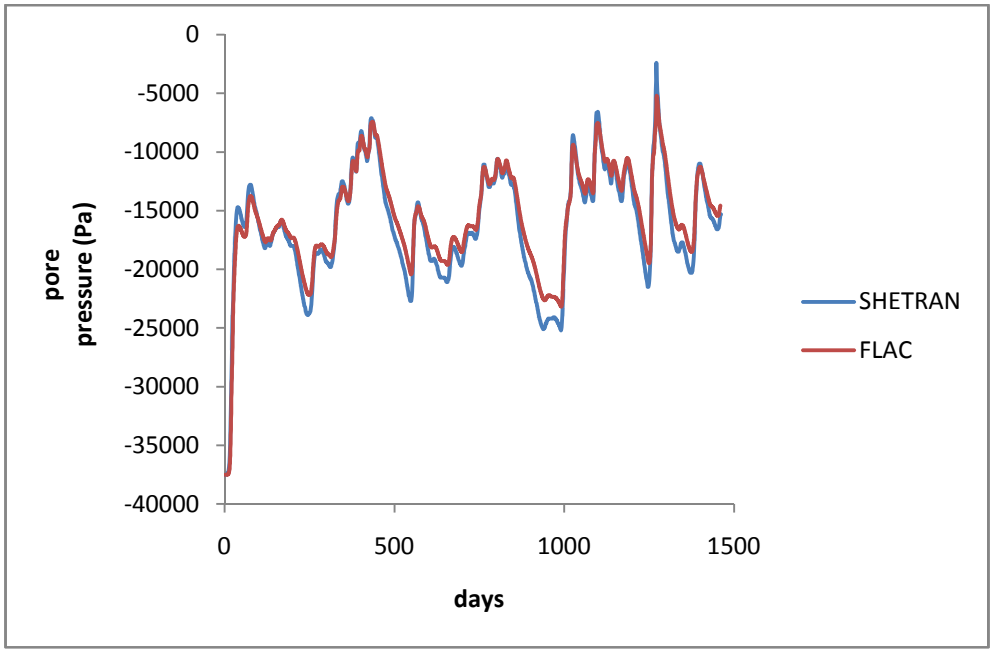

Figure 4.31 Pore pressure time series comparison for SHETRAN and Flac-tp model 1.75m above foundation and 7.5m from centreline.

The pore pressure comparison for the position within the slope is also excellent but there is lightly less comparison during the drainage of the model. SHETRAN has tended to drain faster and achieved lower pore pressures than the Flac-tp model. The Flac-tp model does, however, model the maximum pore pressures very well.

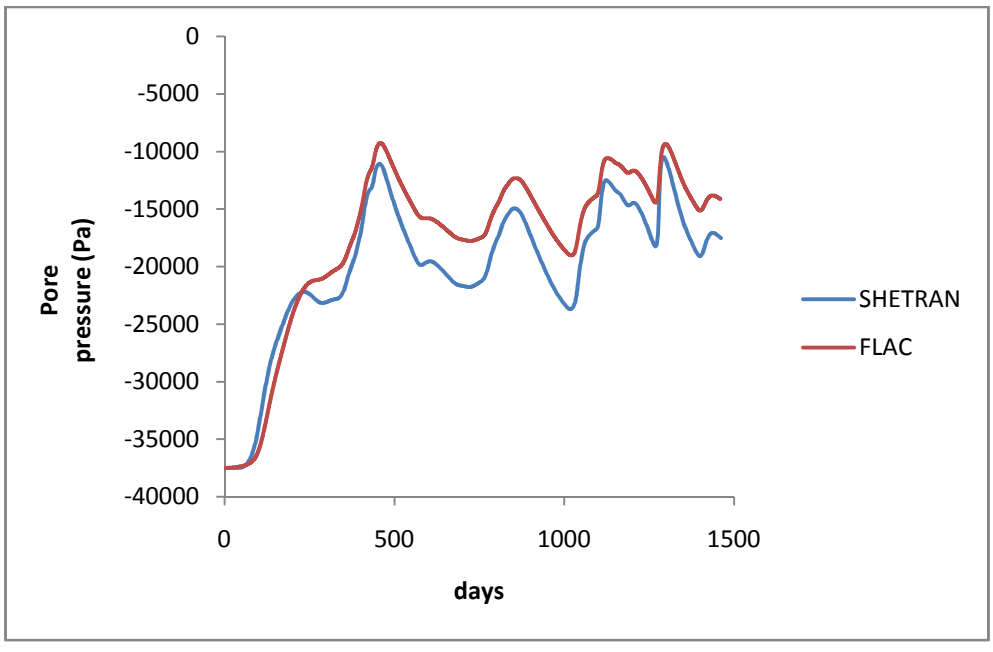

Figure 4.32 Pore pressure time series comparison for SHETRAN and Flac-tp model 1.75m above foundation and 1.5m from centreline.

The comparison between the two models for the position 1.75m above the foundation and 1.5 from the centreline (4 m below the crest) shows the worst comparison of the simulation. The error of the comparison, however, remains below the equivalent of 0.5 m of head consistently with the average error being less than 0.25 m of head. Flac-tp consistently over estimates the pore pressure at this position.

4.3.6 Embankment test with grass slopes

For this simulation the same slope and weather data were used but a grass canopy across the entire surface was simulated within the SHETRAN simulation. The grass canopy was assumed to have a rooting depth of 0.3m. The roots were therefore fully encompassed within the surface cell. The pore pressures within the surface cell were therefore calculated as a result of all infiltration and evapotranspiration processes. These pore pressures were transferred to the Flac-tp grid following the same processes detailed earlier and the pore pressures of both models compared. From Figures 4.33, 4.34 and 4.35 it can be seen that the comparison between the two models was still excellent. The presence of the grass canopy reduced the pore pressures during the summer months. There was also a reduction of the overall pore pressures within the centre of the embankment. This reduction in pore pressures was as a result of the increased evapotranspiration from the model. The figures show that transferring the pore pressures from the SHETRAN model where vegetation is present was still valid. Transferring the surface pore pressures from SHETRAN to Flac-tp had enabled Flac-tp to calculate pore pressure variations at depth for a slope to an accuracy comparable to an established hydrological model.

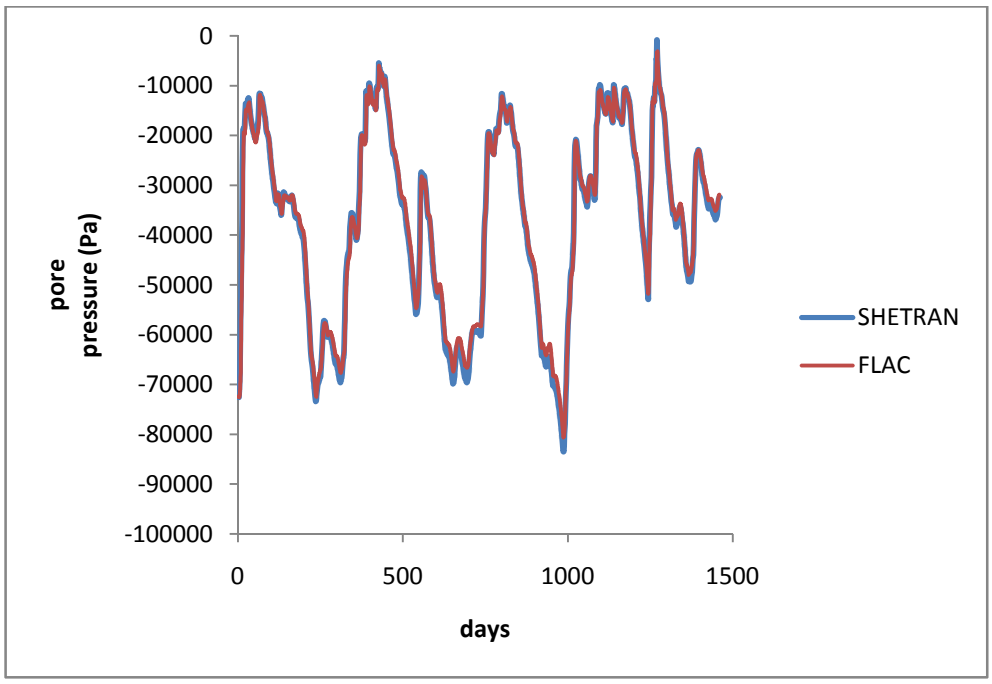

Figure 4.33 Pore pressure time series comparison for SHETRAN with a grass covered slope and Flac-tp model 5.25m above foundation and 0.5m from centreline.

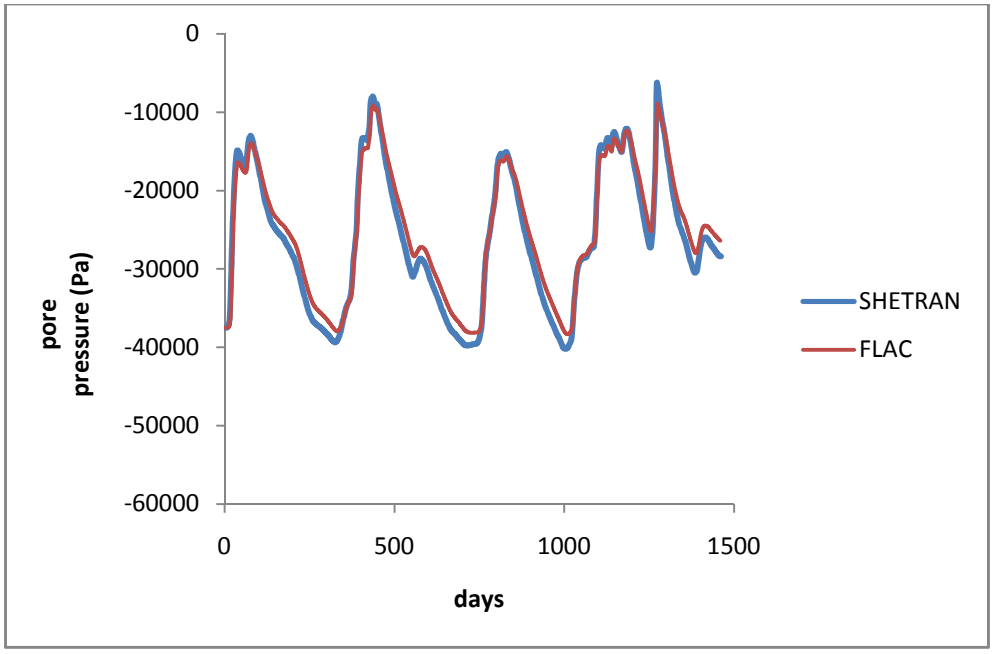

Figure 4.34 Pore pressure time series comparison for SHETRAN with a grass covered slope and Flac-tp model 1.75m above foundation and 7.5m from centreline.

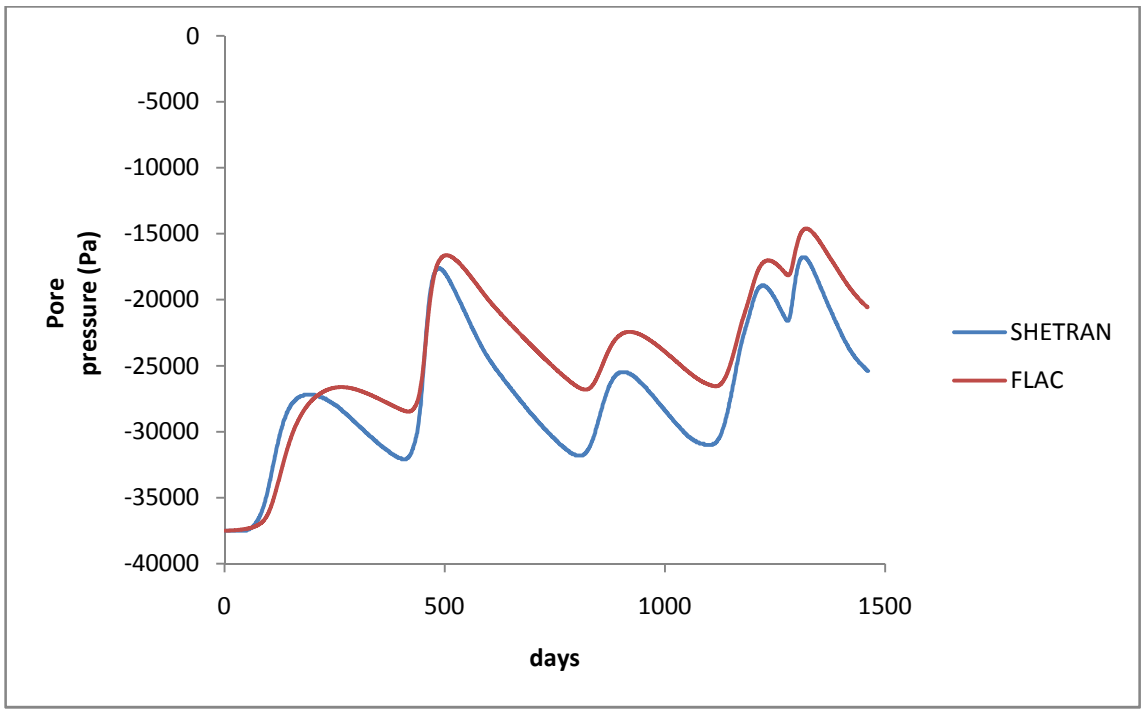

Figure 4.35 Pore pressure time series comparison for SHETRAN with a grass covered slope and Flac-tp model 1.75m above foundation and 1.5m from centreline.

4.3.7 Coupled simulation of embankment with grass

The previous simulations were concerned with the comparisons of pore pressures within the embankment for SHETRAN and the hydrological component of Flac-tp. The advantage of using Flac-tp, however, was within its capability to model the mechanical deformations associated with the pore pressure and therefore effective stress changes. Deformations of the media have the potential to cause significant pore pressure changes. This section will allow the mechanical deformation of the media. The aim was to prove that the mechanical deformations experienced at the surface due to the changing pore pressure would not significantly alter the pore pressures at depth. For this the same hydrological simulation was run as within Section 4.3.6. A simple Mohr-Coulomb constitutive model was used, the mechanical properties for which are shown in Table 4.3. These elastic properties are representative of the average stiffness of a London clay and the plastic properties are those of in-situ London clay.

Table 4.3 Mohr Coulomb properties for mechanical simulation.

Property	Value
Density	18.8 KN/m^3
Bulk modulus	4e6 Pa
Shear modulus	3e6 Pa
Cohesion	7000 Pa
Friction angle	21 degrees

The following plots (Figures 4.36, 4.37 and 4.38) show the pore pressure variations for the model with and without the mechanical component of the calculation enabled.

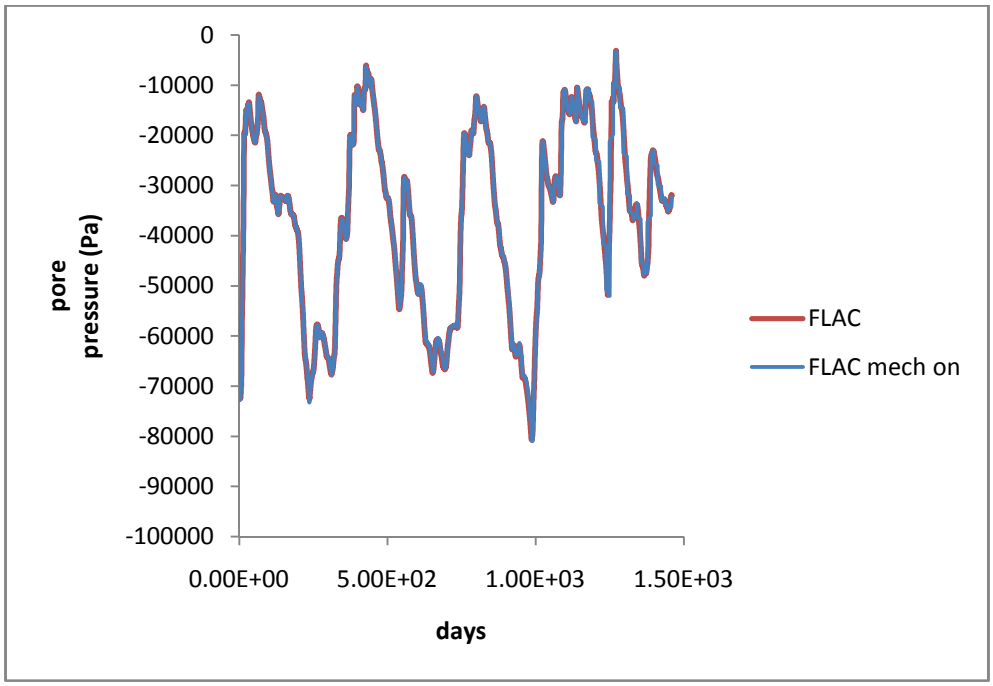

Figure 4.36 Pore pressure comparison for Flac-tp 5.25m above foundation and 0.5m from centreline with mechanical component disabled and enabled (mechanical enabled).

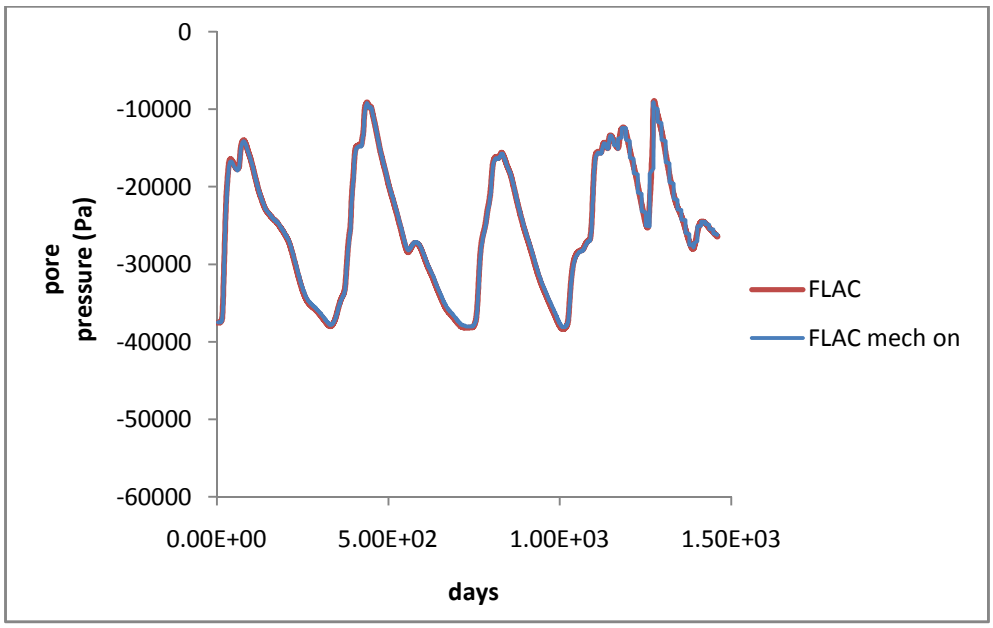

Figure 4.37 Pore pressure comparison for Flac-tp 1.75m above foundation and 7.5m from centreline with mechanical component disabled and enabled (mechanical enabled).

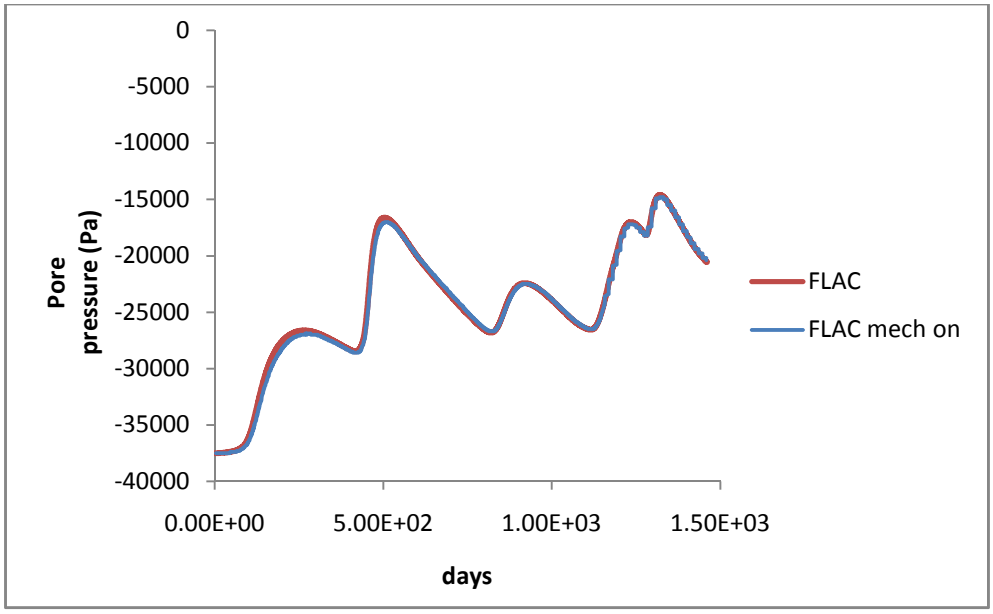

Figure 4.38 Pore pressure comparison for Flac-tp 1.75m above foundation and 1.5m from centreline with mechanical component disabled and enabled (mechanical enabled).

These plots show there has been no significant effect on the pore pressures due to the mechanical component turned on. As there has been no pore pressure variation due to the mechanical component turned on then the pore pressures predicted by SHETRAN can be assumed to be valid for the deforming embankment.

The embankment was stable throughout the simulation, however, with only elastic deformations modelled. The deformations can be seen within the following plots, Figure 4.39 and 4.40.

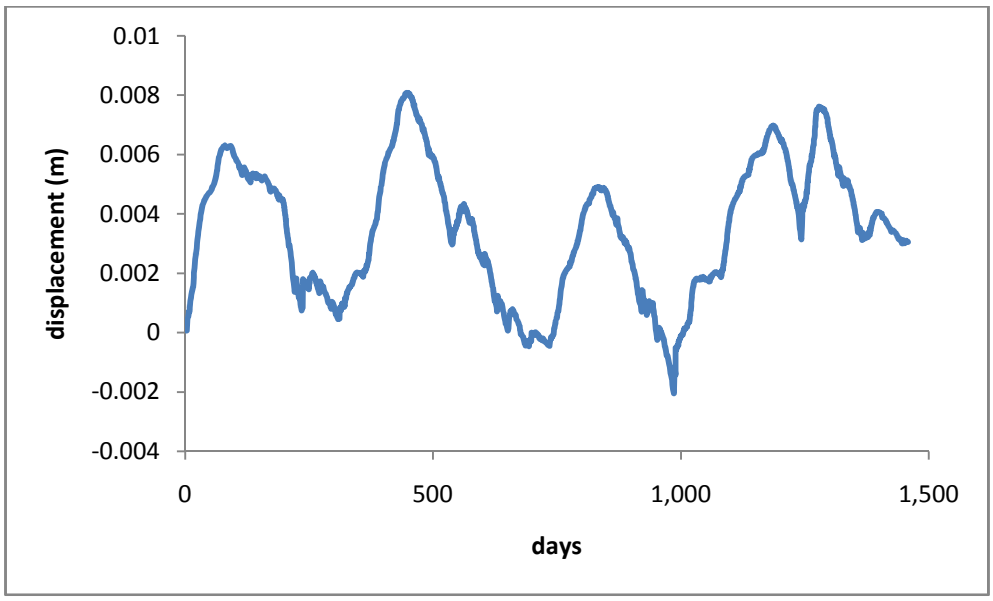

Figure 4.39 Vertical displacement time series calculated by Flac-tp 5.25m above foundation and 0.5m from centreline.

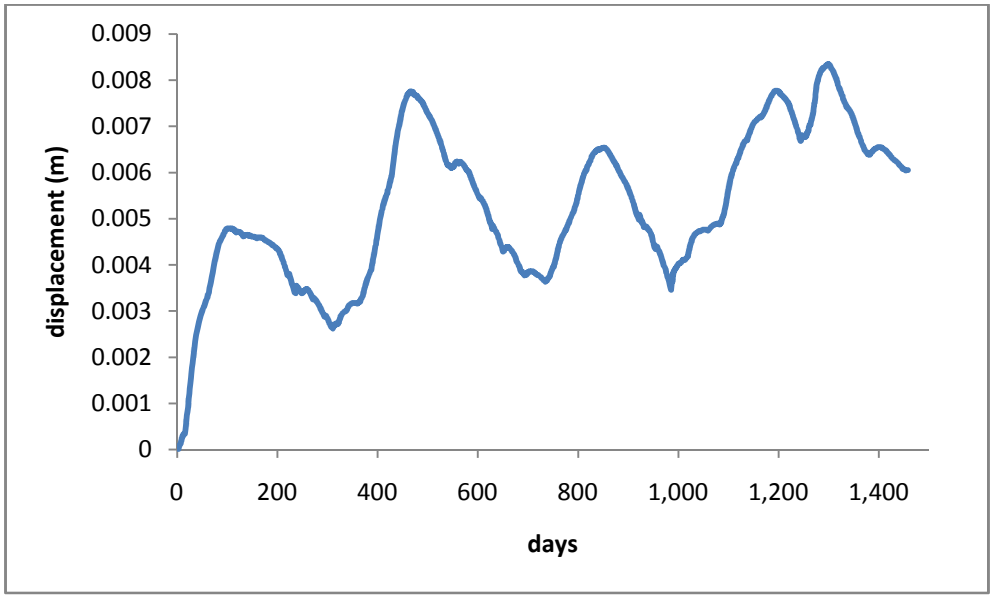

Figure 4.40 Horizontal displacement time series calculated by Flac-tp 1.75m above foundation and 7.5m from centreline.

The figures show significant movement within the embankment. There was shown to be seasonal vertical movement up to 8mm near the crest. The horizontal movement plot shows a net down slope movement of around 5mm and a seasonal variation up to 4mm. The displacement plots when seen in conjunction with the plots of pore pressure at the same locations show the displacements variations are closely related to the pore pressure variations. The pore pressure variations were, in turn dependent upon the soil hydrological properties and meteorological conditions. The SHETRAN and Flac-tp model combination was therefore able to calculate deformation as direct response to

climate. The model therefore highlighted the close relationship between climate and deformation.

4.4 Discussion and conclusions

This chapter compared the relatively new Flac-tp model against an established hydrological model SHETRAN. The SHETRAN model simulates the flow of water using the Richard's equation. SHETRAN therefore assumes that the media is of constant volume and that the air pressure remains zero throughout. These assumptions are used by many established hydrological models (HYDRUS, VADOSE etc.) and are therefore considered appropriate for modelling the flow of water through a partially saturated media. Flac-tp can model both the flow of air and water within a compressible porous media. The caisson comparison study presented above was therefore conducted to establish the effects of modelling the flow of both air and water within a confined porous media. Several assumptions concerning the properties of the air phase were postulated and the results compared to the SHETRAN model.

Where the Flac-tp model assumed zero air pressure throughout the model (Richard's equivalent) the Flac-tp model and the SHETRAN model showed good comparison. When pore air pressures were allowed to develop within the model the Flac-tp pore pressures differed from those of the SHETRAN model. The study showed that the air phase became trapped within the model and interfered with the flow of water. This generated a higher combined capillary pressure. The combined pressure did not affect the rate of progression of the wetting front but could significantly affect the rate at which drainage occurred out of the caisson. Varying the viscosity ratio between air and water enabled the air to move faster but the air was still trapped within the soil. Lowering the bulk modulus of the air allowed the compression of the air phase but again the air was trapped in the soil.

Whilst trapped air may be true of a closed system such as an aquifer it is not something that is observed at the surface. At the surface, it can be assumed that the air can freely escape the soil and enter the atmosphere. For a rough surface it may be assumed that there is a continuous air phase to the surface and therefore no generation of pore air pressures, as described by the Richards equation. Should the air become trapped by an advancing wetting front and excessive pore air pressures generated it can be assumed

that the air may bubble through the water to the surface and hence hinder water flow. For a large scale slope it is considered unlikely that such a wetting front will develop and restrict air flow to the surface. It can therefore be assumed that no air pressures develop within the Flac-tp simulation.

When air pressure generation is restricted the comparisons of pore pressure variation show promising results. The slight divergence between the two models was due to the different equations used to calculate unsaturated flow and differences within the calculation procedure. SHETRAN uses a single phase assumption in the form of a modified Richard's equation whilst Flac-tp models the flow of two liquids within the porous media. Both models, however, are deemed to give reasonable estimations of unsaturated flow and it is not within the scope of this thesis to analyse the small differences between the two models. The interest of this thesis lies within the ability of SHETRAN to model the surface boundary condition. Once the surface condition has been modelled to a reasonable degree of accuracy then this boundary can be applied to a variety of unsaturated numerical models in order to analyse the effects. The reason we need to model the entire embankment within SHETRAN is that the amount of water that can be drawn from the soil is determined by the rate at which water can be transported to the surface which in turn is controlled by the unsaturated permeability of the underlying soil. The entire embankment is therefore modelled to obtain an estimation of the surface pore pressures. Once these pore pressures have been obtained and applied to the Flac-tp model then there is confidence that Flac-tp is able to model the subsequent flow to a reasonable degree of accuracy.

Running fully coupled simulations with transferred pore pressures yields the same pore pressure response within the embankment as the flow only simulation. This has been proven for a stable embankment. The pore pressure response may change significantly for a failing embankment. The transfer modelling will therefore only be capable of modelling the embankment up to the point of a catastrophic failure. The actual failure will not be able to be modelled. This will be due to the pore pressures generated by Flac-tp during the failure affecting the permeability at the level of the failure. This permeability phenomena will affect the flow of water within the embankment and hence has the potential to affect the rate of infiltration and internal flow. The pore pressures generated by Flac-tp cannot be fed back into the SHETRAN program. The surface pore pressures generated by SHETRAN will therefore not be able to account for the

mechanically generated pore pressures. To account for this error a failing embankment will need to be closely monitored to identify any pore pressure generation. The simulation will then need to be stopped at the point significant pore pressures are seen to have developed. The model will be accurate up to this point and as it can be seen the embankment has failed this will not present any problems in identifying the embankment lifespan and failure mechanism.

Although the air within the Flac-tp simulation has been largely ignored the errors present shown in Figures 4.1 and 4.2 are deemed to be within tolerable ranges. The modelling of seasonal pore pressure variations relies on many simplified assumptions and many parameters which may or may not be available for a given simulation. There are therefore inherent errors within the calculations. The calculations performed by SHETRAN are used by many established models. To try to attain a greater accuracy between the two models used would therefore not necessarily give a greater accuracy with the field situation. A small error between the simulations can therefore be permitted. The errors between the simulations have been shown to be minimal. The greatest error being around 17% of the pore pressure range and averaging at 8% of the pore pressure variation.

Chapter 5. Effects of a changing climate on slope stability

5.1 Introduction

Within the previous chapter it was shown that the SHETRAN surface pore water pressure boundary can be successfully transferred to a Flac-tp model boundary with minimal loss of accuracy during the transfer. This transfer method could now be used to model the effect of a changing pore water pressures on the stability of embankments and cuttings. The aim of this chapter is to determine the effects of a future climate scenario on an infrastructure embankment and also a cutting. The second aim is to validate the hydrological model against a fully instrumented cutting, identifying key parameters to obtaining good comparison between simulated and recorded pore pressures.

In order to simulate pore pressures within the slope the model needs climatic data. Climatic data for a future and present day climate scenario has therefore been generated using the Environment Agency Rainfall and Weather Impacts Generator, EARWIG. The first section of this chapter will look at how EARWIG generates the climatic data, how this may be used to analyse the effects of climate on slope stability and the validity of using such an approach. The major differences between projected future climate scenarios and present day scenarios are also discussed. There will then be two more sections where the climate scenarios were applied to infrastructure slopes.

Firstly, a diagnostic case study is presented where a borderline stable steep sided embankment has been modelled for both the present and future climate scenario with a strain softening material. The rates of strain softening for the two scenarios and modes of failure are then discussed.

Secondly, a case study verification exercise is presented whereby a cutting, which has been extensively monitored by Smethurst et al (2006), is modelled within the SHETRAN software. The cutting was monitored to distinguish soil water content, pore water pressure, soil temperature, free water surface, rainfall and runoff. There is, therefore, no deformation data available and also no geotechnical soils data. A

hydrological simulation was run to verify the SHETRAN model and then fully coupled simulations were run using mechanical soils data from the literature and deformations predicted. A study was also performed on the relevance of some more complex constitutive models based on the Mohr-Coulomb criteria. The fully coupled simulations were then run for both the present and future climate scenarios.

The chapter concludes with a discussion on the relevance of the results produced and accuracy of the developed model. Areas where the model performed well are discussed as well as areas in which there is room for improvement. For the areas where improvement has been identified possible strategies and impacts on model results have been discussed.

A summary of the findings of this chapter can be found within Davies et al (2008b and 2008c) and Rouainia et al (2009).

5.2 Weather scenarios

5.2.1 *Introduction*

As stated previously weather data is needed to assess the impact of a future climate on the stability of slopes using the SHETRAN Flac-tp modelling procedure. The climate data used for this study was generated by EARWIG. This section briefly describes how EARWIG generated the weather data and presents the data used for present day and future climatic scenario slope stability assessments.

5.2.2 *Climate models*

Small scale weather data is generated by downscaling the atmospheric processes calculated by larger scale climate models. The global climate is modelled using a General Circulation Model, GCM. These models are becoming increasingly complex and model all the important physical processes in the atmosphere and/or oceans globally. GCM models are validated by comparison to recorded weather data. Typically the 1961-1990 period is taken as a climatological normal for rainfall (Kilsby et al, 2007). These models are used for understanding the climate and future climate projections (DEFRA, 2011). Due to the complexity and global nature of the models a coarse grid size of around 300km is required. Local climate is heavily influenced by regional topographical features which cannot be modelled within a GCM. These

models, therefore, cannot model smaller scale climate variability and extreme events and hence a higher resolution model is required. For reduced scale climate modelling Regional Climate Models, RCM's are used which downscale the GCM output. These models are computationally intensive and so are run over smaller areas, typically between 25-50km grid sizes. The RCM models are nested within a global model using the GCM grid variables as boundary conditions. Weather generators, WG, use the RCM model outputs and regional weather observations to downscale the weather variables further to grid sizes in the range of 5km. It is the weather generator EARWIG which was used to generate the weather variables for the simulations within this chapter.

5.2.3 *EARWIG*

EARWIG generates daily data for rainfall, temperature (max, mean and average), vapour pressure, relative humidity, wind speed and sunshine hours. EARWIG future climate scenarios are based upon the UKCIP02 scenarios which, in turn, were derived from the UK Meteorological Office Hadley Centre RCM HadRM3H model integrations (Hulme et al, 2002). The GCM used for the future climate projection was HadAM3H.

The UKCIP02 developed four scenarios over three time slices. The four scenarios were based on assumed projected CO_2 output ranging from low, drastically reduced carbon emissions, to high, continued, economic growth with associated uncontrolled carbon emissions. The three time slices each represent 30 year periods between the years 2011 and 2100 and are known as the 2020's, 2050's and the 2080's. Transient simulations have been run within the GCM HadAM3H, which estimated the average global temperature rise at the time of CO_2 doubling (representing the medium high 2080's scenario (estimating a 1% rise in CO_2 per year)). The simulations for the intervening time slices and emission scenarios were simply scaled from this simulation. The scaling factors used by UKCIP02 are presented within Table 5.1 below.

Table 5.1 Multiplying factors for conversion from 2080's Medium-High scenario to other scenarios and time slices (from Kilsby et al, 2007)

Time slice	Low emissions	Medium-Low emissions	Medium-High emissions	High emissions
2020's	0.24	0.27	0.27	0.29
2050's	0.43	0.50	0.57	0.68
2080's	0.61	0.71	1.00	1.18

EARWIG is capable of generating weather variables for either a nest of, or single, 5km grid locations. Local weather data is required to firstly develop a stochastic model for rainfall and secondly to develop regressional relationships between wet days and the remaining climate variables. The control, baseline, data is therefore generated using observational relationships between wet days and temperature range, sunshine hours etc. This method is also applied to the future climate generation. The stochastic model is re-fitted to the future rainfall using factored rainfall statistics (Kilsby et al, 2007). The remaining future weather variables are then generated by using the same regression techniques but factoring the variables for the future scenario. The scaling factors used for the weather variables were developed by comparison between RCM models of the present day control scenario and the future scenario. The actual RCM output is therefore not used for the generation. It is worth noting, however, that RCM's indicate that the only remaining weather variable that will substantially change for the projected future climate scenarios will be the mean temperature. Sunshine hours will be dictated by rainfall whilst temperature range, vapour pressure and wind speed are indicated to remain largely unchanged for a future climate scenario (Kilsby et al, 2007). The following summarises the weather generation approach:

1. Local climate data is compiled over the control period
2. Factors of change are developed by comparison of the present climate and future scenario RCM projections
3. A stochastic model of daily rainfall is fitted to the local observed rainfall
4. The stochastic model is re-fitted for future climates using future rainfall statistics factored by using the comparisons derived in Step 2
5. The weather generator then generates the remaining weather variables using regression relations between daily climate variables and rainfall data for the control period and scaled variable for the future climate

5.2.4 *Weather data*

For the purposes of the slope stability simulations, two 20 year climate outputs were generated both representing the weather for a 5km grid at the Newbury area. This area has been chosen as the slopes to be modelled are built using a material common to this area, London clay. This is also the area containing the Newbury cutting which is used for the hydrological verification exercise. The first climate output represented a present day climate and the second represented a high emission 2080 scenario.

During the period of this research UKCIP02 climate projections were superseded by UKCP09 projections. Whereas UKCIP02 projections were based on one climate projection (the medium high projection), the UKCP09 projections were created by an ensemble of model variants (DEFRA, 2011). As a number of scenarios were run with various settings for key parameters for the UKCP09 simulations users can select their scenario based on its probability of occurrence (Kilsby et al, 2007). The UKCIP02 scenario (medium high emission 2080's) temperature increase corresponds to 56% probability within UKCP09 (DEFRA, 2011). This means that there is a probability of 56% that the change in temperature for this scenario will not exceed the UKCIP02 scenario predictions. The UKCP09 predictions also show that the UKCIP02 temperature change predictions were lower than those predicted by UKCP09 (DEFRA, 2011) which leads to the UKCIP02 predictions being more closely comparable to the Medium CO_2 UKCP09 projections. To put the climate scenarios used for this study into context with current climate change projections the monthly average weather variables generated by EARWIG were compared to the 2080 medium emission UKCP09 projections. One hundred control and future climate UKCP09 simulations were run. The weather variables for each month of the 20 year EARWIG simulations were averaged and the weather variables for the 100 UKCP09 simulations were also averaged. The comparisons can be seen below.

The average monthly rainfall generated for the present climate (pc) and future climate (fc) EARWIG simulations is presented within Figure 5.1 with the average monthly rainfall for the UKCP09 simulations. It can be seen from these simulations that the future climate predictions show that on average there will be more rainfall during the winter months and less during the summer months. EARWIG and UKCP09 predictions for the present climate are comparable as expected with only some minor variations

between the two averages. The future climate predictions show, however, that the EARWIG scenario predicts less rainfall during the summer months and slightly more rainfall during the winter months than the UKCP09 scenarios.

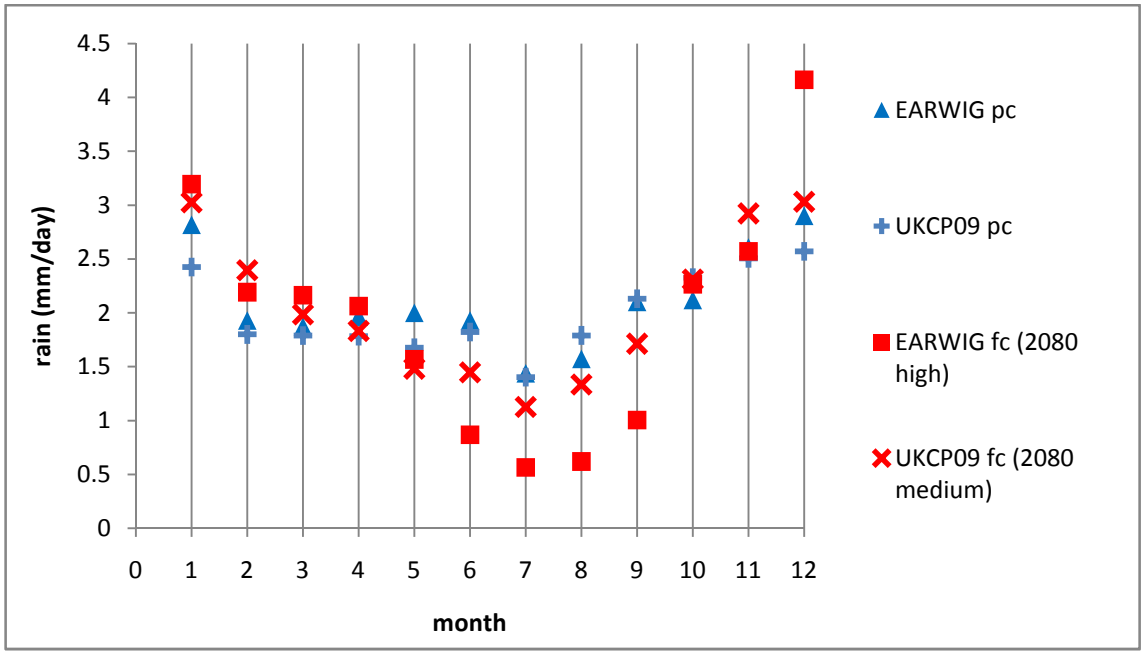

Figure 5.1 Average monthly rainfall data for the 20 year EARWIG simulations and 100, 30 year UKCP09 simulations.

Due to the probabilistic nature of the UKCP09 the averages presented here represent the central estimate of 50% probability. The monthly average rainfall over 30 years is plotted for each of the 100 future scenario simulations in Figure 5.2. It can be seen from this plot that some simulations predict extreme averages of winter rainfall of between 5 and 6 mm per day, far exceeding the averages predicted by the EARWIG simulation. Rainfall during the summer months, however, shows that the EARWIG simulation is more comparable to the extremes predicted from the UKCP09 scenarios.

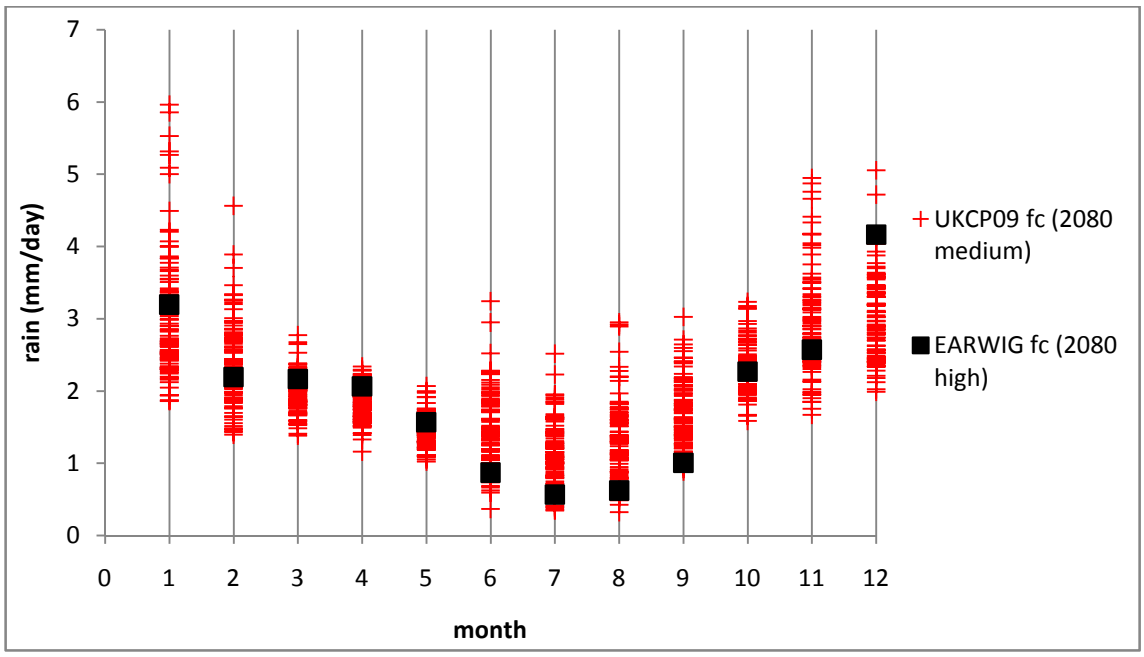

Figure 5.2 Average monthly rainfall (30yrs) for all the UKCP09 2080'S medium emission scenarios (100 in total) and the average monthly rainfall (20 yrs) for the high emission EARWIG scenario.

More rainfall during the winter months and less during the summer months will lead to drier summer months which may, in turn, lead to drier slopes. Suctions may then penetrate deeper within the slope during this period. Within the modelling framework, this would lead to an increase in strength of the material and, therefore, increased stability. EARWIG generates rainfall which is consistent with observed rainfall statistics. The generation of wet and dry periods for the present day scenario is randomly generated by EARWIG but the period and intensity of these periods is statistically comparable to observed data. The wet and dry periods within a future climate scenario have been scaled with respect to the RCM outputs. The frequency, period and intensity of these wet periods will have a profound effect on slope deformation and stability. Prolonged wet periods will increase swelling magnitude and reduce the shear strength of a slope, whilst prolonged dry periods will increase shrink magnitude. Figure 5.3 and 5.4 below show the variation of average monthly rainfall rate for the present day and future scenario climate datasets respectively.

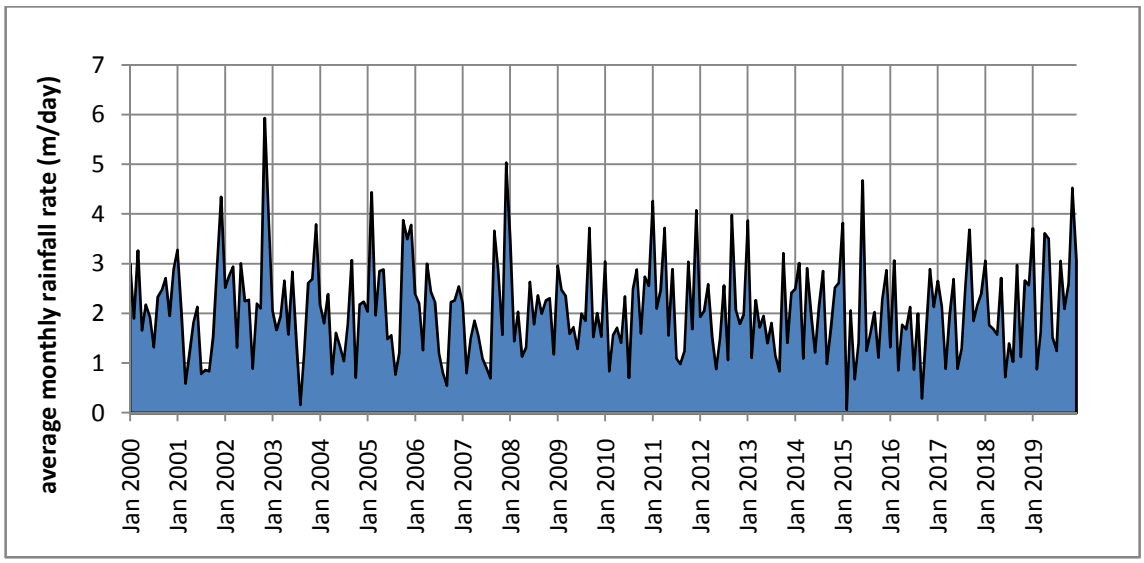

Figure 5.3 Monthly rainfall for present day EARWIG scenario

For the majority of the simulation peak rainfall occurs within the winter months. The average monthly rainfall for the entire period was 2.00mm/day. Extreme wet events, where rainfall exceeded over 5mm/day, occur twice within the simulation.

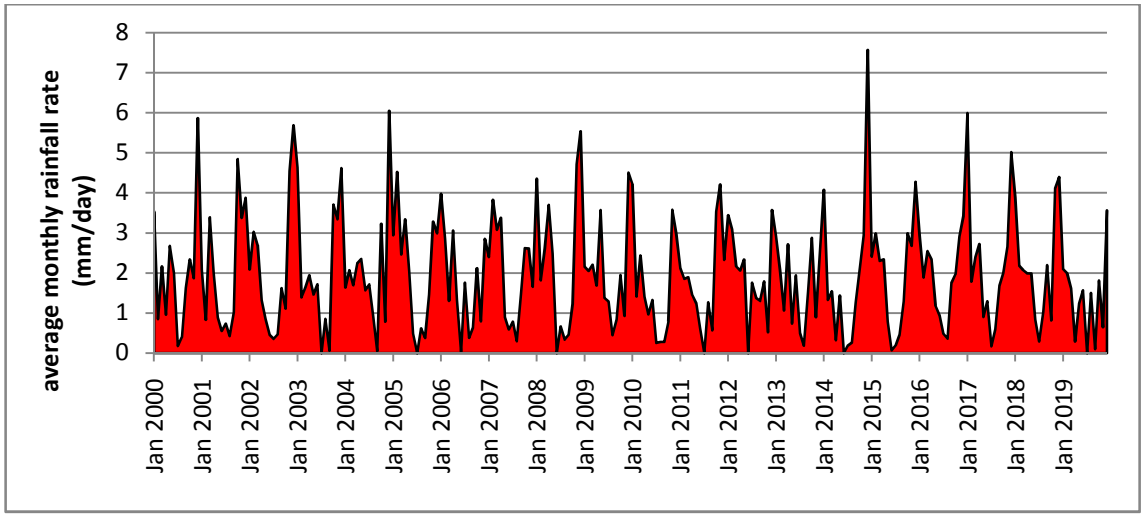

Figure 5.4 Monthly rainfall for future EARWIG scenario (2080 high emission).

It can be seen that the rainfall in the future climate dataset is annually more variable than the present day dataset. The reduced summer rainfall is evident in the future climate dataset and the increased winter rainfall is also evident. Average monthly rainfall for the future simulation is, however comparable at 2.05mm/day. Wet events where the monthly rainfall rate in one month exceeds 5mm/day occur 6 times within this dataset. This implies that although the future climate dataset contains on average less rainfall, wet events are approximately three times more likely to occur.

The monthly average EARWIG minimum and maximum temperatures for the present and future climate simulations are shown in Figures 5.5 and 5.6 respectively. For context, the average monthly temperatures for the 100 UKCP09 scenarios have also been plotted. The present climate EARWIG temperatures once again compare very well with the UKCP09 scenarios. The future EARWIG simulations show that maximum temperatures are comparable to the average of the UKCP09 scenarios but minimum temperatures of the EARWIG simulations are higher during the summer months. It can also be seen from the plots that the EARWIG temperatures are still well within the range of the 100 UKCP09 scenarios. Overall the predicted future temperatures indicate an increase throughout the year. The range between maximum and minimum temperatures for the future simulations are shown to be comparable to those of the present day simulations, yet there is a consistent temperature rise of just under 5ºC on average during winter and just over 5ºC in summer. The increased temperature within the modelling will have the effect of increasing the rate of evapotranspiration from the soil. This would lead to more water being drawn out throughout the year, especially during the summer months. The rainfall data had already shown a decreased rainfall during these summer months. Therefore, very high suctions which penetrate deep into the embankment would be expected for this climate scenario.

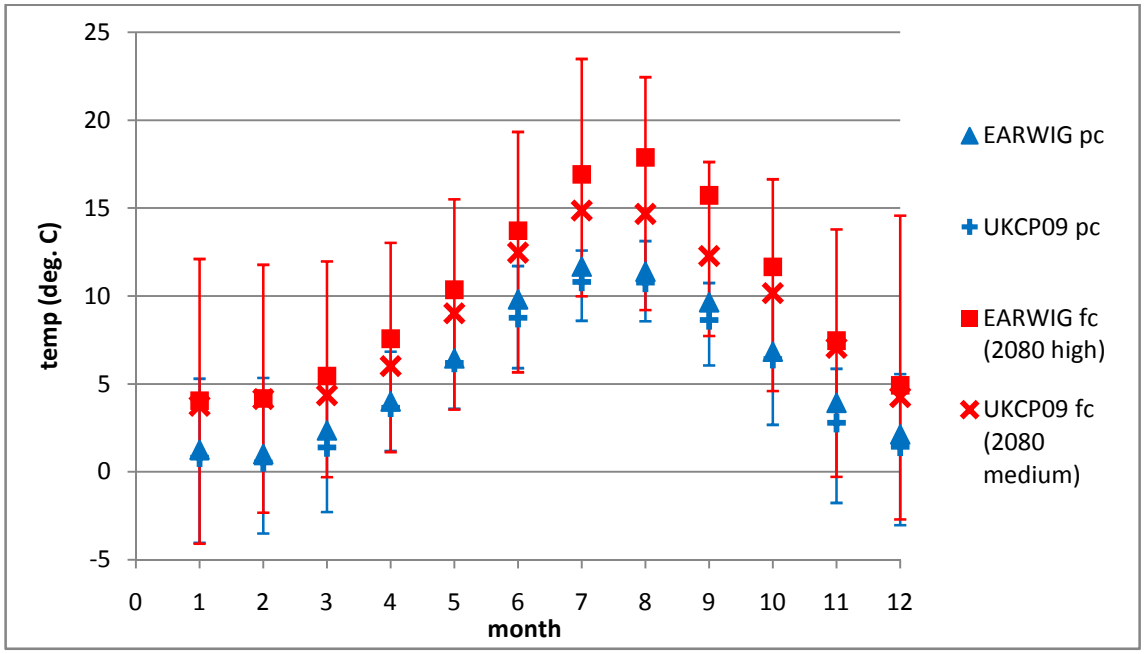

Figure 5.5 Average monthly minimum temperature data for the 20 year EARWIG simulations and 100, 30 year UKCP09 simulations. The ranges indicate the maximum and minimum average for the UKCP09 scenarios.

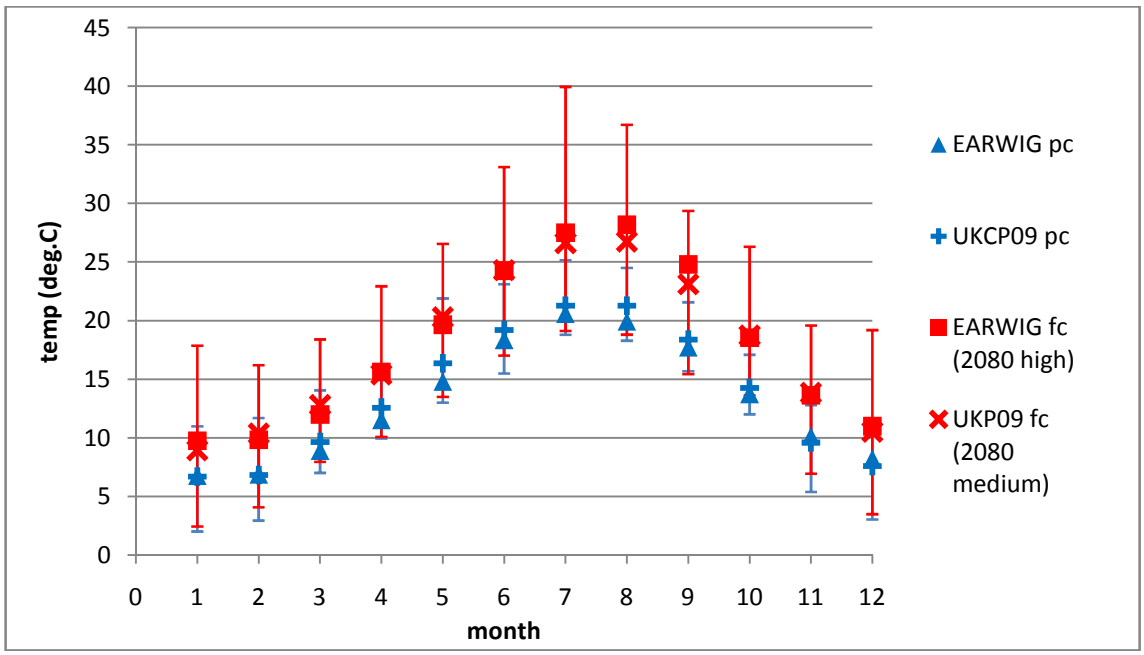

Figure 5.6 Average monthly maximum temperature data for the 20 year EARWIG simulations and 100, 30 year UKCP09 simulations. The ranges indicate the maximum and minimum average for the UKCP09 scenarios.

Figure 5.7 shows the differences between the relative humidity of the present and future EARWIG climate scenario. The future climate scenarios generally indicate a lowering of relative humidity. The air during the winter months of the present climate appears to be near saturated. The UKCP09 future scenarios show a much higher annual relative humidity than the EARWIG future climate scenario. The EARWIG future relative humidity is in some cases much lower than the extreme low relative humidity from the UKCP09 simulations. With high humidity it is more difficult for the water to evaporate from surfaces, therefore, evapotranspiration rates will decrease as a result of the relative humidity increase. Evapotranspiration rates for the EARWIG scenario therefore have the potential to be much higher than the remaining scenarios.

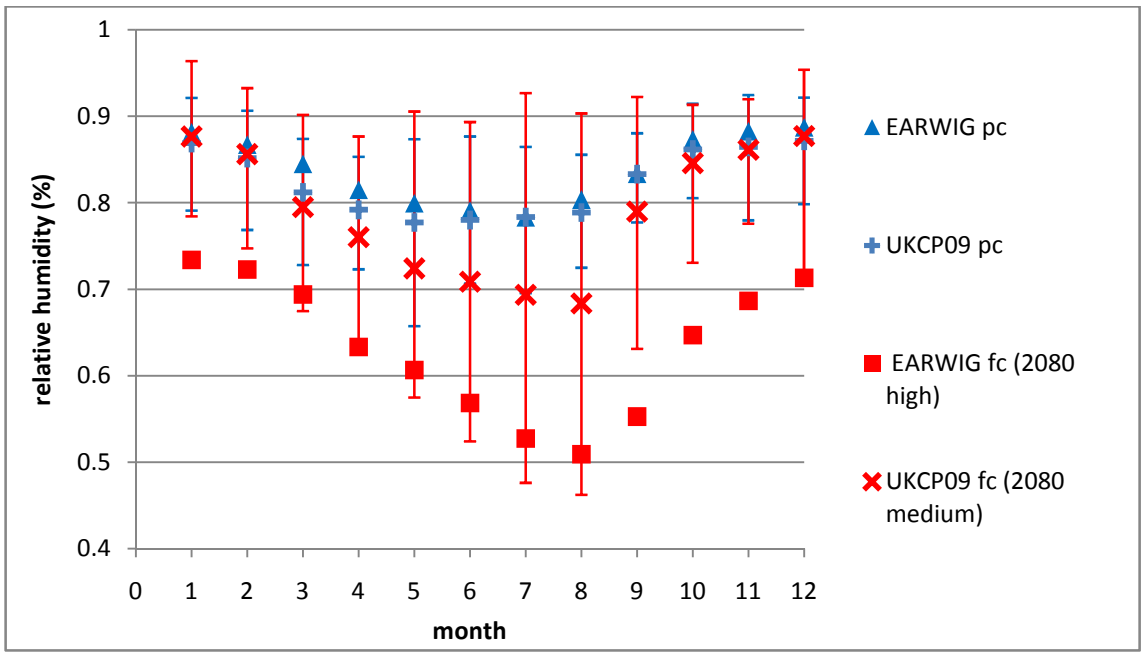

Figure 5.7 Average monthly relative humidity data for the 20 year EARWIG simulations and 100, 30 year UKCP09 simulations. The ranges indicate the maximum and minimum average for the UKCP09 scenarios.

The mean vapour pressure variation for both climate scenarios is shown in Figure 5.8. These values are used to calculate the vapour pressure deficit. As can be seen from the figure, there is no significant increase in the vapour pressure for the majority of the scenarios. The UKCP09 scenarios indicate an average increase in vapour pressure; the EARWIG averages, however, lie within the UKCP09 ranges.

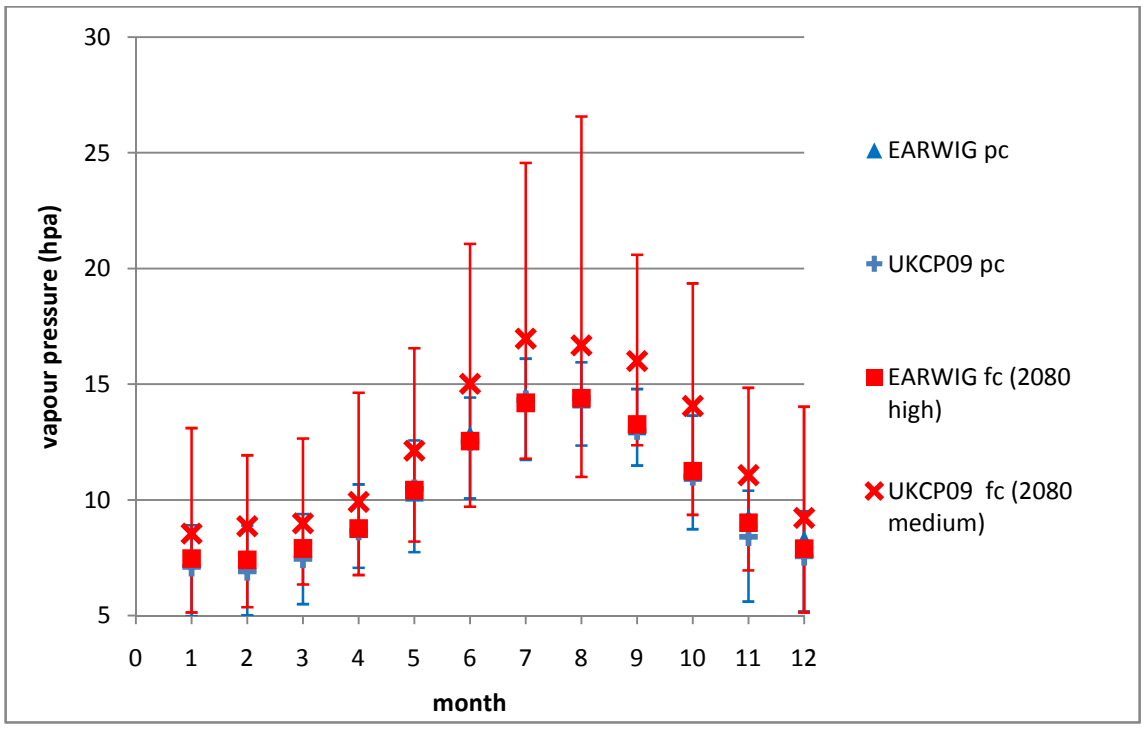

Figure 5.8 Average monthly mean vapour pressure data for the 20 year EARWIG simulations and 100, 30 year UKCP09 simulations. The ranges indicate the maximum and minimum average for the UKCP09 scenarios.

The duration of sunshine hours for the future and present climate scenarios are shown in Figure 5.9. The average of the UKCP09 scenarios and EARWIG compare well for all months. There appears to be a slight increase in the daily sunshine hours for the future climate scenario. This may go some way to explaining the large increase in daily temperatures. The future climate scenario simulation also predicted that extreme events of long sunshine duration are larger at over 16hrs than the present climate scenario which predicts a maximum of just under 14hrs. SHETRAN requires net radiation measurements to simulate the evapotranspiration on the slope. An approximate correlation was found between sunshine hours and net radiation. The relationship takes the form:

$$R_n = 0.575x^2 + 21.7x - 20.78 \qquad \textbf{5.1}$$

where R_n is the net radiation and x is the sunshine hours per day (Muneer, 1997). The same distribution was, therefore, observed for net radiation as for sunshine hours.

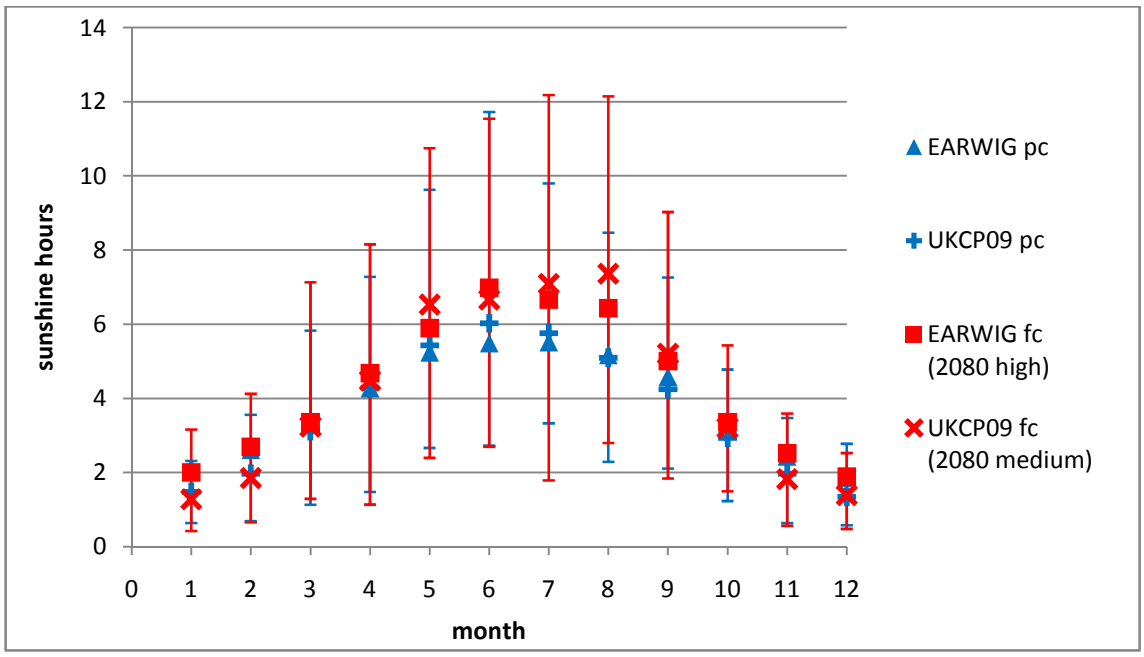

Figure 5.9 Average monthly sunshine hour data for the 20 year EARWIG simulations and 100, 30 year UKCP09 simulations. The ranges indicate the maximum and minimum average for the UKCP09 scenarios.

The daily generated weather data from EARWIG was downscaled to hourly rainfall data using Rain-Clim, this model uses a Neyman-Scott Rectangular Pulses model which is capable of producing rainfall series for resolutions of minutes (Kilsby et al, 2007). The hourly rainfall data for January is shown in Figure 5.10. From this figure it can be seen that the future rainfall occurred at a higher intensity and for shorter periods than the present day rainfall. The rate at which the rain falls is significant for the modelling of slope stability. Saturated permeability and relative permeability of the soil profile determines the rate of infiltration into a soil. There is, therefore, a maximum rate at which water can enter the slope. If the precipitation rate exceeds the infiltration rate water will flow off the slope as run off. The infiltration rate is lower for a dry soil profile as its relative permeability is lower. Therefore, the future climate slope, which may be drier due to increased evapotranspiration and lower precipitation during the summer months, will be less permeable than the present climate slope. Couple this increased dryness with an increase in precipitation rate but no precipitation increase and it follows that the model will predict an increase in run off. Not only will the modelling of a future climate scenario extract more water from the slope but it will also reduce the amount of water able to infiltrate into the slope.

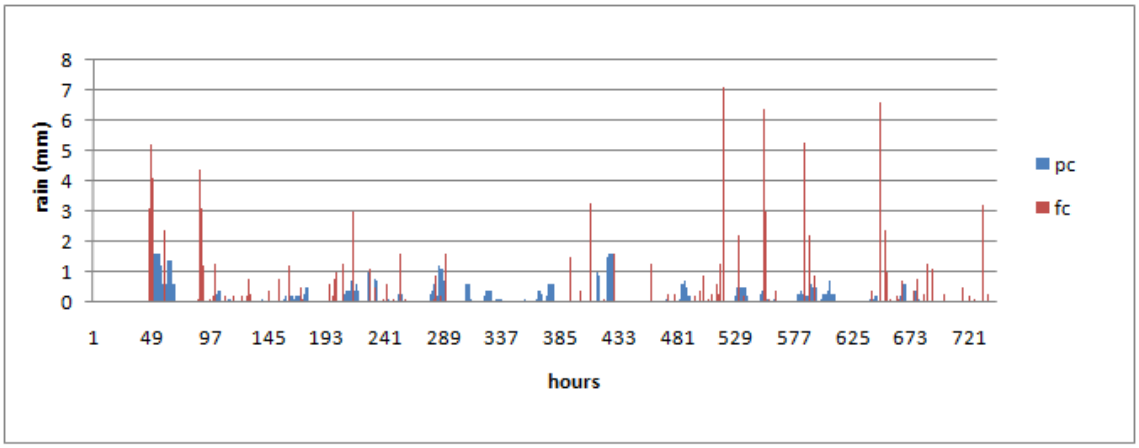

Figure 5.10 EARWIG downscaled hourly rainfall for January for a future (fc) and present day (pc) climate scenario.

5.2.5 Limitations of generated weather data

The downscaling of weather data involves processes of applying statistics of observed weather relationships to generated weather data. The generated weather data therefore has no explicit basis in physics or meteorology (DEFRA, 2011). Although the generated present climate dataset is statistically consistent with observed data for the site, weather generators are notoriously poor at re-creating extreme weather events (DEFRA, 2011). The future climate data set is based on scaling of the present climate data set and therefore any climate feedback, whereby one process triggers changes in another process, cannot be taken into account.

Due to the time required to run the transfer method detailed within Chapter 4 only one weather variable dataset has been used for future climate and one for the present climate. The following analysis will therefore need to be taken in context against the 100 generated scenarios presented within this section. As the distribution of wet and dry periods produced by these two datasets are determined randomly, other weather datasets for the same scenarios have the potential to affect the slope differently. The following simulations are therefore not predictive of what will happen to the modelled infrastructure but serve to differentiate between outcomes associated with a representative present and a high emission 2080 future climate scenario.

5.3 Diagnostic railway embankment case study

5.3.1 Introduction

The aim of this investigation was to establish the effect of a future climate on the progressive failure of a railway embankment. An embankment was therefore constructed within both the SHETRAN and Flac-tp models. Both models had the same slope dimensions. The material properties of the railway embankment were similar to those used by Kovacevic et al (2001) for the simulations of the progressive behaviour of a railway embankment within the ICFEP program. The ICFEP simulations utilised a strain softening model. As outlined within Section 2.5.2 strain softening models are grid dependent. The strain softening parameters for the Flac-tp simulation were fitted to the grid by simulating the Kovacevic et al simulations within the Flac-tp program.

It was expected that the future climate simulation would take longer to fail due to higher suctions. Therefore the slope angle for the simulations was designed to be steep enough so that failure would occur within a relatively short time period within the present climate scenario. This would allow a comparison to be made between the time to failure for the present climate and the time to failure, if failure occurs, for the future climate.

5.3.2 The test embankment

For the purpose of this diagnostic study, a typical railway embankment was constructed within Flac-tp. The embankment modelled is 7m high with a 1:2.5 (vertical:horizontal) slope and a 12m wide crest. The embankment was assumed to be symmetrical and, therefore, only half the embankment was modelled in a plane strain analysis. The embankment was constructed from London Clay with a 1m deep ash layer at the crest of the slope. The foundation of the embankment was also made of London clay and was assumed to extend for a length of 50m beyond the toe of the slope and a depth of 15m below ground level (Vertical and horizontal movement were not permitted at the base of the foundation and only vertical movement was permitted at the embankment centreline).

5.3.3 Material properties

The constitutive model used for the analysis was a Mohr-Coulomb model with built in strain softening function. The properties for the model were derived from those used by Kovacevic et al (2001). These properties were in turn based on similar properties defined during testing and also used within ICFEP by Potts et al (1997) to study the progressive failure of cuttings within London Clay.

Elastic parameters

The Young's modulus varies with respect to effective stress. The Poisson's ratio remains at a constant value of 0.2 within the foundation but switches from 0.2 to 0.3 within the embankment material. A Poisson's ratio of 0.2 is specified when the material is swelling (unloading during the winter months) and a Poisson's ratio of 0.3 for when the material is shrinking (loading during the summer months). The point of switch over for the Poisson's ratio was determined by consulting pore pressure variations within the embankment from the SHETRAN simulations, see Figure 5.11. From these plots it can be estimated at what point the embankment begins swelling and at what point the embankment begins shrinking. An average switch over time to be used for every year within the Flac-tp simulation was estimated by considering the pore pressures over the entire SHETRAN simulation period. This would mean that for certain years within the Flac-tp simulation, for example a year where with a long dry summer, a swelling Poisson's ratio may be specified for a shrinking embankment and a vice versa for a year with a long winter. This would only occur for a matter of days only and the period of error would occur over a period of intermediate pore pressure variation where only limited shrink swell occurs. The assumption of a static switch over time for the Poisson's ratio was, therefore, assumed reasonable.

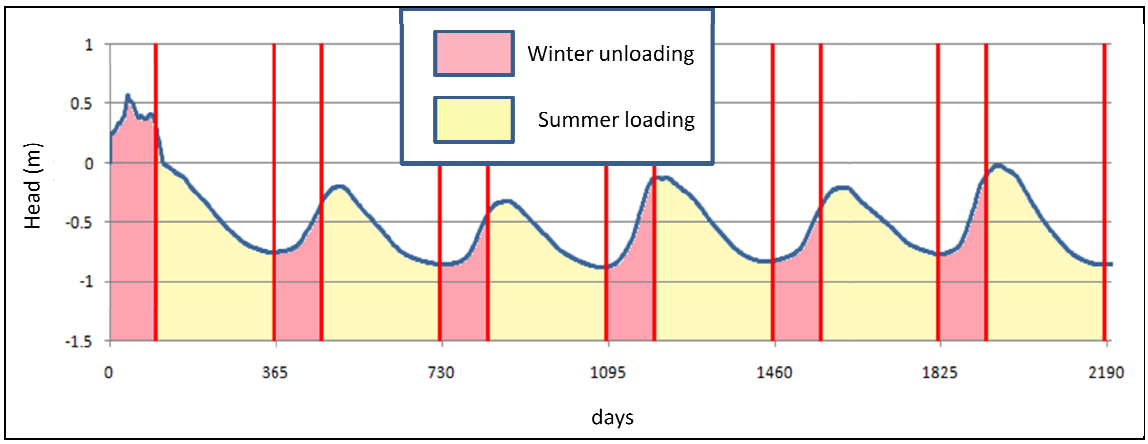

Figure 5.11 Pore pressures from SHETRAN (blue line) showing elastic moduli switch over times from Winter to Summer condition. These times would be averaged for the entire length of a simulation.

Flac-tp requires the use of bulk of shear moduli. The bulk and shear moduli were calculated from the Young's modulus and Poisson's ratio using the equations for shear modulus, *G*, and bulk modulus, *K*, respectively:

$$G = \frac{E}{2(1+v)} \qquad \textbf{5.2}$$

$$K = \frac{E}{3(1-2v)} \qquad \textbf{5.3}$$

Where *E* is the Young's modulus and *v* is the Poisson's ratio.

Plastic parameters

The constitutive model, as stated, allowed for the effects of strain softening. This allowed the reduction of friction and cohesion after the onset of plastic yield. The user must specify the strains at which peak and post peak strengths are mobilised, Flac-tp then forces the model properties to conform to these user defined strengths. The geotechnical properties used within the analysis were again based upon the properties for London clay used by Kovacevic et al (2001). The strain softening properties were scaled for the grid used in this analysis by simulating the analysis carried out by Kovacevic et al (2001). The peak deviatoric plastic strain remained unchanged but the rate of softening needed to be 'fitted' to a known case due to the dependency of this property on grid size (Itasca, 2002). Kovacevic et al (2001) ran numerous simulations

on a generic railway embankment. The simulations ran involved applying a summer boundary condition and running the simulation until equilibrium was attained. A winter boundary condition was then applied and the simulation ran again. The process was repeated until failure occurred. The winter conditions applied were 5 kPa, 10 kPa, 15 kPa and 20 kPa. Simulations were run in Flac-tp for the 5 kPa and 10 kPa winter conditions. The two phase flow option was not used for these comparisons in order to obtain comparable results to the Kovacevic et al (2001) simulations.

The ICFEP program used by Kovacevic et al specified that softening occurred when horizontal plastic shear strains exceeded 5%. As the Flac-tp simulation used the same Mohr-Coulomb constitutive model and soil properties, it was assumed that the response of the ICFEP and Flac-tp model before softening occurred would be identical. For this reason softening within the Flac-tp grid would also occur when horizontal plastic shear strains exceeded 5%. The Flac-tp model however calculates total plastic shear strains as an average of horizontal and vertical plastic shear strains. During simulations, it was noted that there was negligible vertical shear strain at the toe of the embankment. It was deemed that this was the key area to model when modelling progressive failure. Softening within the Flac-tp grid was, therefore, assumed to begin when total plastic strains exceeded 2.5 %. This was assumed to give an identical response to the ICFEP softening model if vertical strains remained negligible. A parametric study to determine the rate of softening was then conducted for the grid shown in Figure 5.12. Varying the rate of strain softening within the Flac-tp simulations varied the number of years to collapse of the embankment. The rate of strain which gave the best comparison to the Kovacevic et al (2001) simulations was used within the remaining simulations. The displacement to residual strength was specified rather than a percentage to better reflect the displacement that must occur across the slip surface before residual strength is attained.

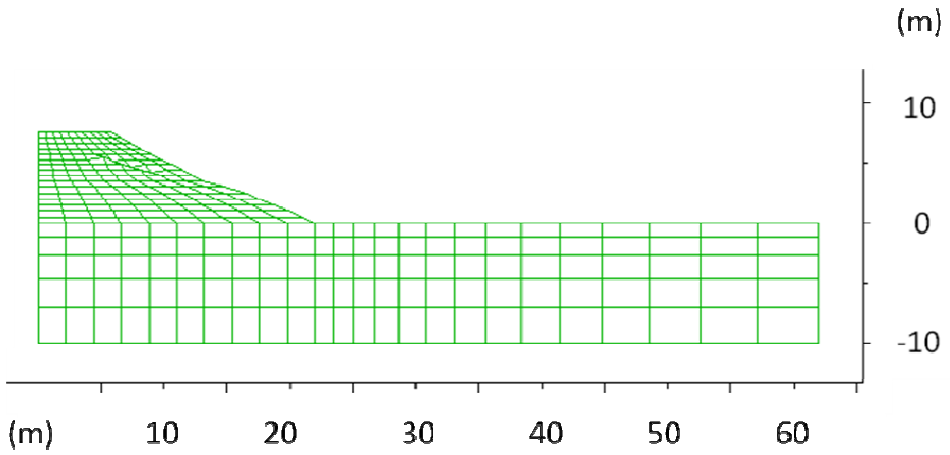

Figure 5.12 The Flac-tp grid used for the parametric comparison to the Kovacevic et al (2001) simulation.

Figure 5.13 shows the development of shear strains for the element at the toe of the slope for the 5 kPa winter condition simulation. From this figure, it can be seen that all strains occur during the winter unloading condition with strains showing a small decrease during the summer period. The increased movement at the toe during the winter months is due to the decrease in effective stress at the toe due to the increased pore pressures.

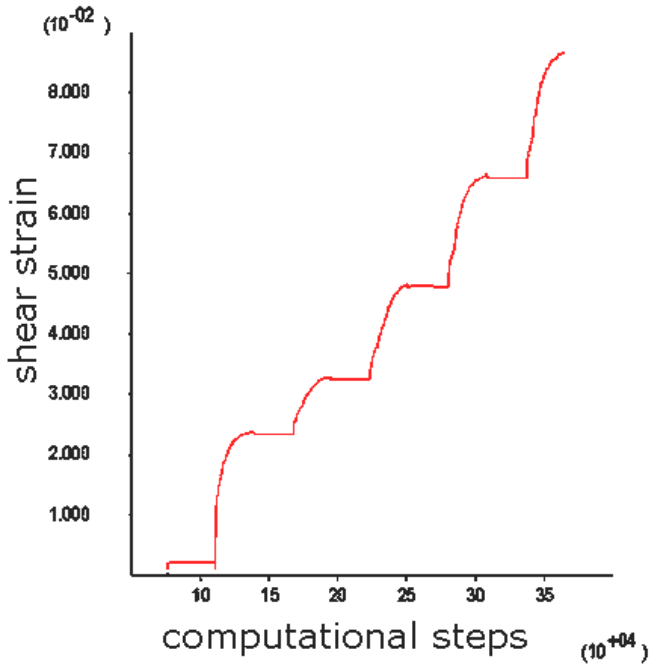

Figure 5.13 Shear strain for element at the toe of the Kovacevic et al comparison exercise.

Figure 5.14 shows the development of shear strains within the slope for the 5 kPa simulation. From these diagrams it can be seen that shear strain begins at the toe of the

embankment and then steadily progresses through the embankment until a catastrophic failure occurs during year 6.

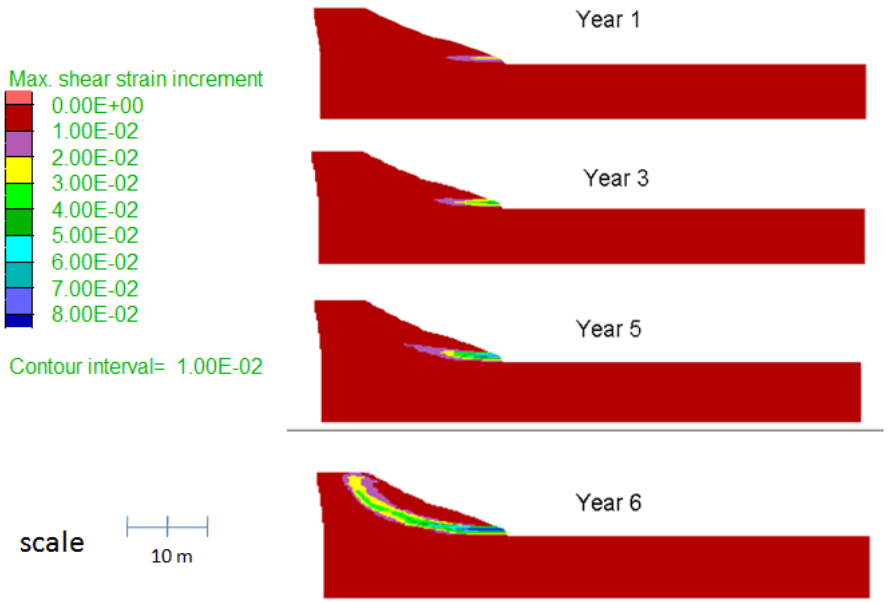

Figure 5.14 Development of shear strain during Kovacevic et al comparison simulation (5 kPa Winter suction).

Failure occurred within the 5 kPa winter condition embankment within the 6th cycle and failure occurred within the 10 kPa winter condition after the 14th cycle. These results are comparable to the results published by Kovacevic et al (2001). The parameters used for these simulations are shown in Table 5.2. The defined properties were to be used for the remainder of the diagnostic embankment study.

Table 5.2 Material properties used for the diagnostic study on the effects of climate change on embankment stability.

	Ash fill	London clay fill	In-situ London clay
Bulk unit weight kN/m^3	10.5	18.1	18.8
c' peak kPa	2	3.4	7
c' residual kPa	-	2	2
φ' peak °	36	22.9	20
φ' residual °	-	13	13
Total strain at peak %	-	2.5	2.5
Displacement at residual (mm)		70	70
Poisson's ratio	0.3	0.3 (0.2 swell)	0.2
Young's modulus During construction (kPa)	1000	15(p'+100) Min 2000	25(p'+100) Min 4000
Young's modulus During shrink/swell (kPa)	1000	50(p'+100) Min 2000	50(p'+100) Min 2000
Coefficient of earth pressure at rest	-	-	2.5 at surface varying to 1 at 15m depth
Permeability m/s	Free draining	5e-9	2e-10

Similar element sizes and rates of softening were used for all the simulations on the diagnostic railway embankment. The assumption is that the similar rates of softening and similar element sizes will reproduce similar softening characteristics. This process effectively gave the following simulations approximately the same rate of strain softening as the material modelled by Kovacevic et al (2001).

5.3.4 The effects of mass permeability

The previous Kovacevic et al simulations were run to equilibrium for each summer and winter condition therefore negating the affects of permeability. If permeability was taken into account then the applied surface pressures may not have been able to penetrate as deep within the embankment. This would result in reduced magnitude shrink swell cycles and therefore increased stability. Preliminary simulations were run within the single phase model to analyse the effects of mass permeability on the

stability of the embankment during construction and also during summer winter cycled pore pressures within the Flac-tp program. These simulations were run for six months with a summer boundary condition and 6 months for a winter boundary condition. The simulations were similar to those run by Nyambayo (2004) within the ICFEP program. The grid used for the simulation can be seen in Figure 5.15.

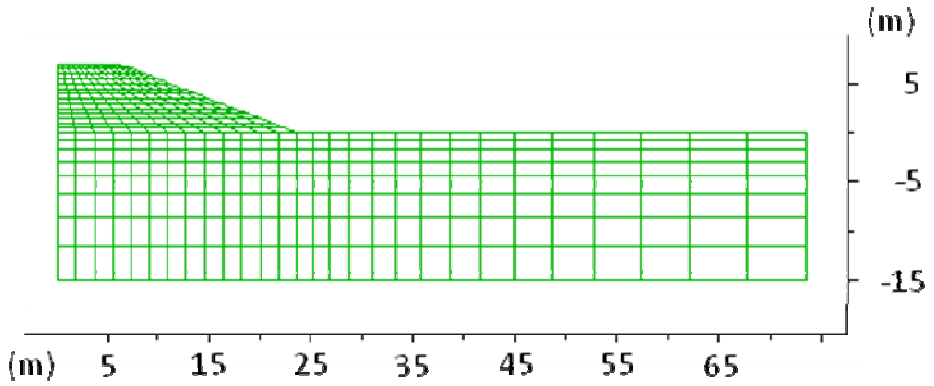

Figure 5.15 Flac-tp grid used for permeability study.

The material properties were the same as for the Kovacevic et al simulation. The embankment was constructed in 7 layers over 28 days. The embankment was then allowed to reach equilibrium pore pressure for 5 years before cycling commenced. The effects of a change in permeability on the pore pressure distribution can be seen within Figure 5.16. For the higher permeability embankment the pore pressures were able to respond faster and therefore have a greater range of pore pressures at depth than the lower permeability embankment.

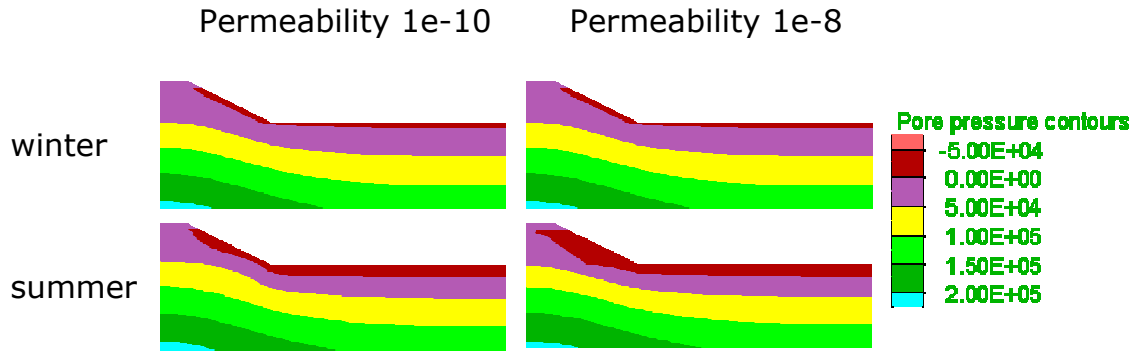

Figure 5.16 Pore pressure contours within Flac-tp single phase embankment models for permeabilities of 1e-8 and 1e-10 m/s.

Figure 5.17 shows the results of the fully coupled single phase analysis on the two separate embankments. As can be seen during the swelling period the shear strains at the toe of the first embankment increase at a fairly constant rate up to the end of the

swelling period whereas the shear strains at the toe of the second embankment increase at a much greater rate within the first year and then at a much slower rate for the rest of the swelling period. The shear strains at the end of the swelling period at the toe of the first embankment are also larger than the shear strains at the toe of the second embankment. The reason why the lower permeability embankment shows more movement can be explained by the rate of dissipation of construction pore pressures. The higher permeability embankment allowed the pore pressures to dissipate quickly with rapid pore pressure change within the first year and little change thereafter. The associated movements also show a period of accelerated movement within the first year and again little change thereafter. Within the lower permeability embankment, the pore pressures took longer to dissipate due to increased resistance to flow. The effective stresses, therefore, remained low over an extended period. It can be seen from the earlier simulations that decreased effective stress results in increased displacements. Displacements associated with the decreased effective stress, therefore, also occurred over a longer period.

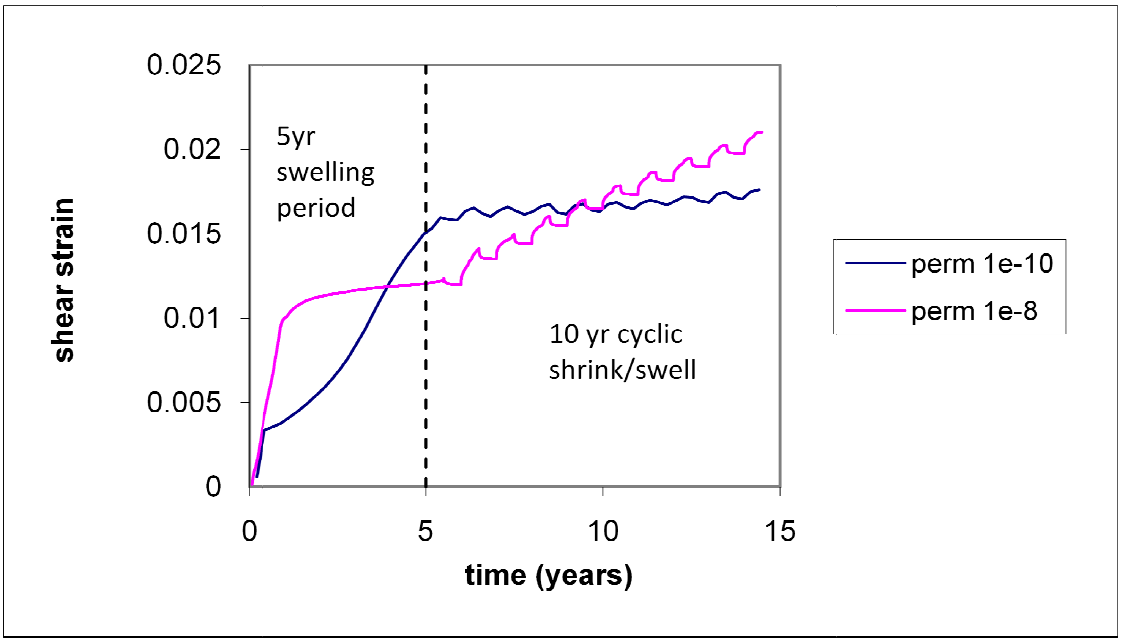

Figure 5.17 Shear strain development at toe for 1e-8 and 1e-10 m/s single phase Flac-tp embankment models.

The situation is reversed during the cycling exercise. The higher permeability embankment allowed relatively free movement of water which lead to greater pore water pressures to penetrate deeper into the embankments. The associated lower effective stresses, therefore, resulted in increased displacement during the winter condition. Conversely, the lower permeability embankment restricted the flow of water more and, therefore, the pore water pressures at depth remained consistently, relatively

low. The annual pore pressure range at depth was also lower which resulted in lower cyclic effective stresses and therefore smaller cyclic movements.

The smaller cyclic movements of the lower permeability embankment resulted in almost no increase in shear strain at the toe of the embankment whereas for the higher permeability embankment the larger cyclic movements resulted in the accumulation of shear strains at the toe. Four years after construction shear strains at the toe of the higher permeability embankment equalled those of the end of construction shear strains at the toe of the lower permeability embankment and the shear strains kept increasing until the end of the simulation period.

One of the conclusions from this study were that lower permeability embankments were relatively less stable after construction but more stable long term and vice versa for higher permeability embankments. The same conclusions were drawn by Nyambayo (2004) using the ICFEP program. It can also be inferred that modelling partially saturated embankments with the two phase program will lead to decreased permeability along the surface, due to reduced moisture contents, which would also lead to decreased surface pore pressure influence at depth. Increasing or decreasing permeability will only affect the depth of influence of surface pore pressures as long as the time of application of the summer or winter condition is restricted, in this case each was restricted to 6 months. The 6 month application may not be representative of on site conditions. The depth of influence of the applied surface pore pressures also depends on the magnitude of the applied pore pressures. An average summer pore pressure of -50 kPa for six months may not penetrate as deep as a -100 kPa pore pressure over a one month period. The length and magnitude of applied suctions may be altered to fit with observed data but observations are not available for future climate conditions. The variation of pore pressures along the surface will also play a factor. It has already been shown within the previous simulations that strain softening begins at the toe of the embankment. Seasonal variations in pore pressure at the toe may not be as large as those along the slopes of the embankment. It was therefore decided to model the embankment within the SHETRAN program. This modelling would prove useful in addressing the issues raised with the present modelling capabilities and highlight the inefficiencies of the single phase, six month summer, six month winter modelling procedure. The SHETRAN modelling, when used with the EARWIG data detailed

within Section 5.2, would also be able to predict pore pressures for a future climate without the need for observational data.

5.3.5 Present and future climate scenarios

The embankment was built within the SHETRAN program, the unsaturated hydrological properties used within the analysis were based upon the curves of gravimetric water content against suction for London clay published by Croney (1977). These properties and a graphical representation of the curve are presented below in Table 5.3 and Figure 5.18 respectively. The embankment was given a permeability of $5x10^{-9}$ m/s and the in-situ foundation a permeability of $2x10^{-10}$ m/s.

Table 5.3 Unsaturated properties of London Clay derived from Croney (1977).

	London clay (embankment and foundation)
Residual volumetric moisture content	0.28
Saturated volumetric moisture content	0.45
Van Genuchten parameter n	1.443
Van Genuchten parameter α (1/m)	0.458

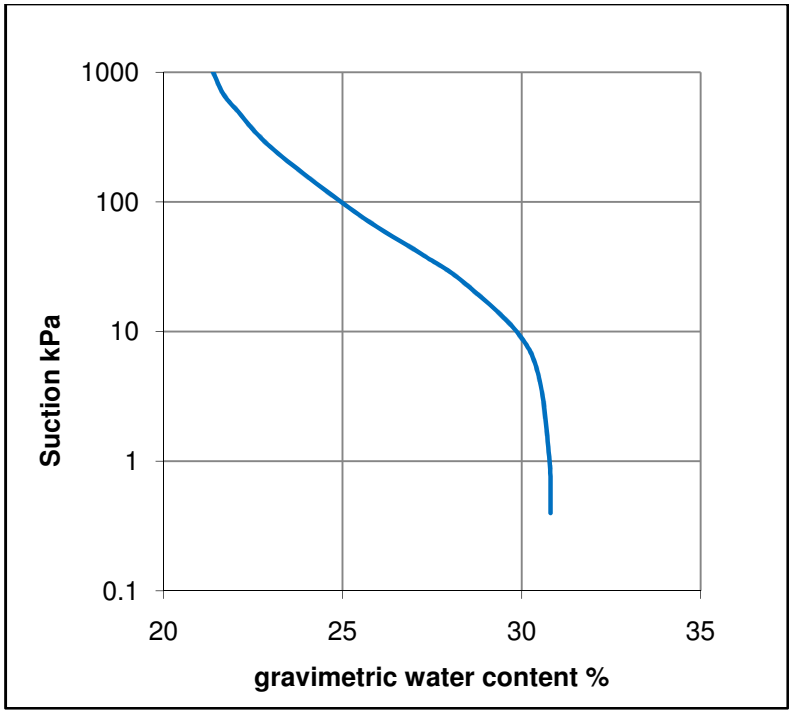

Figure 5.18 Graphical representation of the drying curve given by the van Genuchten parameters in Table 5.3.

The model initial conditions were hydrostatic with a water table one meter below the surface (this equates to a surface suction of 10 kPa) as per the end of construction water table. The slopes of the embankment were bare with no vegetation cover. This assumption was stipulated so that the effects of the climate on slopes can be monitored without the added complexity of transpiration. The simulations were allowed to run for a period of 20 years.

The SHETRAN embankment was subjected to a present and a future climate condition. The climate data used was for the Newbury area as detailed within Section 5.2. The variation in pore pressures for three positions on the slope surface was recorded over a period of five years to observe the effects of the change in climate. The positions are shown in Figure 5.19. These positions were chosen to also show the variation in pore pressures along the length of the slope. Position C would also show the effects of the free draining gravel on the surface pore pressures.

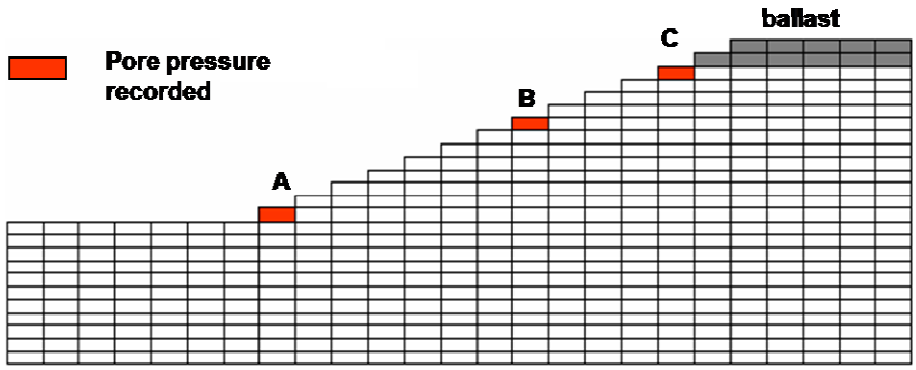

Figure 5.19 SHETRAN simulation grid with monitored cells highlighted in red.

Figure 5.20 shows the pore pressure variations at position A. The future climate scenario shows a much greater range of annual pore pressures around 110 kPa annually. This will be due to the distribution of rainfall within the future climate simulation. Figures 5.1-5.4 showed that there was relatively more rainfall within the winter months and less within the summer months. This rainfall distribution has lead to the slope drying out over summer and then wetting up over winter. The greater variation in annual pore pressure will lead to larger shrink swell cycles within the embankment. The present climate scenario shows much less variation with around 50 kPa annually. The highest pore pressures within the present day climate scenario are also consistently higher than for the future climate scenario. Positive pore pressures are attained every

year within the present climate simulation but are never attained within the future climate simulation. Figures 5.5 and 5.6 show that the temperatures of the future climate scenario will be consistently higher which will lead to increased evaporation from the slope. The increased evaporation has lead to the slope being significantly drier for the future climate scenario than for the present climate scenario. With larger suctions present throughout the year the effective stress within the embankment will be higher which will lead to greater shear strength and hence stability. The present day simulations interestingly show more variation in peak suctions each year with a maximum of around 60 kPa in year two and a minimum of 30 kPa in year four. The future climate scenario shows a consistent peak suction of around 115 kPa variation each year below 10 kPa. This shows that the present day climate embankment simulation was more sensitive to the effects of wet and dry years. The increased sensitivity could be due to a number of factors. The present day climate embankment simulation would be more saturated at the surface, with increased levels of surface saturation there will be an increase in relative permeability. This allows water to enter and leave the slope more efficiently.

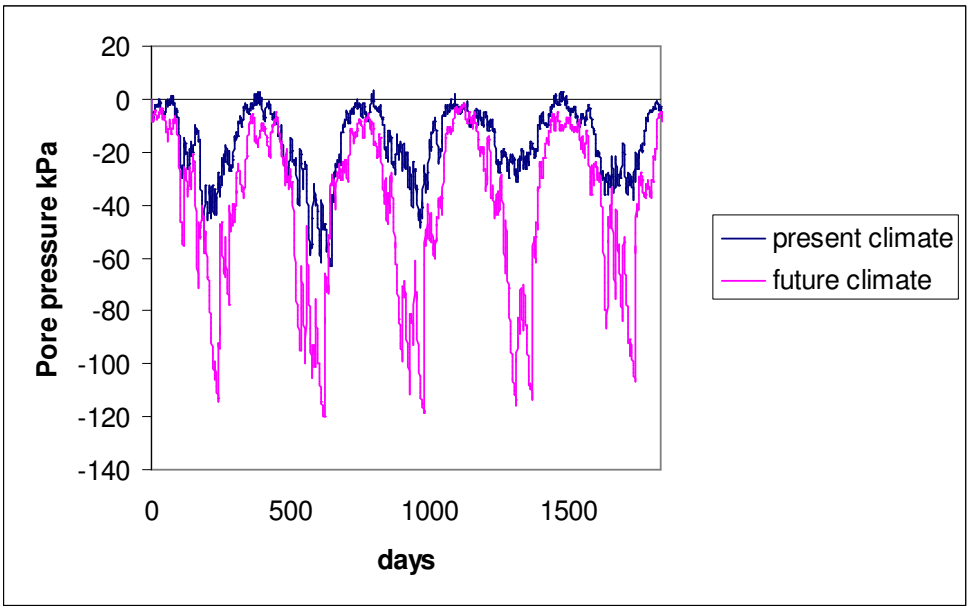

Figure 5.20 Pore pressure variations for position A for a present and future climate condition.

Figure 5.21 shows the pore pressure variations for position B. There is no great difference between the pore pressure plots at this location when compared to the pore pressure plots of position A. It can be observed, however, that the peak pore pressures and suctions of the future climate and present climate scenario have lowered consistently. The reduction in pore pressures can be attributed to a reduction in the

quantity of runoff water at this location. SHETRAN is able to model the run off content for each surface cell, therefore, lower cells have a higher cumulative run off than higher cells. A continued presence of surface run off leads to increased infiltration. Therefore, the cells further down slope will have higher pore pressures than those further up slope. The effect is more noticeable within the future climate scenario winter pore pressure profile. This is due to increased run off within the future climate scenario simulation. Less water is able to enter the slope due to a reduction in saturation levels and, therefore, the relative permeability. This effect is coupled with the rate of rainfall events within the future climate scenario. Shorter, more intense bursts lead to less infiltration during the event. The overall effect is a more pronounced distribution of infiltration along the slope length.

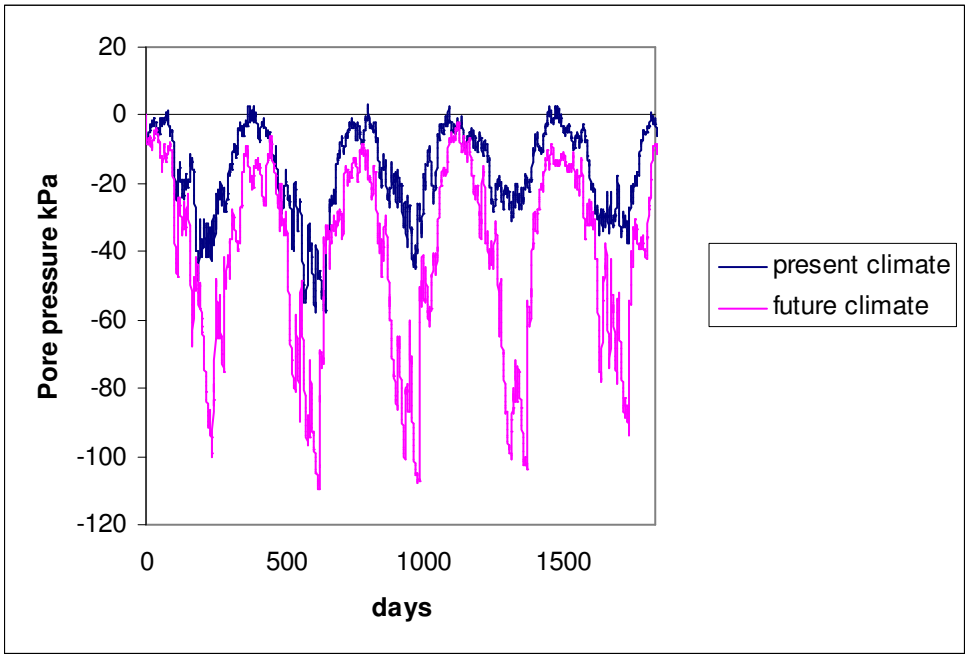

Figure 5.21 Pore pressure variations for position B for a present and future climate condition.

At location C the pore pressure variations are very different to the previous observations. The pore pressure variations at this location are shown in Figure 5.22. Both the future and present climate simulations show an increase in pore pressures coupled with a much smaller annual pore pressure range. This is the opposite of what would be expected. With an increase in elevation of the position it would be expected that there would be no incoming run off and, therefore, even lower average pore pressures than the locations further down the slope. The pore pressure plots show that this is not the case. The pore pressure plots for both the future and present climate scenario are levelling off during the winter months. This indicates the cells are fully saturated and are possible exfiltrating water onto the slope surface.

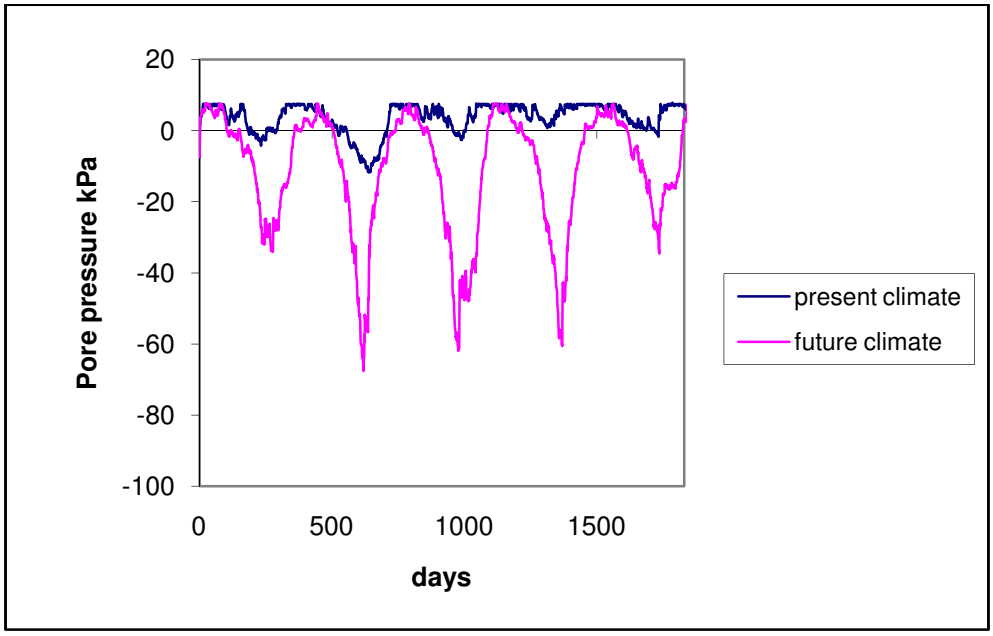

Figure 5.22 Pore pressure variations for position C for a present and future climate condition

The reasons for this were due to the presence of the ballast layer on top of the embankment. The location of the pore pressure measurements are on the surface just below the ballast layer. The ballast layer was much more permeable than the clay of the embankment but can still retain a modest amount of moisture. The ballast layer was, therefore, acting like a small reservoir above the embankment. Infiltration percentages were, therefore, at or near 100% for both scenarios. The ballast was able to hold onto this water and release it at a steady rate. The rate at which the water was released meant that infiltration at the crest increased dramatically. The increased infiltration lead to the material beneath the clay/ballast boundary becoming saturated and, therefore, more permeable. When the rate at which the water was released was greater than the rate of infiltration into the material below then the water flowed laterally down the embankment sides. The cell on the surface below the ballast would then have a steady supply of water. The following figures (Figures 5.23 and 5.24) show head profiles beneath the embankment crest, position C, for both the future and present climate scenario for year 3 of the simulation. This year was chosen as a typical year within the simulation. The present climate simulation showed little variation in pore pressure below the crest with the profile remaining at or near saturation throughout the year. The saturated profile further satisfies the theory that the profile needs to be saturated in order for exfiltration to occur from the surface cell.

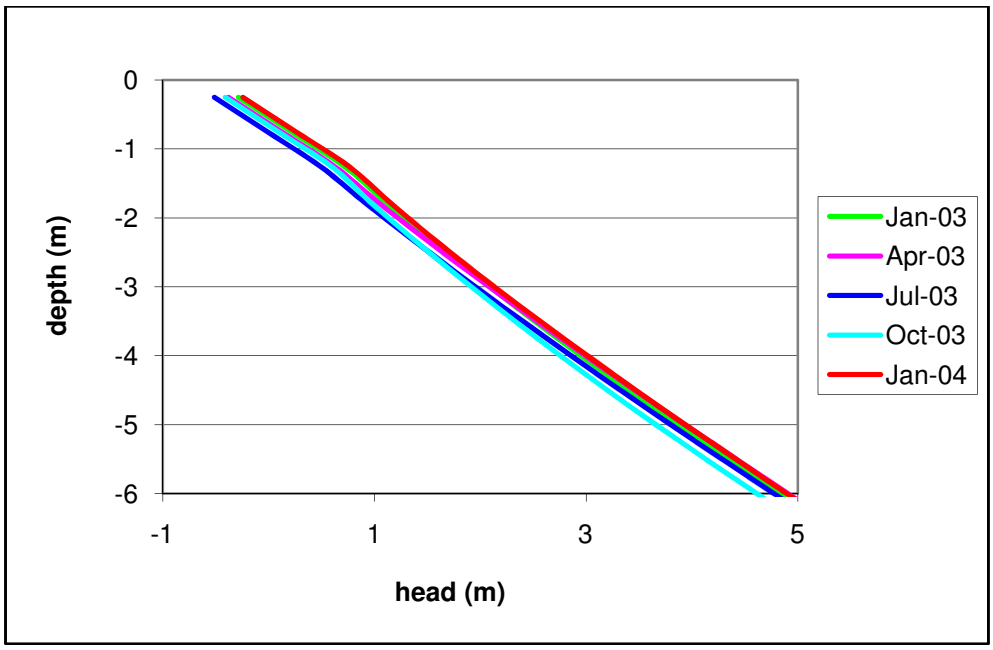

Figure 5.23 Profiles of head of water beneath position C for present climate scenario during year 3 of the simulation.

The profiles for the same year of the future climate scenario showed much greater variation throughout the year. Increased evaporation continued within the future climate scenario simulation. The future scenario therefore showed higher magnitudes of pore pressure variation than the present climate scenario. The profile for January showed a perched water table within the clay of the embankment with the top 0.5m of clay being saturated. Infiltration continued as the water filtered down and the profile was at its highest saturation during the month of April. This was the same time that the surface pore pressure levelled off (Figure 5.22). The profile then began to dry out during July but the profile remained linear indicating that infiltration was still occurring at the crest, albeit at a reduced rate to April. The profile for October showed that evaporation rates exceeded infiltration rates and, therefore, water was being extracted from the surface. The profile became non linear as water was extracted from the surface at such a rate that flow from depth could not replenish the lost moisture. Infiltration then took place again and the profile returned to approximately the same as January 03. Infiltration then once again exceeded evaporation and the clay beneath the ballast became saturated. The infiltration had not yet managed to reach the lower depths during this time though and the pore pressures below two meters remained unaffected by the infiltration.

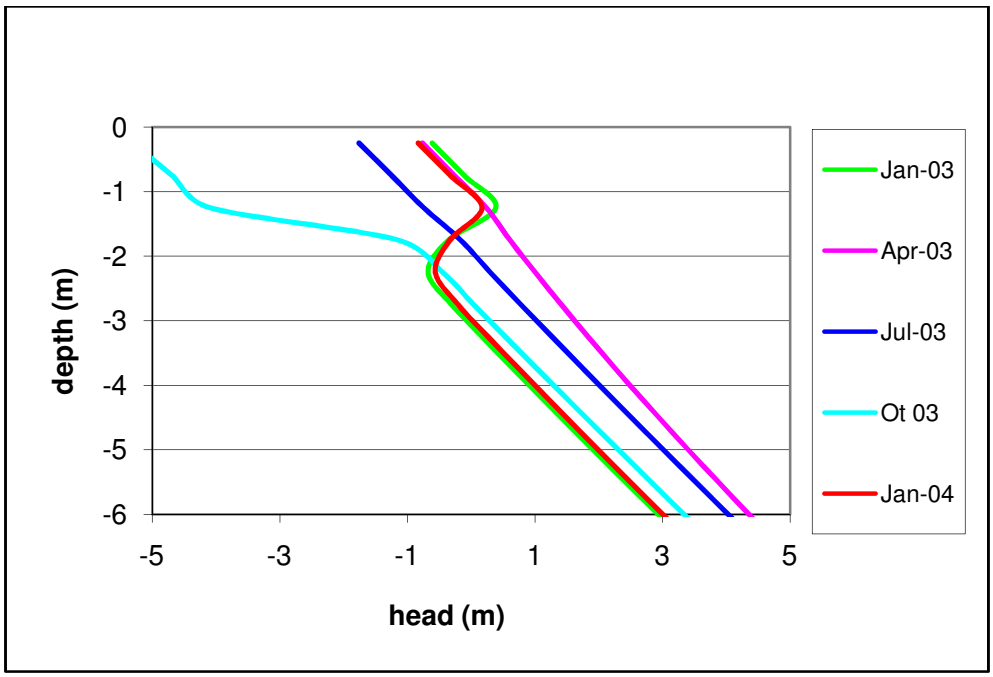

Figure 5.24 Profiles of head of water beneath position C for future climate scenario during year 3 of the simulation.

The cycle showed variation in moisture content throughout the profile which indicates that there would also be a variation in effective stresses below the crest. The annual variation in stresses would lead to shrinkage and swelling below the crest. The shrink and swell cycles would, however, be accompanied with higher suctions and therefore higher shear strengths than within the present climate simulation. The following profiles (Figures 5.25 and 5.26) show the variation in the pore pressures for position B in Figure 5.19. The profile for the present climate, Figure 5.25, showed a surface pore pressure variation of around 25 kPa. Figure 5.20 showed a maximum suction of 45 kPa during year three, although this was achieved for a relatively short period of a few days. This summer suction averaged at a much lower suction than that assumed during the previous simulation of a railway embankment (Section 5.3.4). The lower suctions were most likely due to the absence of vegetation on the slope surface. Seasonal variations persisted to depths of five meters and pore pressures were recovered at the end of each year.

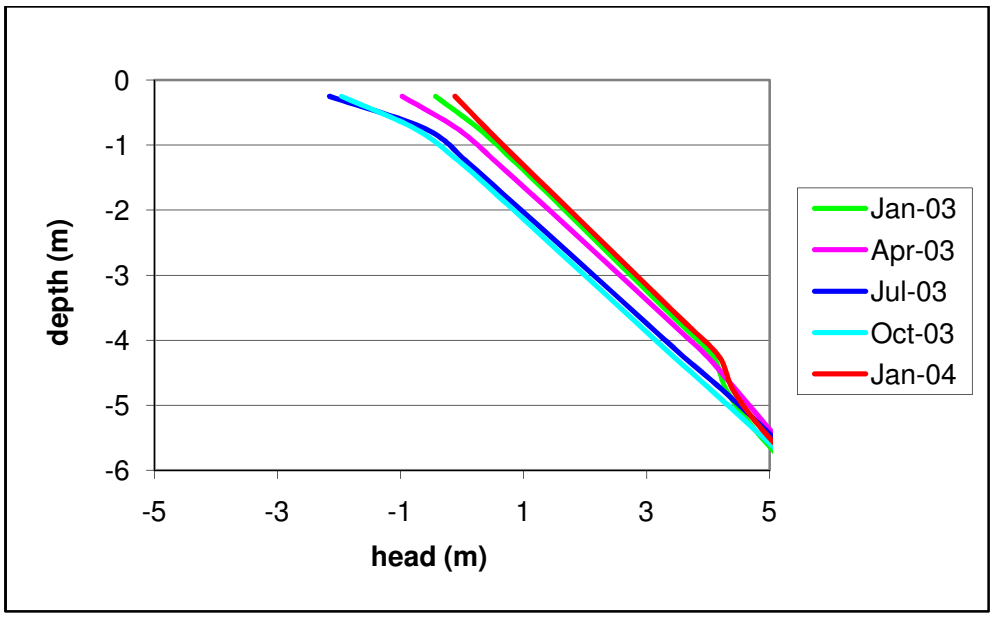

Figure 5.25 Profiles of head of water beneath position B for present climate scenario during year 3 of the simulation.

The future climate scenario simulations showed much greater surface variations although less variation at depth. The surface pore pressures reached over 100 kPa of suction. The high seasonal variations did not persist to depths greater than 1m. The overall pore pressures within the future climate scenario were also on average much lower. The variation in pore pressures also did not persist to depths greater than 5m as per the present climate simulation.

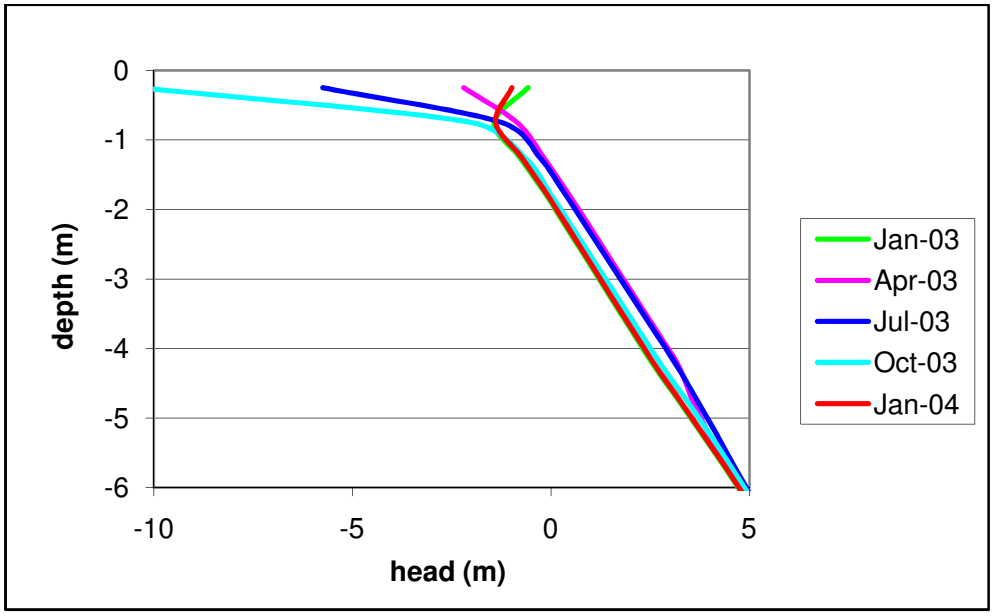

Figure 5.26 Profiles of head of water beneath position B for future climate scenario during year 3 of the simulation.

The greater variation in the pore pressures at depths between one and five meters coupled with the lower shear strengths due to lower effective stresses would lead to a less stable embankment. The greater variation in pore pressures at depth within the present climate simulation was due to the increased relative permeability of the profile allowing the water to move more freely through the profile. The drier profile of the future climate simulation did not allow such free movement of water.

The present day simulation highlighted the shortcomings of the single phase, six month summer, six month winter simulation. Pore pressures were shown to vary along the surface and peak summer suctions were shown to occur over a period of a few days. The hydraulic simulations showed how the pore pressures responded to two different climate scenarios. The change in climate did not only give a change in surface pore pressure variation but also pore pressure variation at depth. The differences between the two climates were also not uniform across the embankment. The future climate showed greater variation at depth below the crest due to evaporation from the ballast layer but the present climate scenario showed greater variation at depth on the sides of the embankment due to variations in effective permeability. The future climate simulation showed an overall average decrease in pore pressures which would therefore lead to higher shear strengths and greater stability. The future climate scenario would also lead to greater pore pressure variation at depth which would lead to larger shrink swell cycles and therefore enhanced strain softening of the clay material. The greater deep pore pressure, variation, however was limited to beneath the crest of the embankment. On the embankment sides the deeper pore pressures of the future climate scenario vary less than those of the present climate scenario. This would lead to greater shrink swell within the present climate scenario simulation. The surface pore pressures of the future climate scenario showed the greatest variation but this variation did not persist to depths greater than one meter. These two different climate scenarios showed great divergence in pore pressure variation which would lead to very different shrink swell cycles and therefore stability. By applying these two different scenarios to the geotechnical model the level of impact on the stability of the embankment could be gauged.

5.3.6 Flac-tp analysis

The same grid as used for the permeability analysis was constructed within the Flac-tp program, Figure 5.12. To simulate the staged construction all the embankment material was allocated the null material parameter. This effectively gave the material zero

weight, stiffness and strength. A hydrostatic pore pressure profile and associated saturations were then applied to the clay foundation assuming a water table present at one meter depth. The embankment was then built in seven layers over a period of 28 days. Each layer of clay fill was prescribed an initial suction of 50 kPa. This suction was considered reasonable for the clay fill at the time of construction of a typical railway embankment (Nyambayo et al, 2004). The construction was simulated by allocating the embankment material properties to the embankment layers. The large displacements modelled during this process within the applied layer were removed before the next layer was constructed. Each layer was allowed to settle for a period of four days during which a suction of 10 kPa was applied to the surface. After the construction the embankment was allowed to settle with a surface suction of 10 kPa for a period of five years as per the permeability study. This period was stipulated to allow the embankment to reach equilibrium and, therefore, create the initial condition of a built embankment with uniform pore pressure distribution for the application of the present and future climate scenarios.

The results of the SHETRAN simulation were analysed to determine the average time of year for the swell and shrink condition switch over. These times were then applied to the simulation code to command the Poisson's ratio switch over. A file was then created for both the present and future climate daily surface pore pressures. These files were placed within the respective simulation files and the fully coupled simulations run.

5.3.7 Flac-tp results

The surface pore water pressures were transferred to the Flac-tp program. The simulations were run as per the method set out in chapter 4 with the mechanical component of the model turned on. The models run for these simulation were, therefore, fully coupled simulations. The models were then both run for a period of 20 years. Figure 5.27 shows a plot of the variation of pore pressures for the first three years of the simulations. This plot shows that there was no discernable difference between the pore pressures of the coupled and uncoupled simulations. The process of transferring the surface pore pressures from SHETRAN for a fully coupled analysis therefore seems reasonable.

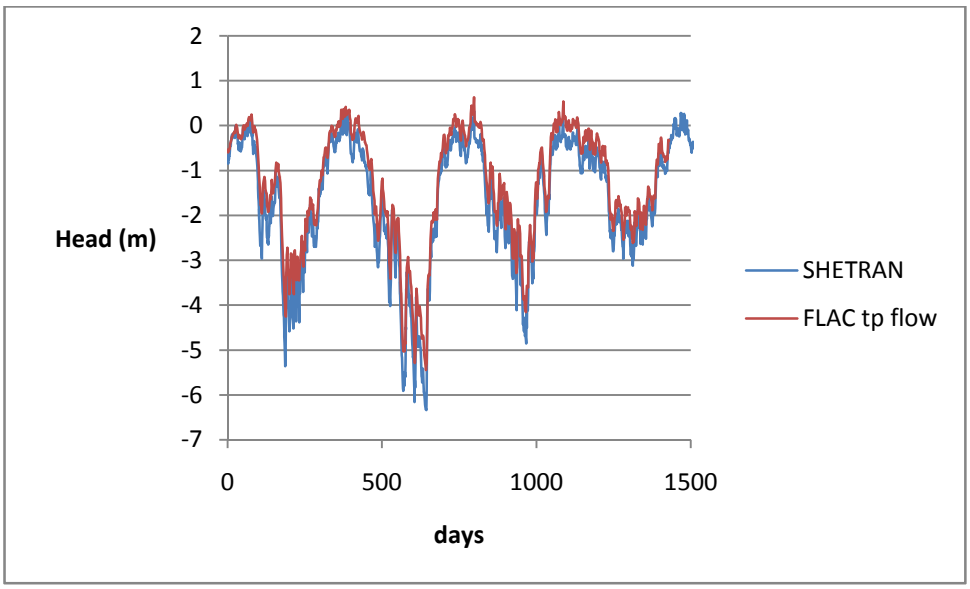

Figure 5.27 Plot of pore pressure variation at the toe of SHETRAN and Flac-tp for a coupled simulation

The present climate slope failed within the fifth year. Figure 5.28 shows the variation in horizontal displacement before failure occurred. The accumulated slope displacement after the five years swelling, prior to cycling, can be seen to have reached 30mm. After the first winter the effects of the saturation were seen as the slope moved up to 15mm during this period. The summer suctions then took effect and the slope midpoint regressed by about 5mm. The next winter resulted in another large displacement and after this point the displacements reduced although there was still a net down slope movement after each cycle. The failure was seen to occur at the beginning of the fifth winter. Figure 5.28 can be compared with the pore pressures at the toe of the slope shown within Figure 5.20. This shows maximum displacement occurs after the maximum pore pressures were reached, sometimes up to 75 days since the slope was saturated. Failure occurred within the slope after a particularly wet summer where suctions reached only around 20kPa. It can be seen from these plots that the variations in horizontal movement the slope experiences are closely related to the pore pressure variation. The failure occurred after a particularly wet winter. This seems reasonable as the slope during this summer would have had relatively low suctions. These suctions did not persist long into the winter. This effectively lengthened the period the embankment was saturated for. Infiltration was also less hindered by the wetter slopes which lead to higher pore pressures throughout the embankment and, therefore, increased displacement which lead to failure.

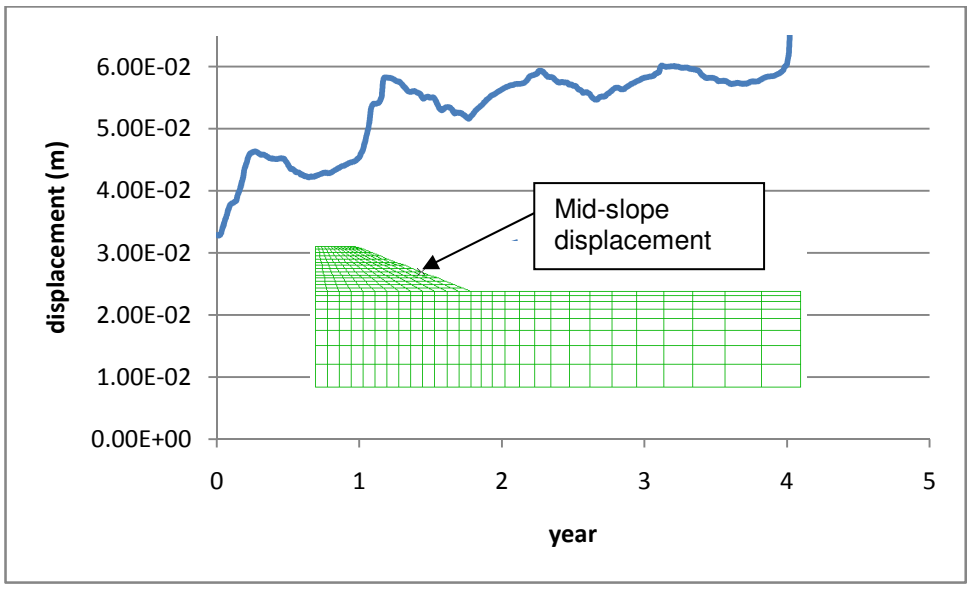

Figure 5.28 Horizontal displacement at mid-slope of embankment subjected to a present climate (positive displacement downslope).

The future climate slope remains stable after the 20 year cycle although significant softening has occurred. Figure 5.29 shows the mid-slope displacement for this simulation. After an initial swelling the net horizontal displacement reduces and the slope shows an initial net shrinkage. This was due to the slope drying out as a response to the high summer suctions (Figure 5.20). The slope did, however, begin to soften at the toe and the net annual displacements showed the midpoint began to move down slope. The movements were however small due to the high suctions loading the embankment effectively pulling the slope back to near its original position. The end of winter pore pressures were also much lower than those of the present climate. This overall lower annual pore pressure cycle increased the annual effective stresses and, therefore, the stability of the embankment.

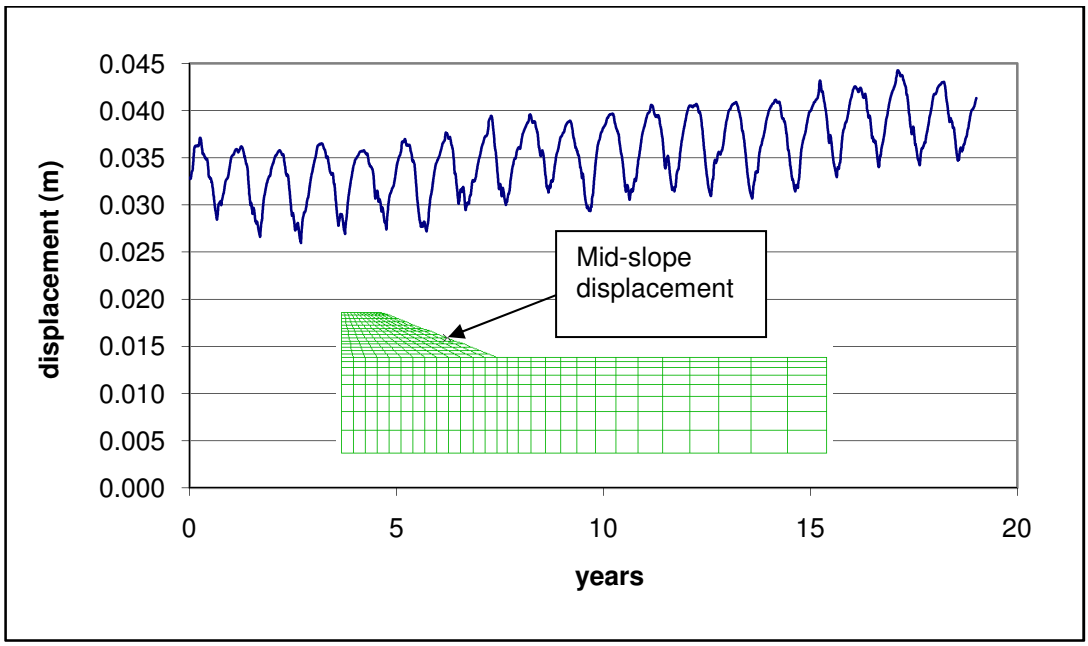

Figure 5.29 Horizontal displacement at mid-slope of the embankment subjected to a future climate (positive displacement downslope).

As per the present climate simulation the periods of increased displacement coincide with the extremities of pore pressure variation. The hydrological modelling has predicted a high surface pore pressure at year four. This high pore pressure has resulted in a relatively high mid-slope movement. The opposite is also true with low winter pore pressures resulting in a relatively low magnitude mid-slope movement.

Figure 5.30a shows the shear strains of the embankment subjected to a present climate after failure during the fifth year and Figure 5.30b the shear strains of the embankment subjected to a future climate after 20 years. It can be seen that the shear strains have developed within the future climate embankment over the 20 years yet the softening has not progressed enough to cause failure.

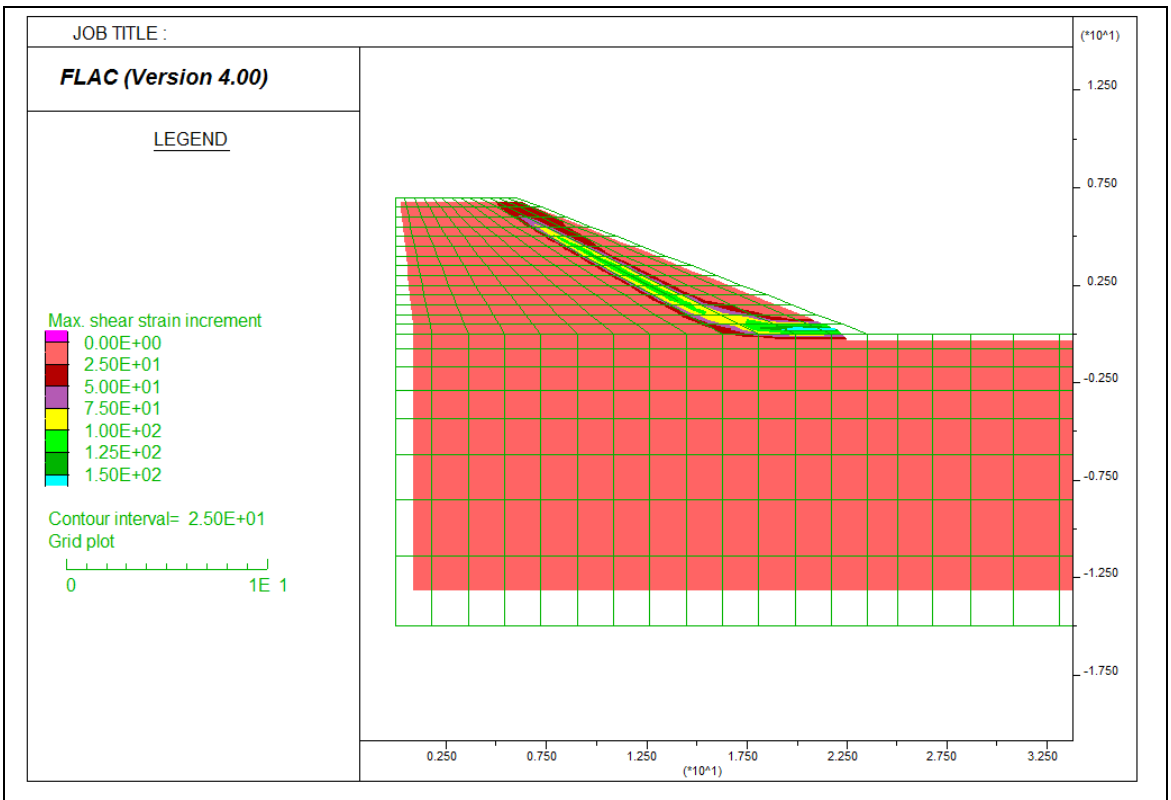

a) Present climate after 5 year simulation

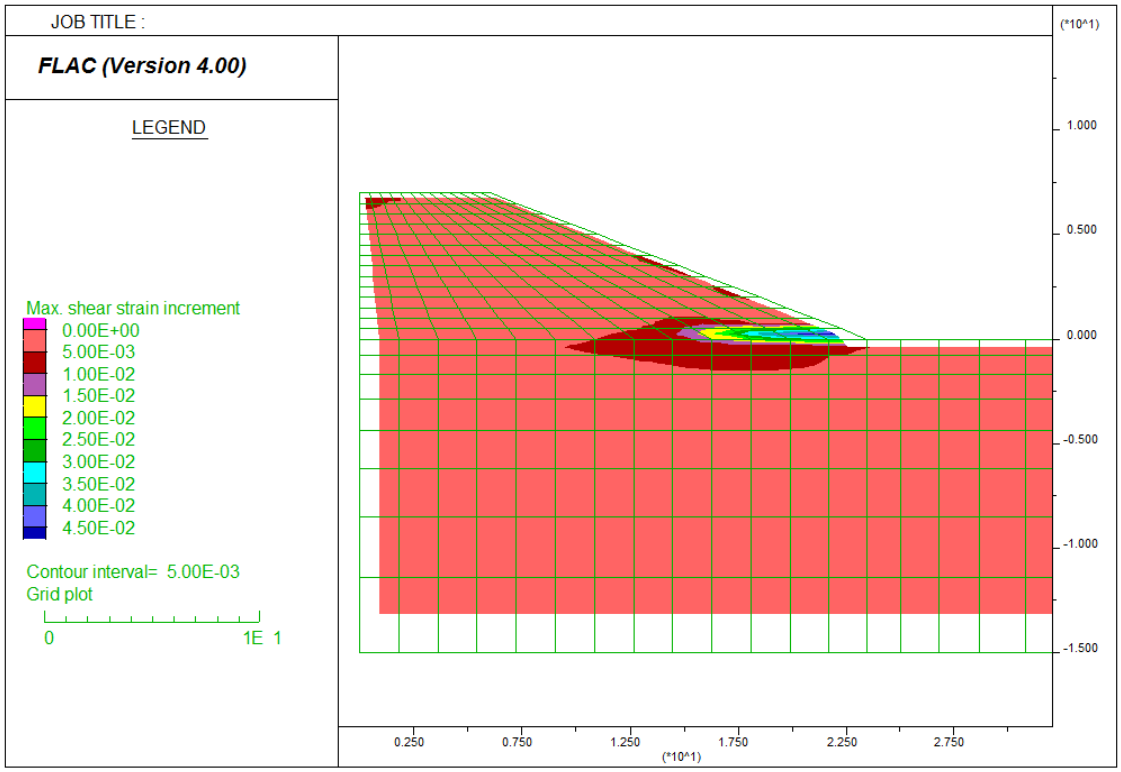

b) Future climate after 20 year simulation

Figure 5.30 Shear strain of embankments subjected to a present (a) and a future (b) climate.

The softening which developed within the present climate simulation began at the toe of the embankment and continued along and just above the foundation. The softening then accelerated through the slope body as the failure occurred. It can be seen when comparing the failure surface to the grid that the shape of the failure surface was influenced by the grid geometry. The grid elements became smaller towards the crest of the embankment which leads to a localisation effect. Each higher layer of elements required relatively less displacement to reach residual strength than the lower elements. The initial softening at the toe had been captured well whilst the elements are of relatively uniform size but the final failure mode through the smaller elements was not representative of a true failure mechanism. The present climate slope may have remained stable for a longer period if uniform elements were used but the relative stability period when compared with the future embankment can be assumed to remain similar. The simulations, therefore, show that the rate of strain softening of the embankment is considerably greater for a present climate simulation.

The future climate simulation was continued by recycling the 20 years of weather data within the SHETRAN model and then applying the additional surface pore water pressure data to the mechanical model. The model was shown to fail during year 44. A plot of the failure is shown in Figure 5.31.

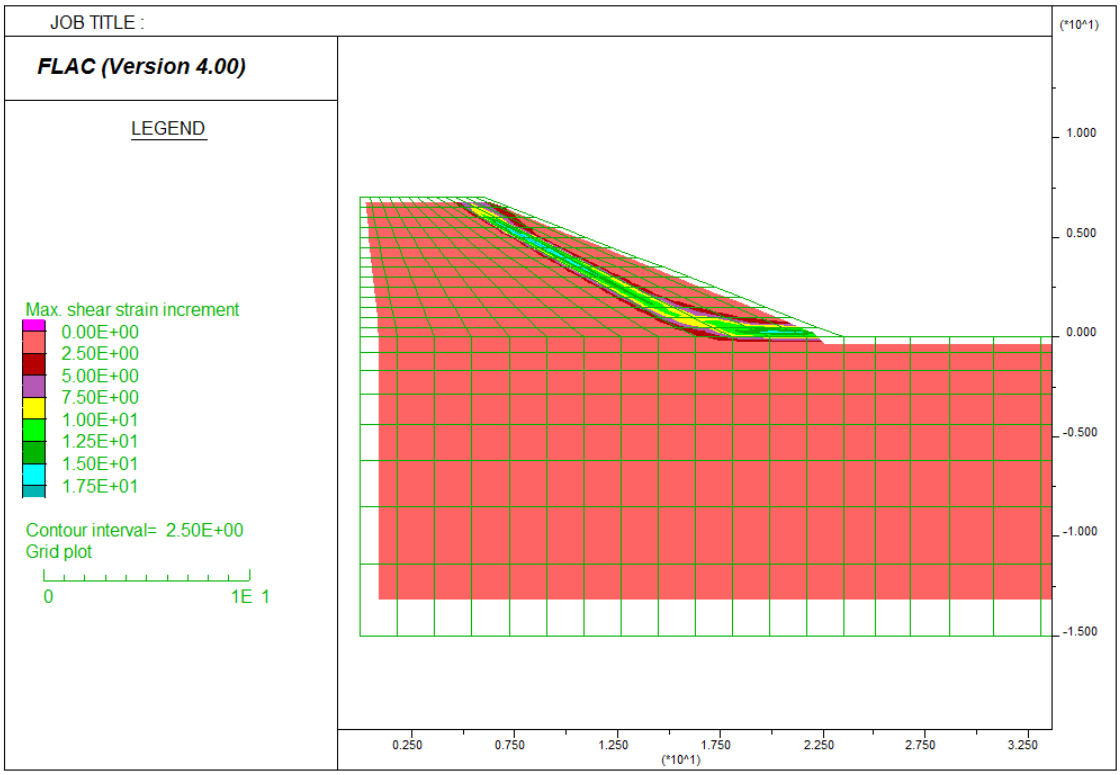

Figure 5.31 Failure plane of future climate embankment simulation during year 44.

The failure occurred during a year with pore pressures higher than average. The development of the progressive failure together with mid-slope displacement can be seen within Figure 5.32. The failure occurred even though there was no net increase in horizontal displacement over the preceding 28 years.

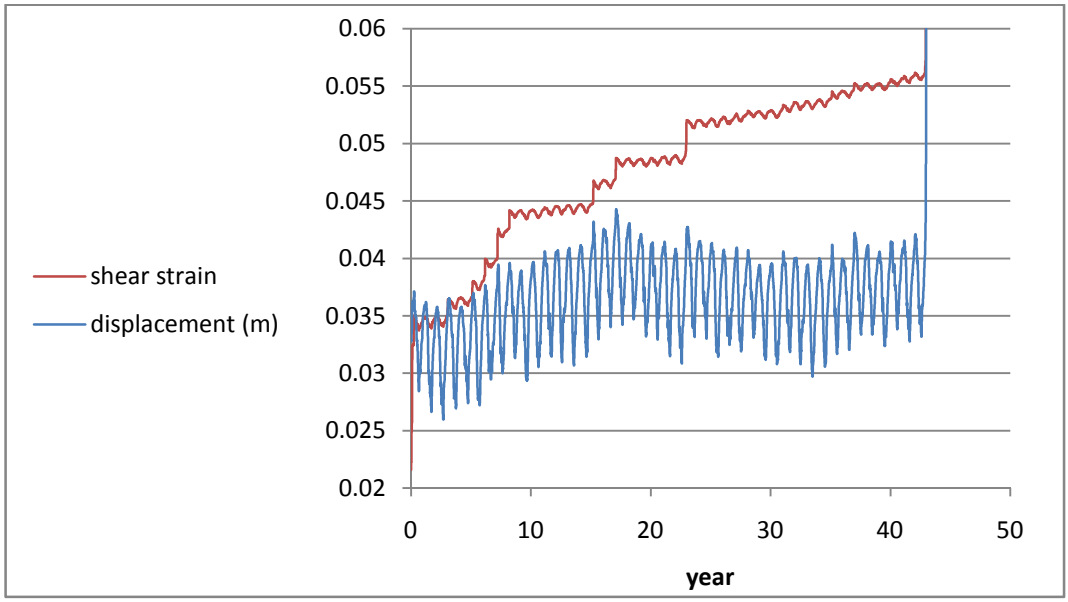

Figure 5.32 Shear strain development at the toe and horizontal displacement mid-slope during the future embankment simulation

The cyclic shrink and swell caused the softening of the toe whilst the remainder of the shear strength of the potential failure plane was mobilised. Figure 5.33 shows the state of the elements within the grid prior to failure. It can be seen the elements along the back of the failure plane are beyond maximum available shear strength. The toe softened during the cycling of the pore pressures but failure was prevented due to the high suctions within the toe. These high suctions were due to the higher future climate scenario temperatures drawing water out of the slope. The high suctions at the location of the toe resulted in high shear strength which enabled the toe to prevent failure of the slope. When the suctions dissipated during a year with higher than average pore pressures the high shear strength at the toe was lost and it could no longer prevent failure of the slope. As the toe was retaining the material during the preceding years there was no significant net down-slope displacement up until failure occurred.

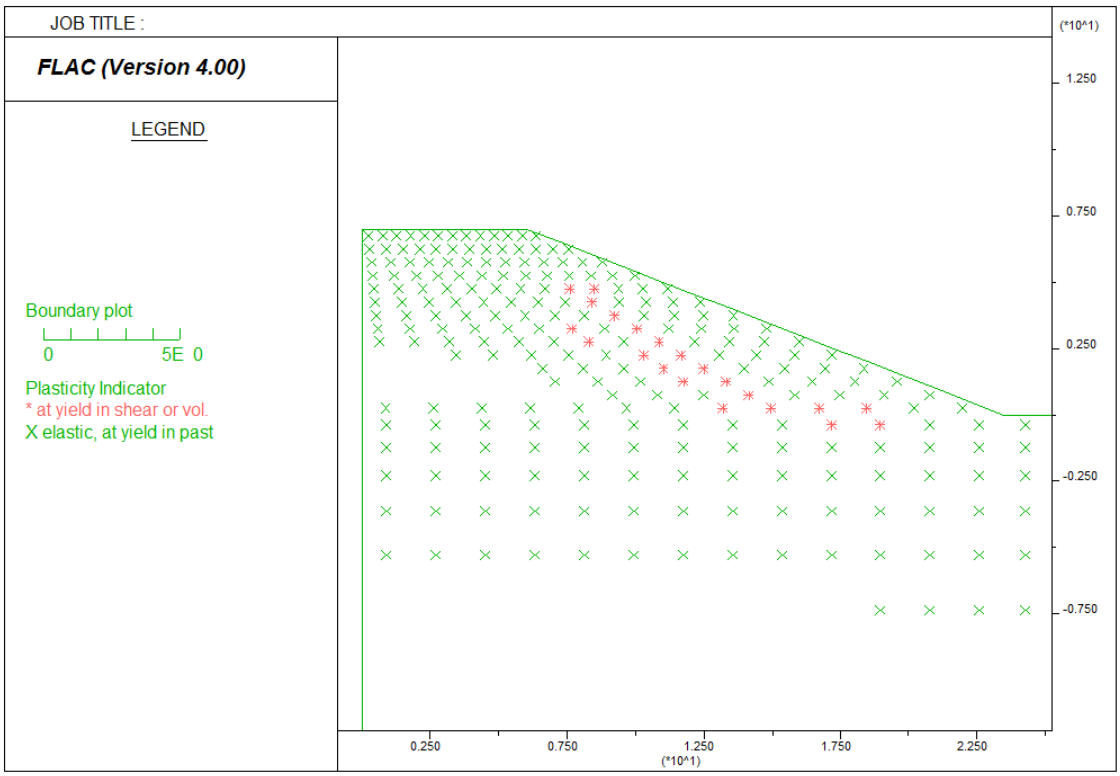

Figure 5.33 Plot of plastic state of elements for the future climate the summer prior to failure, year 43.

5.3.8 Discussion

The simulation of the diagnostic railway embankment shows that for a UKCIP02 future climate scenario for the 2080's with high carbon emissions the embankment will have lower overall pore pressures. This is due to the increase in temperature increasing evaporation from the slopes and the increase in the rate of rainfall increasing the amount of run-off. The coupled simulations show that an embankment subjected to the future climate remained stable for a longer period whilst the same embankment subjected to the present climate scenario collapse relatively quickly. The lower pore pressures within the future climate scenario lead to an overall higher effective stress. This lead to an increase in shear strength due to the suctions present and also an increase in material stiffness due to the model used to calculate the bulk and shear modulus with respect to effective stress. The seasonal pore pressure changes within the embankment subjected to a future climate were much larger (100kPa as opposed to present 60kPa fluctuations). This did not have the effect of creating significantly larger cyclic movements (due to associated increase in shear and bulk modulus) and therefore the rate of progressive failure did not increase significantly. The overall effect for the future climate simulation was less cyclic displacement and, therefore, less overall displacement. Within the present climate simulation the high pore pressures lead to swelling and softening at the

toe of the embankment. The softening at the toe progressed into the embankment as per previous simulations. The softening then accelerated into the embankment and a reasonably shallow failure was predicted.

The present climate simulation showed the greatest displacement of around 15mm after the first winter as the embankment swelled. This first swell, therefore, softened the embankment considerably before cycling began. The initial future climate displacement was much lower at around five mm. The failure for the present climate simulation was, therefore, partly due to reduced shear strength as a consequence of the high pore pressures achieved each year as well as the cyclic deformation.

The future climate, due to high temperatures and run off, did not achieve the high pore pressures required to generate the deformations seen within the present climate simulation and, therefore, retained high shear strengths throughout the beginning of the simulation. The rate of progressive failure was, therefore found not to be just a consequence of the magnitude of shrink swell cycles but also of the maximum pore pressure magnitude within the slope.

This simulation shows that for saturated embankments with a marginal factor of safety a future climate would reduce the overall pore pressures and, therefore, increase stability. Progressive failure would still occur but due to the reduced maximum pore pressures the rate would be greatly reduced.

There was confidence in the prediction of softening at the toe of the present climate embankment; however, the accelerated softening that occurs within the embankment follows the grid orientation. This softening, therefore, seems to be influenced by the grid used. The elements become smaller with increasing height within the embankment. As a unique strain softening rate was specified throughout the grid the smaller elements required less displacement to reach residual strength than the larger lower elements. This coupled with the lower slope having already softened and unable to take the pressure exerted by the upper slope lead to the accelerated softening and catastrophic failure of the slope. It is, therefore, clear from this study that when using the strain softening model a uniform grid size should be stipulated.

5.4 Newbury cutting case study

5.4.1 Introduction

The aim of this simulation was to verify the hydrological modelling for a monitored infrastructure cutting. Once this aim was achieved the surface pore pressures were prepared for transfer to the Flac-tp program. The site to be modelled was a cutting on the Newbury bypass in Southern England. The site had been extensively monitored by Smethurst et al. (2006). The cutting height was 8m and its length was 28m, the profile of the slope can be seen in Figure 5.34. It was cut in London clay in 1997. The London clay in the area was about 20m thick and the top 2.5m (from original ground level) has been extensively weathered. The cutting material consists of predominately stiff grey clay although there are several bands of silty clay and also bands of large flints present within the slope. The weathered clay was found to be a highly variable material changing from a stiff orange brown clay to a clayey silt over small distances and depths. Vegetation on the slope consisted of mainly rough grass and herbs with some small shrubs of less than 0.5m high (Smethurst et al, 2006).

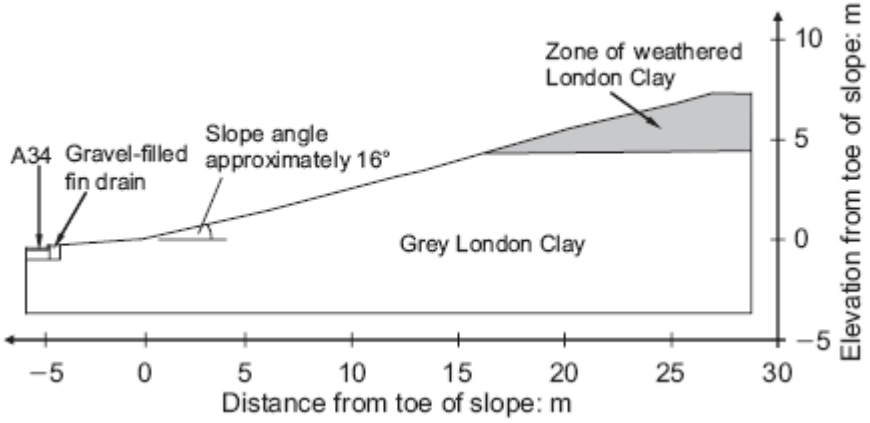

Figure 5.34 Newbury cutting instrumented by Smethurst et al (2006)

5.4.2 Seasonal pore pressure changes within the Newbury cutting

Soil suction was measured on the site using tensiometers, piezometers and equitensiometers at various depths within four clusters of instrumentation named clusters A, B, C and D. Cluster A being near the crest of the slope and cluster D about 6m from the toe of the slope. Clusters B and C were approximately evenly spaced between A and D. Various results were published by Smethurst et al (2006) but it was the pore pressure measurements which were of particular interest to the modelling work for this study. In order to validate SHETRAN the pore pressure variations would need

to be reproduced within SHETRAN. Pore pressure variation figures were produced by Smethurst et al (2006) for the tensiometer readings these are reproduced here for reference within Figure 5.35.

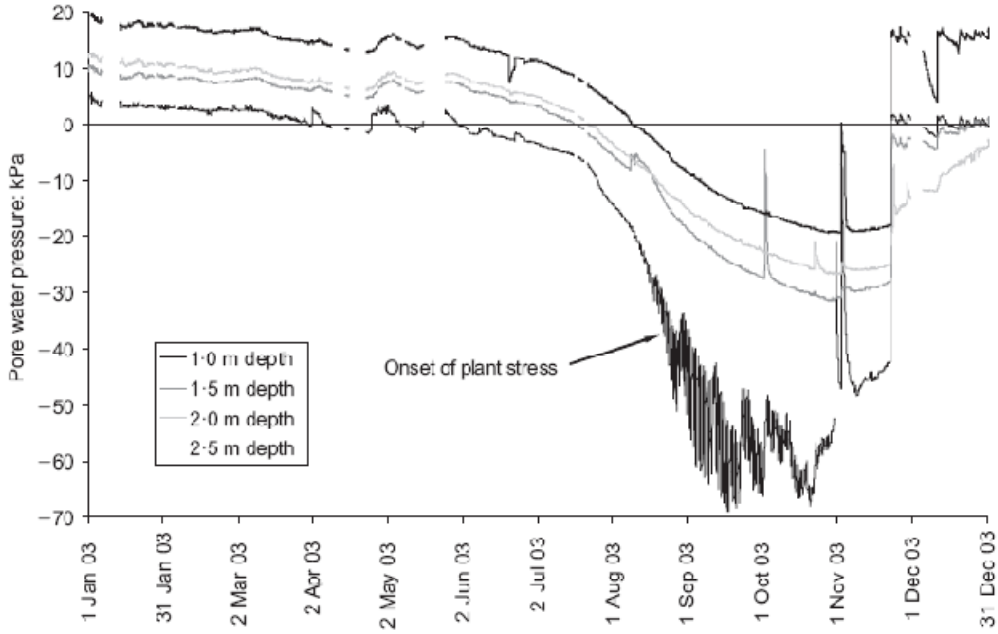

Figure 5.35 Tensiometer readings as published by Smethurst et al (2006).

Pore pressure profiles were also produced and are included for reference within Figure 5.36.

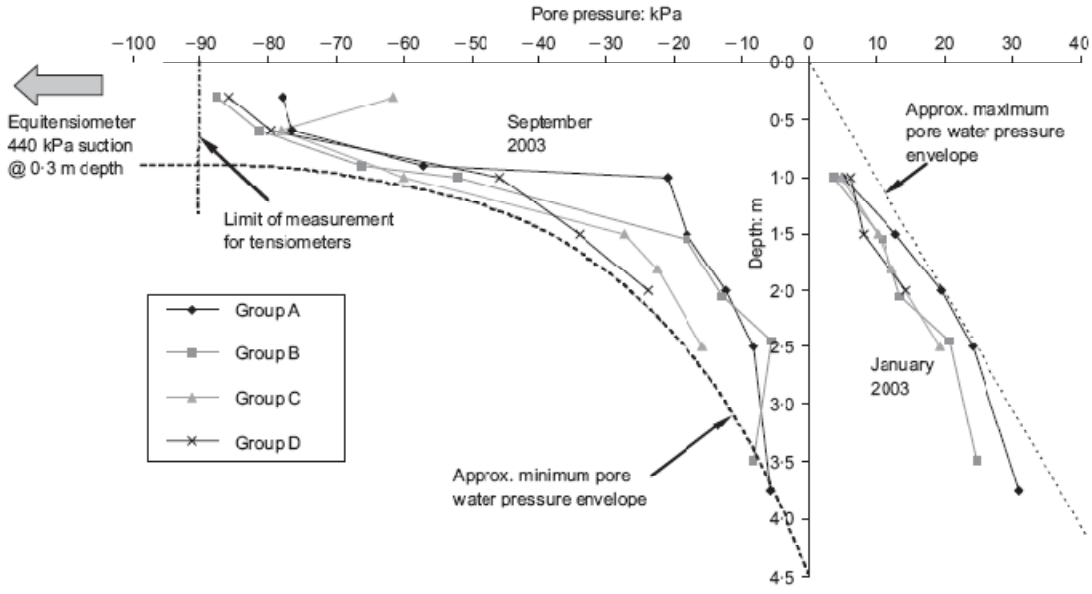

Figure 5.36 Pore pressure profiles (after Smethurst et al, 2006).

It was decided to validate the SHETRAN model by comparing the profiles created at the locations of instrument group A and instrument group C. These two profiles represent the most extreme pore pressures for the year and hence would be the most difficult to

reproduce. If SHETRAN could reproduce a satisfactory comparison then it would give confidence in the ability of this model.

5.4.3 Weather data

On the site of the slope there was a weather station that provided rainfall, air temperature, humidity, wind speed and solar radiation. The monthly rainfall readings from this weather station were published within Smethurst et al (2006). The hourly data required for the SHETRAN simulation was sourced from a nearby MET office weather station located at Larkhill (British Atmospheric Data Centre, 2008). The location of this weather station is within 15 km of the slope and was the nearest weather station to the site with the available data. The hourly rain fall data obtained from Larkhill was summed up to monthly rainfall in order to assess comparability between the two observations. The results are shown within Figure 5.37.

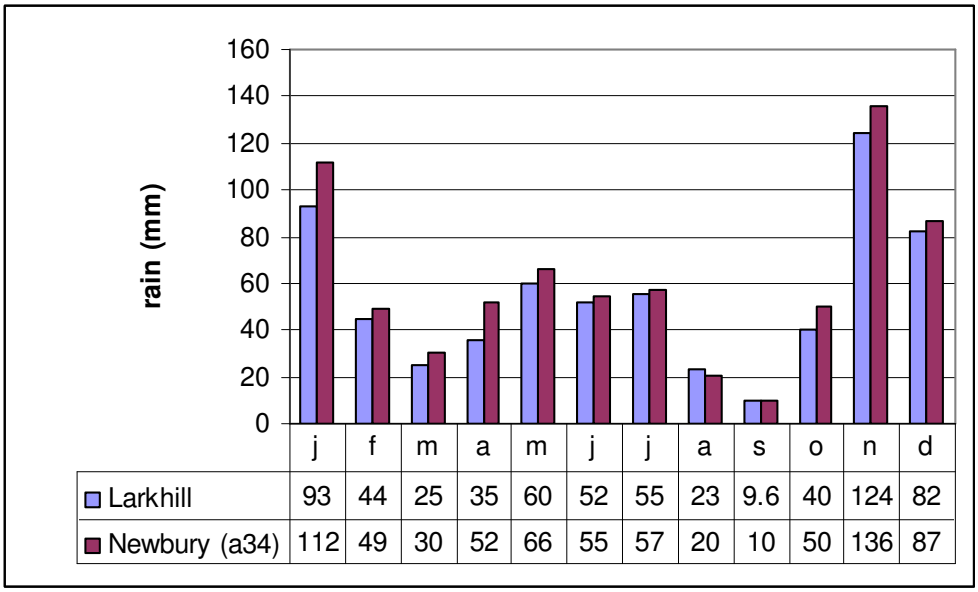

	j	f	m	a	m	j	j	a	s	o	n	d
Larkhill	93	44	25	35	60	52	55	23	9.6	40	124	82
Newbury (a34)	112	49	30	52	66	55	57	20	10	50	136	87

Figure 5.37 Comparison of rainfall data published by Smethurst et al (2006) and summed hourly rainfall data from Larkhill weather station (British Atmospheric Data Centre, 2008).

It can be seen from Figure 5.37 that the rainfall observations compared well with the weather station on the slope observing slightly more rainfall per month than the Larkhill weather station. This simple comparison exercise highlights the very site specific nature of rainfall magnitude. The climatic data from the on site weather station was used to estimate potential evapotranspiration levels using the Penman-Monteith method as discussed within Chapter 2. The monthly values of PET were also published within Smethurst et al (2006). PET was therefore also calculated using Penman-Monteith

method for the Larkhill hourly climatic data. For the purposes of this calculation the reference vegetation cover was assumed to be grass. The hourly PET levels were combined into monthly readings in order to again assess the comparability with the published on site data. The comparability can be seen within Figure 5.38.

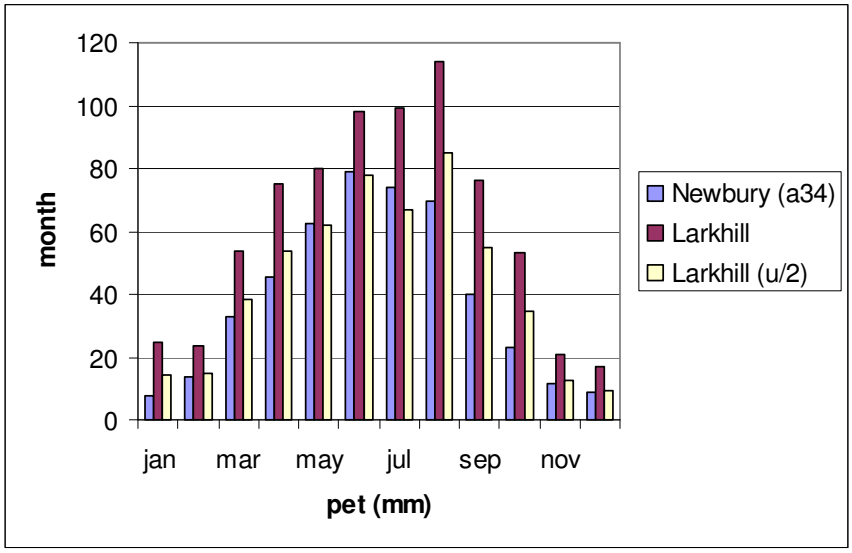

Figure 5.38 Monthly PET levels as published within Smethurst et al (2006) (Newbury a34), monthly PET levels calculated from Larkhill (British Atmospheric Data Centre, 2008) weather station data and monthly PET levels calculated from Larkhill weather station data with scaled down wind speed (Larkhill (u/2).

Figure 5.34 shows that the calculated PET from the weather station at Larkhill was much larger than the PET measured on site. The reason given for this is that the MET office weather stations are required to be located in open ground and exposed to the elements. The weather station on the slope at Newbury was not on open ground. The weather station on site was on an East facing slope which was fringed at its crest by mature trees. These observations coupled with the fact that the winds within the U.K. are predominantly Westerlies would suggest that the on site weather station was experiencing much less wind than the MET office weather station. The Penman-Montieth equation is very dependent upon the wind speed measurements used. This observation can also go some way to explaining the apparent increase in divergence between onsite weather station and the MET office weather station over the summer months. During the summer months the difference between the onsite and MET office weather stations reaches over 40mm whilst during the winter months the reduces to around 10mm. This could be explained by the effects of the canopy of deciduous trees at the top of the slope providing more shelter during the summer months therefore reducing PET. During the winter months the canopy of the trees has been vastly

reduced therefore allowing more wind through and hence more comparable PET rates to the weather station on open ground. It was decided to reduce the wind speed measurements, *u*, of the MET office climate data by a factor of 2 (u/2) to allow for shelter of the slope to be modelled. The new PET measurements calculated using the adjusted wind measurements is also shown within Figure 5.34. The new PET measurements calculated using the revised wind speeds give much better comparison to PET calculated from the onsite climatic data although there is still a greater divergence through the summer months August, September and October. This may be due to a thicker canopy at the top of the slope although the effects would be expected to be seen from at least March onwards. Again this variation between the calculated PET for weather stations 15 km apart highlights the need for site specific data to correctly assess slope stability with respect to climate. The data was, however, deemed sufficiently accurate to be used for the simulation exercise.

5.4.4 Vegetation data

The slope was vegetated with mainly rough grass and herbs with some shrubbery less than 0.5m high (Smethurst et al, 2006). For the purposes of the SHETRAN simulation it was assumed that the slope was vegetated with predominantly grass. The parameters used for the grass within the simulation were obtained from previous vegetation modelling experience within SHETRAN. The parameters are detailed within Table 5.4.

Table 5.4 Vegetation properties for grass used within SHETRAN simulations.

Canopy storage capacity	1e-4	m
Fractional rate of change of drainage water storage	5.1e3	1/mm
Leaf drainage rate when storage = C_s	14e-9	mm/s
Canopy resistance factor	100	s/m
Root density function Given as a number of pairs (layer depth : amount of soil moisture absorbed as fraction of total transpiration)	0.3m 100% of roots	-
Leaf Area Fraction Given as a number of pairs (layer thickness : ratio of leaf area to area of element) Time series used enabling LAF to vary throughout the year	18th Nov LAF=0.5 10th April LAF =0.50 10th May LAF =0.7 10th July LAF =0.9 LAF	-

5.4.5 Hydrological simulations

The hydrological simulations were run within SHETRAN. All cells used to model the first 3m of the sub-surface had an equal height and length of 0.5m and 1.75m respectively. The remainder of the cells below this depth were scaled up in order to reduce run times. The crest of the slope was assumed to be horizontal. A crest length of 6m was specified after which it was assumed the pore pressure profile was also assumed to be horizontal. At the base of the slope the ground was considered to extend horizontally for 8m beyond the toe. No flow boundaries were applied to both horizontal extremities. Hydrostatic initial conditions were applied throughout the grid with a phreatic surface assumed at a depth of 1m. Figure 5.39 shows the initial pore pressures and the geometry of the model. This pore pressure profile was an approximation of the profile within the slope at the beginning of the simulation period (January 2003). The bottom boundary was at a depth of 12m. This depth corresponded with the depth of the London clay in the area. The bottom boundary condition varied from a free boundary to various specified heads during the simulations. A free boundary allowed the head at the base to vary considerably. Specifying a head at the base allowed the head to increase at the base boundary but not drop below the specified level, i.e. recharge from the surface can raise head at the base but if the base level drops significantly recharge is provided at

the base to keep the head at the specified level. Free draining soil was specified for a column of material at furthermost distance from the toe of the slope. A fixed head was specified as the bottom boundary condition for the soil in this column. This allowed the drainage of surface water run off from the model. The van Genuchten properties required by SHETRAN were derived from the soil suction verses gravemetric water content curve for London clay published by Croney (1977). The permeability values were taken as the minimum values from borehole bailout tests published by Smethurst et al (2006).

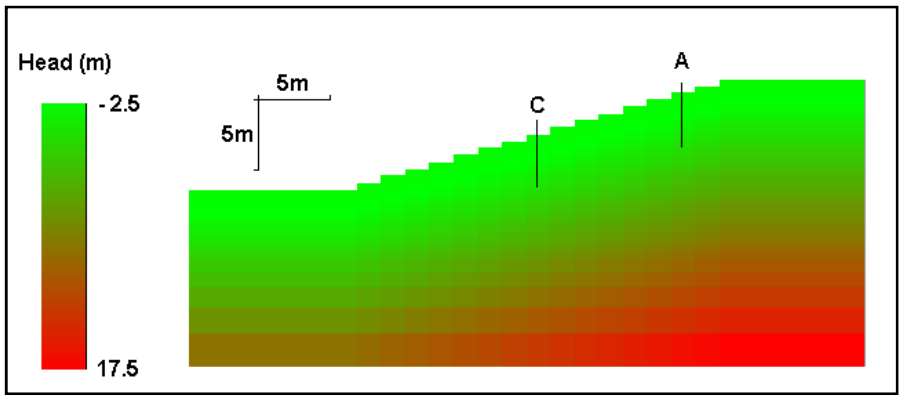

Figure 5.39 SHETRAN representation of the Newbury cutting detailing the initial pore pressure profile.

The pore pressure profiles at the locations of instrument group A and C were drawn for September 2004 and January 2004 and compared to the profiles published by Smethurst et al (2006). The comparison profiles are shown in Figure 5.40.

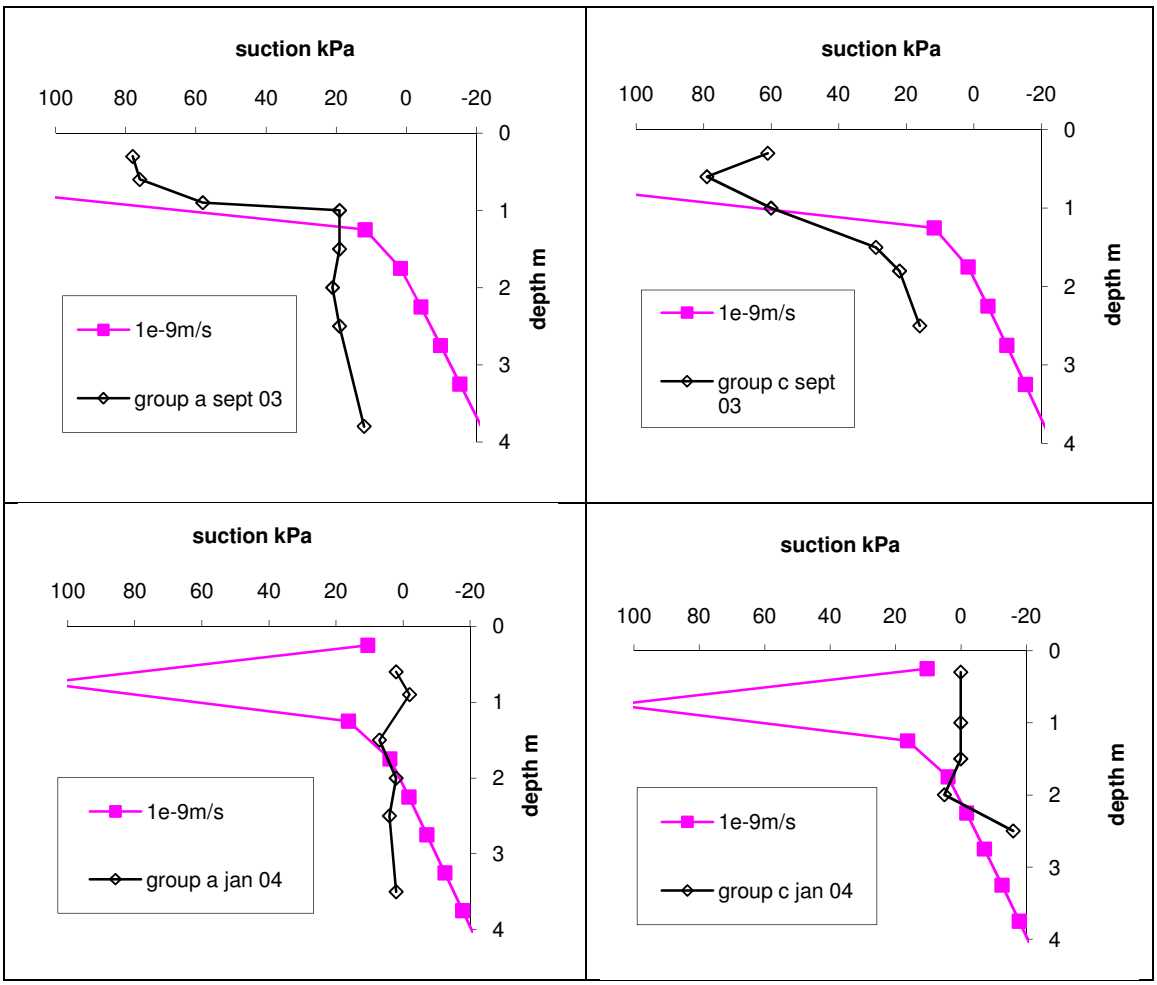

Figure 5.40 Comparison profiles of SHETRAN simulations and those published by Smethurst et al (2006) for locations of instrument groups a and c and dates September 2003 and January 2004.

It can be seen from these profiles that there was no good comparison between the observed and simulated pore pressures. The simulated pore pressure profiles show that seasonal surface processes have not infiltrated more than 1m into the embankment whereas within the published data the surface processes have managed to influence depths greater than 4m. It was considered that with all that with the all the data being comparable to the Newbury slope the only parameter which could reasonably allow the level of seasonal variation was the mass permeability. The mass permeability of the slope was, therefore, decreased by first one order of magnitude and then another order of magnitude.

Figure 5.41 shows the profiles for the original mass permeability and a mass permeability of $1x10^{-8}$ m/s and $1x10^{-7}$m/s. These profiles show that the simulated profiles became more comparable to the published profiles with each decrease in mass permeability. The $1x10^{-7}$ m/s permeability simulation gave the best comparison. The

measured data at instrument group C showed a maximum suction of 80 kPa, this maximum suction was most likely exceeded as this was close to the limit of the tensiometer instrument used. Equitensiometer data at this location showed that this suction increased to a maximum of 440 kPa at 0.25m depth (Smethurst et al, 2006). At this location SHETRAN captured the variation of pore water pressure with depth very well. The maximum suction of 440 kPa was not reproduced yet a very high suction of 250kPa was simulated at 0.25m depth (see Figure 5.42). The comparison at the same permeability for the location at instrument group A was not as close as that at instrument group C. SHETRAN had, however, managed to model the pore pressures at the top of the profile (suctions too high for measurement) and at the bottom of the profile reasonably well. This profile was within the weathered London clay material which was highly spatially variable. The soil within the SHETRAN simulation was assumed to be homogenous. This would explain why SHETRAN has not managed to fully capture this complex pore pressure profile.

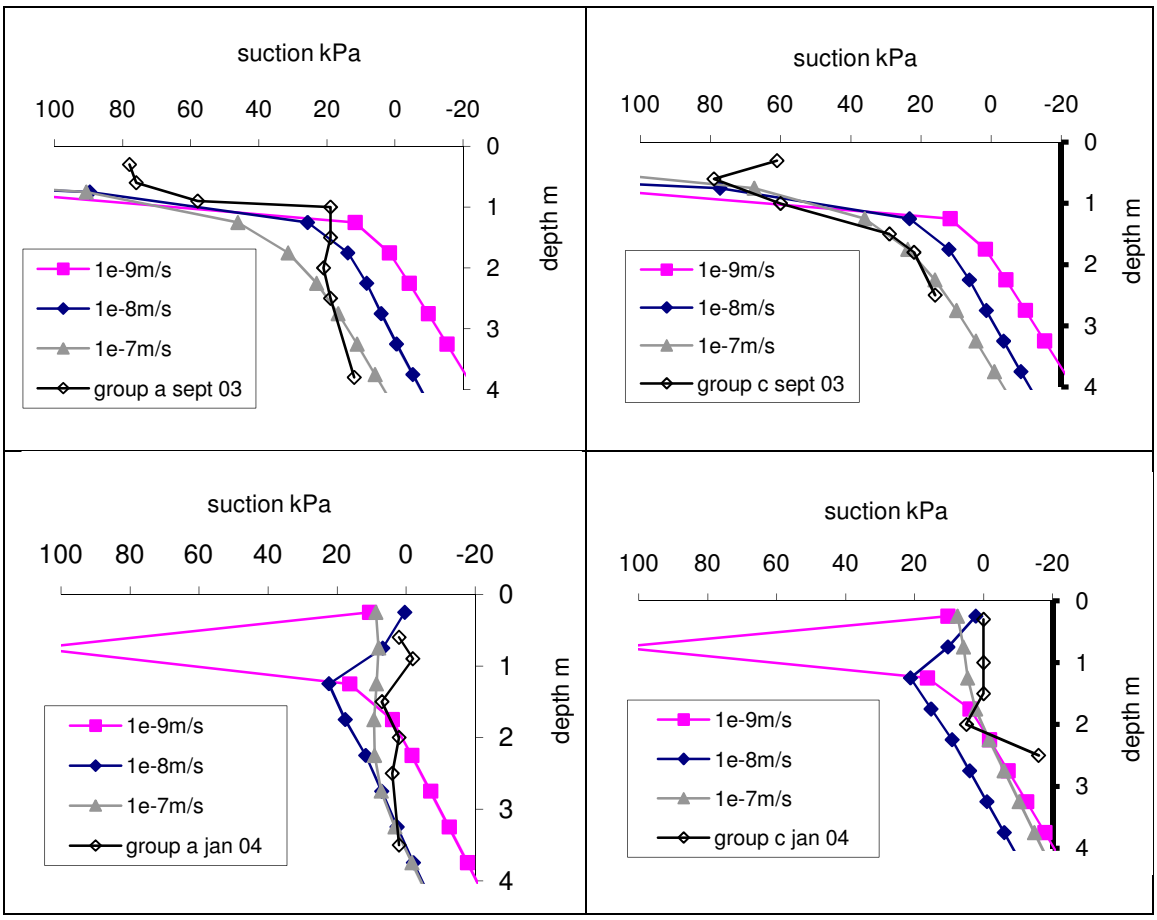

Figure 5.41 Comparison profiles of SHETRAN simulations with reduced mass permeability and those published by Smethurst et al (2006) for locations of instrument groups a and c and dates September 2003 and January 2004.

The simulations were continued for another three years. The variation in pore pressures below instrument group C can be seen within Figure 5.42. This figure shows the variation in seasonal pore pressure variation. The winter of 2002 was very wet which gave rise to very high pore pressures at the beginning of 2003. The summer of 2003 was also exceptionally dry and that resulted in the high negative pore pressures within the slope at the end of September 2003. The pore pressures at the end of 2003 have also not recovered to their end of 2002 maximum owing to the dry summer. Also the suctions at the end of September 2004 were not as high as the previous year. 2005 was similar to 2004 but 2006 was once again a dry summer and high suctions similar to those of Sept 2003 were once again calculated within the cutting. This dry summer was then followed by a wet period at the end of 2007 which resulted in the wetting up of the cutting once more with maximum pore pressures comparable to those of January 2003. These pore pressures were transferred to the Flac-tp program to analyse their effects on calculated cutting displacements.

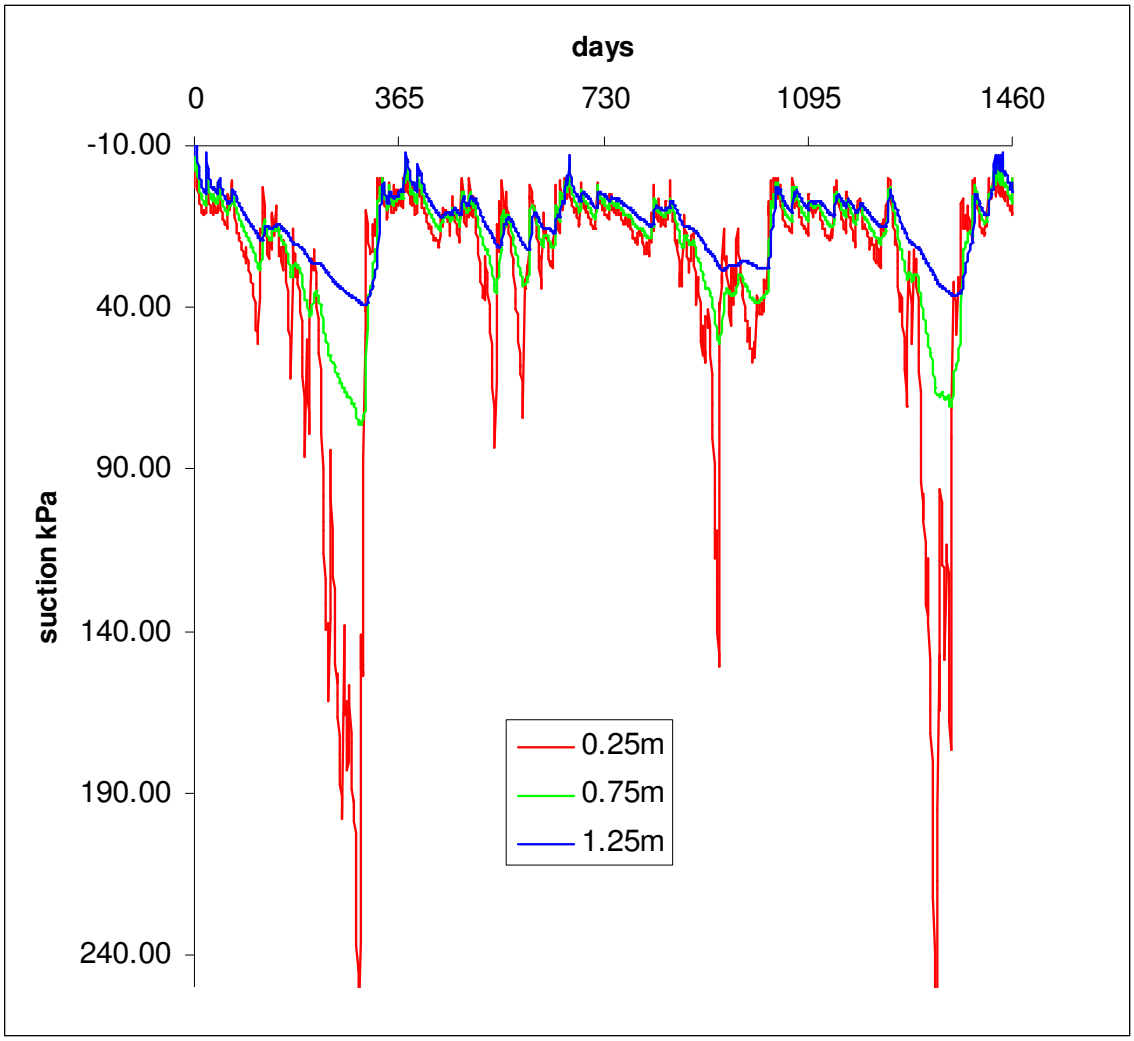

Figure 5.42 SHETRAN pore pressure variations below instrument group C from the beginning of 2003 to the end of 2006.

5.4.6 Fully coupled simulations

Fully coupled simulations for the cutting were run using parameters based on the in-situ London clay defined within the latter simulation. These are detailed within Table 5.5. As can be seen there was no distinction made between loading and unloading stiffness for this model. There was no deformation data for the Newbury embankment therefore the coupled analysis was purely diagnostic. The grid and monitoring points can be seen in Figure 5.53.

Table 5.5 Material properties of London Clay used for coupled Newbury analysis.

Dry unit weight kN/m^3	14.2
c' kPa	7
φ' °	20
Poisson's ratio	0.2
Young's modulus (kPa)	2500(p'+100) Min 4000
Coefficient of earth pressure at rest	1.5

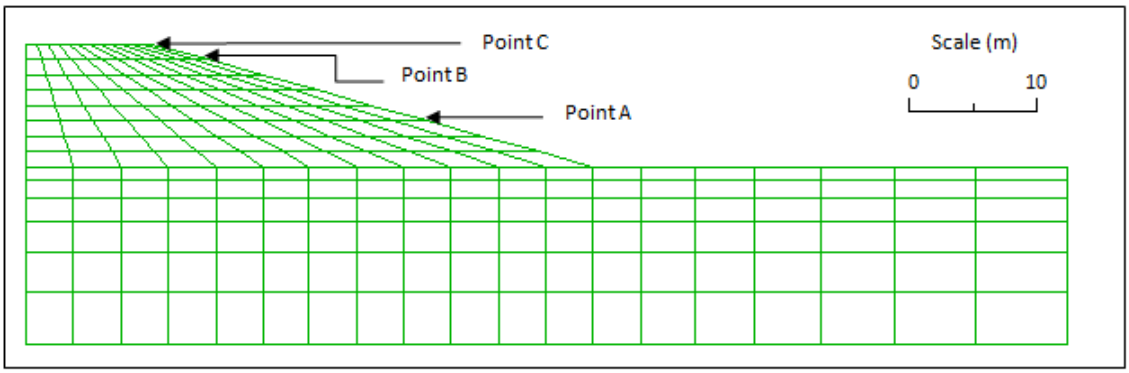

Figure 5.43 Grid used for coupled deformation analysis of Newbury cutting.

Figures 5.44 and 5.45 show the horizontal and vertical deformation respectively. The cutting shows a maximum horizontal cyclic movement of under 0.04m and vertical cyclic movement of 0.06m for the first year of the calculation. This was the period of exceptionally wet winter and dry summer. The cyclic displacements for the next two years then reduces to a horizontal average of 0.03m and vertical average of 0.04m before once again there is a dry summer and a wet winter. The model also calculates a net downward movement of the crest of about 0.04m.

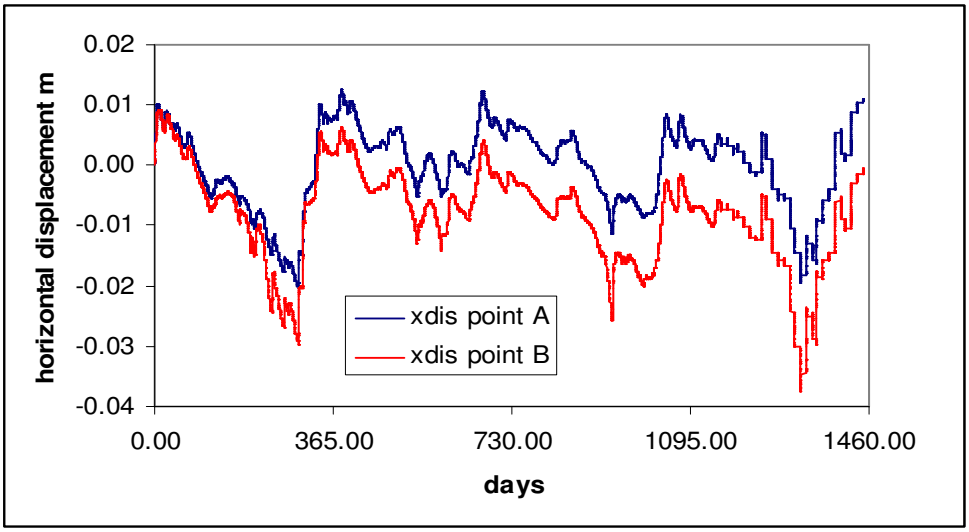

Figure 5.44 Horizontal deformation of Flac-tp coupled Newbury embankment.

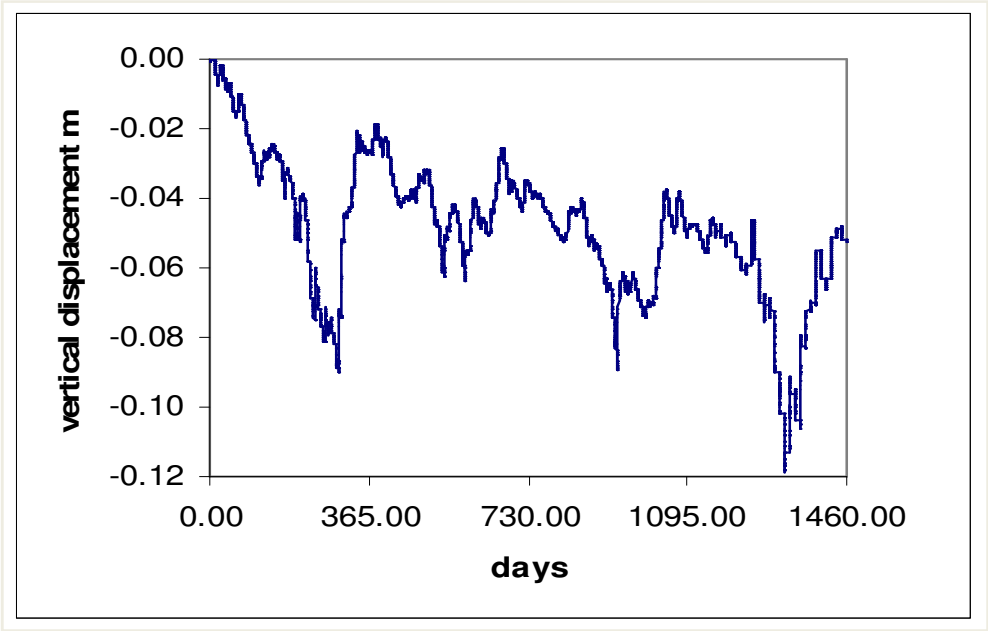

Figure 5.45 Vertical deformation of Flac-tp coupled Newbury embankment.

The cyclic movements of the Newbury slope show the dependency of movement on the climate, particularly extreme seasonal variations. Correctly calculating the seasonal pore pressure variations within a cutting could be seen to be critical in order to accurately model deformation and subsequently the rate of strain softening which may occur.

5.4.7 Discussion

There was a great difference between the observed weather data from the site and the observed weather data from a nearby weather station. This observation has highlighted the fact that the weather variables used for hydrological simulations is very site dependent. Slope aspect and orientation together with local environment factors which may shelter the site will have a significant impact on the amount of potential evaptranspiration. This in turn will greatly effect the range of pore pressures within the slope and, therefore, the magnitude of the shrink swell cycles. In order to correctly assess the pore variation of a particular site it would be beneficial to have an on-site weather station. Observations of the climatic variables can then be compared to past historcal climatic data, such as obtained from a nearby weather station, or generated weather data from weather generator software such as EARWIG. Correction factors can then be introduced to the remote weather station data or the generated weather data to take into account site specific environmental factors. The process used within this exercise was a simple reduction of MET office Larkhill windspeed by a factor of 2. The results show that the PET of the corrected weather station data compared well with the

PET observed on site. The rainfall data compared well with no correction factor used. This may not be the case where the site may be sheltered and a corection factor must also be used for this data set in all simulations. It will not always be practical to place a weather station on every slope to be simulated. The simulations for these sites will need to use either generated data or data from an remote location. It will be usefull in these situations to obtain as much information about the site as possible regarding slope aspect and possible sheltering from both wind and sunlight. Further simulations can then be run using estimated correction factors. Coupled simulations will then need to be run for all these corrected scenarios. Where other hydrological obserations have been made around the site, such as pore pressure data observations, these observations can be used with the simulation results to determine the best fit weather correction factors. The effects of the correted weather data can be seen within figure 5.38. The original weather data from Larkhill had a higher PET rate than that observed directly on the slope. Using the weather data directly from Larkhill would have, therefore, resulted in more water being drawn from the slope and therefore reducing the pore pressures significantly. Comparison of Figures 5.42, 5.44 and 5.45 shows the close relationship between pore pressures and displacement. It could, therefore, be assumed that without the corrected weather data the stability of the slope would be overestimted.

The study of the cuting has also highlighted shortcomings in the determination of macroscopic permeability of geotechnical structures. The initial SHETRAN runs used a permeability equivalent to that determined from on-site borehole bailout tests. These tests derived a permeablity of around 3.7e-9 m/s. When the SHETRAN results were compared to the published pore pressure profiles it could be seen that the pore pressures at depth within the SHETRAN simulation were not responding as quickly as the measured pore pressures on site. As the weather data was shown to be comparable and the initial conditions were also correct it became apparent that the only parameter variable which could account for the sluggish pore water response was the permeability. When the permeability was reduced the pore pressures at depth became more responsive to the surface fluctuations and a good comparison to the measured data was achieved. The permeability which gave the best cpmparison was 1e-7 m/s, around 2 orders of magnitude greater than that measured on site and three orders of magnitude greater that that measured on triaxial samples within the laboratory. Soil fabric, particularly silt partings and fissures, and anisotrpy in the field were suggested as reasons form the greater permeability in the boreole tests (Smethurst et al, 2006). It has already been

stated that soil permeability is heavily dependant upon the volume of the soil being tested (Lu and Likos, 2004). The volume of the slope is much greater than that of the borehole and will contain many silt partings and fissures. As the considered soil volume increase theses features can become linked and will therefore begin to influence the macroscopic permeabilty more by increasing it significantly. As much larger scale testing of soil permeability is often not practical it appears that the most accurate way of measuring permeability is by measurment of pore pressures and back analysis such as performed within Section 5.4.5. As this in itself can prove costly and time consumming a less accurate alternative will be to scale the permeability from field tests used empirically based observations. It is the opinion of the author, however, that measurement and back analysis will be far more adavantageous as it will also be able to identify the effects of hidden macroscopic features, with a particular volume of soil, on pore water flow which could easily be missed by field testing alone.

5.5 Newbury cutting climate sensitivity study

5.5.1 Introduction

This section of the study has taken what was learnt from the diagnostic embankment exercise and the Newbury cutting comparison exercise to develop a model capable of determining the effect of a changing climate on an actual infrastructure cutting. For this simulation a strain softening model was used.

5.5.2 Present and future climate SHETRAN simulations

The generated weather data reviewed in Section 5.2 was used for the simulations. The wind speed of the generated data was scaled down by a factor of two to allow for the orientation of the slope and fringe vegetation as per the hydrological study earlier. An identical SHETRAN grid to that used for the Newbury comparison was also used together with identical vegetation and hydrological properties. As the largest permeability of 1e-7 m/s gave the best comparison to the instrument data this permeability was applied to the cutting throughout the climatic sensitivity study. Figure 5.46 shows the pore pressure variations over a 20 year period for instrument group C for a present climate simulation.

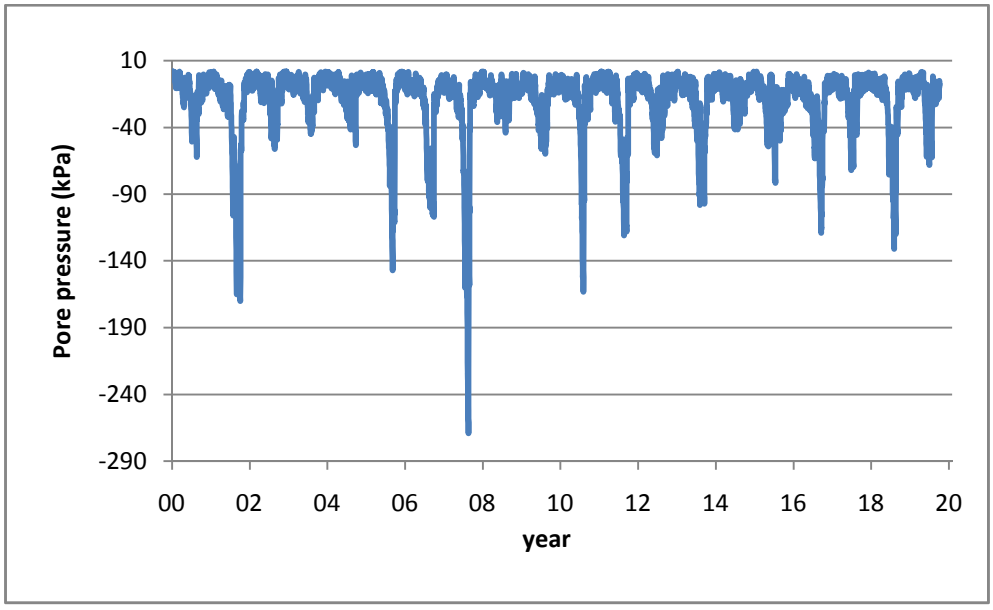

Figure 5.46 SHETRAN present day Newbury scenario.

Figure 5.46 can be compared to Figure 5.42. It can be seen that the present day climate simulation resulted in a similar pore pressure response to that of the recorded weather data. During the recorded weather data simulation the maximum suctions varied from 90 to 240 kPa. The present day simulation resulted in maximum suctions which varied

from 50 to 270 kPa. The maximum pore pressures for the present day simulation are also similar to those of the recorded weather data simulation with slight positive pressures being achieved most years. Figure 5.47 shows the pore pressure variation over a 20 year period for group C position for the future climate simulation.

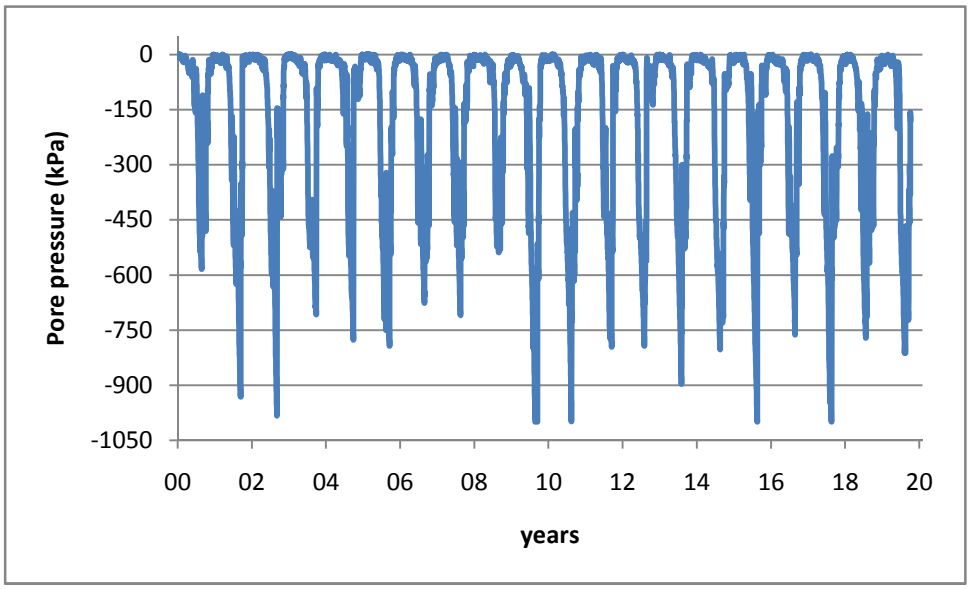

Figure 5.47 SHETRAN future climate Newbury scenario.

The future climate scenario shows that there are much higher suctions present at the slope surface. Maximum suctions were reached more often than within the present climate simulation and these suctions were around four times the suctions seen within the present climate simulation. The higher permeability of the cutting has also lead to water being able to penetrate into the embankment during the winter months more easily than seen within the embankment simulation. This has lead to pore water pressures recovering to positive pore pressures at the surface during every year.

Figure 5.48 shows the variation in head during year three for the present climate simulation. This figure shows that the seasonal pore pressure variation persists to depths greater than 6m.

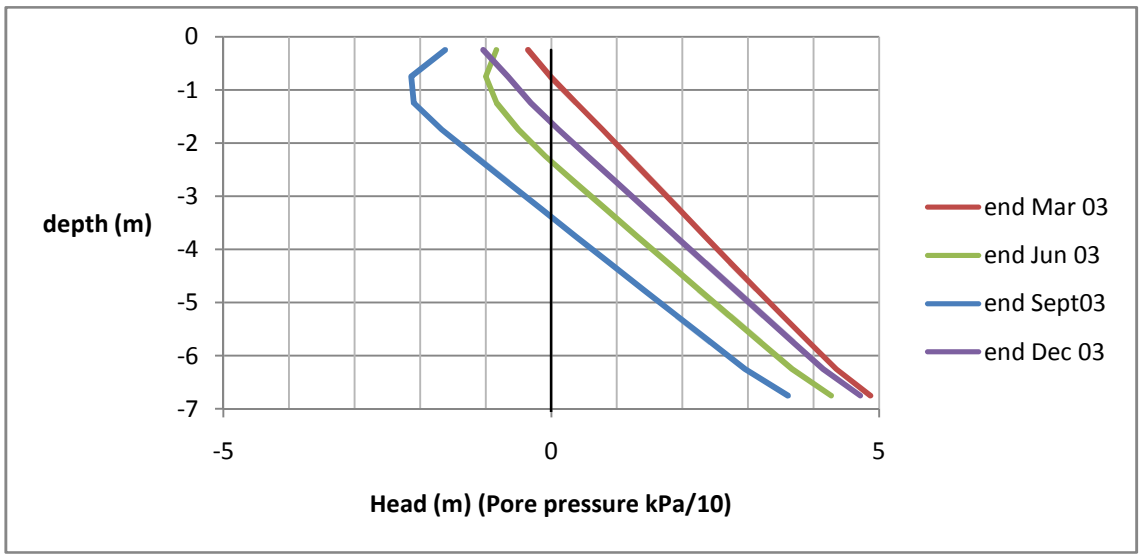

Figure 5.48 Pore pressure profiles for year 3 of the present climate simulation.

Figure 5.49 shows the pore pressure profiles for year 3 of the future climate simulation. Firstly the larger suctions during and at the end of summer are noticeable, secondly the shape of the profile shows that the greater suctions are restricted to around 2m depth. Below 2m depth the pore pressure profiles during summer become more linear. The greater pore pressure variations will therefore be restricted to this depth. This depth is controlled by the saturated permeability of the cutting. The seasonal pore pressure variation below this depth is comparable to that of the present climate simulation albeit with a net pore pressure decrease of around 5 kPa (0.5m head).

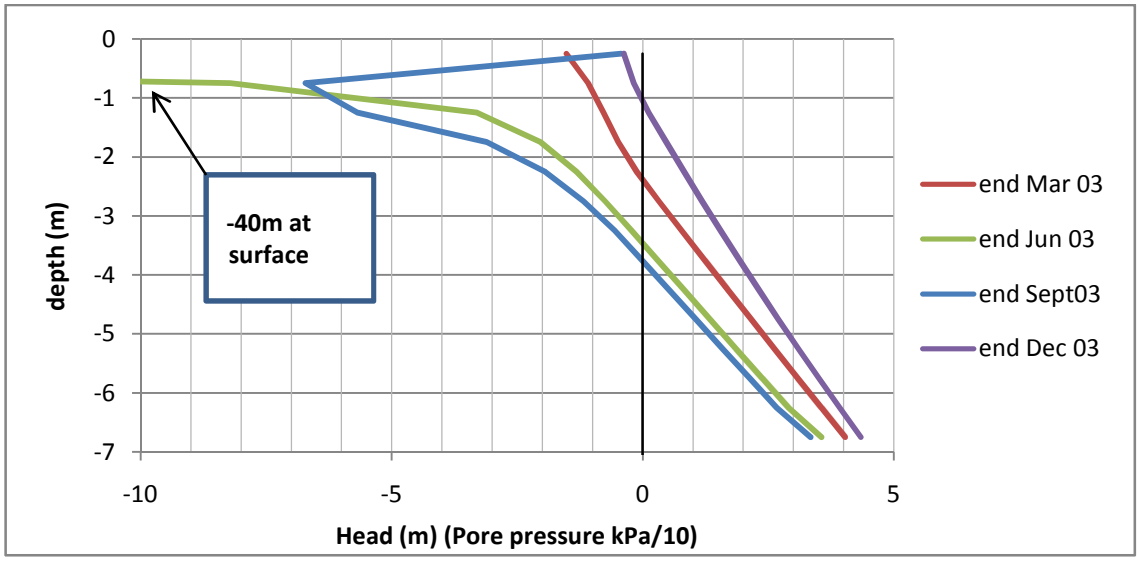

Figure 5.49 Pore pressure profiles for year 3 of the future climate simulation.

5.5.3 Flac-tp mechanical properties

The London Clay properties for the cutting were modified for the coupled mechanical simulation. Mott Macdonald had done extensive assessment work on embankments and cuttings within London clay. The model proposed for the strain softening characteristics of London clay was developed by Mott Macdonald upon earlier research by Imperial College London and is described within the publication 'Old Railway Embankment Clay Fill- Laboratory Experiments, Numerical Modelling and Field behaviour' O'Brien et al (2004). The strength degradation model can be seen within Figure 2.28.

The stiffness properties of the London Clay fill were also discussed within the paper and the properties adopted reflect those findings. The stiffness of the models was based on effective stress and constant, *k,* value using the Equation 5.4. Minimum stiffness values also varied from 4000 kPa to 5000 kPa.

$$E = k(p'+100) \qquad \textbf{5.4}$$

The *k* value within the Mott Macdonald studies was found to vary between 25 and 75. Extensive numerical studies on London clay structures by Mott Macdonald concluded that a stiffer pre-yield stiffness resulted in mobilisation of shear strength at the back of the slope and, therefore, less displacement and hence shear softening at the toe (Mott Macdonald, 1999a). In the absence of any test data for the Newbury slope a relatively large *k* value of 65 was adopted. Within previous embankment simulations it can be seen that for London clay fill the Poisson's ratio was manually changed from 0.3 for the loading condition to 0.2 for the unloading condition. This lead to embankment swell over successive cycles. The same approach was adopted for the cutting study to reflect the successive swelling of infrastructure earthworks.

London clay has undergone extensive over consolidation since being deposited during the Eocene. This has resulted in a K_0 value of around 2.0 in the top 15m (Mott Macdonald, 1999b). A K_0 of 2.0 was, therefore, specified throughout the model.

The permeability of the material was that which had been calculated by the back analysis detailed above. The properties adopted for the study are summarised within Table 5.6.

Table 5.6. Material properties adopted for Newbury climatic study (after O'Brien et al, 2004)

	In-situ London clay
Bulk unit weight kN/m^3	18.8
c' peak (kPa)	7
c' post rupture (kPa)	2
c' residual (kPa)	2
φ' peak (º)	21
φ' post rupture (º)	21
φ' residual (º)	13
Total strain at peak (%)	3
displacement at post rupture (mm)	5
displacement at post rupture (mm)	100
Poisson's ratio	0.3 load, 0.2 unload
Young's modulus (kPa)	65(p'+100) Min 5000
Coefficient of earth pressure at rest	2.0
Permeability (m/s)	1e-7

5.5.4 Flac-tp grid

The grid used for the previous Newbury Flac-tp analysis (Section 5.4) had non-homogenous element sizes. As seen within Section 5.3 the progressive failure became influenced by the size of the elements used once softening began. The smaller elements softened quicker than the larger elements due to the reduced strain required to initiate softening. A revised grid was, therefore, developed which comprised of identically sized elements within the cutting material. The element height was also modified to give an identical height to the grid used for the analysis by O'Brien et al (2004). The elements within the area of expected failure were square, therefore, softening of the grid would be relatively comparable in all shear directions. The expected strength degradation of the cutting was therefore identical to the simulations run by O'Brien et al (2004). The modified grid can be seen within Figure 5.50.

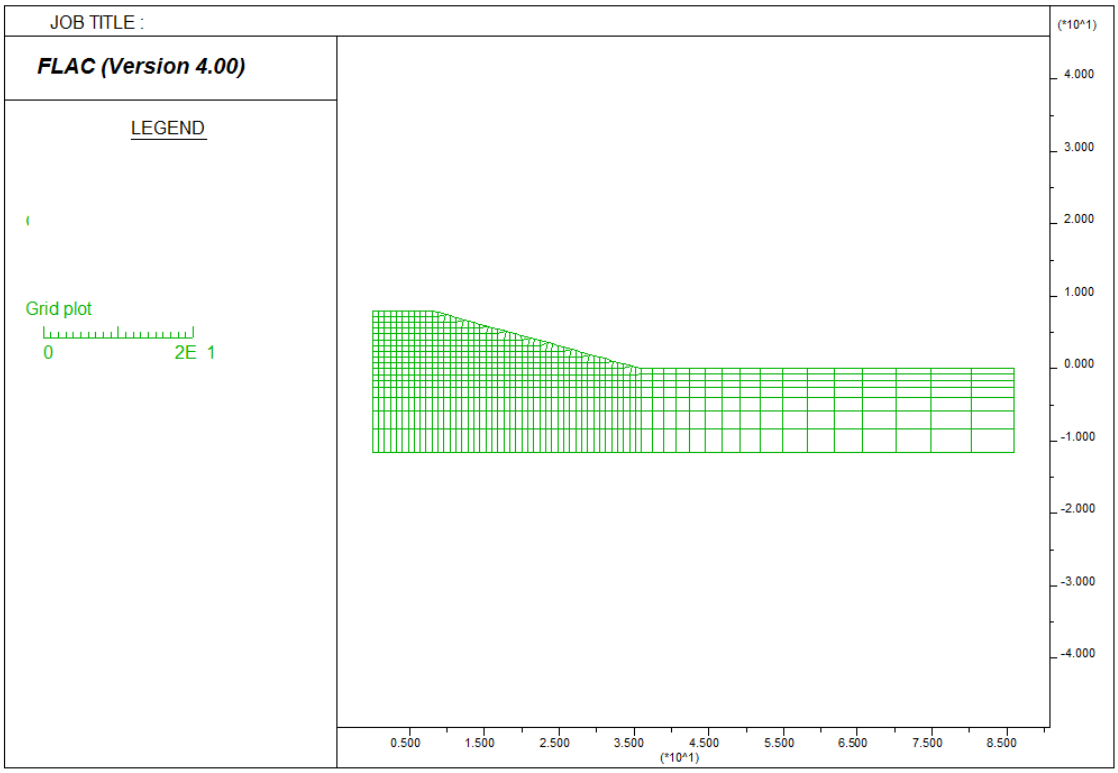

Figure 5.50 Homogenous sized element Flac-tp grid for the Newbury slope (all units in meters).

As can be seen within Figure 5.50 the strain softening elements continue within the foundation to allow the development of softening through the foundation. Below this depth the elements increase in size to reduce the number of elements and, therefore, run times. Due to the modified element height the grid points along the slope surface of this grid were not comparable to the SHETRAN centre grid spacing. The SHETRAN pore pressures could not, therefore, be directly applied to the Flac-tp grid points. The transfer method, therefore, required modifying. A modified code was, therefore, written within FISH language which took the range of pore pressure from two neighbouring SHETRAN surface cells and applied this range over the equivalent length of the Flac-tp grid. The Flac-tp range would be defined to encompass a number of grid points. Flac-tp then automatically applied a linearly scaled pore pressure, relevant to the applied range, to each grid point within the range. The modified transfer method was tested and the results can be seen within Figure 5.51. It can be seen from Figure 5.51 that the comparison remains excellent.

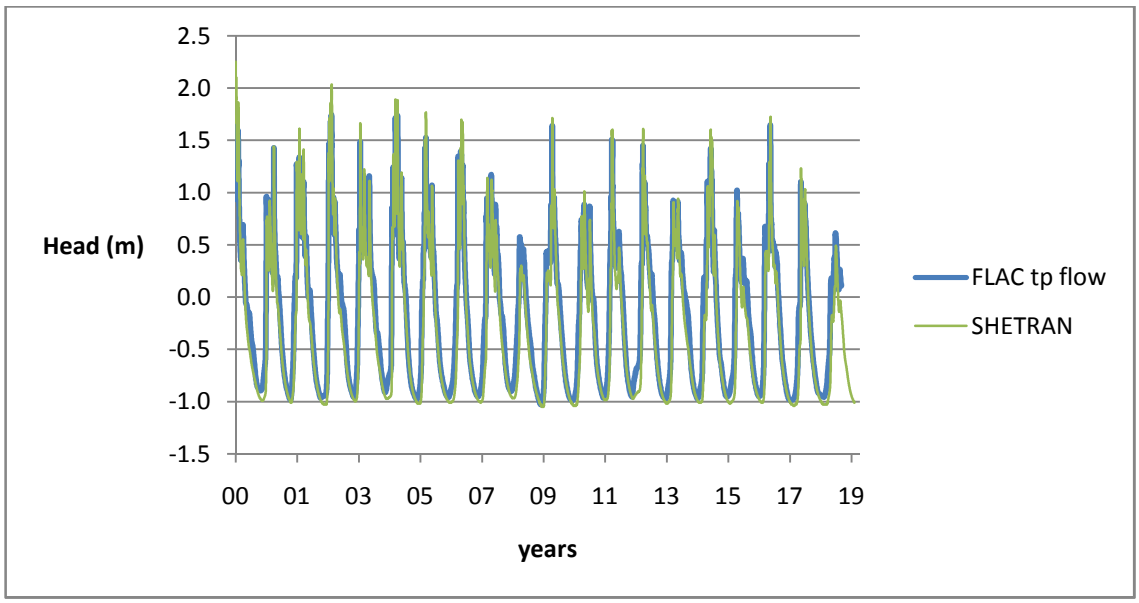

Figure 5.51 Pore pressure comparison of Flac-tp (square elements) and SHETRAN near the toe of the Newbury embankment.

5.5.5 Cutting construction

The cutting was constructed in layers. For the initial condition the ground surface was assumed to be horizontal and vertical and horizontal stresses were applied. A suction of 10 kPa was applied to the surface which equated to a phreatic surface 1 m below the surface. The model was then allowed to reach equilibrium.

The construction was simulated in five stages. At each stage a 1.6 m excavation was specified. A suction of 10 kPa was instantaneously applied to the newly excavated surface to simulate surface suctions due to unloading and swelling. The model was run for a period of seven days after each excavation. The entire construction was, therefore, performed over a period of 35 days. The pore pressure contours at the end of each construction stage can be seen within Figure 5.52.

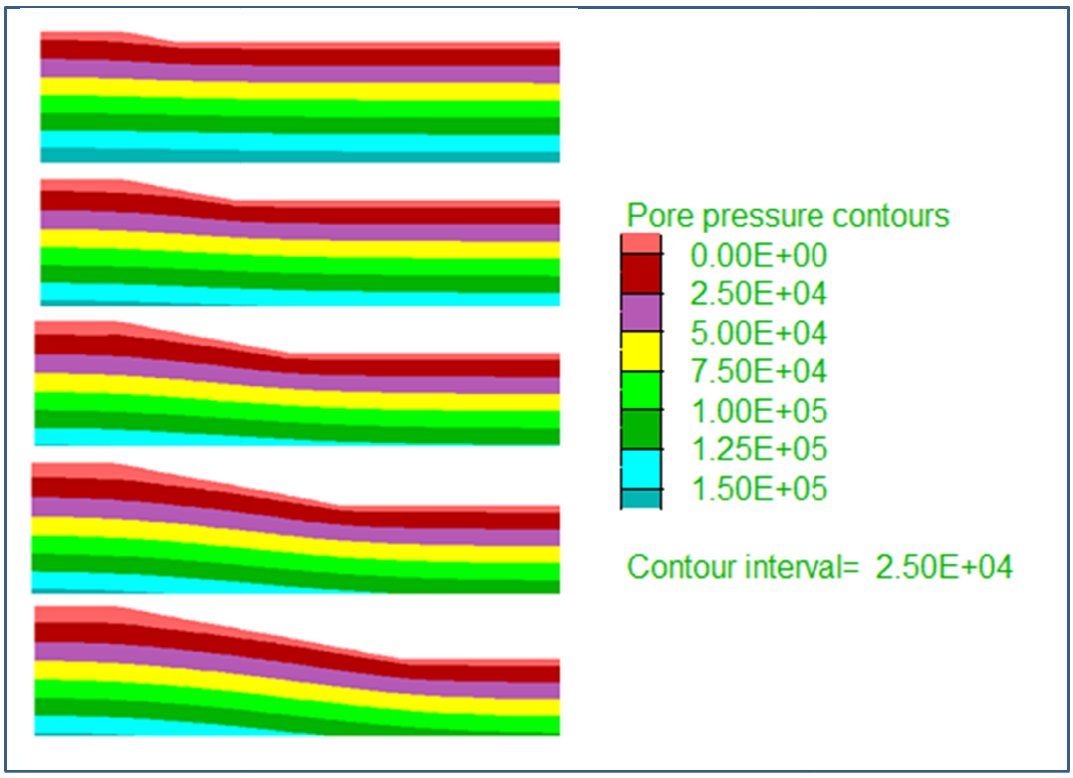

Figure 5.52 Pore pressure contours (Pa) at the end of each construction stage.

The horizontal and vertical displacements at the end of construction can be seen within Figure 5.53. It can be seen from these figures that the slope has swelled both horizontally and vertically. The swelling had persisted through the entire depth of London Clay. Horizontal displacements up to 0.08 m were seen within the slope and vertical swelling up to 0.20 m were seen at the toe of the slope. These displacements resulted in shear strains developing within the slope. The maximum shear strains were of the order of 2.5% and were seen at the toe of the slope. These shear strains resulted in some trivial softening of material ahead of the cutting toe.

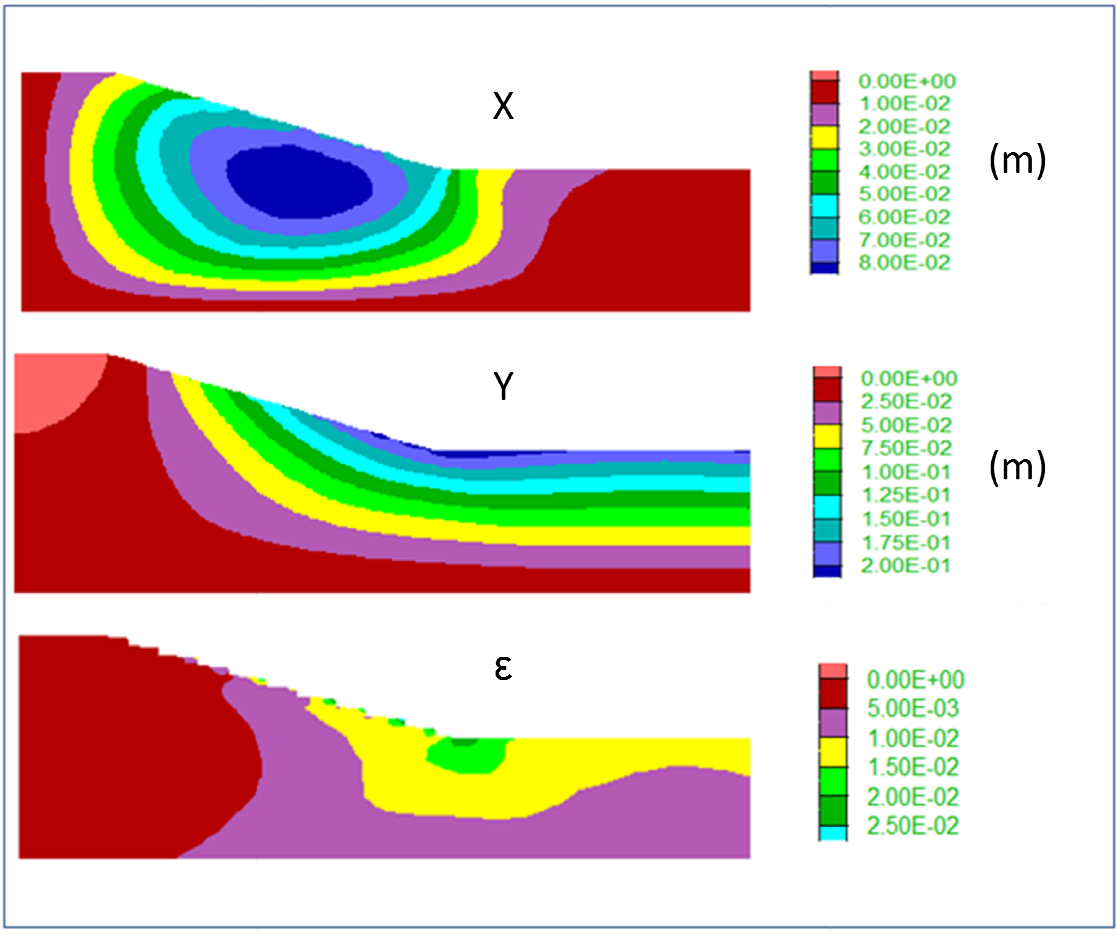

Figure 5.53 x and y displacement contours and shear strain contours at the end of construction.

The cutting was stable at the end of construction and there was no significant continuing displacement. The initial condition was now prepared for the surface pore pressures calculated by SHETRAN for a present and future climate.

5.5.6 Climate comparison study

The pore pressures from the SHETRAN simulation were applied to the surface of the end of construction Newbury cutting. The pore pressures were applied directly to the slope surface instantly after construction. Displacements were, therefore, not zeroed before the climate study commenced. This effectively simulated a cutting constructed during a present climate and a cutting constructed during a future climate.

The SHETRAN simulations provided just less than 20 years of surface pore water pressures. Both the future and present climate simulations remained stable at the end of this 20 year period. The SHETRAN simulation was therefore run for 20 further years, beginning at the end of year 19 loading, with the same weather data, therefore, providing just less than 40 years worth of surface pore pressures. At the end of this

period the cutting subjected to the future simulation pore pressures had failed yet the present climate cutting was still stable. The SHETRAN simulation was, therefore, extended for a further 20 years and these pore pressures once again applied to the present climate simulation. The present climate cutting failed within the latter period.

Figure 5.50 shows the x displacement for the midpoint on the slope surface together with pore pressure variation within the centre of the slope (4 m depth). It can be seen that the slope failed during the unloading cycle of year 22. The plot also shows the pore pressure at depth within the slope rather than the surface pore pressures at the toe. The surface toe pore water pressures shown within Figure 5.47 demonstrates that the phreatic surface reached the surface every year. The pore pressures within Figure 5.54 reveal that maximum pore pressures deep within the slope varied considerably as a consequence of climatic influence. Pore pressure peaks can be seen during years 3 and five and again during year 22. The peak during year 22 was caused by the same climatic conditions as the peak during year three. The slope displacement reacted quickly to the increased pore pressures as can be seen from the displacement plots. The slope was cyclically, progressively failing but at a very slow rate. During wet years the slope would displace much more and hence soften much more. This observation once again highlights the importance of modelling the peak pore pressures from abnormally wet years. Without these peaks the model would have continued for a greater number of years.

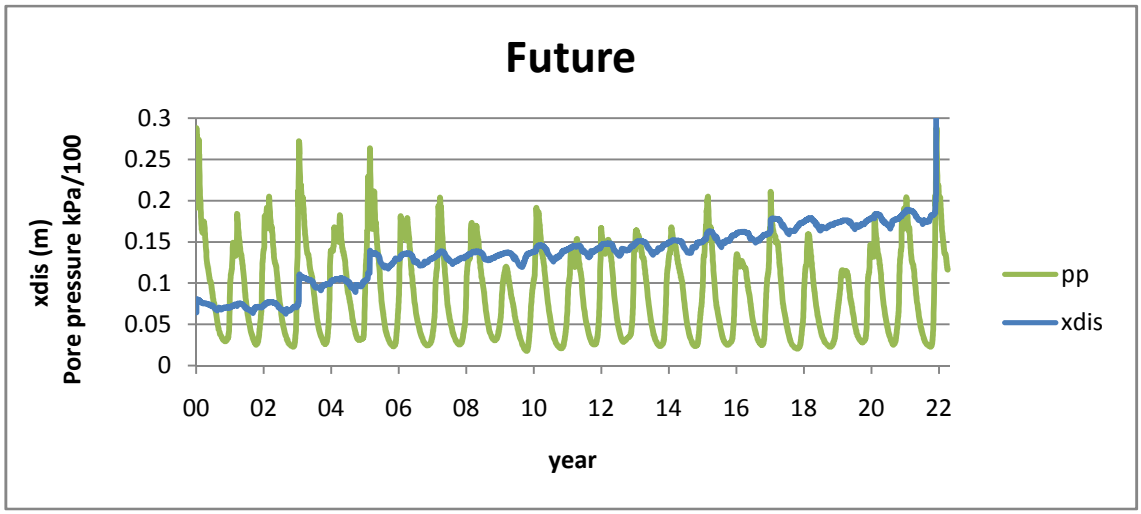

Figure 5.54 Mid-slope surface x displacement and pore pressure within the centre of the slope for the Newbury cutting subjected to a future climate scenario.

Figure 5.55 shows an identical comparison to Figure 5.54 for the present climate simulation. The pore pressures at 4 m depth are generally higher than those of the future climate simulation but the range is generally higher. The displacement of the slope at first reacted to the higher pore pressures as it can be seen as soon as the climate model was applied displacement quickly increased to over 0.12 m. The rate of progressive failure was, however much lower. The mid-slope displacement the year before failure was also much lower than that of the future climate simulation at just over 0.15 m as opposed to 0.18 m.

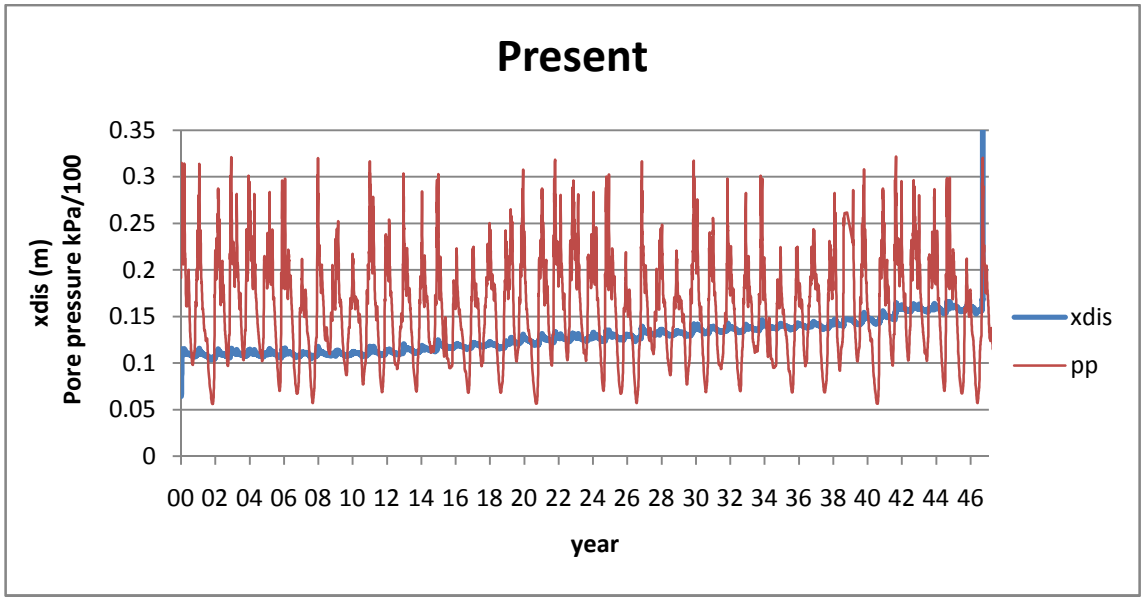

Figure 5.55 Mid-slope surface x displacement and pore pressure within the centre of the slope for the Newbury cutting subjected to a present climate scenario.

Figure 5.56 shows the failure plane of both the future and present cutting failure. It can be seen that both failure planes begin at the toe of the cutting and progress horizontally within the cutting. The future climate failure then exits within the slope and the present climate failure exits through the crest. The depth of the failure plane was comparable for both simulations.

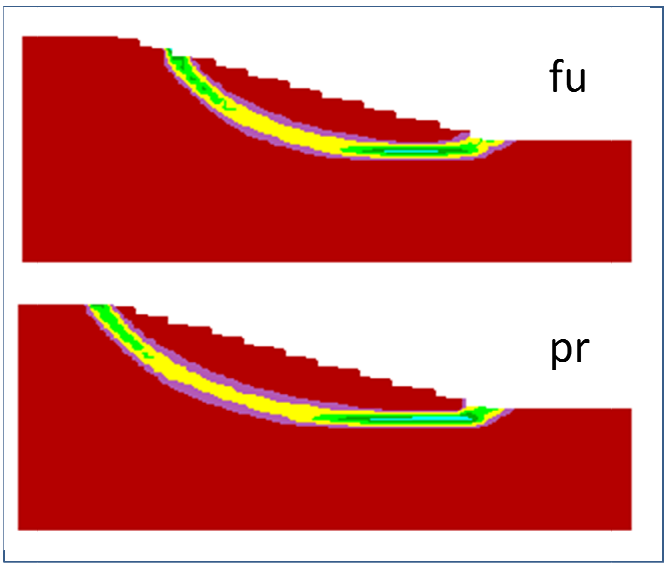

Figure 5.56 Shear failure plane within cutting for a future climate (fu) and present climate (pr) simulation.

The reason for the difference in shape of the slip surfaces became apparent when the figure of horizontal displacements was studied, Figure 5.57. It was evident that there was much greater displacement at the toe of the future simulation cutting. The displacement at the toe of the future simulation slope reaches around 0.35 m whilst the present climate slope maximum was around 0.25m. The greater displacements reduced to displacements comparable to the present climate simulation towards the rear of the slope.

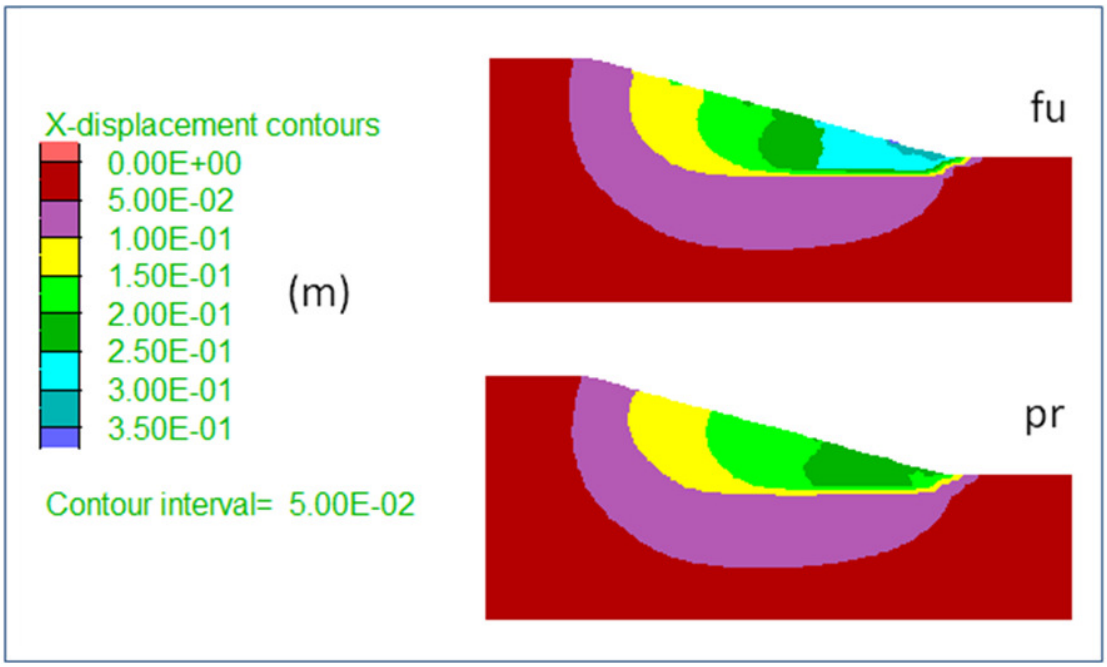

Figure 5.57 Horizontal displacements for the load cycle pre-failure for the future (fu) and present (pr) simulations.

The greater displacements at the toe were a result of the large shrink swell cycles imposed by the future climate simulation softening the material at the toe. Figure 5.58 shows a comparison of the future and present climate simulation pore water pressures near the surface at the toe of the embankment. It is clear from this plot that the annual cyclic pore range at the toe of the future embankment is consistently and substantially higher than the range of the present climate simulation. Furthermore it can also be seen that full saturation (0 kPa pore water pressure) is achieved, and sustained for a significant period, every winter, unlike within the diagnostic embankment study. This saturation at the toe indicates that there is no additional shear strength available from high suction such as those seen within the diagnostic embankment study. The large pore pressure cycles and the reduced strength coupled together result in a greater rate of softening at the toe.

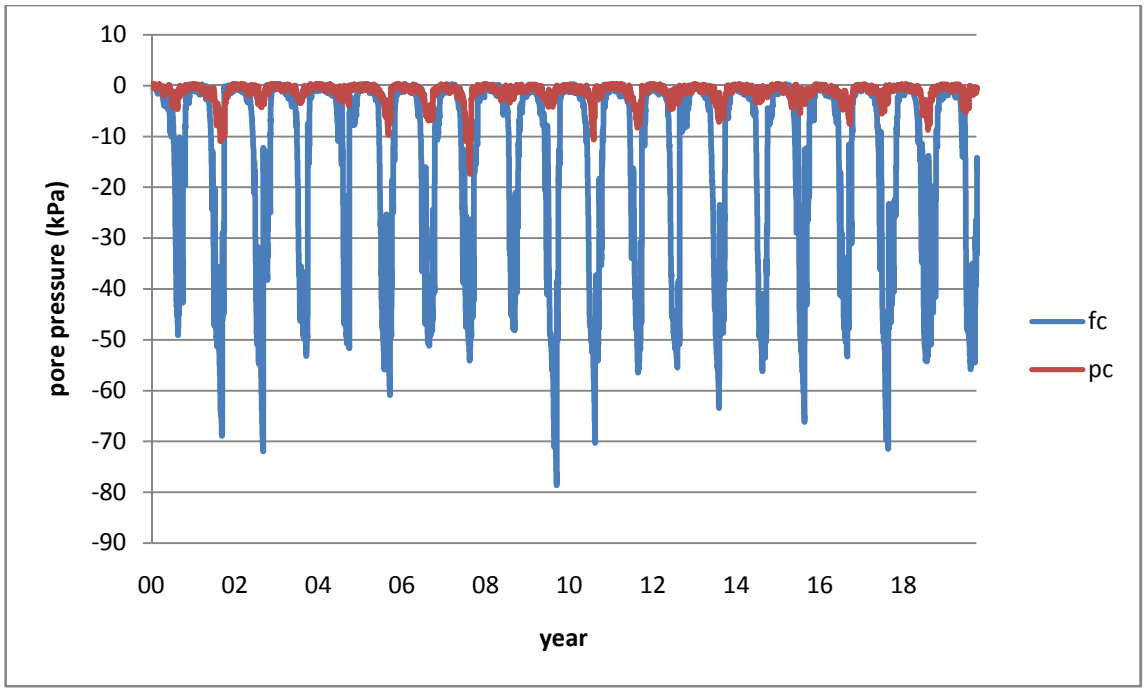

Figure 5.58 Pore pressure cycles at the toe over a 20 year period for the future and present climate scenarios.

Figure 5.59 shows the softening of the material for the load cycle prior to failure. It can be seen that the softening of the future climate cutting had occurred throughout the area of the toe and was beginning to progress upwards into the slope. The softening of the present climate slope was restricted to below the depth of the cutting toe and there had been no softening within the slope. The softening had also not begun to progress upwards.

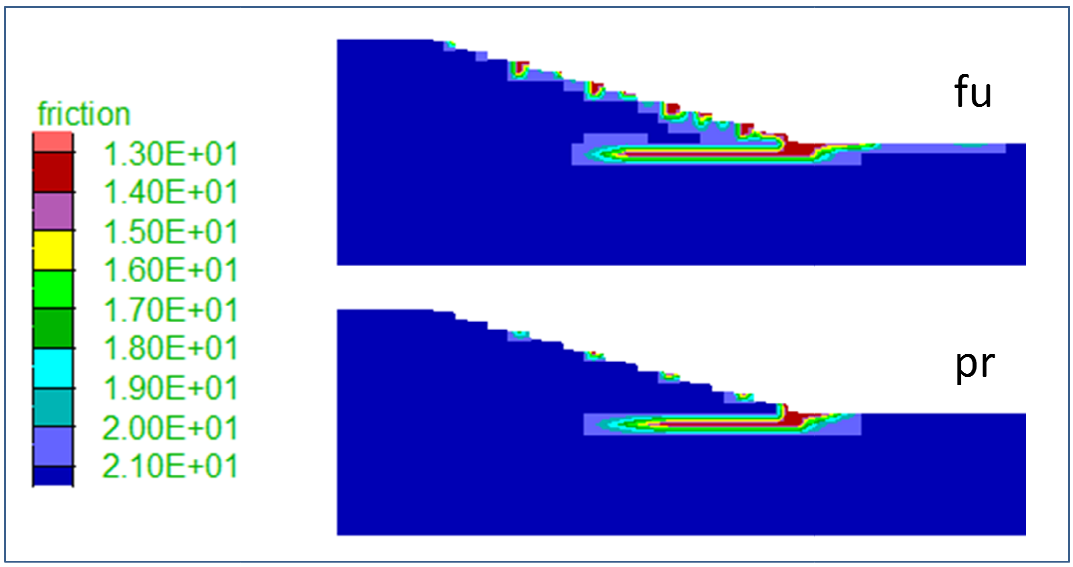

Figure 5.59 Friction plots for the future climate (fu) and present climate (pr) simulations.

5.5.7 Newbury simulation summary

The strength of the toe of the cuttings was critical to stability. The toe of the slope provided support to the remainder of the slope and restricted the seasonal movement and hence softening of the remaining material within the slope. The rate at which the toe softened was, therefore, the catalyst for increased horizontal displacement within the future climate cutting. Increased softening and displacement lead to decreased toe support. When pore pressures rose within the slope and the slope swelled it tended to swell down slope. With decreased toe support this swell became increasingly less restricted, especially at the toe, and hence increased until the toe support became too small to retain the pressures of the upper slope and failure occurred. The actual failure occurred during a period of increased pore pressures within the slope caused by a very wet year. The shortened failure plane was due to the suctions being retained below the crest of the slope. The lower pore pressures below the crest resulted in higher effective stress and therefore higher strengths, see Figure 5.60. The eventual failure, therefore, by-passed this area.

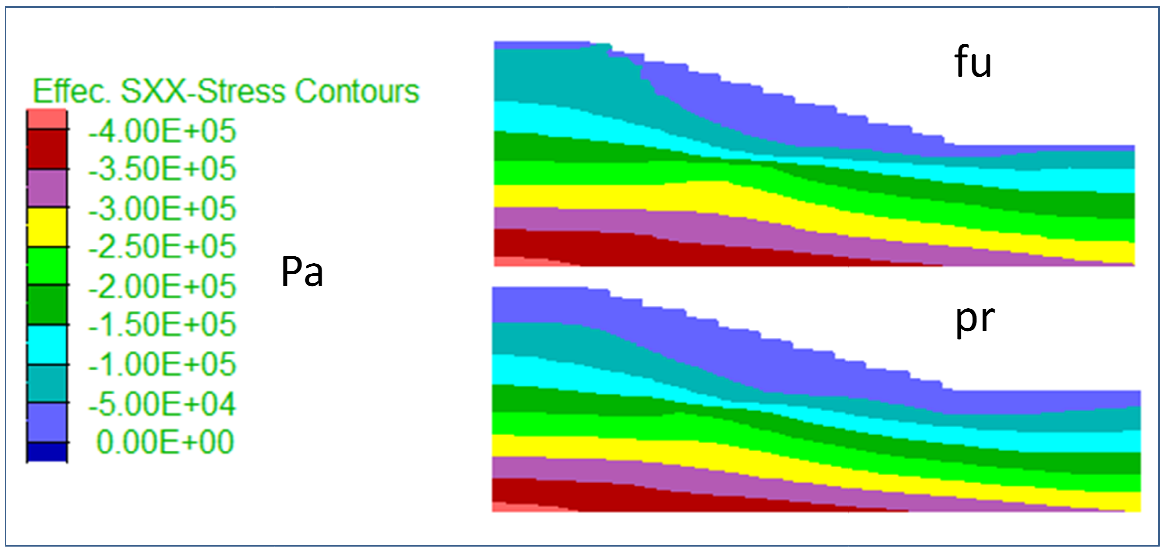

Figure 5.60 Horizontal effective stress plots before failure for the present and future climate simulations (negative values indicated compression).

The softening of the present climate simulation was restricted to a shear zone, one grid element high, extending horizontally into the cutting from the toe, indicated by the red zone (φ = 13°) in figure 5.59 (pr). There was no further softening above this shear zone. Whereas within the future climate simulations softening occurred along the same shear zone but also extended throughout the toe of the embankment, indicated by light blue (φ = 20°) figure 5.59 (fu). The upper toe material within the present climate simulation retained its strength. This was due to the toe material being subject to the moderate shrink swell cycles of the present climate. The rate of softening was also much slower. Shear strain along the base was due to the annual swelling of the entire cutting slope resulting in softening along the base of the toe only. The toe was able to retain the upper slope until the softened zone extended laterally enough and failure occurred. The failure occurred during an averagely high pore pressure year as per the future cutting failure.

Both failures occurred during years of either abnormally high, or averagely high pore pressures. These high pressures aided failure by decreasing the available shear strength and increasing the total pressures within the slope. These increases have been seen to accelerate the rate of progressive failure but failure can be seen to have eventually occurred with continual average years. The increased pore pressure events are directly due to the climate. Increased rainfall during a wet year leads to increased pore pressures for both the future and present climate scenarios. The higher pore pressures within the slope lead to higher displacements. It follows that, the inclusion of wet years vastly

reduce the number of years to eventual failure. It is, therefore, important to be able to model the magnitude of pore pressures during and after such years and also the frequency of these years in order to estimate the un-maintained lifetime of the structure.

The results are interestingly comparable to the permeability study performed earlier, Figure 5.17. The future climate simulation initially appeared more stable due to lower pore pressures but then became more unstable due to the larger shrink swell cycles, Figure 5.61. Within the simulation depicted in Figure 5.14 the higher permeability embankment initially displaced less due to lower pore pressures but then larger shrink swell cycles were caused by larger pore pressure cycles which resulted in increased displacement. For the climate study the initial displacement were due to the application of the climate boundary condition. The future climate boundary condition consisted of lower pore pressures and hence displaced less. The larger shrink swell cycles for the future climate were due to larger pore pressure variation as a consequence of climate. Both instances lead to larger shrink swell cycles and increase rate of progressive failure.

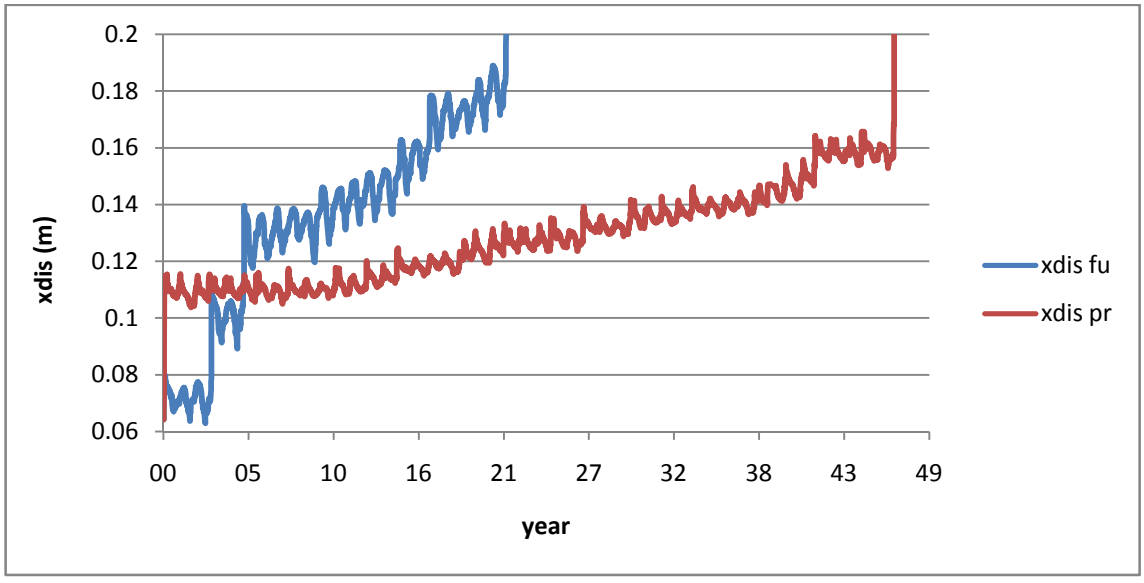

Figure 5.61 Comparison of x displacement mid-slope for future climate and present climate simulation.

5.6 Discussion

For the embankment study the lower permeability embankment remained far more stable for the future climate condition due to persistent high suctions within the slope. For this simulation, the dominant mechanism was the increased strength and stiffness due to higher suctions. With increased strength the embankment material was able to sustain higher shear stress without failure. The present embankment simulation failed relatively quickly due to the high annual pore pressures and inherent reduced shear strength. The magnitude of the shrink swell cycles was less of a factor in the failure of this embankment.

The magnitude of maximum annual pore pressures was the dominant difference between the present and future climate embankment failure rates. These maximum pore pressures were reduced within the future climate simulation by increased evaporation from the slope. The low permeability of the slope also reduced infiltration, which meant that reduced pore pressures were not able to recover. The temperature comparison plots for the present and future climate scenario (Figures 5.5 and 5.6) show that for the 100 UKCP09 scenarios future climate average temperature is consistently higher than the present climate average. It follows that average potential evapotranspiration rates for all future climate datasets are also most likely to increase. Therefore, although only one future and one present climate dataset were modelled fully, it can be reasonably suggested that the decrease in future climate pore pressures modelled within the embankment by SHETRAN, due to the increased 2080 scenario temperatures, will be typical for the vast majority of future climate datasets. For this particular diagnostic embankment the future climate is therefore likely to increase stability.

The cutting simulation had a much higher permeability. The future climate simulation showed that much higher suctions would be achieved during the summer months, but occasionally similar maximum pore pressures to the present climate would be achieved during the winter months. This was due to the higher permeability allowing the rainfall of the future climate simulation to infiltrate the slope more readily. These maximum winter pore pressures combined with larger shrink swell cycles (due to much larger summer suctions) resulted in an increased rate of softening at the toe and, therefore, a much greater rate of progressive failure.

The permeability of the cutting allowed quick recovery of pore pressures. This coupled with high evapotranspiration rates due to consistently higher temperatures, within the future climate, lead to large shrink swell cycles and increased softening rates. The occurrence of wet events also became critical in determining failure rates. Wet events where higher pore pressures were achieved can be seen within the plot of pore pressures at the centre of the embankment in Figure 5.54. It was seen from this plot that when pore pressure peaked above average down-slope displacement also peaked. The pore pressure peaks can be roughly correlated with the peak rainfall events shown in Figure 5.4. Peak pore pressures during years 3, 5, 15 and 17 correlated well with peak wet events shown within Figure 5.4. The cutting simulation, therefore, highlighted the importance of wet events on cumulative slope displacements. The critical magnitude and frequency of these events therefore needs to be determined in order to estimate the probable rate of failure. Increased frequency of return periods of wet years is very likely to increase failure rate for a simulation. Figures 5.62 and 5.63 show the percentage of months where average monthly rainfall rate exceeded 5mm/day for the present and future scenario.

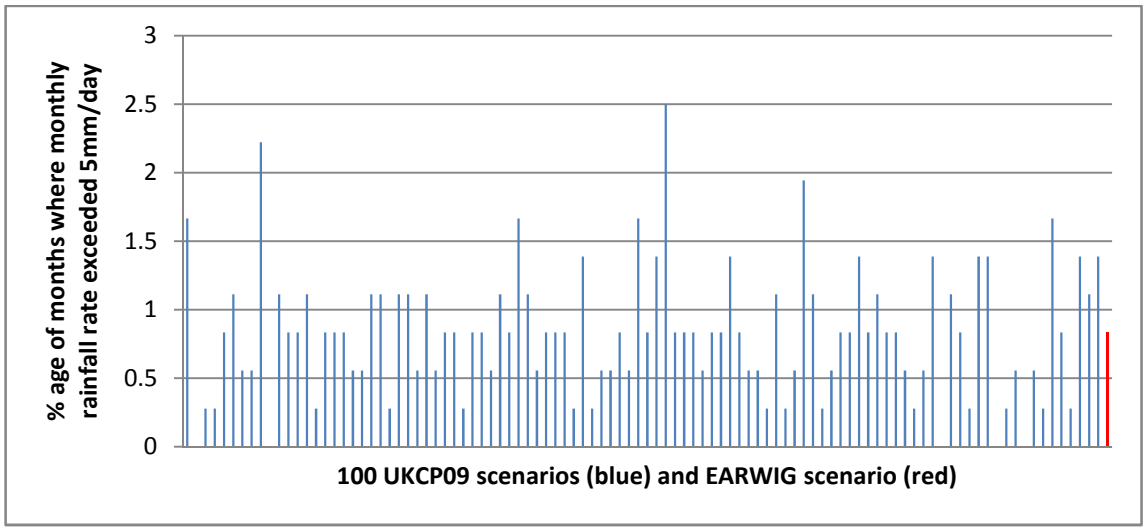

Figure 5.62 Percentage of months for all present datasets where average rainfall rate for the month exceeded 5mm/day.

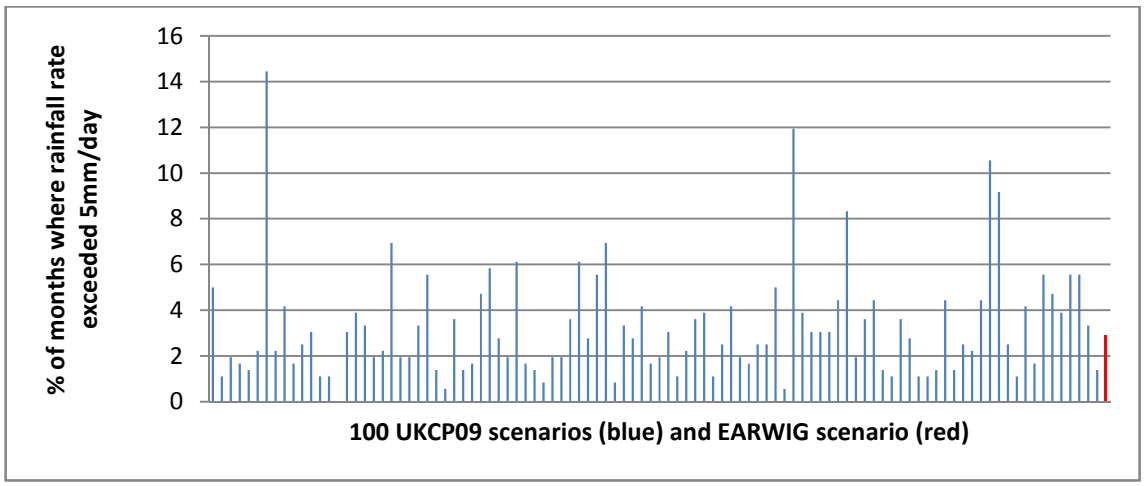

Figure 5.63 Percentage of months for all future datasets where average rainfall rate for the month exceeded 5mm/day.

For the present day EARWIG scenario the percentage of months where monthly rainfall rate exceeded 5mm/day was 0.833%, this frequency was exceeded 31 times out of the 100 UKCP09 datasets indicating a slightly higher than average return period. For the future EARWIG scenario the percentage of months where monthly rainfall rate exceeded 5mm/day was 2.917%, this frequency was exceeded 46 times out of the 100 UKCP09 datasets also indicating a slightly higher than average return period for wet events. As wet events have been seen to considerably increase softening rates it is likely that the failure rates of the simulations presented would be above average should a simulation be conducted for each of the 100 UKCP09 present and future simulations.

The Newbury cutting simulation highlighted the importance of determining the field permeability correctly. Had similar permeabilities to the field data been used then it was likely that the future climate simulation would have been more stable as per the diagnostic embankment study. It is the opinion of the author that laboratory and borehole tests are not sufficient in determining the mass permeability of an infrastructure earthwork. The permeability of soil is related to the volume of the soil being tested due to macroscopic features such as sand layers, fissures etc. (Lu and Likos, 2004). This has been proven to the case through back analysis of the Newbury slope using the SHETRAN hydrological model. It appears that the most accurate way of determining the permeability is by in-situ monitoring and back analysis. This is time consuming and costly, yet the only reasonable alternative would be field tests and scaling the permeability using empirically based observations. All simulations show that the consequence of underestimating permeability is overestimating stability.

The presented simulations have determined the difference in likely progressive failure rates for future and present climate scenarios. If an insight into the statistical rate of failure of a particular structure subjected to a particular climate scenario is required then several EARWIG models would need to be run and a SHETRAN and Flac-tp model run for every EARWIG model. Such an analysis would provide a range of predicted failure rates and therefore statistical minimum, maximum and average rates of failure for that structure.

Climate data has been shown to be very site specific. The Newbury slope weather data showed that the PET can vary significantly over a relatively short distance. The weather data provided from an open location has the potential to severely over estimate slope stability by overestimating PET. Models run with the raw weather data would have had reduced pore pressures and therefore increased strength. It is, therefore, important that, where possible, site specific weather data is obtained. This weather data need not be collected over tens of years but only for a period over which a correlation to weather data from nearby long term sources (such as MET office weather stations) can be established.

The generated climate scenarios are also very site specific. EARWIG provides weather data for 5 km square grids throughout the UK. The grid used for the presented studies was for the Newbury area where annual rainfall remains consistent for a range of climate scenarios. EARWIG climate predictions for other parts of the UK, particularly NW England and Scotland, show that there will be an overall increase in precipitation. Studies for embankments in these parts will show a different outcome and will therefore need to be studied separately.

It is worth noting that the effects of desiccation occurring have not been taken into account during this modelling work. The perceived effect of desiccation will be that surface permeability will increase and that more water will be able to infiltrate into the slope surface. It has been shown that permeability increase has a significant effect on failure rate. Increasing surface permeability is likely to reduce surface strength and increase surface shrink swell cycles, therefore, shallow failures would be likely to occur. The rate of such desiccation, depth of influence and inherent magnitudes of permeability increase are not known and so have not been included within this study, the effects can not, however, be ignored.

Chapter 6. Belvoir Park Case Study

6.1 Introduction

For this case study a model was built of a natural slope located within the Forest Park South East of Belfast. The slope has been the site of a slip in 1989 and was re-profiled after this. The slip was thought to have been caused by heavy rainfall. Another slip was recorded during February 2001 near the site of the previous slip. The slope consists of inter-bedded fine sands, silts and clays and is heavily vegetated. The angle of the slope varies along its length and reaches angles of up to 30^{o}. After the last failure the slope was monitored by Atkins from 2003 to the present day. The monitoring involved the use of several piezometers and inclinometers. This monitoring revealed that the slope was still moving and the rate of movement roughly correlated with pore water pressure variation. There had also been some testing carried out on the material within the slope. This chapter outlines the method applied to attempt to model the slope at Belvoir using the data provided from testing, monitoring and a nearby weather station. The results of the numerical model are analysed and comments made on the correlation between the recorded data and numerical results. Particular attention is paid to the choice of parameters used and simplifications made to model such a complex slope.

The slope itself is covered by bare ground and deciduous trees. The numerical model attempted to use a generic canopy to simulate the overall effect of all the vegetation types present on the slope. As only surface pore pressures are to be transferred the rooting depth would need to be restricted to the depth of the SHETRAN surface cell. As discussed within Chapter 4, the transfer to the Flac-tp model assumes that the Flac-tp boundary is half a SHETRAN cell depth below ground level. It was therefore assumed that there existed a topsoil above the Flac-tp surface boundary of a depth equal to half that of the SHETRAN surface cell depth. This topsoil depth has been kept to 0.25m (0.5m depth SHETRAN surface cell) within previous simulations due to only a grass vegetation with 0.3m rooting depth being considered. The surcharge added to the simulation to represent this topsoil depth has had little if any effect on the simulations. Increasing the topsoil depth and, therefore, the surcharge will result in the associated assumptions having an increasing effect on the model output. The topsoil depth was, therefore, restricted to values comparable to previous simulations.

This case study identified the use of the surface pore pressure transfer method for modelling a failing slope. As outlined in chapter 4 there is no facility for mechanically generated pore pressures within Flac-tp to be fed back into the SHETRAN flow calculation. This has not created a problem when modelling the progressive failure of a cutting or embankment as the movements and hence mechanically generated pore pressures up to failure have been small. For this case study, however, the movements of the slope are considerable. This chapter documents attempts to model the slope and identify whether the pore pressure development is significant enough to invalidate the surface pore pressure transfer method.

Taking into account the restrictions of the model and the complexities of the slope at Belvoir this modelling exercise proved very difficult for the existing modelling strategy. The exercise highlighted areas where the assumptions were proved to be valid and areas where future modelling work needs to be improved.

6.2 Slope description

A plan of the slope is shown in Figure 6.1. As can be seen from the plan the area consists of an upper and a lower slope. There is a near horizontal area between the upper and the lower slope. There is also a footpath which runs between the upper slope area and the lower slope area. This path also forks round to run along the toe of the lower slope. Along the toe of the lower slope there runs the river Lagan. For the purpose of this investigation a cross section has been analysed. This cross section is shown as cross section 4 in Figure 6.1.

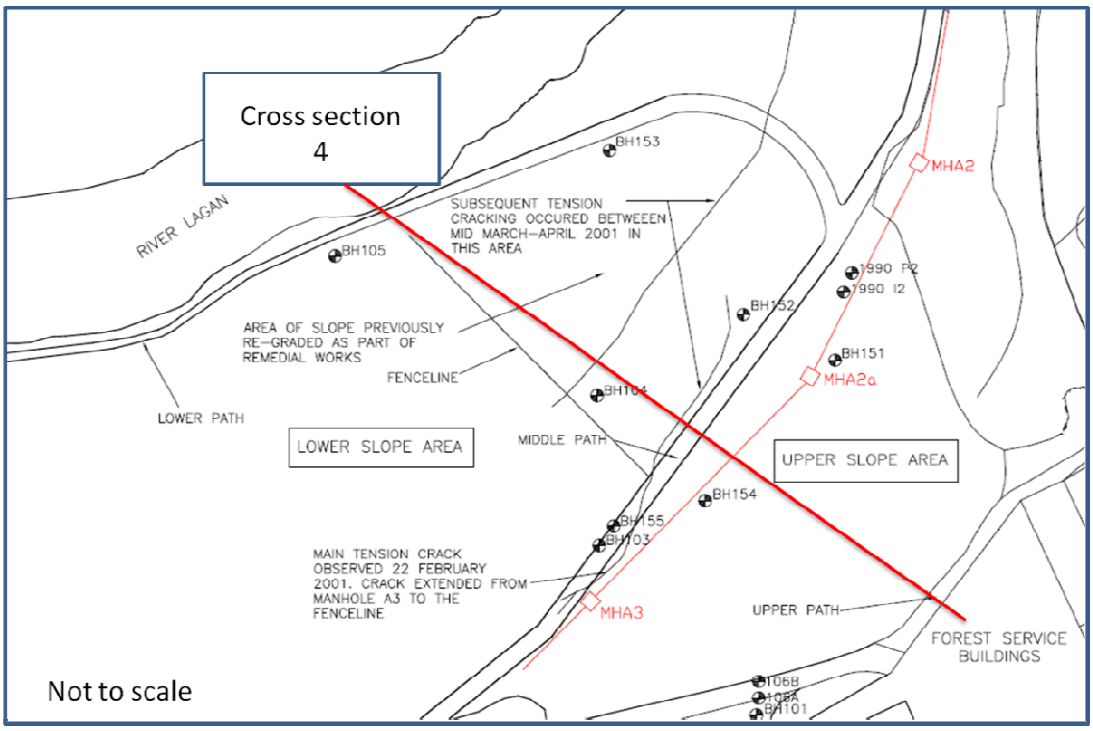

Figure 6.1 Plan of slope showing the modelled cross section (cross section 4) (Atkins report, 2008).

6.3 Cross section analysis

For the site investigation conducted by Atkins a topographical survey was conducted along several cross sections, including cross-section 4. Boreholes near the vicinity of the cross sections were used to estimate the ground conditions beneath each cross section. The borehole log descriptions together with the testing data have been used to group the material encountered into; Made ground, Upper boulder clay, Malone sands, Stiff clays, Soft clays, Brown sands or Gravels. Material below the gravels was thought to have little effect on the stability of the slopes and has been omitted for clarity.

Cross section 4 cuts through the area of the most current landslip and Atkins has also conducted an independent back analysis of this section of the slope using a limit equilibrium program Talren. The cross section together with a simplification of the borehole data nearby the section can be seen in Figure 6.2.

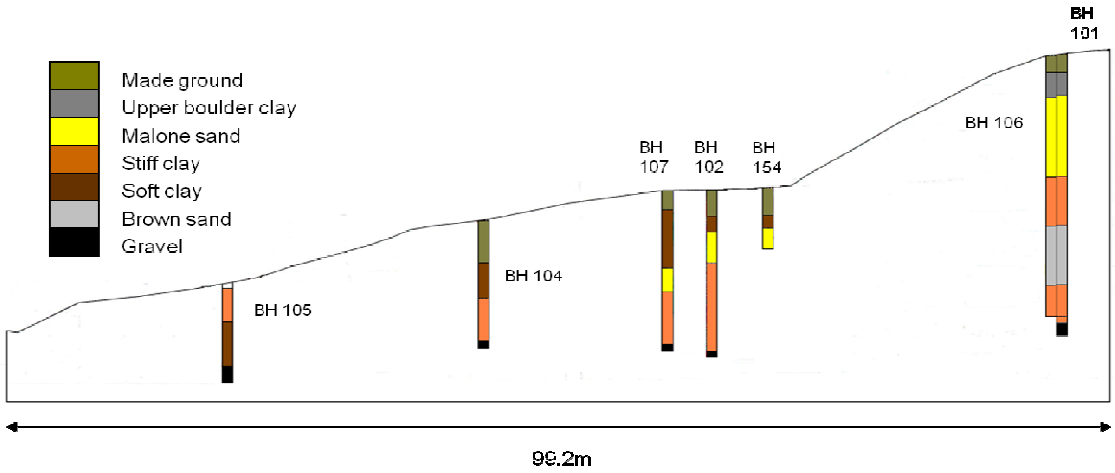

Figure 6.2 Cross section 4 with superimposed borehole data.

The upper slope was approximately 10 m long and was approximately 30 degrees steep. The upper slope consisted of near horizontally bedded sands and clays. The top of the slope consisted of approximately 1.5 m of made ground underlain by 2.5 m of firm to stiff clay. The majority of the upper slope, however, consisted of a silty fine sand. This silty fine sand is known locally as the Malone sand. The Malone sand persisted to the bottom of the upper slope. Beneath the Malone Sand there was 5 m of stiff brown clay which contained occasional laminations of fine sand before another large silty fine sand layer over 4m thick.

The material mid slope had been shown to vary along its length. At the base of the upper slope along the near horizontal section there was over 2.5 m of made ground. Below the made ground was a layer of clay which varied from soft to soft/firm. The clay also varied in depth from over 1 m, near the toe of the upper slope, to just under 6 m in a distance of 12 m. Under the clay layer lay a sand layer. This consisted of a silty fine sand similar to the material found in the upper slope. This sand layer varied in thickness and depth beneath the horizontal section of the slope. Beneath this sand lay a firm clay. The angle of the lower slope varied over its length. The slope angle began at 11 degrees in the upper section and increased to 18 degrees in the mid-slope before again decreasing to 13 degrees at the lower slope. The slope then dipped steeply towards the river. Within the upper lower slope there existed, once again, a significant thickness of made ground which thinned out down slope. In the upper sections of the lower slope the made ground overlay a soft clay and then a firm clay whilst the lower section comprised of a firm clay overlying a softer clay.

The present state of the lower slope is thought to have been defined by both the previous 1989 landslip and the subsequent re-profiling. The made ground found at the upper section of the lower slope was placed during works to lay the access path after the failure occurred. The thickness of the made ground suggests that significant excavation took place before hand. The strata below the made ground was most likely to be the remnants of the past failure or a previous failure. The strata sequence before the slip was most likely a continuation of the sequence of the upper slope. It is proposed that the slip was quite deep and the material now seen as sand within the upper slope would have been a continuation of the Malone sand. The material described as soft clay overlaying this sand would therefore be the same material as the clay observed above the Malone sand in the upper slope. The difference in observed stiffness of the material may have been due to the material becoming reconstituted during the slip. The material below the sand was thought to be in-situ and a continuation of the horizontal strata seen beneath the upper slope.

6.4 Monitoring data

6.4.1 Weather data

There was no weather station at the Belvoir site. The weather data was therefore obtained from a nearby Met office weather station (British Atmospheric Data Centre, 2008). The nearest weather station with the required weather data at the required time intervals (hourly weather data) was the Katesbridge weather station. This station was located approximately 15 miles from the site of the Belvoir slope. There was no site recorded weather with which to compare the weather station with as per the Newbury simulation so the weather data was used in its raw unaltered form.

The chart in Figure 6.3 shows the variation in annual rainfall since 2001. The chart shows relatively dry years during 2001 and 2003 and a relatively wet year during 2002. The annual rainfall was fairly consistent for the years 2004 to 2007.

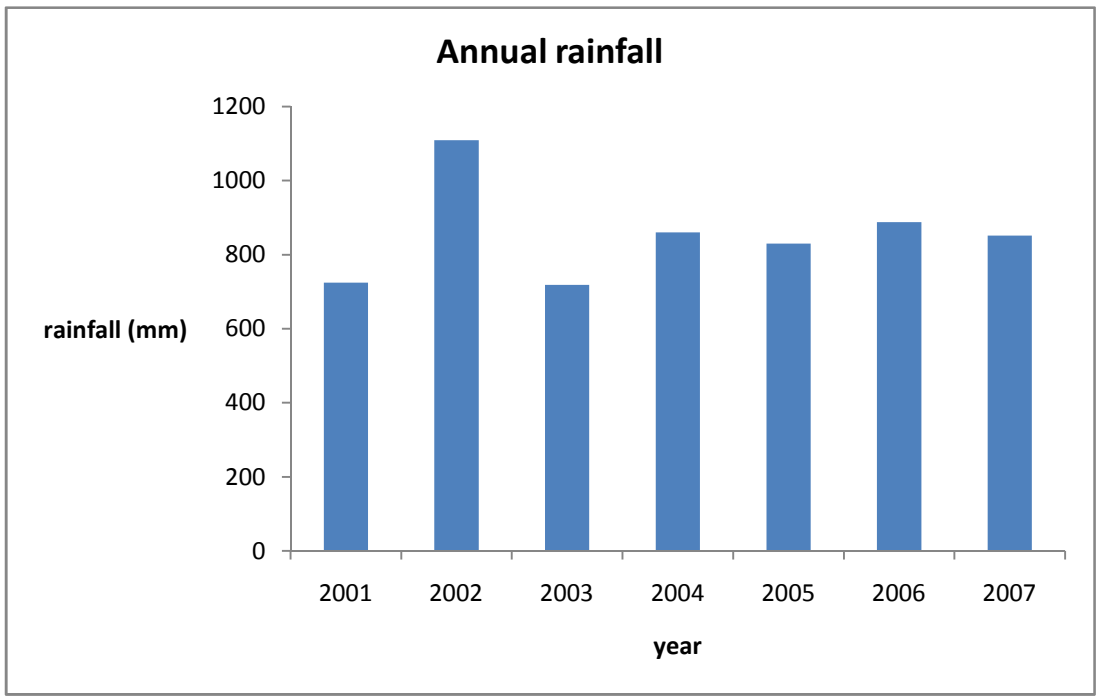

Figure 6.3 Annual rainfall recorded by the Katesbridge weather station 15 miles from the Belvoir site, (British Atmospheric Data Centre, 2008).

The distribution of the annual rainfall can be seen in the daily rainfall chart (see Figure 6.4). This also shows the rainfall over the period from 01/01/2001 to 01/03/2008. This Figure shows the distribution of the rainfall throughout each year. It can be seen that although 2002 was by far the wettest year the most intense rainfall occurred towards the end of 2004. Figure 6.4 also shows that the period of most intense rainfall occurs generally at the end of each year. Notable exceptions were 2001 and 2003 where rainfall was fairly evenly distributed and 2007 where the majority of rainfall fell during the middle of the year during the months of June, July and August.

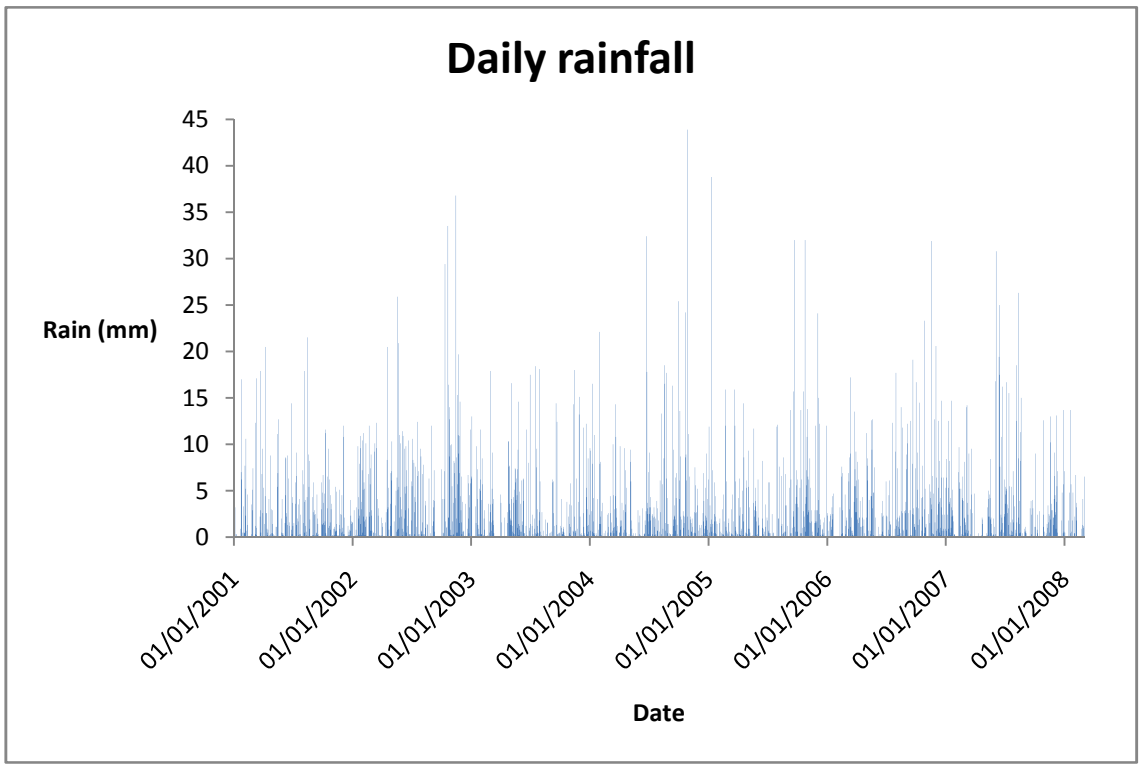

Figure 6.4 Daily rainfall for the period 01/01/2001 to 01/03/2008 as recorded by the Katesbridge weather station (British Atmospheric Data Centre, 2008).

6.4.2 Piezometer data

The piezometric data relevant to the cross section was obtained from standpipe piezometers within boreholes BH 104, BH 105, BH101, BH 106A and BH 106B. The monitoring period began in March 2006 and continued at monthly intervals. The rainfall data for the period can be seen within Figure 6.5. This data shows that there were no abnormal rainfall events during this period. The water levels, with reference to ordnance datum, are also shown in Figure 6.5. BH 105 was closest to the toe, see Figure 6.1 and 6.2. The water level at this location was just below, or sometimes above, ground level throughout the monitoring period. It can be assumed that under normal circumstances the slope at this location remains fully saturated throughout the year, for most years. At BH 104 the water level shows some variation over the monitoring period. At the beginning of March 2006 the water level could be seen to be just over 6m, this was around 4m below ground level. There was then little variation in water level until April 2007 where there was a sharp decrease followed by a sharp increase in water level before it settled to around 7m above ordnance datum. The upper slope water levels were recorded by boreholes BH 106A, BH 106B and BH101. There can be seen to be some variation in the water levels at this position.

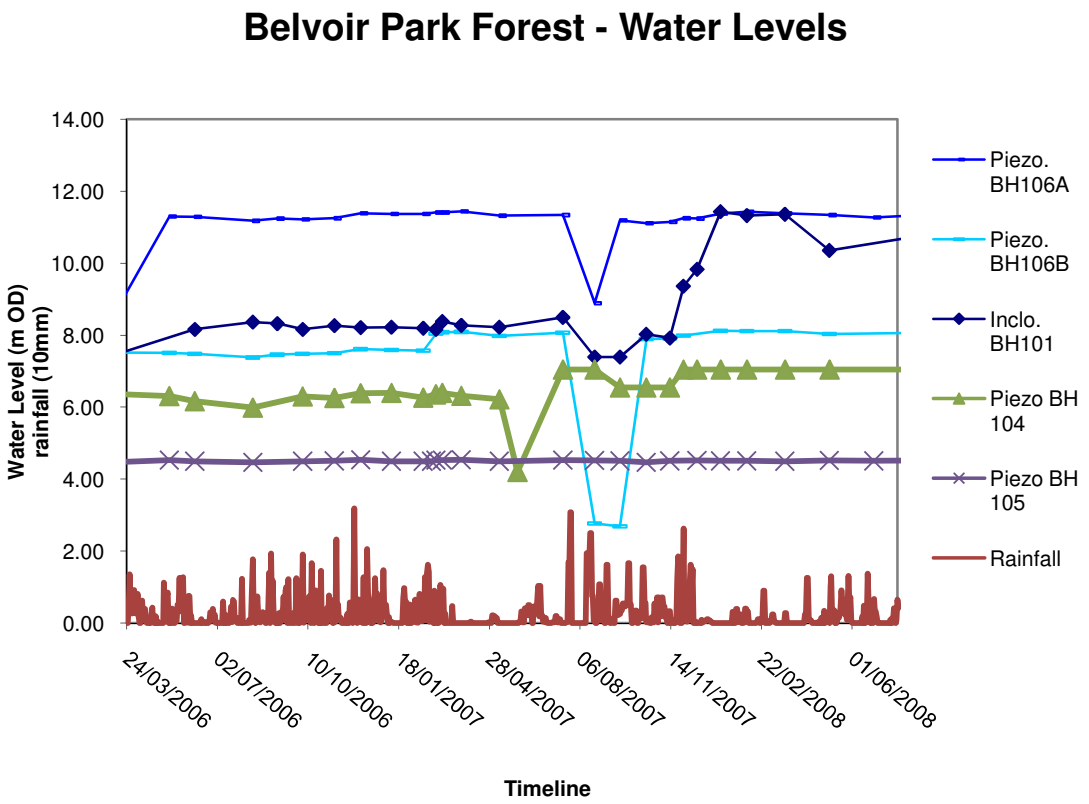

Figure 6.5 Rainfall data and piezometer data for the period 01/03/2006 to 01/0/2008 (British Atmospheric Data Centre, 2008 and Atkins, 2008).

All three piezometers considered within the upper slope were located relatively closely together (see Figures 6.1 and 6.2). Piezometer 106A was located at around 9.1 mAOD, 106B at 2.7 mAOD and 101 at -1.2 mAOD. When considering the results from BH 106A the water level from A varied from about 9mAOD to just over 11mAOD. As the piezometer's response zone was located at around 9mAOD, it could not measure a water level below this depth, so there may have been a lower water level that the instrument could not record. The water level was around 11mAOD for most of the year. At the same location BH 106B showed a water level of around 8mAOD for most of the year with a minimum of around 3mAOD. Again as the level of the piezometer's response zone was at 2.7 mAOD lower water levels could have been present that were not recorded by the instrument. The differences in the water levels for this location indicate that within this profile the pore pressure profile was not hydrostatic. The pore pressures at the deeper location are lower than the pore pressures at the higher location. This implied that either a low permeability layer was restricting the flow of water from the higher levels to the lower levels or a high permeability layer below the lower level is draining water away from the base of the sequence. Interestingly the piezometer within

BH 101 showed a water level corresponding with BH 106B for the beginning of the monitoring period and then after the sudden drop of pore pressures the water level rose to level corresponding with BH 106A. There may therefore exist some limited hydraulic continuity between the two levels.

The water levels show some correlation with the rainfall data (Figure 6.5). The dip in water levels at location BH 104 occurred after the relatively dry period during March and April 2007. There could be seen to be a significant delay between the lull in rainfall and the drop in water levels as, at the end of April, the water levels had not dropped yet there had been little or no rain for at least a month. Within the upper slope all three piezometers showed a drop in water levels at the same time. The drop to the lowest water level, however, occurred almost 3 months after the drop at location BH 104. In fact the water levels at BH 104 had recovered by the time the drop was seen in the upper slope. This may have been due to the rate at which the water seeped through the greater depth of material within the upper slope.

6.4.3 Inclinometer data

Inclinometer data was available for boreholes 105, 104 and 101. The cumulative deflection for bh101 can be seen in Figure 6.6. The data showed that there had been no discernable movement in this location. The small movements which were recorded were shown to fully recoverable and most likely caused by slight seasonal shrinkage and swelling of the slopes. There had been no overall down slope movement.

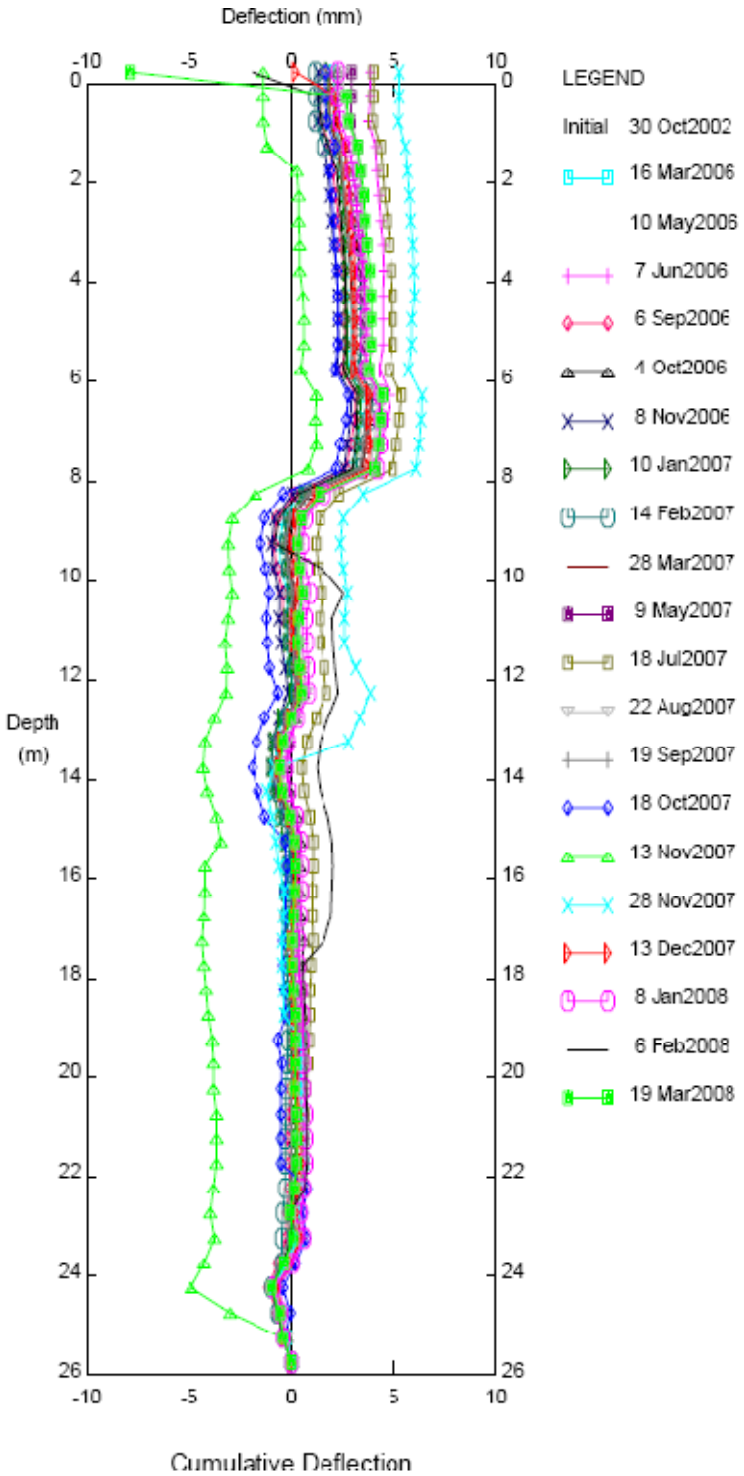

Figure 6.6 Cumulative deflection within borehole 101 (Atkins, 2008).

Borehole 104, Figure 6.7, showed continuing down slope movement. The maximum down slope movement occurred between 1 and 3m. The movement then reduced to insignificant levels at around a depth of 7m. This was also the depth at which the clay became increasingly stiffer, as identified by the site investigation. The movement within this borehole was significant and had been shown to be continuous. The rate of movement also varied over time. From this inclinometer no definite slip plane could be

identified. The movement occurred over the entire depth of the inclinometer. It could therefore be assumed that there was no plane of weakness bisecting the inclinometer.

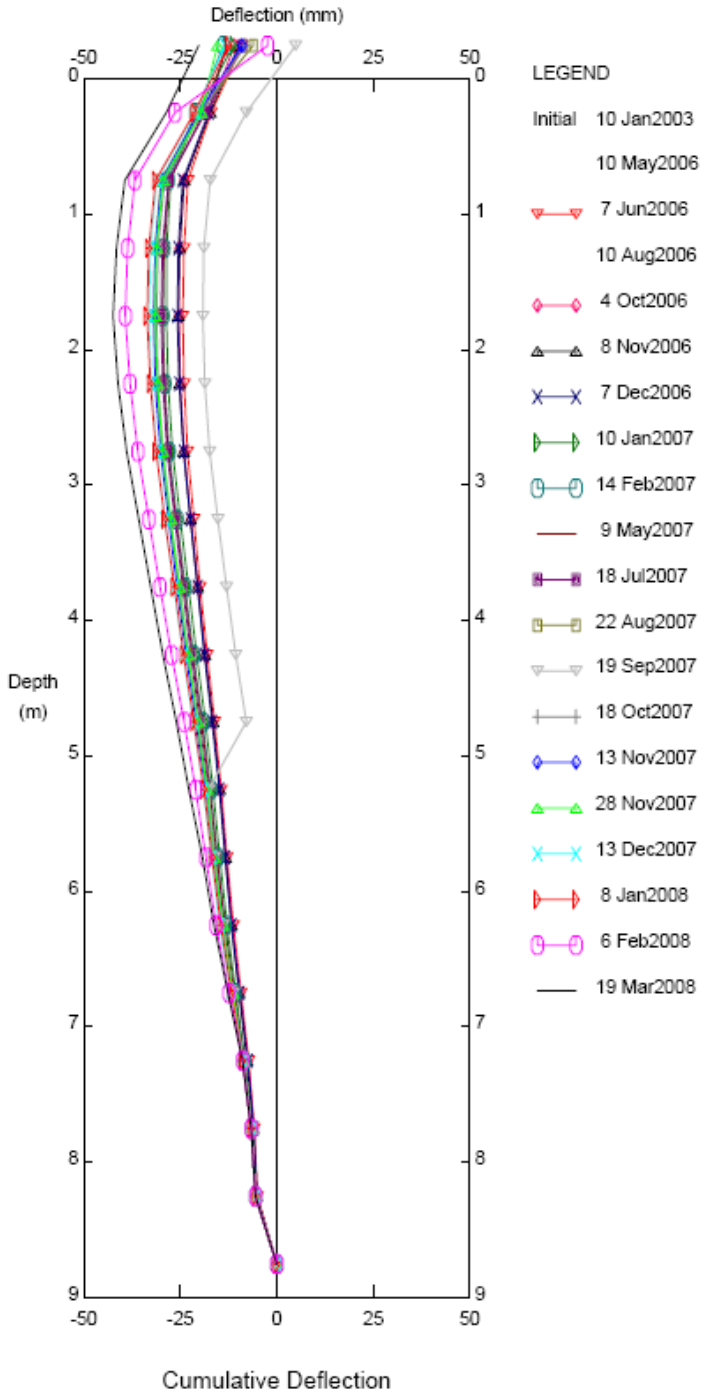

Figure 6.7 Cumulative deflection within borehole 104 (Atkins, 2008).

Borehole inclinometer 105, Figure 6.8, also showed significant down slope movements. The movements were also continuous with rates varying over time. The movements decreased with depth and became insignificant at a depth of around 3.75m. Significantly

this was again the boundary depth between the stiff clays and the soft clays identified during the investigation.

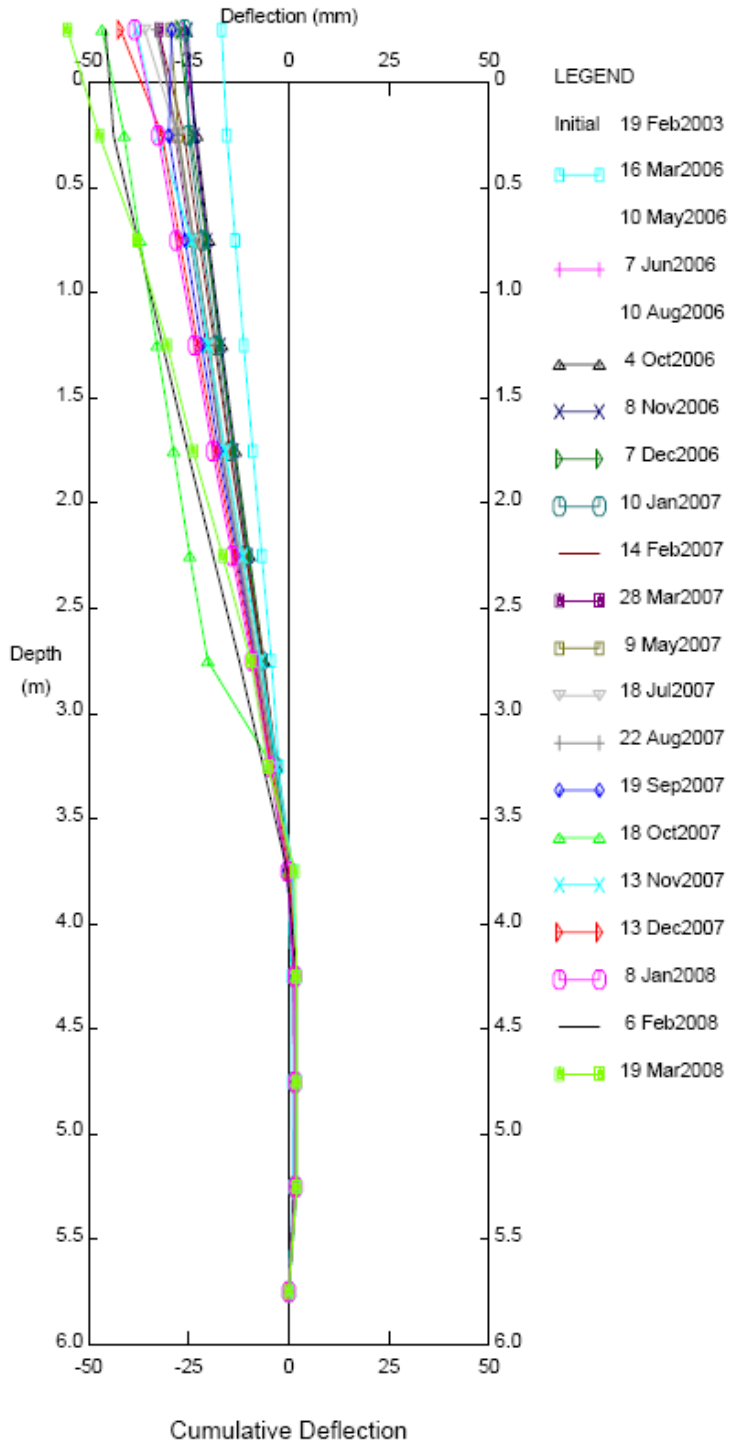

Figure 6.8 Cumulative deflection within borehole 105 (Atkins, 2008).

From the inclinometer data it was clear that the lower slope was moving and that the upper slope was not. There was no definite slip surface identified by the inclinometer data and the material seemed to creep down slope. The upper slope remained relatively stable with little down slope movement. It was proposed earlier that the current ground

conditions were due to a previous failure, possibly similar to the one shown in Figure 6.9. It was assumed that the slope consisted of mainly horizontal horizons with sands and mainly stiff clays. The failure in the lower slope, most likely due to water softening and erosion from the river Lagan, caused further softening of the clay along the slip surface. This assumption explained the presence of the stiff clay resting on the soft clay and also the presence of the Malone sand in the lower slope. The made ground present at the top of the lower slope was assumed to be the result of the previous works after the last slope failure, which occurred to the North of the site. It could be reasonably assumed that the previous work dug out failed material and replaced it with the made ground.

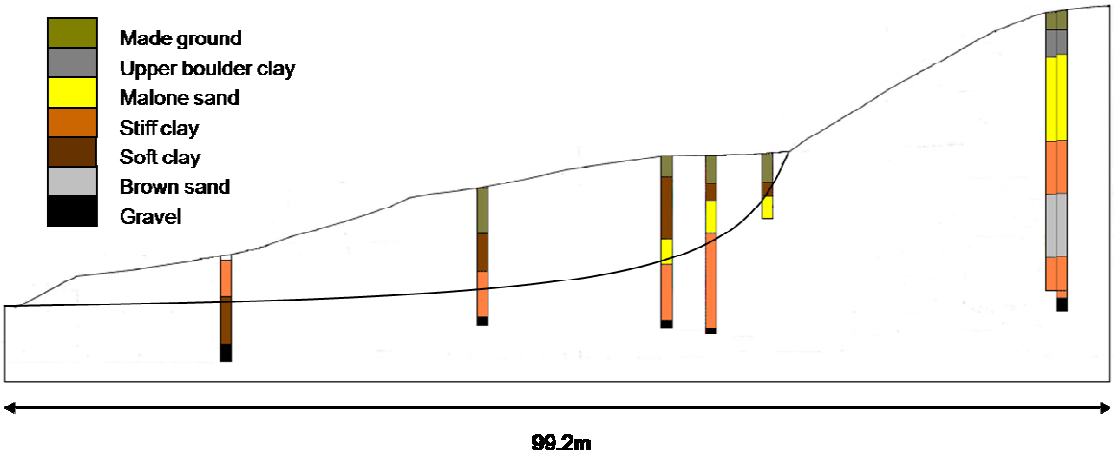

Figure 6.9 Possible position of historic slip surface within Belvoir slope.

The depth of the proposed historical slip plane coincides with the limit at which movement had been detected within the inclinometers and also the boundaries between the soft and stiff clays. The absence of a defined slip surface may be due to the coarse grained components within the boulder clay. Within a more homogenous clay a slip surface will have formed with a much reduced strength due to the clay platelets lining up along the direction of movement. Within the boulder clay, boulder and gravel could have consistently churned the material along the slip surface preventing this alignment and significant strength reduction. The result was a softer reconstituted material within the vicinity of the slip surface. It could be assumed that the churned material had been identified as the soft clay during the site investigation.

6.4.4 Correlating observational data

The following charts collated the water level data, displacement data and rainfall data for BH 104 and BH 105. Figure 6.10 for BH 104 shows the relationship between rainfall, water levels and displacement. During 2006 there was seen to be a slight drop in rainfall. This dry period resulted, after about a month delay, in a slight drop in water levels. There was a slight negative displacement at this time. Then as rainfall increased the water levels also increased and positive down slope displacements were recorded. A long dry period resulted in a large drop in water levels but there was no displacement reading at this time so the response was unknown. The water levels, however, recovered and increased to a new high of around 7 mAOD. This resulted in an acceleration of down slope displacement. Water levels dropped again temporarily and this time there was a displacement reading which shows a corresponding upslope movement. Water levels once again resumed their maximum level and down slope displacement once again resumed and accelerated. Another dry period was shown by the rainfall data at this point but the water levels remained at 7m. The last displacement reading, however, showed a slight reduction in the displacement acceleration.

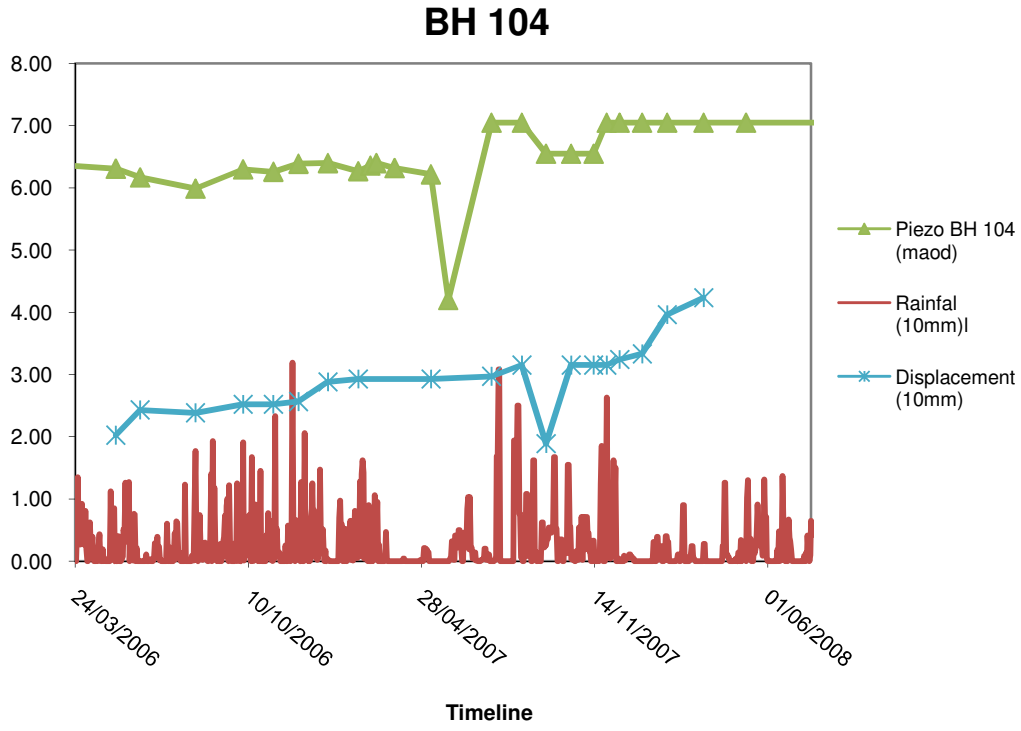

Figure 6.10 Piezometer, displacement and rainfall data within BH104, (British Atmospheric Data Centre, 2008 and Atkins, 2008).

At the location of BH 105 the water levels remained unchanged throughout the monitoring period (see Figure 6.11). The displacements recorded, however, do show

good correlation with the rainfall data. The period of prolonged rain from July 2006 to February 2007 lead to an acceleration of down slope movement beginning during December 2006 and lasting until March 2007. The down slope movement was not recovered during the dry period and it became very responsive to the future rainfall events of July 2007 and November 2007.

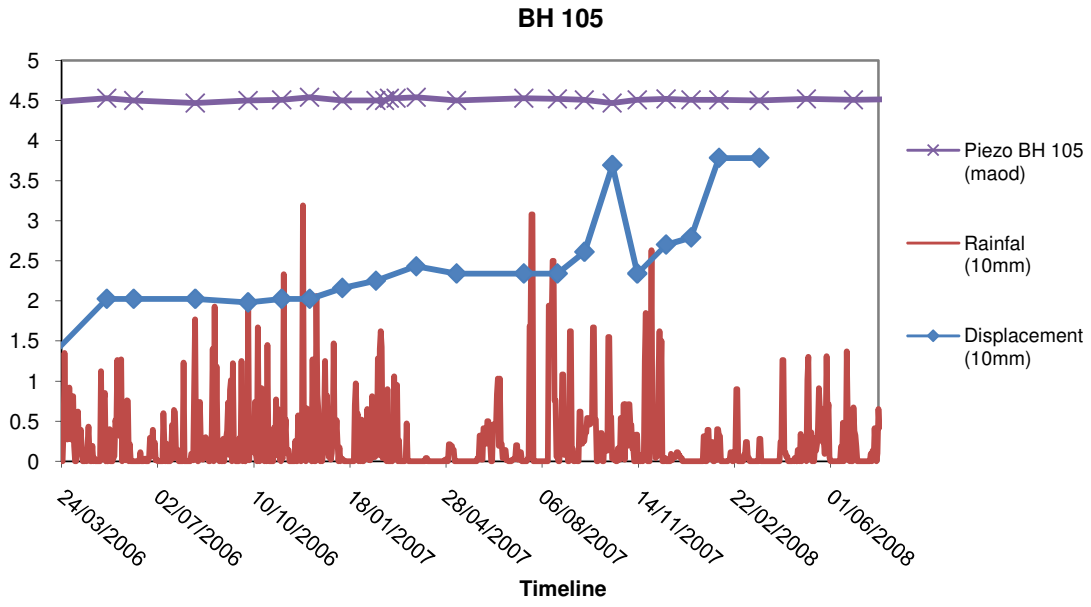

Figure 6.11 Piezometer, displacement and rainfall data within BH105, (British Atmospheric Data Centre, 2008 and Atkins, 2008).

The water levels at this location were at surface level. It was therefore feasible that artesian pore pressures existed at this location. On walkovers it was noted that water was pouring out the top of the standpipe. If this was the case then the down slope movement was likely to be a direct consequence of changes in pore pressures caused by either infiltration of rainfall upslope or an increase in artesian pressure due to mechanisms beyond the considered boundaries. These artesian pressures could not be recorded by the stand pipe piezometer. If artesian pore pressures do not exist the movement at this location would be more likely to be due to the horizontal displacements further upslope. The movements at locations BH 104 and BH 105 do correlate quite well apart from movement up slope at BH 104 at 19/09/2007 being followed by down slope movement at location BH 105 approximately 1 month later. This may be explained by the development of a tension crack between the two locations. The movement at both locations, however, can be seen to be accelerating towards the end of the monitoring period.

Overall the hydrological regime of the slope could be seen to be complex. Data from the instrumentation could also be interpreted in several ways. The next stage of the analysis involved the modelling of the slope. It was expected that the complex regime may have been beyond the capabilities of the model. Reproduction of the instrumentation data would involve several assumptions. It was considered, however, that the modelling exercise, together with trial and error assumptions, may have been able to provide insight into the factors influencing the movement and which of these factors were dominant within the slope.

6.5 Creating the model

6.5.1 Introduction

The objective of this study was to use the transfer model developed within chapter 4 and used within Chapter 5 to model the deformations recorded on the Belvoir slope. As stated previously a site investigation was undertaken by Atkins (2008). This investigation comprised of several boreholes around the site with samples taken and tested. Monitoring equipment was also installed and readings taken at regular intervals, the results of which were discussed within Section 6.3 and 6.4. From this information it was possible to build a numerical model of the cross section and the characterisation of the materials within the slope was estimated from available testing data. This data was used to build a model of the slope within the SHETRAN and Flac-tp.

6.5.2 Creating the grid

The profile of the slope and the material within the slope, as discussed, varied considerably along the length of the slope. Many of the strata identified within the intrusive site investigation were found to be discontinuous. A number of assumptions were therefore needed to build a conceptual model from the information available.

Firstly the surface profile of the slope was simplified. This was done to simplify the grids within the SHETRAN and the Flac-tp model. This allowed an identical profile for both of the models. The profile taken from the site survey was for a particular cross section illustrated within Figure 6.1. Considering the variation in profile along the slip surface it was deemed reasonable to assume some limited simplification to the complex profile of the cross section. Figure 6.12 shows the cross section. The slope was split into 9 distinct sections. These sections represented the areas for which a linear slope

was assumed for the conceptual ground model. The greatest simplification was around the area of river Lagan. This area was shown to be submerged and was not subject to any significant failure other than periodic surface erosion by the river Lagan and subsequent shallow slips.

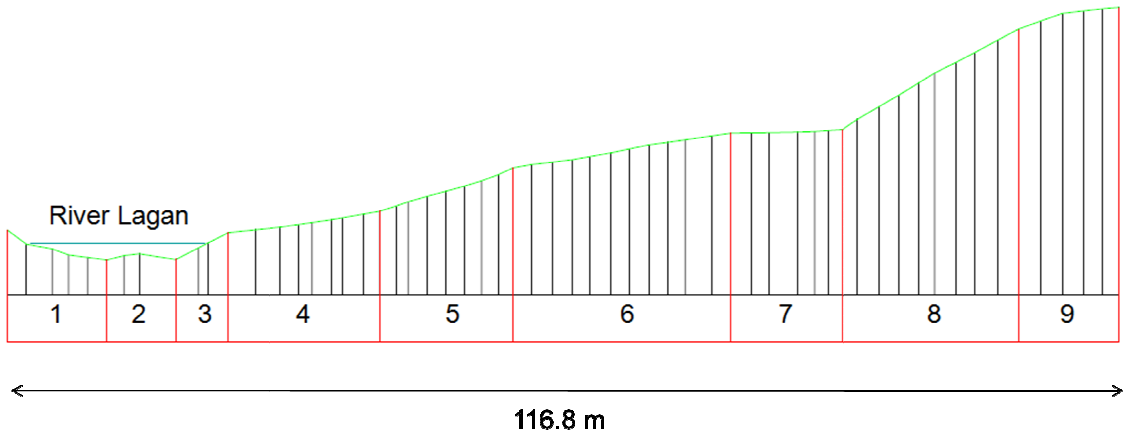

Figure 6.12 Belvoir slope cross section split into 9 simplified sections.

The slope length was over 100m and the model required a consistent grid size. The size of the elements needed to be determined taking into account accuracy and computational time. For the purpose of the simulation an element size of 1m height and 2m length was assumed. This dimension would give sufficient accuracy for the length of the slope involved with a satisfactory run time. The geometry of the elements within the Flac-tp model were also required to be rectangular enough so that the triangles within the elements were not overly distorted (see Section 3.6.3). The conceptual model was therefore also designed so that this would not occur. Table 6.1 shows the measured lengths, heights and average slope angle of each section and the corresponding simplified values used for the conceptual model. Section 1 varied considerably along its length and was therefore simplified the most. This section was deemed to be stable and therefore not the area of interest. Section 2 was submerged below the river and it was also assumed there was significant no movement there either. The remainder of the simplified sections followed the measured profile within reasonable accuracy. The horizontal co-ordinates were rounded to the nearest 2m intervals and the vertical co-ordinates to the nearest 1m interval. Where the rounding of measurements created a slope which was not of comparable steepness to the measured slope the length of the conceptual model slope was altered accordingly.

Table 6.1 Conceptual model levels for the sections identified within Figure 6.12.

Section	1	2	3	4	5	6	7	8	9
Measured length (m)	10.4	7.2	5.5	16.0	14.0	22.9	11.8	18.5	10.5
Measured height (m)	3.1	0	2.8	2.3	4.6	3.7	0.4	10.6	2.3
Simplified length (m)	8	8	6.0	14.0	16.0	22.0	12.0	18.0	12.0
Simplified height (m)	3	0	3.0	2.0	5.0	4.0	0.0	10.0	3.0
Average angle (degrees) (measured)	17	0	27	8	18	9	2	30	12
Average angle (degrees) (simplified)	21	0	27	8	17	10	0	29	14

The original profile and adopted profile can be seen within Figure 6.13. This Figure shows the adopted profile is a very reasonable approximation of the Belvoir slope and will therefore offer insignificant levels of any stability increase or decrease due to geometry.

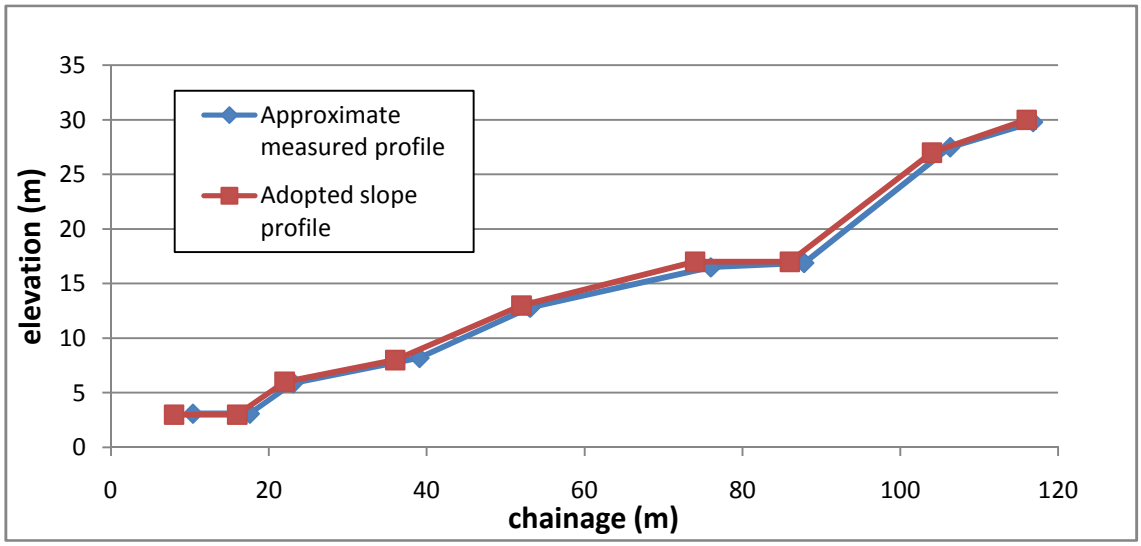

Figure 6.13 Approximate slope profile due to sectioning of Belvoir slope and adopted slope profile for SHETRAN and Flac-tp modelling.

The SHETRAN model generally had 2m long elements. At locations where the slope geometry was such that the slope angle was small then 4m long elements were used. The depth of the SHETRAN elements at the surface was 0.5m. This depth was

stipulated to keep the surcharge needed to compensate for the topsoil on top of the Flac-tp surface to a minimum. The rooting depth of the vegetation was also restricted so as to be contained within the surface cell. The rooting depth needed to be kept within the surface cell so that all surface processes were accounted for in the SHETRAN surface cell. Transferring the surface pore pressures from this cell to the Flac-tp surface then allowed Flac-tp to yield pore pressure variations at a depth comparable to SHETRAN as per previous simulations within Chapters 4 and 5.

The geology of the Belvoir slope as stated earlier was complex. Within the region of the upper slope the strata is horizontal and fairly well defined. Within the lower slope the history of failures has created significant irregularities. Lithologies were not always horizontal or continuous. A simplified conceptual model was therefore developed to best represent the ground conditions encountered by the site investigation and assumptions outlined within Section 6.3.

The levels of the horizons were once again simplified in order to preserve element geometry within the Flac-tp program, Figure 6.14. The brown sand and gravel was also omitted from the model as their effects on the surface failure were assumed to be minimal. As there was limited information for the brown sand below the upper slope and the material horizon was thought to have a limited effect on model output it was assumed the material would have similar properties to those of the Malone sand. A continuous layer was therefore assumed encompassing the brown sand below the upper slope and the Malone sand layer within the lower slope. It could be assumed that the two materials were of similar composition and that this assumption would not significantly affect model output.

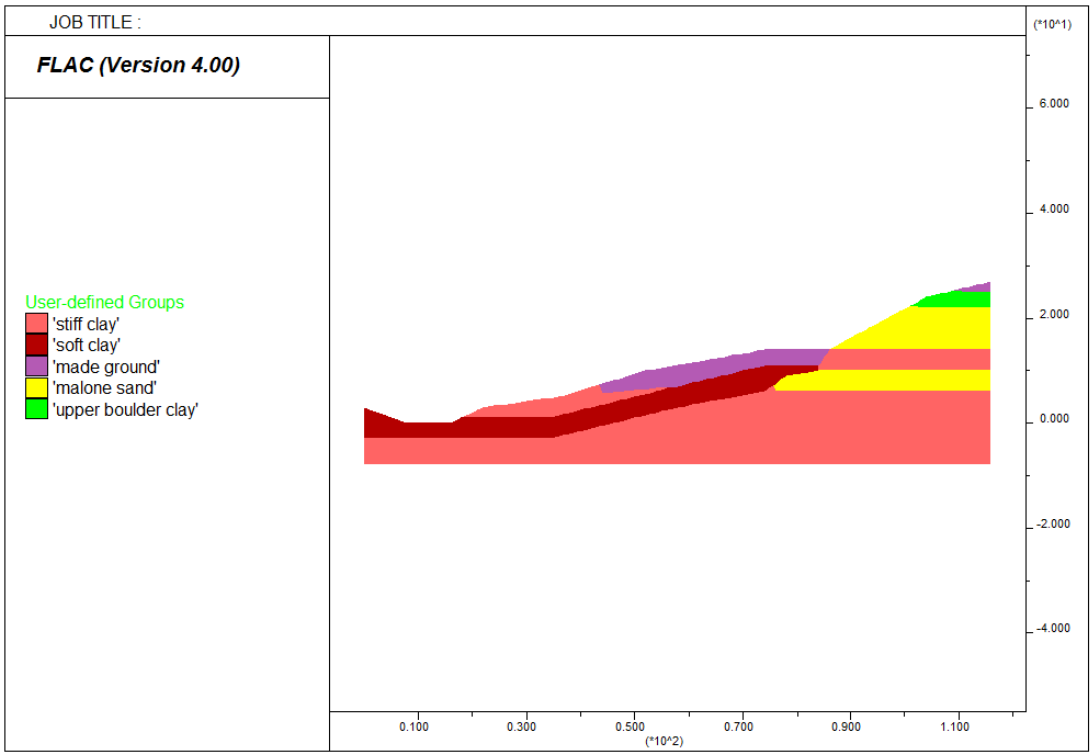

Figure 6.14 Conceptual model boundaries for the Belvoir model, scale in metres.

This conceptual model allowed the deformation of elements within the slope to be kept to a minimum. Figure 6.15 shows the Flac-tp grid used for the mechanical analysis.

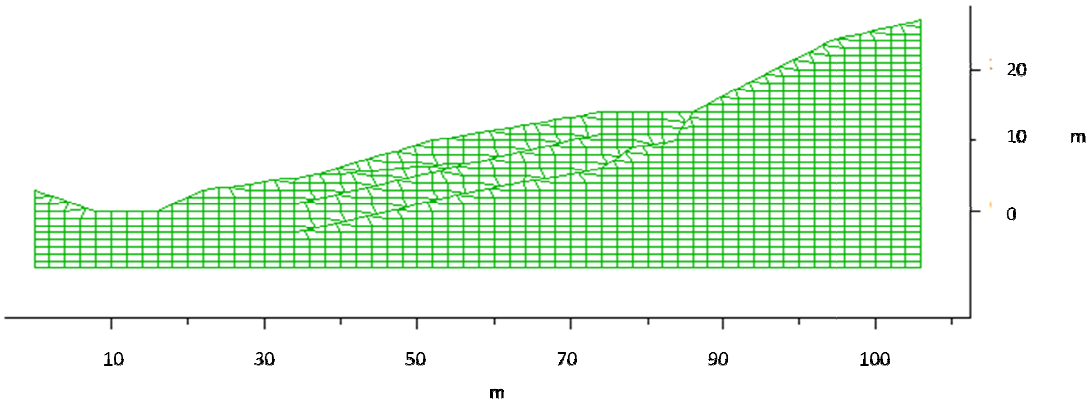

Figure 6.15 Flac-tp grid used for the Belvoir slope analysis.

6.5.3 Material Parameters

The parameters required for both the SHETRAN and Flac-tp models were assumed from the back analysis conducted by Atkins (2008). These parameters were derived from the laboratory tests on recovered samples from the site investigation. Where the data was not available the parameters were assumed from experience with similar material. Not all parameters required for the modelling were available from the Atkins report. Where the parameters were not available they were assumed from the literature.

Generally, density and shear strength data was available from the Atkins back analysis but there was no data available regarding the elastic properties. The mechanical properties assumed are summarised within Table 6.2. The properties that were derived from the literature are highlighted in red.

Table 6.2 Mechanical material properties assumed for the Belvoir Flac-tp analysis.

	Density ($Kg/m^{3)}$	Bulk modulus (kPa)	Shear modulus (kPa)	Cohesion (kPa)	Friction angle (degrees)
Made ground	1880	2e5	1e4	5	20
Upper boulder clay	2060	2e3	1e3	10	26
Malone sand	2000	1e4	6e3	0	33
Soft clay	1980	2e5	1e4	0	22-18
Stiff clay	2080	2e5	1e4	10	27

There was limited information regarding the soil water characteristic curve of the materials on site. The unsaturated hydrological properties were therefore derived from charts published by Geostudio (Geo-slope, 2002). Permeability data was also assumed from experience gained from previous simulations. Particularly, the experience gained during the SHETRAN verification simulation conducted on the slope at Newbury, Chapter 5, was drawn upon to determine permeability characteristics. A parametric study was conducted on the permeability to get the best fit between recorded and simulated data. The initial hydrological properties are listed in Table 6.3.

Table 6.3 Hydrological parameters used for SHETRAN simulation of Belvoir slope.

	Permeability m/s	Residual saturation	Porosity	Van Genuchten n	Van Genuchten α
Made ground	1e-8	0.115	0.45	3.2	0.048
Upper boulder clay	5e-9	0.045	0.226	2.7	0.015
Malone sand	1e-8	0.115	0.45	3.2	0.048
Soft clay	5e-9	0.055	0.3	2.2	0.03
Stiff clay	5e-9	0.045	0.226	2.7	0.015

6.5.4 Vegetation parameters

Vegetation on the site was seen to consist of deciduous trees and bare ground with some shrubbery. The canopy within the SHETRAN program therefore assumed a homogenous canopy of 10% deciduous trees and 90% bare ground. From previous SHETRAN analysis Table 6.4 represents a typical example of the deciduous tree rooting depths. It can be seen that the total rooting depth of a deciduous tree was assumed to be around 2.82m.

Table 6.4 Example of deciduous tree rooting depths from previous SHETRAN analysis.

Root depth (m)	Percentage of roots	Total depth (m)	Total percentage of roots
0.12	6	0.12	6
0.12	19	0.24	25
0.12	18	0.36	43
0.18	14	0.54	57
0.18	11	0.72	68
0.18	9	0.9	77
0.18	8	1.08	85
0.54	6	1.62	91
0.6	5	2.22	96
0.6	4	2.82	100

These depths were plotted to give an indication of the distribution of roots with depth in Figure 6.16. This Figure showed that the majority of the trees roots were confined to near the surface with more than 50% present in the top 0.5m.

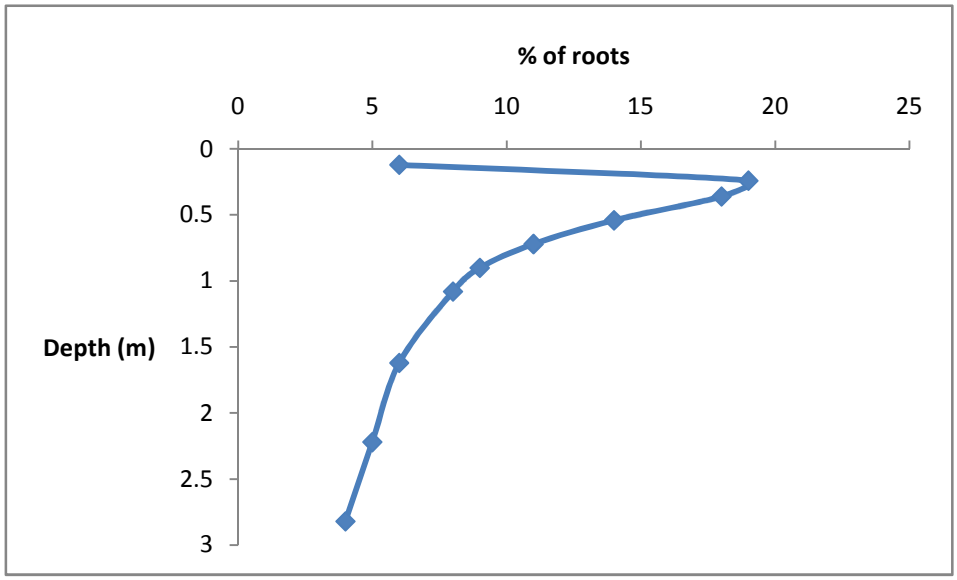

Figure 6.16 Typical example of a deciduous tree root distribution with depth.

As discussed within the introduction, the rooting depth was required to be entirely encompassed within the surface cell which had a depth of 0.5m. This depth was required to minimise the magnitude of surface pressure needed to simulate topsoil within the Flac-tp simulation. As only surface pore water pressures were to be transferred then water extracted by SHETRAN from cells below the surface cell would not be accounted for in the Flac-tp simulation. This would result in the Flac-tp simulation overestimating the amount of water in the subsurface. If the tree roots were to be restricted to 0.5m, depth the simulation would be unrealistic as the uptake of water would realistically occur over a greater depth than that modelled. The slope, however, was seen to remain largely saturated for most of the year with a phreatic surface near or at the surface, Figure 6.5. The abundance of available water near the surface would reduce the depth that the tree routes would need to penetrate to find water. As the subsurface was saturated, water was also able to move freely to the tree roots at the surface. Modelled water uptake by roots restricted to 0.5m near the surface would therefore be able to reasonably simulate the shallow variations of the phreatic surface. Should the phreatic surface fall below 0.5m then the surface suctions simulated by such a method could be assumed to be larger than those on site. The effect of such suctions would need to be closely monitored to identify any unrealistic suctions and deformations. A root depth distribution restricted to 0.5m would therefore be valid, with some close observation. The modelled root depth distributions are outlined within Table 6.5 and Figure 6.17.

Table 6.5 Modelled tree root distribution within SHETRAN model.

Root depth (m)	Percentage of roots	Total depth (m)	Total percentage of roots
0.01	4	0.01	4
0.05	15	0.1	19
0.15	23	0.16	42
0.15	28	0.31	70
0.2	30	0.51	100

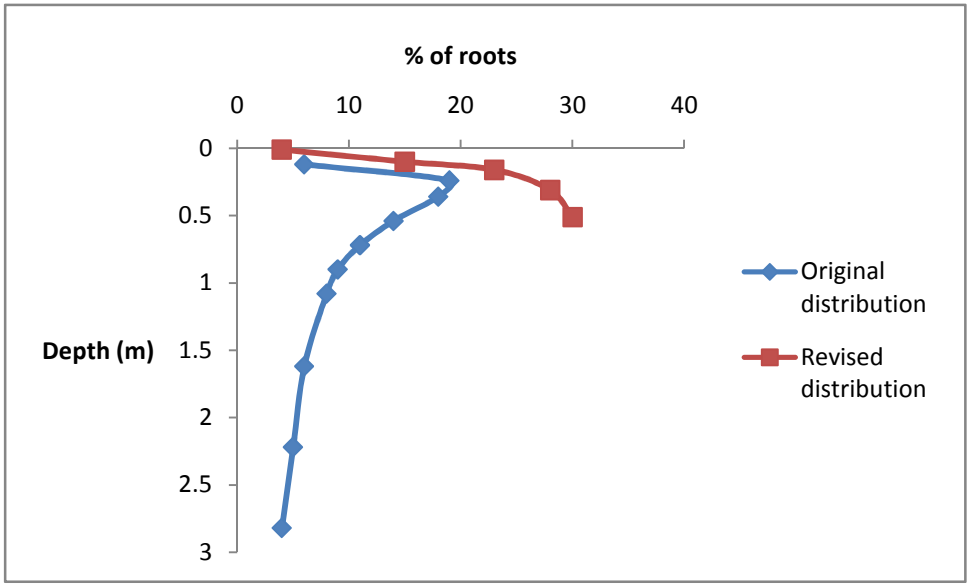

Figure 6.17 Typical and modelled tree root distribution with depth.

During the site walkover, roots were seen to surface, the root profile has therefore been raised to surface level. The rest of the profile has been kept low in an attempt to reduce large surface suctions which may affect infiltration rates and increase uptake from depth within the saturated zone. The remainder of the vegetation properties are as per previous SHETRAN simulations and are listed below within Table 6.6.

Table 6.6 Deciduous tree properties for SHETRAN modelling.

Canopy storage capacity	15e-4	m
Fractional rate of change of drainage water storage	3.7e3	1/mm
Leaf drainage rate when storage = C_s	19e-9	mm/s
Canopy resistance factor	RCF	s/m
Actual transpiration as a fraction of potential (Given as a number of pairs of fraction: soil moisture tension)	FET	-150m – 0 -3.33m - 1
Leaf area fraction Given as a number of pairs (layer thickness : ratio of leaf area to area of element)	LAF	1m – 0 4m - 3

6.6 SHETRAN simulations

6.6.1 Introduction

The grid was built within SHETRAN to the specifications discussed earlier and the material properties listed within Table 6.3 were applied to the relevant media. The hydrological models were initially run from the beginning of January 2006 to the end of December 2008 with initial permeabilities and a bottom boundary pore pressure fixed to initial conditions. This allowed the modelled pore pressures to be compared with the water levels recorded by the piezometers on site. The permeability of the media and bottom boundary pore pressure could then be back analysed from these comparisons if good agreement could not be attained. Once a good agreement was established between the hydrological model and the piezometer readings a hydrological model for the period between January 2001 and December 2008 was run. The surface pore pressures from this model were then transferred to Flac-tp for deformation analysis.

6.6.2 Determining field conditions from back analysis

All the models were run with initial hydrostatic conditions. The initial model was run with the pore pressures at the base of the model fixed as per the initial condition throughout the analysis. This was assumed as the land behind the slope will have its own water regime hence water table. This water table will be able to supply the slope with water throughout the year and hence an elevated water table will be present within the slope. An elevated water table can be simulated within SHETRAN by specifying a head at bottom of the grid. Extraction of water from the surface of a column would

therefore lead to infiltration from the base of the column in order to maintain a hydrostatic profile. Conversely, infiltration at the surface leads to exfiltration at the base. The rate at which these processes occur is determined by the effective permeability of the material.

Initial simulations showed the assumed permeability of the made ground was too high. Water immediately drained out of the material leaving the material dry for the remainder of the simulation which did not compare well with the recorded data. Conversely the remainder of the assumed permeabilities proved too low with no variation in pore pressures over the length of the simulation. A number of simulations were run with a variety of combinations of permeabilities. Table 6.7 details the permeability combination which gave the best comparison to the recorded data. These permeabilities were therefore used for the remainder of the SHETRAN and Flac-tp simulations. Figure 6.18 shows the variation in water levels at borehole 104 location.

Table 6.7 Revised model permeabilities.

	Permeability m/s	Revised Permeabilities m/s
Made ground	1e-8	5e-9
Upper boulder clay	5e-9	5e-8
Malone sand	1e-8	1e-7
Soft clay	5e-9	5e-8
Stiff clay	5e-9	5e-8

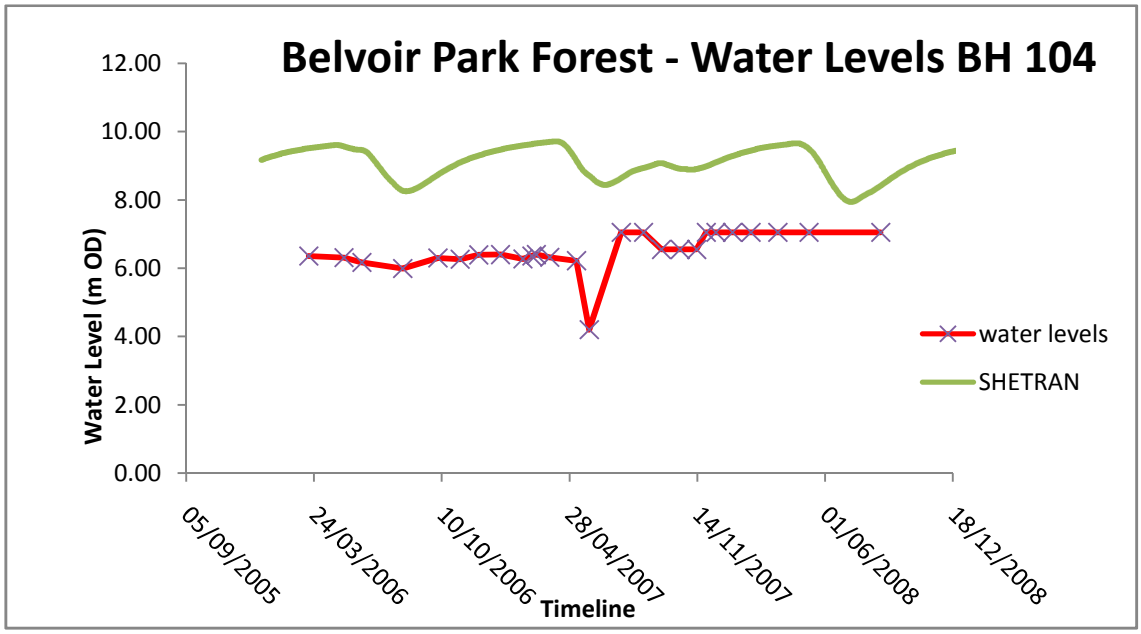

Figure 6.18 Simulated and recorded water levels for borehole 104 with SHETRAN bottom boundary fixed to initial conditions and initial permeabilities.

The simulation with the revised permeabilities shows that the height of the initial water table was overestimated by around 2-3m (see Figure 6.18). The simulation, however, showed encouraging results with regards to the response of the water levels to infiltration events. The rise and fall of the water table within the SHETRAN model showed good correlation with the fall and rise of the water table observed by the piezometer at BH 104. The magnitude of the water table variation remained constant within the SHETRAN simulation at around 2m. The piezometer at BH 104 showed that the water table remained fairly constant apart from a sharp decrease at the beginning of May 2007. The pore pressure within the borehole then recovered just as swiftly and the water table settled to a steady height around 1m higher than the before the sharp drop.

Lowering the water table to a maximum height of 6 mAOD (depth of 5m) within the vicinity of BH 104 resulted in lowering the average water levels. Figure 6.19 shows the revised water levels for BH 104.

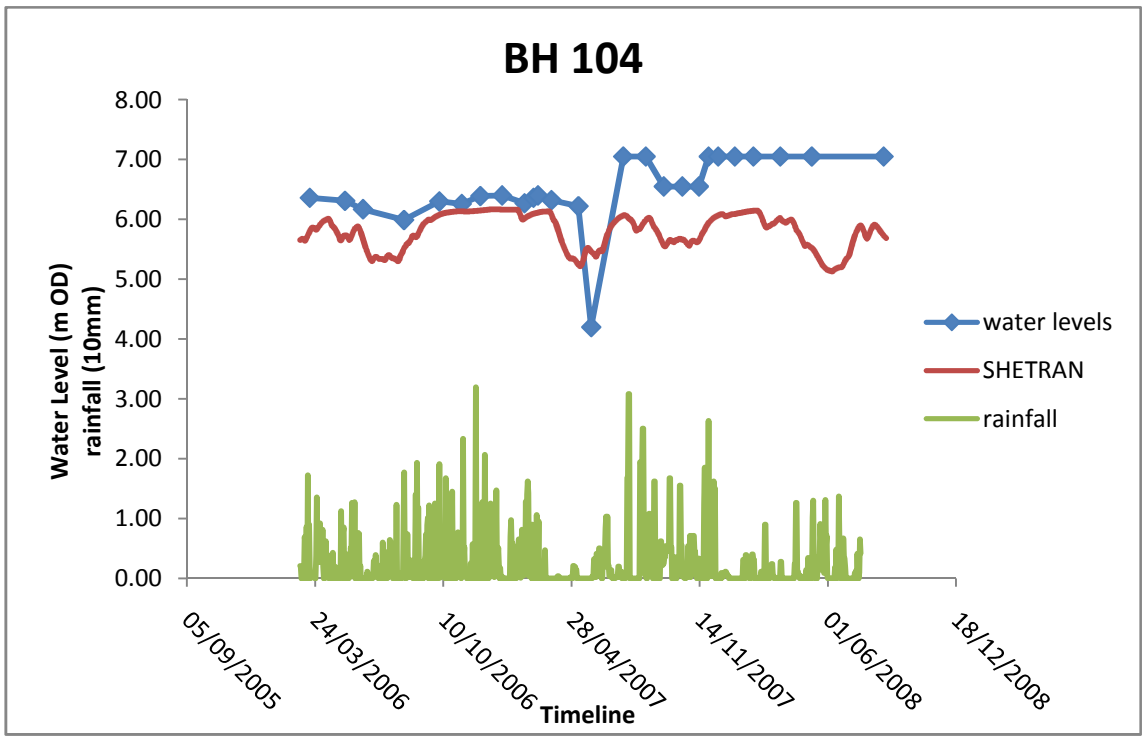

Figure 6.19 Simulated and recorded water levels for borehole 104 with lowered bottom boundary pore pressures and daily rainfall data.

It can be seen from Figure 6.19 that SHETRAN had managed to capture some aspects of the water level changes reasonably well, particularly the first half of the simulation. The large drop in water levels at 29/05/2007 was not fully captured within the SHETRAN simulation. There was a drop in water levels within the simulation but this occurred slightly before the recorded drop and the magnitude was approximately half of that recorded. The water levels within the simulation recovered at approximately the same time as the recorded water levels but the water levels peaked at just below the previous high at slightly under 6 mAOD. The next few months of the simulation up to 15/02/2008 captures the rate and magnitude of the changes in water level very well but at a consistently lower water level. The previous water level high was around the boundary between the clay and the made ground, the new water level high was over 0.5m within the made ground. The simulation then showed the water levels drop off which when compared to the rainfall data seemed reasonable. The recorded water levels, however, remained at a constant high of just over 7 mAOD. It seemed from this chart that something other than surface infiltration and evaporation was affecting the pore pressures within the slope at around 29/05/2007. The SHETRAN simulation showed that there was no reason for such a large water level drop mid simulation and again no reason for a new higher water table during the latter half of the simulation. The SHETRAN simulation was backed up by the rainfall data, which is also shown in

Figure 6.19. This showed that for the latter half of the simulation there was no significant increase in rainfall, there was actually a slight decrease.

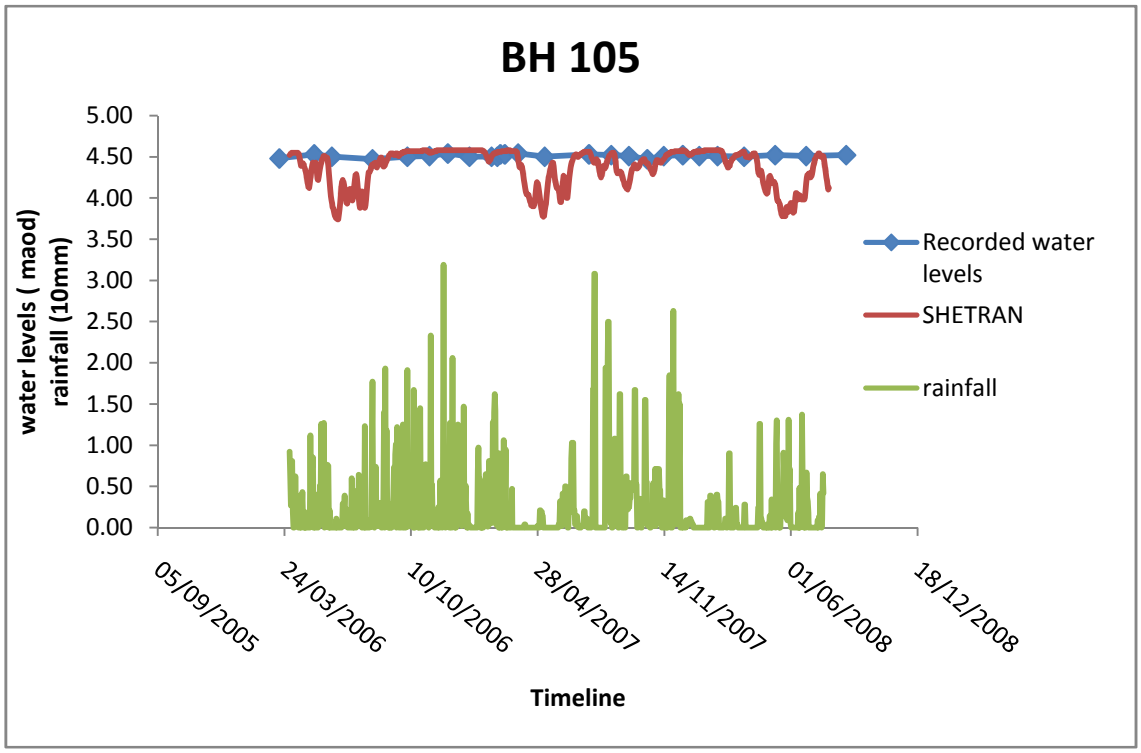

Figure 6.20 Simulated and recorded water levels for borehole 105 location with initial permeabilities and revised bottom boundary pore pressures and daily rainfall data.

The simulated water levels at location BH 105 are plotted against the recorded water levels in Figure. 6.19. The simulated water levels show more variance than the recorded water levels. Water can be seen to be extracted from the slope much more readily within the simulated data. One possible explanation for the discrepancies is that the vegetation is extracting too much water. The low water levels occurred during the summer months and hence the months when evapotranspiration is highest. The canopy, however, is already quite sparse at 90% bare ground and 10% tree cover. Reducing coverage further would have negligible effect on the water level variance. Another explanation is that some artesian pore pressures existed which were capable of maintaining the water levels at this depth. As mentioned earlier, walkover studies of the site conducted by Atkins noted water coming out the top of the piezometer throughout the year.

At this stage of the analysis it could be seen that the permeability could be altered to give a good comparison to half of the field data as per the Newbury simulation within Chapter 5. From these preliminary analyses it could be seen that the water regime

within the slope was far more than a simply a response to surface processes. It seemed likely that water pressures were being introduced into the system from another source other than the surface. It was also probable that some movement within the slope affected the pore pressures especially at the BH 105 location. The next section of the analysis was carried out within the Flac-tp program to attempt to distinguish whether there had been any mechanical influence on the pore pressures.

6.7 Flac-tp simulations

6.7.1 Introduction

The SHETRAN modelling had limited success in modelling the water levels within the slope at Belvoir. The difficulties may have been caused by artesian water pressures which can be modelled within SHETRAN by manually altering the bottom boundary condition. The other possibility is that movement within the slope had caused the changing water levels. The purpose of the Flac-tp modelling was to determine whether the pore pressure variations predicted by SHETRAN for the first half of the simulation were likely to have caused instability within the slope.

6.7.2 The transfer method

Due to the complexities of the cross section surface the Flac-tp surface grid points were not at regular intervals (see Figure 6.14) and therefore did not coincide with the centre points of the SHETRAN cells. The code developed to transfer pore pressures to a square grid, within section 5.4.6, was therefore utilised.

6.7.3 Initial conditions

For a simulation such as this it can be difficult to determine the exact initial conditions of the problem. There had been a lot of activity at the site of the slope which included previous failures and also excavation and backfilling. The full details of this past activity are not fully known. It was therefore decided that the model be constructed with regards to the most current site investigation. All material parameters were set as elastic and the initial pore water profile was assumed hydrostatic and as per the SHETRAN initial conditions. The bottom hydrological boundary was also set to the conditions determined by the SHETRAN simulations. The pore pressures were then fixed and the model allowed to reach mechanical equilibrium under self weight. The displacements at this point were then re-set to zero.

This method was not ideal for determining the initial conditions as features such as developed slip planes and over-consolidation will have been omitted from the model. It was thought, however, that to try and second guess the processes that the slope went through would introduce yet more uncertainty into the model. It was already established by the hydrological modelling that without manually altering boundary conditions the models would be incapable of simulating the recorded water levels. The purpose of the modelling was therefore diagnostic, to establish the mechanisms active within the slope which were likely to produce such recordings and not an attempt to blindly and accurately simulate the slope recordings.

6.7.4 Pore pressure transfer

For the initial pore pressure transfer the mechanical part of the Flac-tp calculation was turned off. This allowed the direct comparison of the Flac-tp model with the SHETRAN model. Figure 6.21 shows the pore pressure variation within the made ground of the lower slope for both models after the pore pressure transfer.

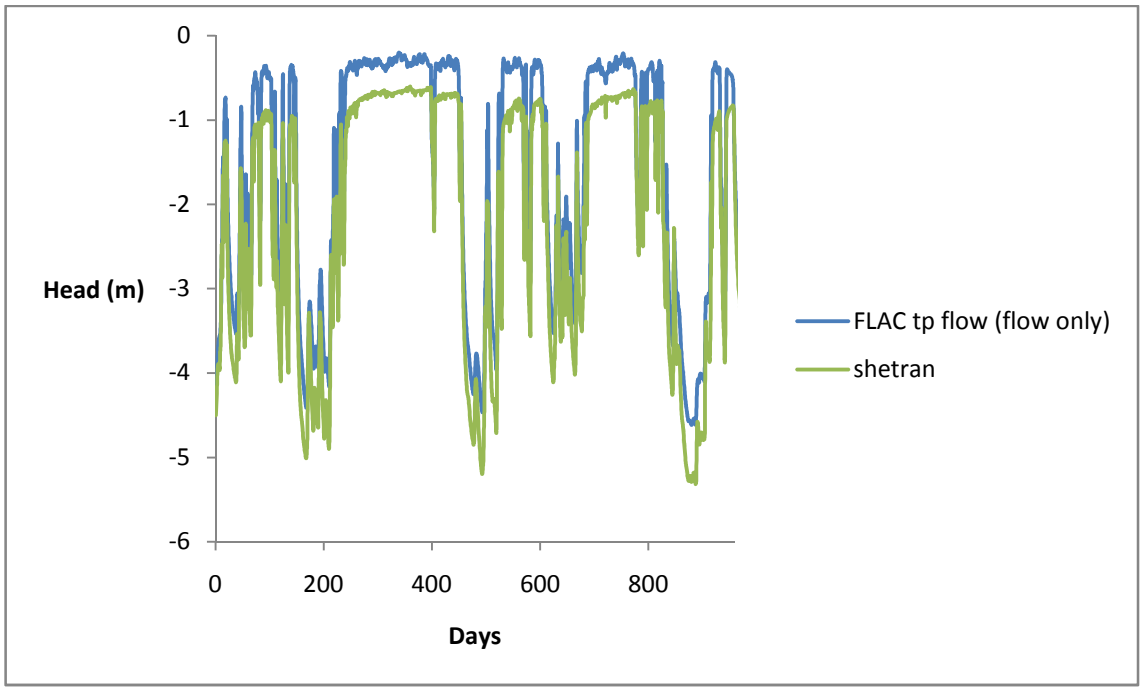

Figure 6.21 Simulated water levels from SHETRAN (1.91m depth) and Flac-tp (1.5m depth flow only) calculations.

Due to the different grids of the Flac-tp model and the SHETRAN model a there was no reference gridpoint, for which readings could be taken, at the exact same depth for both models. The closest similar reference points were at 1.91m depth for the Flac-tp model

and 1.5m depth for the SHETRAN model. Figure 6.21 shows that the two models compare very well with the maximum head difference being around 0.4m which is due to the height difference between the two reading points.

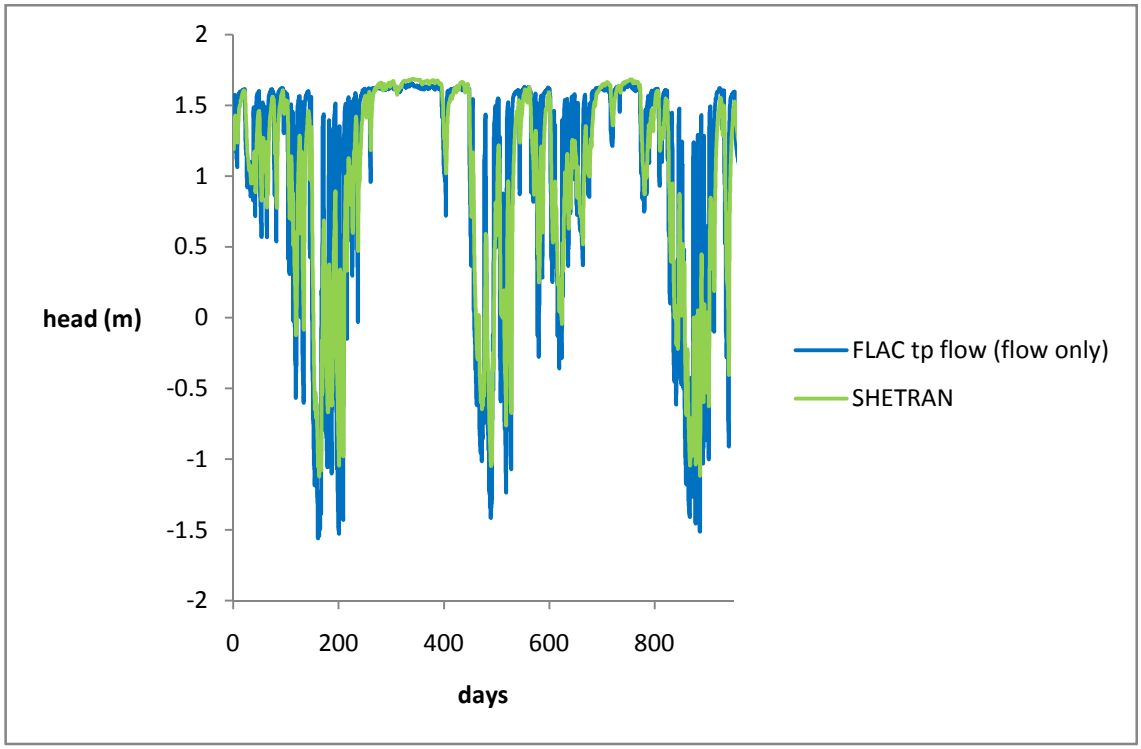

Figure 6.22 Simulated SHETRAN and Flac-tp water levels for a 1.7m depth.

Another comparison was performed further down slope at around a depth of 1.7m, Figure 6.22. The comparison between the two models was once again very good. This exercise gave confidence that the Flac-tp model was capable of modelling the unsaturated flow through such a complex slope and that the transfer method adopted was capable of giving a reasonable level of accuracy.

6.7.5 Fully coupled elastic simulations

For the next stage of the simulations the mechanical component of the calculation was turned on. The simulation was first run elastically with an assumed bulk and shear modulus detailed within Table 6.2 for the slope materials.

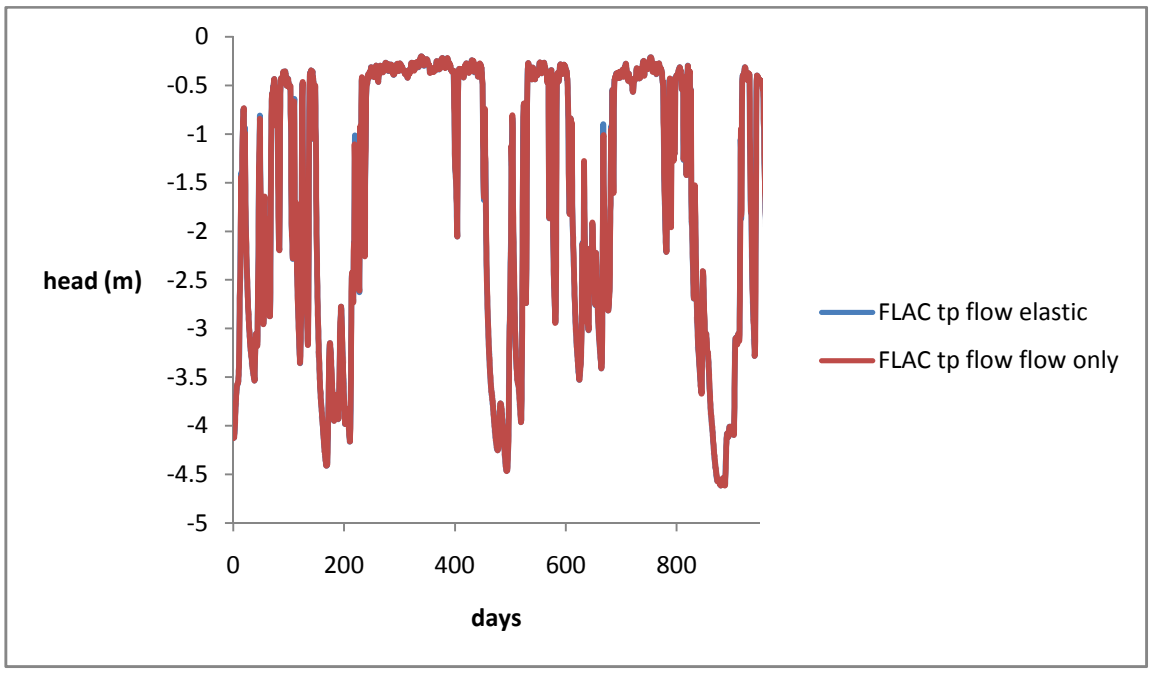

Figure 6.23 Simulated water levels for Flac-tp with mechanical calculation turned off and on.

Mechanical generation of pore pressures was again not permitted. This would ensure that the SHETRAN and Flac-tp pore pressure regimes would remain consistant. Significant deformation could, however, affect pore pressures due to porous media volume changes. Figure 6.23 showed that the calculated pore pressure variation was not significantly affected by the mechanical component of the calculation. Figure 6.24 and 6.25 show the horizontal and vertical surface displacements at the locations of borehole 104 and 105 for the simulation. The horizontal displacement (see Figure 6.24) showed an initial down slope movement at both locations during the first 100 days, although magnitude of this displacement was larger at the BH 104 location. The down slope movement was instigated by the steady rise in pore pressures at the begining of the simulation. There was a much larger increase in pore pressure at the BH104 location which lead to the larger down slope movement. After the intial movement the horizontal displacement followed a seasonal movement pattern with the BH 104 showing a larger cyclic magnitude due to the higher seasonal pore pressure variations.

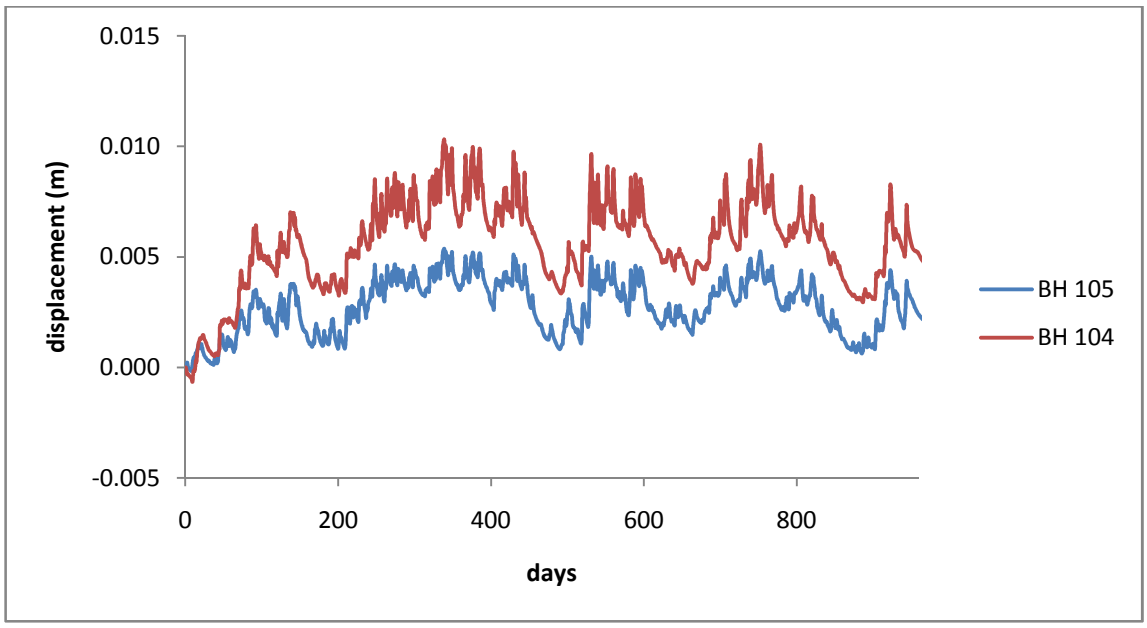

Figure 6.24 Flac-tp simulated horizontal displacements for elastic simulation at locations of borehole 104 and 105.

The vertical displacement plot (Figure 6.25) showed little vertical movement. Again the higher magnitude pore pressure variation at BH 104 resulted in relatively higher displacements. The gridlines on Figure 6.25 show that at BH 105 location the slope heaved during the wet periods and settled during the dry period. BH 104 location higher up the slope showed a higher net settlement throughout the simulation which even persisted during the wet periods. This may imply that the initial condition pore pressures at this location were overestimated and that the slope has drained slightly.

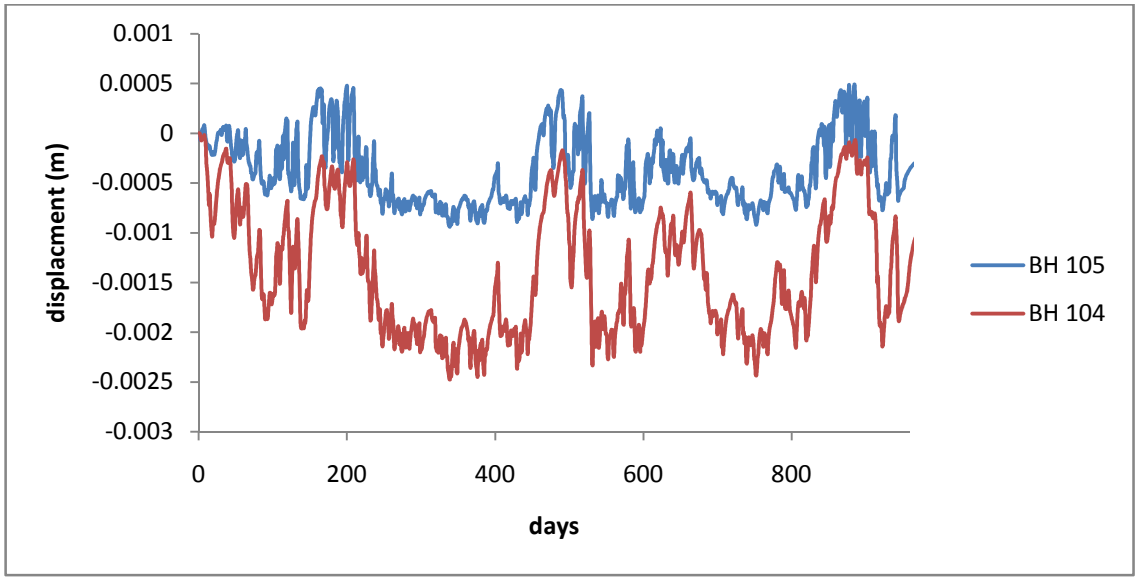

Figure 6.25 Flac-tp simulated vertical displacements for elastic simulation at locations of borehole 104 and 105.

Reducing the elastic parameters for the material within the slope by one order of magnitude increased the displacements by over 1 order of magnitude as shown in Figure 6.26. The relative displacements remain the same as the previous simulation. The simulation showed the close relationship between magnitude of displacement and elastic moduli.

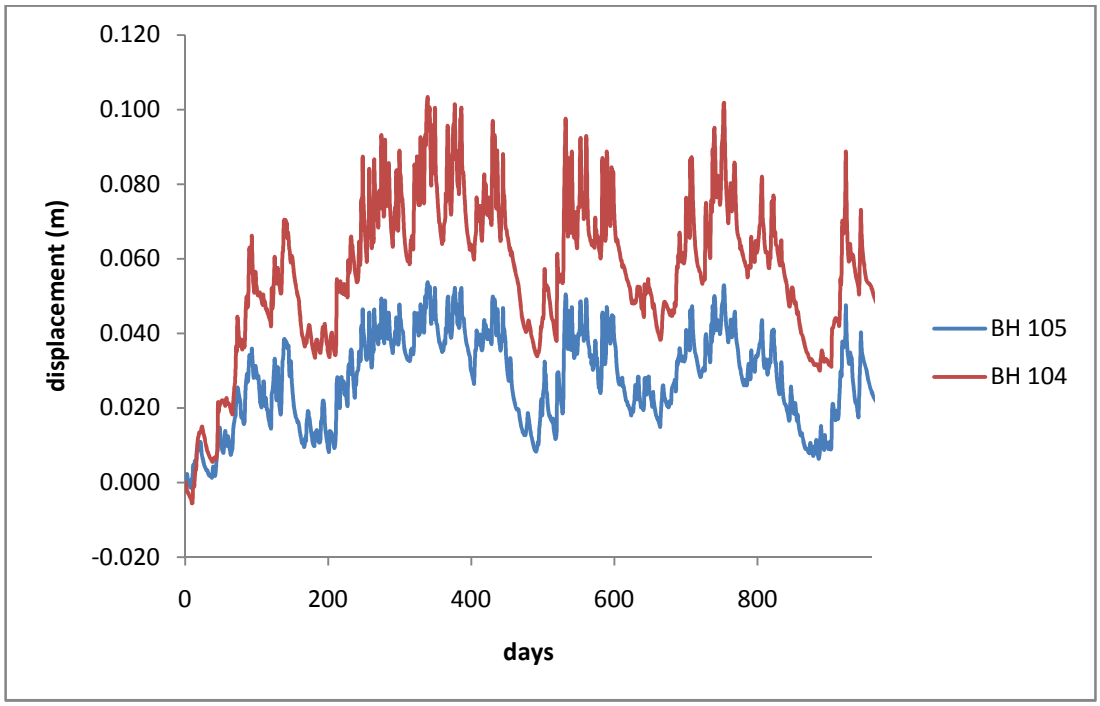

Figure 6.26 Flac-tp simulated horizontal displacements with reduced elastic parameters.

6.7.6 Fully coupled elasto-plastic simulations

For this section of the simulation the plastic parameters were input into the model. The parameters used were taken from the Atkins (2008) desk study for the slope and are detailed within Table 6.2. The soft clay was defined by the report as anisotropic with friction angles varying from 18 to 22 degrees. The modelling performed, however, assumed an isotropic constitutive model for simplification. The first simulations were run with the maximum bulk and shear moduli and the maximum recorded soft clay friction angle of 22 degrees subsequent analyses reduced the friction angle and also the bulk moduli. These simulations showed the relevant effects of these parameters on the slope displacements. The pore pressures are monitored throughout the simulations to check that the deformations were not causing the development of pore pressures. Such a development would mirror the results seen within the instrumentation but would invalidate the pore pressure transfer method.

The displacements for the material within the upper slope showed very large displacements at the surface indicating shallow surface failures. The same was true for the steep slope entering the river. These failures are shallow and therefore do not significantly affect the overall stability of the slope. Observations during the walkover support these results as the upper slope was overly steep and showed shallow failure scars (see Figure 6.27) as did the slope adjacent to the river.

Figure 6.27 Overly steep upper slope at Belvoir Park.

The displacements at BH 104 and BH 105 can be seen in Figures 6.28 and 6.29. These Figures showed that the magnitude of displacements for the simulations at the reduced bulk moduli were far larger than the displacements measured on site. It could therefore be assumed that the original bulk moduli were more representative of the onsite conditions. Reducing the angle of friction of the soft clay to 18 degrees lead to failure within all simulations. Reducing to 20 degrees lead to increased displacements within all simulations that were all far larger than the measured displacements. It could therefore be assumed that the 22 degree friction angle was more representative of the

soft clay material. None of the simulations gave rise to a significant increase in pore pressures at any location. The opposite was true with pore pressure reducing for the failed simulations.

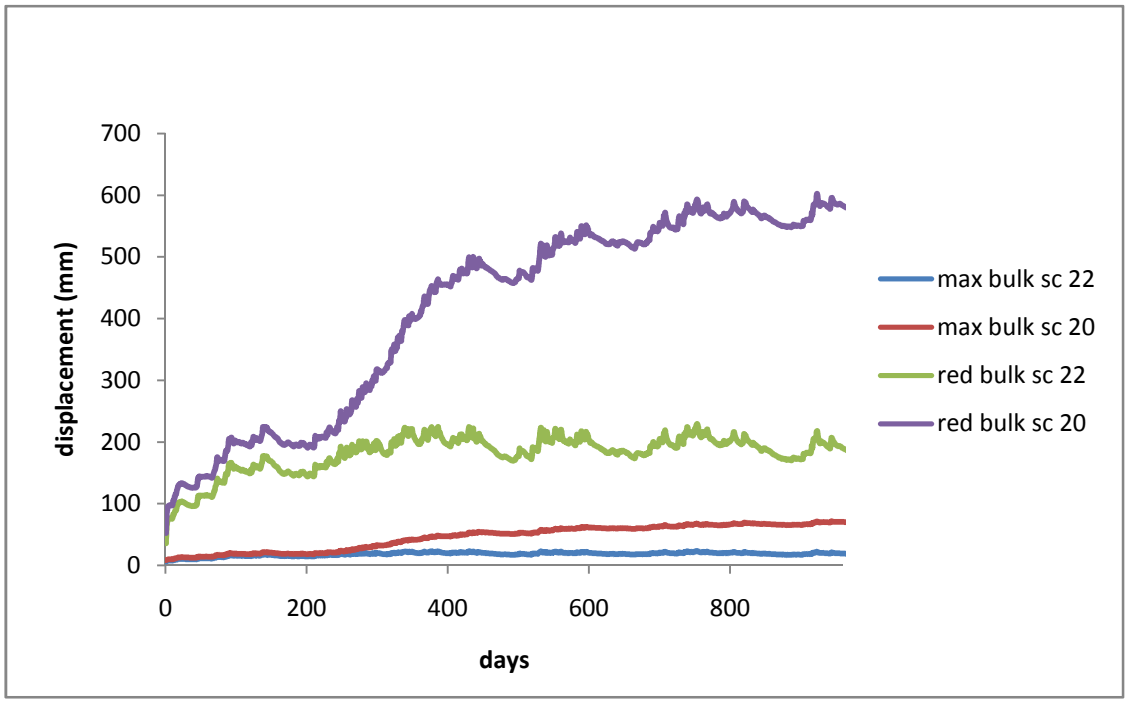

Figure 6.28 Flac-tp simulated horizontal displacements at borehole 104 for maximum and minimum bulk moduli and friction angles within the soft clay.

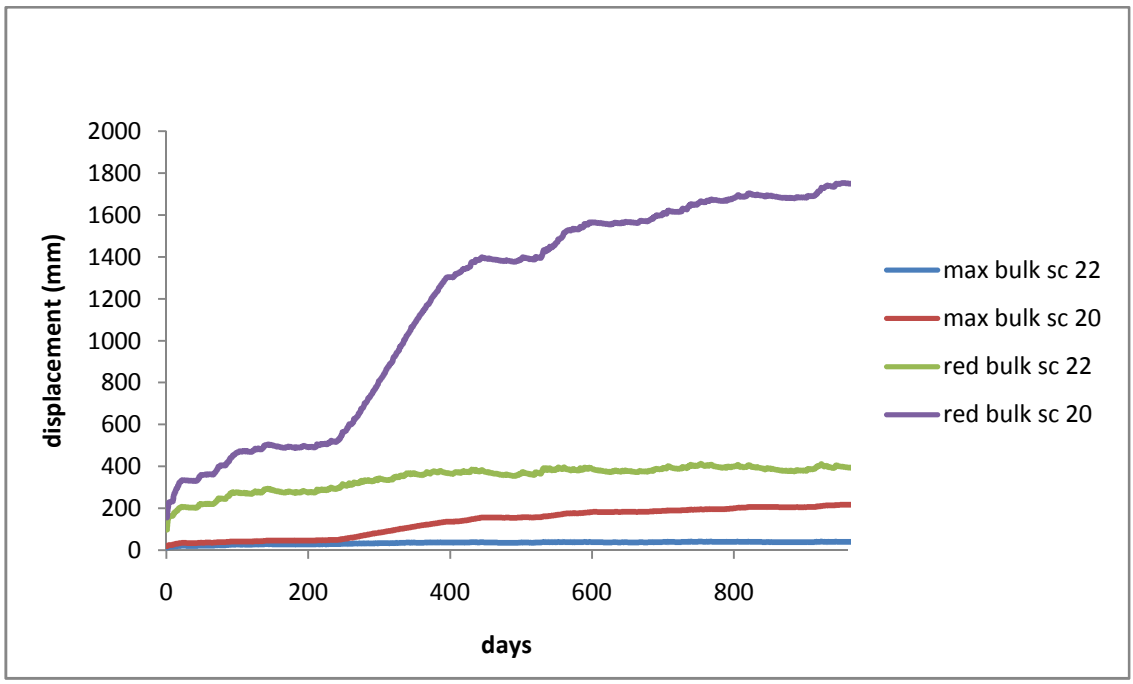

Figure 6.29 Flac-tp simulated horizontal displacements at borehole 105 for maximum and minimum bulk moduli and friction angles within the soft clay.

The parameters used for the following simulations were therefore the parameters detailed within Table 6.2. With the soft clay modelled as an isotropic material with an

angle of internal friction equal to 22 degrees. Figure 6.30 shows the Flac-tp calculated change in horizontal displacement since the first measured displacement reading (10/05/2006) and associated pore pressures. The chart also shows the measured displacement and head at BH 104 together with rainfall readings.

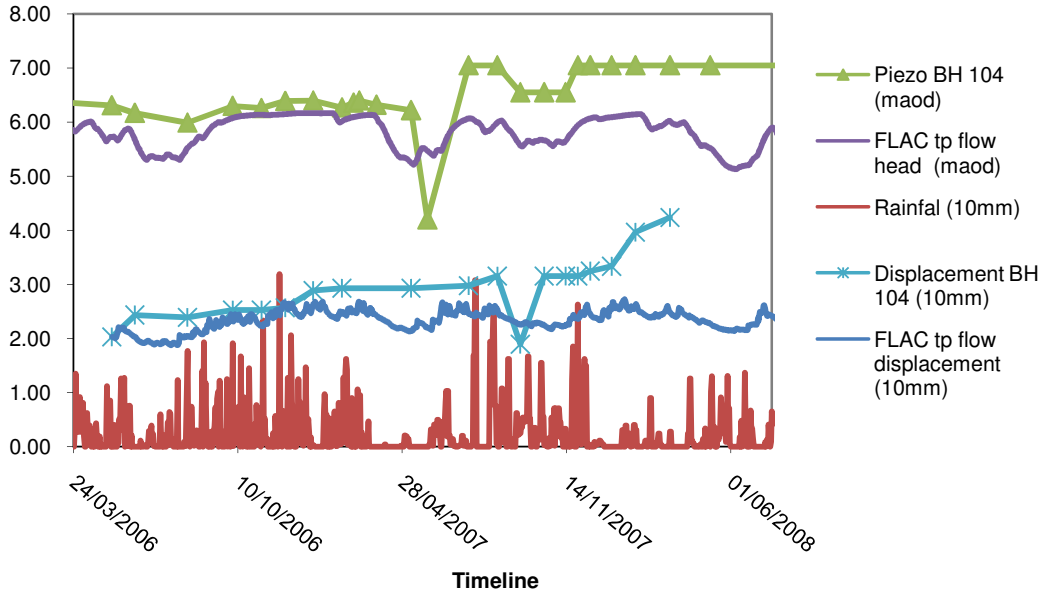

Figure 6.30 Simulated and recorded water levels and horizontal displacements at borehole 104 location together with daily rainfall data.

There was reasonable comparison of displacement up until September 2007. At this time the measured displacement showed a sharp up slope movement followed by a steady but increasing down slope movement. This was not captured by the simulation. The measured head levels also show a sharp decrease followed by sustained increase in water levels a few months earlier. This, as discussed earlier, was also not captured by the hydrological model.

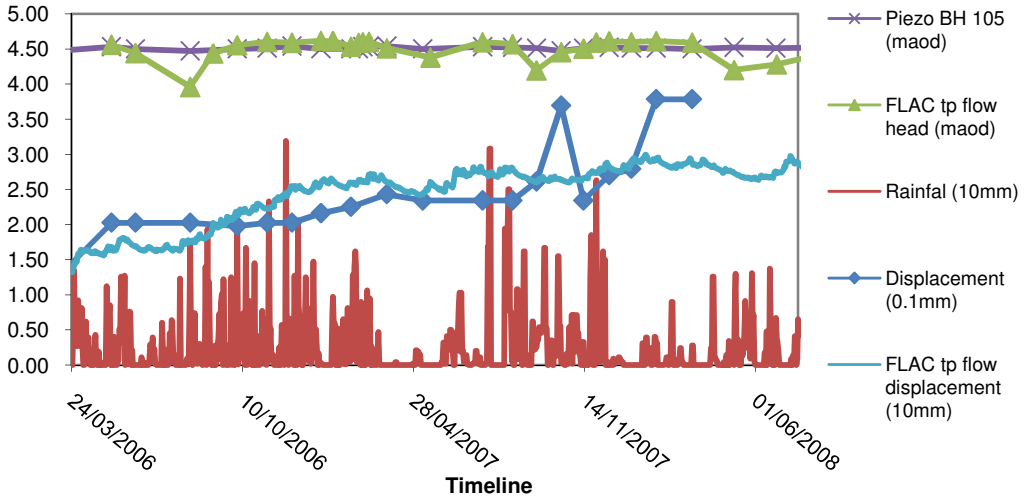

Figure 6.31 Simulated and recorded water levels and horizontal displacements at borehole 105 location together with daily rainfall data.

Figure 6.31 findings were similar to the BH 105 location. The displacement calculations from Flac-tp compare very well to the displacements measured on site up until shortly after September 07 where a sudden down slope movement was measured. This movement was subsequently recovered and the comparison is recovered also until January 2008 where the measured displacement rate increased whereas the calculated rate remains constant. The levels of measured and calculated head are fairly constant throughout the period monitored period. This is due to the water level being at the surface as discussed earlier.

From the measured results it could be seen that an event took place which resulted in elevated water levels in the upper part of the lower slope. The nature of the event was uncertain yet it could be seen that the increase in down slope movement occurred after the water level increase. It could therefore be reasonably assumed that the water level increase occurred independently of any slope movement and may have been actually been the cause. From Figure 6.5 it can be seen that the water levels below the upper slope increase by almost 4m and the water levels at the BH105 location increase by just less than 1m. In order to determine if such an increase in water levels could be the cause of increased down slope movement the bottom head boundary condition of both the SHETRAN and Flac-tp model was increased linearly by 0 to 4m over the length of the lower slope and linearly by 4 to 5 m over the length of the upper slope. The

hydraulic boundary condition was altered on the 19th September 2007. This date was chosen as an average of the dates at which the pore pressures increased over all the boreholes. The following charts show the revised plots of head and displacement for this simulation.

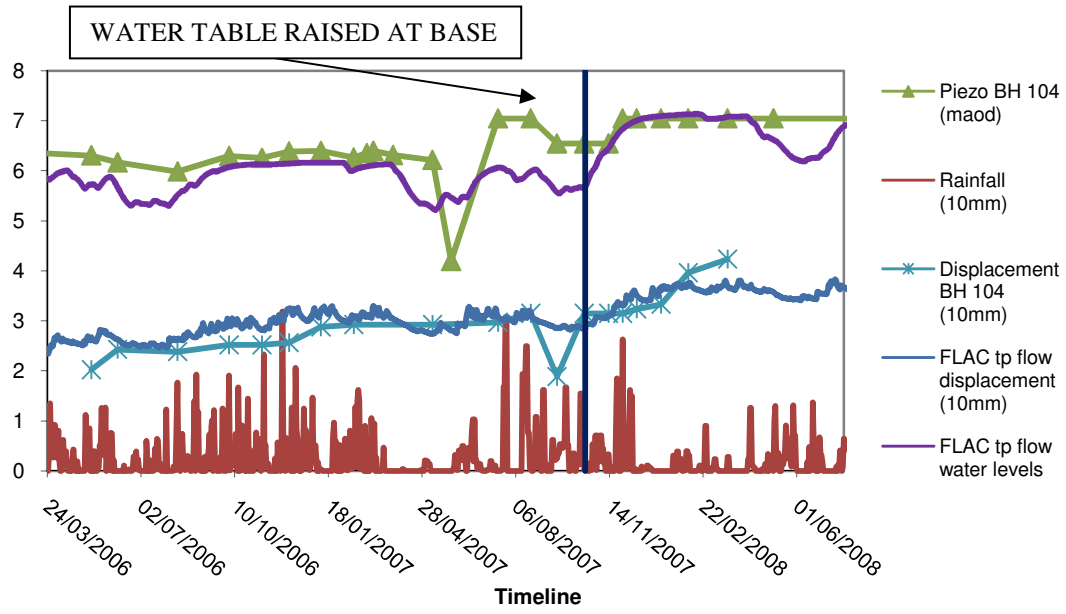

Figure 6.32 Simulated and recorded water levels and horizontal displacements at borehole 104 location with an increase in bottom boundary pore pressure together with daily rainfall data.

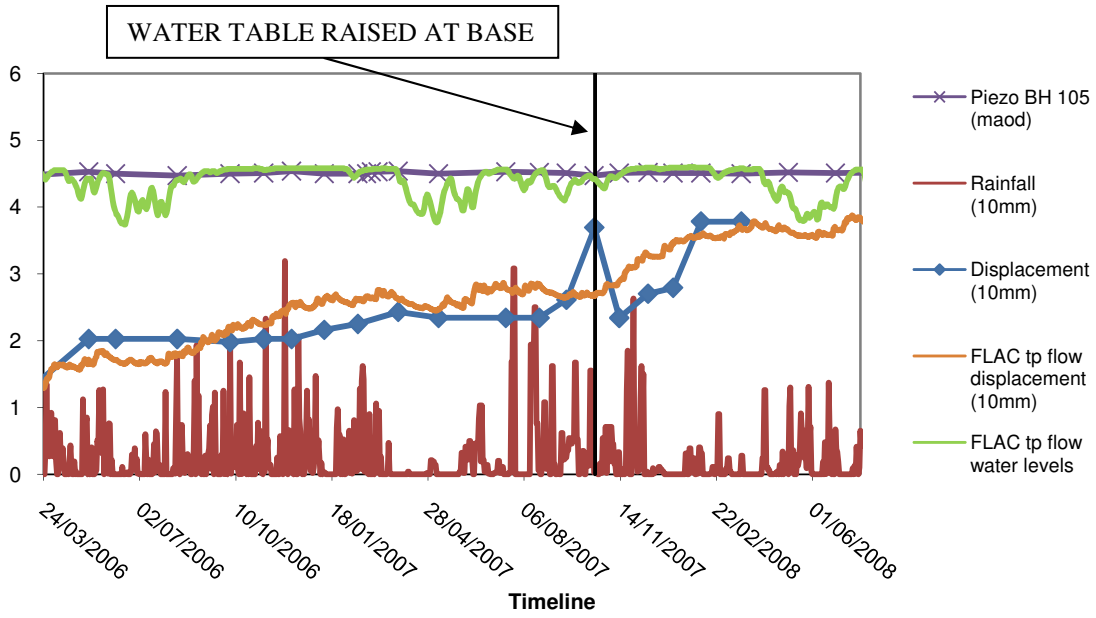

Figure 6.33 Simulated and recorded water levels and horizontal displacements at borehole 105 location with an increase in bottom boundary pore pressure together with daily rainfall data.

Increasing the pore pressure at the base to simulate artesian pore pressures increased the water levels observed at BH 104. The timing of the modelled increase lags behind the timing of the observed water level increase by approximately 2 months. At location BH 105 there was no change in the modelled water levels. This was due to the fact that water levels were at a maximum level at this location and water was being exfiltrated to the surface. The results agreed well with the walk over observations at this location where water was seen to flow from top of the standpipe.

The effect that the increase in pore pressures had on slope displaceement also compared well with the observed data. At BH 104 the displacement increased and there was improved comparison with the observed data. At location BH 105 there was also a similar good comparison with the observed data.

6.8 Discussion

The slope at Belvoir park was very difficult to model given the limited data and results available. The conceptual model developed was based on the findings of the intrusive site investigation conducted by Atkins. The conceptual model was a simplification of the actual ground conditions on site. A compromise needed to be found between model accuracy and run time. Due to the many complexities and unknowns within the ground conditions any additional accuracy was deemed to be futile.

Despite the shortcomings in site data from a modelers perspective the situation was typical of current instrumentation practice for a problem slope. The modelling had therefore been a very worthwhile exercise in learning how to apply advanced models to real situations and also establishing the merits of such models over more traditional practices. Furthermore the modelling had identified data which was critical to simulating slope displacement, such as stiffness. This type of modelling could therefore inform either preliminary investigations or future more targeted investigations.

The transfer method used was the modified transfer method developed within Section 5.5 which gave the Flac-tp models freedom to use non-comparable grids as long as the surface profiles and strata boundaries remain identical. The modified method was been shown to have improved accuracy which allowed for good comparison between the SHETRAN and Flac-tp models despite a complex geological profile. This method enabled one SHETRAN model to be run for a number of refined Flac-tp grids which in

turn could allow for the refinement of the Flac-tp grid in areas of interest to increase accuracy and coarsen the grid in areas not of interest to reduce run times. The method therefore allows more flexibility and is therefore a significant advantage over the previous transfer method.

It could be seen from the complexity of the results gained from the slope monitoring that this slope would be difficult to model. There were features of the results that were difficult to explain such as the increase in water levels with no apparent cause. The many variances in lithologies, with some appearing discontinuous, also caused difficulties in developing a conceptual model. The model was therefore developed to explain and either prove or disprove theories on the mechanisms at work within the slope rather than accurately simulate the displacements and pore pressures recorded by the instrumentation.

Early hydrological models with permeabilities from site investigation data, where available, showed no comparison to the site recorded data. Reasonable comparisons to site data for the first half of the monitoring period were obtained using permeabilites defined from back analysis. This again highlighted the problems identified within Chapter 5 of defining large scale permeabilities with small scale tests.

The coupled modelling revealed that the parameters from the laboratory testing gave a good comparison, to the recorded data, for the first half of the monitoring period. Then during the latter half deformation was underestimated. Reducing the strength of the materials within the model did not return better comparisons with the recorded data or produce the elevated pore pressures seen within the latter half of the recorded data. A parametric study reducing the assumed stiffness parameters also did not return better comparisons. It was therefore concluded that the elevated pore pressures were caused by some influence external to the area modelled. The most likely explanation was that pore pressures became elevated within the gravels beneath the slope. The assumption was that these increased pore pressures within the gravels triggered the increase in the rate of deformation observed within the recorded data.

A model was therefore built within both the SHETRAN and Flac-tp models where the base pore pressure was increased at approximately the same time as the observed increase in water levels. This increase in base pore pressure was assumed to simulate

the pore pressure increase in the gravels. The magnitude of the increase was assumed to equal the magnitude of the rise in observed water levels. This modelling presented results which compared well to the observed data throughout the monitoring period.

From this modelling exercise it was seen that the modelling work was able to reproduce the observed results. Assumptions were required regarding the vegetation and permeabilty parameters, stiffness of the matrial on site and pore pressures at the base of the model. Vegetation parameters were seen to have little or no effect on the water levels within the model. Permeability had a significant influence on the water levels modelled. The larger permeabilities resulted in lower water tables due to the ease at which water was abe to flow out of the slope. Smaller permeabilities resulted in water not penetrating into the slope and therefore little change in water levels. Stiffness parameters also had a large effect on the magnitude of displacement experienced on site with relatively smaller stiffness models showing much larger displacemnts. Base pore pressure could also be seen to have a large effect on modelled displacement as after the onset of increased base pore pressure displacements began to increase. The exercise was therefore succesful in identifying which parameters the slope deformations were sensitive too. The exercise was also succesful in identifying the mechanisms which were most likely to cause the instability. The work would therefore assist in identifying areas for further slope monitoring which could varify the results of the modelling and eventually inform on the best engineering solution to prevent instability.

Features of the combined SHETRAN and Flac-tp model which worked well in describing the mechanisms at work were the ability to apply climatic data to the model boundary. Applying the climatic data to the hydrological model gave an insight into how the pore pressure varied over the monitoring period. The influence of parameters such as permeability on the hydrological regime could also be ascertained. Coupling the hydrological model with the geotechnical model revealed how the pore pressure variations affected the displacements of the slope. From this analysis it could be seen that the slope displacements were not responsible for the water level increases. It was during this stage of the analysis that it became clear that water level increase was due to some influence external to the modelled boundaries. This could be assumed from limit equilibrium analysis but could not be proven.

Chapter 7. Conclusions and Recommendations

7.1 Introduction

This thesis has broached the three separate modelling disciplines of climate, hydrology and geotechnics. To broach these three different disciplines inevitably leads to a compromise in each. The strength of the study presented here is the amalgamation of all three separate disciplines in order to quantify the significance of each on the stability of slopes. Chapter 2 reviews past attempts to model climatic impacts on slopes and highlights areas where improvement can be made. Chapter 3 discusses current modelling tools which are capable of modelling either the effect of climate on pore pressures or the effects of pore pressure on failure rates. A modelling transfer method which could link these two modelling tools was then detailed within Chapter 4.

This Chapter summarises the major conclusions of the modelling method presented within Chapter 4, and applied to slopes within Chapters 5 and 6. Important areas of the modelling procedure are then discussed and the Chapter concludes with recommendations as to where further research can improve upon the present modelling methodology.

7.2 Conclusions

This thesis concludes with the following key findings:

- Macroscopic permeability of infrastructure is an important factor when assessing the stability and performance of slopes (see below) but measuring this parameter on a macroscopic scale has been proven to be wholly inadequate. It is the opinion of the author that, at present, the most accurate way to determine permeability at macroscopic scale is to monitor the site and back analyse using hydrological modelling techniques.
- The pore pressure distribution along the surface of a slope is not consistent at any one time. Due to factors including down-slope run off and subsurface flow, pore pressures at the toe of the slope are generally considerably higher than the remainder of the slope. Higher pore pressures reduce the available shear strength at the toe and therefore stability. Also, as the toe of the slope is where progressive failure usually initiates, it is vital that pore pressure variation and shrink swell cycles in this area are modelled correctly.

- Rate of progressive failure of a slope is not constant. The rate of failure and softening is closely linked to the variations in pore pressures, which are, in turn, controlled by the climate. Peak displacements have been seen to be linked to peak maximum pore pressures. It is therefore important to be able to model the entire annual pore pressure cycle and not just average the pore pressures for winter and summer.
- Wet events, due to increased rainfall and/or reduced evapotranspiration, lead to accelerated rates of irrecoverable down-slope movement and hence softening. More frequent wet events will increase failure rates considerably. It is therefore important to characterise the impact of a wet event on a slope and also the likely return periods of such events in order to assess the probable impact on failure rate.
- The UKCIP02 and UKCP09 climate models indicate that increased carbon emissions will increase global temperatures. Increased temperatures will increase potential evapotranspiration rates leading to drier slopes on average.
- The UKCIP02 and UKCP09 scenarios indicate that, for increasing carbon emission scenarios, rainfall will increase during the winter months and decrease during the summer months. The annual range of pore pressures within a slope subjected to a future climate scenario will therefore increase leading to larger shrink swell cycles.
- The UKCP09 medium 2080 scenarios show wet event frequency is likely to increase, again leading to a likely increase in progressive failure rates.
- The permeability of a slope will determine the effect a future climate will have on the stability of that slope. For low permeability slopes the dominant effect of a future climate is the increased evapotranspiration due to average temperature increase. High temperatures will dry out the slopes, whilst the low permeability will restrict infiltration preventing pore pressure recovery during winter months. Persistent high suctions within the slope will increase the available shear strength of the slope and hence reduce failure rates. For higher permeability slopes the dominant effect of the future climate is the large annual pore pressure range. The higher permeability allowed water to be drawn out during dry summers and to infiltrate the slope during wet winters, leading to larger shrink swell cycles and increased progressive failure rates. Due to the higher permeability, pore pressure will be able to recover during winter months which will lead to reduced shear strength and hence reduced stability.
- Strain softening within a slope subjected to a future climate occurs over a wider area. Due to the large range of pore pressures experienced at the toe of the Newbury cutting

the entire toe area experienced some softening which resulted in decreased toe support and a shallower failure than the present day cutting.

- Back analysis of failing slopes can be performed within coupled hydrological and geotechnical models to accurately determine the mechanisms which are causing failure. The developed pore pressure transfer process is therefore a useful tool for engineers working to stabilise complex slopes.

7.3 Discussion

7.3.1 Climate generation

The use of generated climate data for climatic slope stability studies is a new concept. The climate generator used here was developed for use in the agricultural industry. The data is developed to be representative of a 5 km square grid. The climate data is therefore quite general for the area concerned. The infiltration and evapotranspiration from a slope is not only dependent upon its geographical location. Chapter 5 highlighted the importance of the slope orientation on the evapotranspiration levels. Other factors which will have a significant impact on infiltration and evapotranspiration will be local factors such as such prevailing winds, sheltering from nearby forests and also the steepness of the slope.

It is unreasonable to suggest that a weather station be placed upon every slope to be modelled. The simple scaling of relevant factors is often enough to gain a reasonable approximation adequate for modelling purposes, as shown by reducing wind speed within Chapter 5. A reasonable approach would be to facilitate a study in which weather stations are positioned on slopes with differing attributes such as steepness, aspect, shelter etc. The data from the different weather stations can then be compared with weather data from a standard MET office weather station positioned at a fixed height in an open area. Simple scaling factors can then be derived for each slope attribute. This approach would enable the data from the extensive MET office weather station coverage or data from climate generation models to be scaled for individual slopes without the need for additional monitoring and their associated costs.

The current model uses hourly weather data. This hourly data, as stated in Chapter 2, is far superior for modelling infiltration than daily data. The hourly approach does, however, miss the effects of some individual storm events which, within a future climate scenario, may only

last for minutes. Climate data is rarely available at this resolution yet the need for this resolution will become increasingly necessary, especially for modelling future climate scenarios.

7.3.2 Hydrological modelling

The hydrological modelling presented within this thesis is based upon standard hydrological modelling practice. The SHETRAN model can simulate numerous processes which are not always covered by similar models. The following highlights areas where cutting edge hydrological models are developing.

Hysteresis of the soil water characteristic curve has been ignored by many hydrological models including SHETRAN. Some hydrological models do now have the capability to model hysteresis within the soil water characteristic curve, notably HYDRUS. The advantages of this capability lie in being able to more accurately model the moisture content and therefore the relative permeability of a soil regardless of whether the soil is drying or wetting. This ability will have implications on the infiltration into the slope and evapotranspiration from the slope.

Run off has also been largely ignored by many hydrological models. SHETRAN has a simple run off model but the parameters are based on judgment and previous numerical studies using the program. In-situ testing or measurement of run-off is therefore recommended to fully define these parameters. The rate at which water flows down a slope will ultimately affect the amount of water which can infiltrate into the slope. Run off towards the toe of the slope may lead to increased infiltration in this area. Stability analysis shows that this area is critical to the stability of the slope. It is therefore imperative that the infiltration into this area be defined as accurately as possible.

For the modelling work carried out within this thesis all hydrological parameters were derived from either the literature or from back analysis. Again it is impractical to derive these parameters for each slope to be analysed. One possibility for modellers is to develop a database covering a wide range of materials.

The mass in-situ permeability of a slope is the single most influential parameter in defining the infiltration and evapotranspiration into and out of the slope respectively. As highlighted

in Chapter 5, attempts to define this parameter from undisturbed samples and simple in-situ tests prove wholly inadequate. Modelling within Chapter 5 also highlights the significant effect this parameter has on shrink swell cycles and therefore stability. It is therefore strongly recommended that this parameter be defined as accurately as possible for any seasonal slope stability analysis. The problem lies with the mass permeability being defined by both the microscopic and macroscopic permeability characteristics. This problem is exasperated by the area being monitored often being partially saturated resulting in the relative permeability being measured rather than the saturated permeability. There is therefore no instrumentation known to the author that is adequate to measure the mass permeability parameter for use within numerical models. The present recommended method to determine this parameter is therefore by monitoring pore pressures and performing parametric modelling in order to back analyse the permeability. This method may prove expensive and will be time consuming for new sites. Instrument development will therefore be preferential and research into this area is strongly recommended.

The hydrological modelling within this thesis has proved to be very successful once the permeability has been determined from back analysis. The comparison of the modelling with the results from the monitoring at the Newbury site shows that the assumptions made and the parameters derived are adequate to correctly simulate pore pressure variation within the slope. Pore pressures from instrumentation and modelling using EARWIG-generated present climate data were also shown to compare well. This analysis gave confidence in the generated weather data as well as the SHETRAN modelling.

The simulations at Belvoir also proved to be successful. Although agreement between the instrument data and simulations could not be achieved throughout, the modelling work showed that there must have been additional mechanisms causing pore pressure increase and displacement outside of the modelled boundaries. These mechanisms were identified using the model. These mechanisms were subsequently included into the model and the results showed very good comparisons with the site data. The simulation method, however, had its restrictions. The routes within the model were restricted to the depth of a single cell. This did not prove to be too great a restriction on the Belvoir slope model due to the high water table. For water tables at greater depth the model would have overestimated surface suctions and also pore pressures at depth. The depth of the routes was restricted due to restrictions of the surface pore water pressures transfer method to the Flac-tp model. This restriction may

be addressed by transferring pore pressures below the surface to Flac-tp or even all pore pressures throughout the SHETRAN grid to the Flac-tp grid. This response, however, sidesteps the obvious solution of coding a vegetation model into Flac-tp using fish language. Such an inclusion is discussed later.

7.3.3 Geotechnical modelling

The stand alone geotechnical modelling work carried out within this thesis is not cutting edge with regard to the modelling work carried out within the literature. The novelty of this thesis is, however, based upon the coupling of the geotechnical modelling with the hydrological modelling. There are therefore many areas where the geotechnical modelling can be improved upon.

The constitutive model used within this thesis is based upon a linear elastic perfectly plastic Mohr-Coulomb model. There has been a lot of development over the last decade on constitutive models that are more representative of the materials they model. Of note are small strain models, partially saturated models, and structured models. Each of these models would demand a new set of parameters. These parameters will require extensive specialist testing which may not be economically viable for the slopes which require modelling. The infrastructure slopes which require modelling may also vary considerably over their length. It may therefore prove that the use of complex constitutive models will not be representative of the entire structure. The effort required to obtain the relevant parameters will therefore outweigh the added accuracy of the calculation.

There are a number of constitutive models which may be capable of simulating the response of a slope more accurately by addressing some of the issues discussed previously. The most advantageous development will be achieved by improving upon the stiffness model. The non-linear stiffness model used for the stability analysis within this thesis is a very basic model. The model procedure does not accurately differentiate between loading and unloading. It is therefore recommended that a model be used which would be capable of differentiating between loading and unloading. Such a model would be more capable of reflecting the response of a slope to seasonal climate changes.

The strain softening model used within the analysis, as with other strain softening and critical state models, is highly dependent upon the grid size used. The modelling work presented here has been based upon the parameters defined by authors working with similar materials. Extensive work has been carried out by MottMacdonald to define softening rate by slope displacement rather than as grid strain. This work has shown some success. There is, however, huge scope for improvement. Research into developing a grid independent strain softening model is therefore recommended.

The pore pressure transfer method used within this thesis has proved successful for the modelling of the infrastructure slopes. The method, however, was not as successful for the Belvoir slope. The primary reason for this is that the pore pressure transfer is one way only with no feedback from Flac-tp to SHETRAN. This method cannot allow for the mechanical generation of pressures within the model. The only practical way to improve upon this method is to re-write the SHETRAN surface model into the Flac-tp code. This will have the added advantage of only needing to run one program. This will be no small undertaking as SHETRAN is a highly developed and capable tool. Simplification of the SHETRAN model may be required for preliminary models and in the short term the pore pressure transfer method may therefore prove more accurate than the application of a simplified SHETRAN surface condition coded into Flac-tp. With development, however, such a tool would prove to be very powerful in assessing the influence of vegetation on earthworks. Once a surface model has been developed then it could easily be used in conjunction with other developments within Flac-tp such as more advanced partially saturated constitutive models.

7.4 Recommendations

In summary the following recommendations for further research, in order of perceived significance, are advised:

- Identify and implement a non linear stiffness model capable of distinguishing between load and unload stiffnesses.
- Improve upon instrumentation or procedures to accurately measure slope mass permeability.
- Develop scaling factors to estimate site specific climate data from regional climatic data.

- Apply surface hydraulic model to Flac-tp.
- Develop grid independent strain softening model.
- Develop hysteretic hydraulic model within Flac-tp.
- Design project to define parameters for a precipitation run off model.

8. References

Abbott, M. B., Bathurst, J. C., Cunge, J. A., O'Connell, P. E. and J. Rasmussen (1986a) 'An Introduction to the European Hydrological System - Systeme Hydrologique Europeen, "SHE",2: Structure of a Physically-Based, Distributed Modelling System', *Journal of Hydrology,* 87, pp. 61-67.

Alehossein, H. and A. Korinets (2000) 'Mesh-independent finite difference analysis using gradient-dependant plasticity', *Communications in Numerical Methods in Engineering,* 16, pp. 363-375.

Allen, R. G., Pereira, L. S., Raes, D. and M. Smith (1998) 'Crop evapotranspiration - Guidelines for computing crop water requirements', *FAO Irrigation and drainage paper 56*, FAO - Food and Agriculture Organization of the United Nations: Rome

Alonso, E. E., Gens, A. and A. Josa (1990) A constitutive model for partially saturated soils, *Géotechnique,* 40 (3), pp. 405-430.

Anderson, M. G. and P. E. Kneale (1980). 'Pore water pressure changes in a road embankment', *Journal of the Institution of Highway Engineers*, 5, pp 11-17.

Apted, J. P. (1977) *Effects of weathering on some geotechnical properties of London Clay,* Unpublished PhD Thesis: University of London.

Arya, L. M. and J. F. Paris (1981) 'A Physicoempirical Model to Predict the Soil Moisture Characteristic from Particle-size Distribution and Bulk Density Data', *Soil Science Society of America Journal*, 45, pp: 1023-1030.

Atkins (2008) *'Belvoir Park Slope - Back Analysis and Remedial Measures Options Report',* Reference: 5075461.62.DG.01, Unpublished Report for Water Service of the Department for Regional Development, Northern Ireland, Atkins: Newcastle upon Tyne.

Averjanov, S. F. (1950) 'About permeability of subsurface soils in case of incomplete saturation', *English Collection*, 7, pp. 19-21.

Bear, J. (1972) *Dynamics of fluid in porous media,* Dover Publications, Inc.: New York.

Biot, M. A. (1941) 'General Theory of Three Dimensional Consolidation', *Journal of Applied Physics,* 12 (2), pp.155-164.

Bishop, A. W. (1959) '"The principle of effective stress," lecture delivered in Oslo Norway, in 1955', *Teknisk Ukeblad,* 106 (39), pp. 859-863.

Borah, D. K. and M. Bera (2003) 'Watershed-scale hydrologic and non-point source pollution models: review of mathematical bases', *American Society of Agricultural Engineers,* 46 (6), pp. 1553-1566.

British Atmospheric Data Centre, UK Meteorological Office. MIDAS Land Surface Stations Data (1853-current) [Online]. Available at: http://badc.nerc.ac.uk/data/ukmo-midas (Accessed: 2008).

Brooks, R. H. and A. T. Corey (1964) 'Hydraulic properties of porous media', *Hydrology Papers*, 24.

Brunt, D. (1932) 'Notes on radiation in atmosphere', *Quarterly Journal of the Royal Meteorological Society,* 58, pp 389 - 420.

Croney, D. (1977) *The Design and Performance of Road Pavements,* Her Majesty's Stationary Office: London.

Davies, O., Rouainia, M. and S. Glendinning (2008a) ' Numerical predictions of seasonal pore pressure fluctuations using FLAC-tp flow', *Proceedings of the 1st European Conference on Unsaturated Soils, E-UNSAT 2008,* Durham, 1, pp. 817-822.

Davies, O., Rouainia, M., Glendinning, S. and S. J. Birkinshaw (2008b) 'Predicting seasonal shrink-swell cycles within a clay cutting', *Proceedings of the 1st ISSMGE International Conference on Transportation Geotechnics*, Nottingham, 1, pp 481-486.

Davies, O., Rouainia, M., Glendinning, S. and S. J. Birkinshaw (2008c) 'Assessing the influence of climate change on the progressive failure of a railway embankment' *Proceedings of the 12th International Association for Computer Methods and Advances in Geomechanics Conference*, Goa, CD-rom.

DEFRA. UK Climate Projections.[Online]. available at: http://ukclimateprojections.defra.gov.uk/ (Accessed: 2011).

Dingman, S. L. (1994) *Physical Hydrology.* Prentice Hall: London.

Durner, W. (1994) 'Hydraulic conductivity estimation for soils with heterogeneous pore structure', *Water Resources Research*, *32*(9), pp.211-223.

Escario, V. (1980) 'Suction Controlled Penetration and Shear Tests', *Proceedings of 4th International Conference on Expansive Soils,* Denver, 2, pp 781-797.

Escario, V. and J. Juca (1989) 'Strength and deformation of partially saturated soils', *Proceedings of the 12th International Conference of Soil Mechanics and Foundation Engineering,* Rio de Janeiro, 3, pp 43-46.

Ewen, J., Parkin, G. and P. E. O'Connell (2000) 'SHETRAN: Distributed River Basin Flow and Transport Modelling System', *ASCE Journal of Hydrologic Engineering*, 5, pp. 250-258.

Feddes, R. A., Kowalk, P. J. and H. Zaradny (1978). *Simulation of field water use and crop yield*, Halsted Press, John Wiley and Sons, New York.

Forsyth, P. A., Wu, Y. S. and K. Pruess (1995) 'Robust Numerical Methods for Saturated-Unsaturated Flow with Dry Initial Conditions in Heterogeneous Media', *Advances in Water Resources*, 18, pp. 25-38.

Fredlund, D. G. and A. Xing (1994) 'Equations for the soil-water characteristic curve', *Canadian Geotechnical Journal*, 31, pp. 521-532.

Fisher, J. B., DeBiase, T. A., Xu, Y. Q. M. and A. H. Goldstien (2005) 'Evapotranspiration models compared on a Sierra Nevada forest ecosystem', *Environmental Modelling and Software,* 20, pp. 783-796.

Fredlund, D. G., Morgenstern, N. R. and R. A. Widger (1978) 'Shear strength of partially saturated soils', *Canadian Geotechnical Journal,* 15 (3), pp. 313-321.

Fredlund, D. G. and H. Rahardjo (1979) *Soil mechanics for Partially saturated soils,* Wiley: Canada.

Fredlund, D. G., Xing, A., Fredlund, M. D. and S L Barbour (1996) 'The Relationship of the Unsaturated Soil Shear to the Soil-Water Characteristic Curve', *Canadian Geotechnical Journal;*33, pp. 440-448.

Freeze, R. A. and J. A. Cherry (1979) *Groundwater,* Prentice Hall: London.

Gan, J. K. M. and D. G. Fredlund (1988) 'Determination of the shear strength parameters of an unsaturated soil using the direct shear test', *Canadian Geotechnical Journal,* 25, pp. 500-510.

Georgiadis, K. (2003) *Development, implementation, and application of partially saturated soil models in finite-element analysis.* Unpublished PhD Thesis: University of London.

GEO-SLOPE International Ltd. (2002) *User's Guide*, Calgary, Alberta: Canada.

Hughes, P. N., Glendinning, S., Mendes, J., Parkin, G., Toll, D. G., Gallipoli, D and P. E. Miller(2009) 'Full-scale testing to assess climatic effects on embankments', *Proceedings of the Institution of Civil Engineers, Engineering Sustainability*, 162, ES2, pp 67-79.

Hulme, M., Jenkins, G. J., Lu, X., Turnpenny, J. R., Mitchell, T. D., Jones, R. G., Lowe, J., Murphy, J. M., Hassell, D., Boorman, P., McDonald, R. and S. Hill (2002) *2002: Climate Change Scenarios for the United Kingdom: The UKCIP02 Scientific Report,* Tyndall Centre for Climate Change Research, School of Environmental Sciences, University of East Anglia, Norwich, UK.

Itasca (2002) *Flac - Fast Lagrangian Analysis of Continua - Version 4.0 Users Guide.* Itasca Consulting Group: Minneapolis, USA.

Jennings, J. E. and J. B. Burland (1962) 'Limitations to the use of effective stresses in partially saturated soils', *Geotechnique,* 12 (2), pp. 125-144.

Josa, A., Balmaceda, A., Gens, A. and E. E. Alonso (1992) 'An elastoplastic model for partially saturated soils exhibiting a maximum of collapse', *Proceedings of the 3rd International Conference of Computational Plasticity*, Barcelona.

Khalili, N., Geiser, F. and G. E. Blight (2004) 'Effective stress in partially saturated soils, a review with new evidence', *International Journal of Geomechanics,* 4 (2).

Khalili, N. and M. H. Khabbaz (1998) “A unique relationship for shear strength determination of unsaturated soils”, *Geotechnique*, 48(5), pp. 681-688.

Kilsby, C. G., Jones, P. D., Burton, A., Ford, A. C., Fowler, H. J., Harpham, C., James, P., Smith, A. and R. L. Wilby (2007) 'A daily weather generator for use in climate change studies', *Environmental Modelling and Software*, 22, pp. 1705-1719.

Konukcu, F. (2007) 'Modification of the Penman method for computing bare soil evaporation', *Hydrological Processes*, 21, pp. 3627-3634.

Kool, J. B. and J. C. Parker (1987) 'Development and evaluation of closed-form expressions for hysteretic soil hydraulic properties', *Water Resources Research,* 23, pp. 105-114.

Kosugi, K. (1996) 'Lognormal distribution model for unsaturated soil hydraulic properties', *Water Resources Research*, *32* (9), pp. 2697-2703.

Kosugi, K. (1994) 'Three-parameter lognormal distribution model for soil water retention', *Water Resources Research*, 30 (4), pp. 891-901.

Kovacevic, K., Potts, D. M. and P. R. Vaughan, (2001) 'Progressive failure in clay embankments due to seasonal climate changes*', 5th International Conference of Soil Mechanics and Geotechnical Engineering,* Istanbul, pp. 2127-2130.

Lamb, T. W. and R. V. Whitman (1969) *Soil Mechanics,* John Wiley and Sons Inc.: London.

Lenhard, R. J., Parker, J. C. and J. J. Kaluarachchi (1991) 'Comparing simulated and experimental hysteretic two-phase transient fluid flow phenomena', *Water Resources Research,* 27 (8), pp. 2113-2124.

Li, K. Y., De Jong, R. and J. B. Boisvert (2001) 'An exponential root-water-uptake model with water stress compensation', *Journal of Hydrology,* 252, pp. 189-204.

Li, K. Y., De Jong, R. and J. B. Boisvert (2000) 'Comparison of root-water-uptake models*', Proceedings of Tenth International Soil Conservation Organization Conference,* Purdue University, West Lafayette, IN.

Li, X. S. (2005) 'Modelling of hysteresis response for arbitrary wetting/drying paths', *Computers and Geotechnics,* 32, pp. 133-137.

Linsey, R. K., Kohler, M. A. and J. L. H. Paulhus (1982) *Hydrology for Engineers,* McGraw-Hill Book Company.

Lu, N. and W. J. Likos (2004) *Partially Saturated Soil Mechanics,* John Wiley and Sons: Hoboken.

Mao, L. M., Bergman, M. J. and C. C. Tai (2002) 'Evapotranspiration measurement and estimation of three wetland environments in the upper St. Johns river basin', *Journal of the American Water Resources Association,* 38, (5), pp. 1271-1285.

Maulem, Y. (1976) 'A new model for predicting the hydraulic conductivity of partially saturated porous media', *Water Resources Research,* 12, (3), pp. 513-522.

Milly, P. C. D (1982) 'Moisture and heat transport in hysteretic, inhomogeneous porous media: A matric head based formulation and a numerical model', *Water Resources Research*, 18(3), pp. 489-498.

Montieth, J. L. (1965) 'Evaporation and Environment', *Proceedings of the 19th Symposium of the Society for Experimental Biology,* Cambridge University Press, New York, pp 205-233.

Morgenstern, N. R. (1979) 'Properties of compacted clays. In contribution to Panel Discussion, Session IV' *Proceedings of the 6th Pan-american Conference on Soil Mechanics and Foundation Engineering,* Lima, Peru, 3, pp 349-354.

MottMacdonald (2006) *Interpretive Monitoring and Modelling Report,* Reference :212374/FNG/IMR/005/A, Unpublished report for London Underground Limited, MottMacdonald: Croyden.

MottMacdonald (1999a) *LUL Research Stage II Assessment of Embankments,* Reference :51683/REP/F&G/200/B, Unpublished report for London Underground Limited, MottMacdonald: Croyden.

MottMacdonald (1999b) *LUL Research Stage II Assessment of Cuttings*, Reference :51683/F&G/REP/300/B, Unpublished report for London Underground Limited, MottMacdonald: Croyden.

MottMacdonald (1998) *Ground Investigation of Central and Metropolitan Lines, FLAC analysis*, Reference :45581/F&G/REP/360/A, Unpublished report for London Underground Limited, MottMacdonald: Croyden.

Muneer, T. (1997) *Solar Radiation and Daylight Models for Energy Efficient Design of Buildings*, Oxford Architectural Press: Oxford.

Ng, C. W. W. and Y. W. Pang (2000) 'Influence of stress state on soil-water characteristics and slope stability', *Journal of Geotechnical and Geoenvironmental Engineering,* 126 (2), pp. 157-166.

Nyambayo, V. I. (2004) *Numerical Modelling of Evapotranspiration and its Influence on Embankments,* Unpublished PhD Thesis: University of London.

Nyambayo, V. P., Potts, D. M. and T. I. Addenbrooke (2004) 'The influence of permeability on the stability of embankments experiencing seasonal cyclic pore water pressure changes', *Advances in Geotechnical Engineering: Proceedings of the Skempton Conference,* 2, pp. 898-910.

O'Brien, A. S., Ellis, E. A. and D. Russell (2004) 'Old railway embankment clay fill - laboratory experiments, numerical modelling and field behaviour', *Advances in Geotechnical Engineering: The Skempton Conference,* London, Thomas Telford.

Parker, J. C., Lenhard, R. J. and T. Kuppusamy (1987) 'A parametric model for constitutive properties governing multiphase flow in porous media', *Water Resources Research,* 23 (4), pp. 618-624.

Parkin, G. (1996) *A Three Dimensional Variably-Saturated Subsurface Modelling System for River Basins*, Unpublished PhD Thesis: University of Newcastle upon Tyne.

Peaceman, D. W. (1977) *Fundamentals of numerical reservoir simulation,* Elsevier Scientific Publishing Company.

Penman, H. L. (1956) 'Evaporation: an introductory survey', *Netherlands Journal of Agricultural Science,* 4, pp. 9-29.

Penman, H. L. (1948) 'Natural evaporation from open water, baresoil and grass', *Proceedings of the Royal Society of London, Series A: Mathematical and Physical Sciences,* 103, pp. 120-146.

Perry, J., Pedley, M. and M. Reid (2001). *Infrastructure Embankments – condition appraisal and remedial treatment*, CIRIA publication C550.

Pham, H. Q., Fredlund, D. G. and S. L. Barbour (2003) 'A practical hysteresis model for the soil-water characteristic curve for soils with negligible volume change', *Geotechnique,* 53 (2), pp. 293-298.

Potts, D. M. and L. Zdravkovic (1999) *Finite element analysis in geotechnical engineering theory,* Thomas Telford.

Potts, D. M., Kovacevic, K. and P. R. Vaughan (1997) 'Delayed collapse of cut slopes in stiff clay', *Geotechnique,* 47 (5), pp. 953-982.

Prassad, R. (1988) 'A linear root water uptake model', *Journal of Hydrology*, 99, pp 297-306.

Priestly, C. H. B. and R. J. Taylor (1972) 'On the assessment of surface heat flux and evaporation using large scale parameters', *Monthly Weather Review*, 100, pp. 81-92.

Richards, L. A. (1931) 'Capillary conduction of liquids through porous porous mediums', *Physics,* 1, pp. 318-333.

Ridley, A., Brady, K. C. and P. R. Vaughan (2003) *Field Measurements of Pore Water Pressures*, TRL Report TRL555 ISSN 09648-4107.

Rouainia, M., Davies, O., O'Brien, T. and S. Glendinning (2009) 'Numerical modelling of climate effects on slope stability', *Proceedings of the Institution of Civil Engineers, Engineering Sustainability*, 162, ES2, pp 81-89.

Rushton, K. R. (2003) *Groundwater hydrology conceptual and computational models,* Wiley.

Rutter, A. J., Kershaw, K. A., Robins, P. C. and A. J. Morton (1971/1972) 'A predictive model of rainfall interception in forests,1. Derivation of the model from observations in a plantation of corsican pine', *Agricultural Meteorology,* 9, pp. 367-384.

Sillers, W. S., Fredlund, D. G. and N. Zakerzadeh (2001) 'Mathematical attributes of some soil-water characteristic curve models', in D. G. Toll (ed) *Partially saturated soil concepts and their application in geotechnical practice,* Kluwer Academic Publishers.

Simunek, J., Van Genuchten, M. T. and M. Sejna (2005) '*The HYDRUS-1D Software Package for Simulating the One-Dimensional Movement of Water, Heat, and Multiple Solutes in Variably-Saturated Media',* Department of Environmental Sciences University of California Riverside: Riverside, California

Skempton, A. W. (1985) 'Residual strength of clays in landslides, folded strata and the laboratory', *Geotechnique,* 35 (1), pp. 3-18.

Smethurst, J. A., Clarke, D. and W. Powrie (2006) 'Seasonal changes in pore water pressure in a grass-covered cut slope in London Clay', *Geotechnique,* 56 (8), pp. 523-537.

Smith, P. G. C. (2003) *Numerical Analysis of Infiltration into Partially Saturated Slopes.* Unpublished PhD Thesis: University of London.

Stannard, D. I. (1993) 'Comparison of Penman-Monteith, Shuttleworth-Wallace, and modified Priestly-Taylor evapotranspiration models for wildland vegetation in semiarid rangeland', *Water Resources Research,* 29 (5), pp. 1379-1392.

Staple, W. J. (1974) 'Modified Penman equation to provide the upper boundary condition in computing evaporation from soil', *Soil Science Society of America Proceedings, 38, pp. 892-839.*

Summer, D. M. and J. M. Jacobs (2005) 'Utility of Penman-Monteith, Priestly-Taylor, reference evapotranspiration, and pan evaporation methods to estimate pasture evapotranspiration', *Journal of Hydrology,* 308, pp. 81-104.

Tami, D., Rahardjo, H. and E. Leong (2004) 'Effects of Hysteresis on Steady-State Infiltration in Partially Saturated Slopes', *Journal of Geotechnical and Geoenvironmental Engineering,* 130 (9), pp. 956-967.

Terzaghi, K. (1943) *Theoretical soil mechanics,* John Wiley and Sons: New York

Tindall, J. A. and J. R. Kunkel (1999) *Partially saturated zone hydrology for scientists and engineers,* Prentice Hall: London.

Toll, D. G. (1990) 'A framework for partially saturated soil behaviour', *Geotechnique,* 40, (1), pp. 31-44.

Vanapalli, S. K. and D. G. Fredlund (2000) 'Comparison of different procedures to predict the shear strength of unsaturated soils uses the soil-water characteristic curve', *American Society of Civil Engineers, Special Publication,* 99, pp. 195-209.

Vanapalli, S. K., Fredlund, D. G. and D. E. Pufahl (1999) 'The influence of soil structure and stress history on the soil-water characteristics of a compacted till', *Geotechnique,* 49 (2), pp. 143-159.

Vanapalli, S. K., Fredlund, D. G., Pufahl, D. E. and A. W. Clifton (1996) 'Model for the prediction of shear strength with respect to soil suction', *Canadian Geotechnical Journal,* 33 pp. 379-392.

Van Genuchten, M. T. (1980) 'A closed-form equation for predicting the hydraulic conductivity of partially saturated soils', *Soil science society of America journal,* 44, pp. 892-898.

Vogel, T. and M. Cislerova (1988) 'On the reliability of unsaturated hydraulic conductivity calculated from the moisture retention curve', *Transport in Porous Media,* 3, pp. 1-15.

Wheeler, S. J. and V. Sivakumar (1995) 'An elastoplastic critical state framework for unsaturated soil', *Geotechnique,* 45 (1), pp. 35-53.

Wilson, G.W. (1990) *'Soil evaporative fluxes for geotechnical engineering problems'*, Unpublished PhD Thesis, University of Saskatchewan: Saskatoon, Sask.

Wilson, L. G. and J. N. Luthin (1963) 'Effect of air flow ahead of the wetting front on infiltration', *Soil Science,* 96, pp. 136-143.